UNIVERSITY OF SILESIA IN KATOWICE

Faculty of Science and Technology

August Chełkowski Institute of Physics

Patryk Rurka

DOCTORAL DISSERTATION

NEW INSIGHTS INTO MULTIFACETED TARGETED THERAPY FOR TREATMENT OF GLIOBLASTOMA MULTIFORME

Supervisor: dr hab. Anna Mrozek-Wilczkiewicz, Prof. UŚ

Co-supervisor: dr Katarzyna Malarz, Prof. UŚ

Chorzów, 2026

This work was supported by the OPUS research grant titled "*New insights into multifaceted targeted therapy for treatment of glioblastoma multiforme*" (grant no. 2019/35/B/NZ5/04208) from the National Science Centre, Poland.

NATIONAL SCIENCE CENTRE
POLAND

Podziękowania (Acknowledgements)

Składam serdeczne podziękowania moim promotorom w szczególności dr Katarzynie Malarz, za cierpliwość, wsparcie oraz życzliwość w okresie pisania doktoratu oraz czasu kiedy powstawał ten doktorat.

Dziękuję także, mojej Rodzinie za wsparcie i obecność.

Serdecznie także dziękuje, wszystkim moim kolegom i koleżankom z zespołu Biofizyki Farmaceutycznej oraz z Wydziału Nauk Ścisłych i Technicznych za okazaną życzliwość, rady oraz spojrzenie na tą pracę z innej perspektywy.

Dziękuje także wszystkim ludziom dobrej woli, którzy przyczynili się do powstania tego dzieła.

Contents

1. List of publications included in the doctoral thesis

1. Malarz K., Kuczak M., **Rurka P.**, Rawicka P., Boguszewska-Czubara A., Jampilek J., Mularski J., Musiol R., Mrozek-Wilczkiewicz A.: “Unveiling the role of Ndrg1 gene on the oxidative stress induction behind the anticancer potential of styrylquinazoline derivatives”. Scientific Reports, 15, 16081 (2025). doi.org/10.1038/s41598-025-99277-1.

IF_{2025} = 3.9; MNiSW: 140

2. **Rurka P.**, Mularski J., Ziola P., Boguszewska-Czubara A., Jampilek J., Mrozek-Wilczkiewicz A., Malarz K.: “An insight into the anticancer potential of sulfonated styrylquinazolines as multifunctional agents targeting microtubules”. Bioorganic Chemistry, 170, 109517 (2026). doi.org/10.1016/j.bioorg.2026.109517.

IF_{2026} = 4.5; MNiSW: 100

3. **Rurka P.**, Cieślik W., Płaziński W., Stępnik K., Boguszewska-Czubara A., Kot E., Musioł R., Jasica M., Mrozek-Wilczkiewicz A., Malarz K.: “A novel quinazolinone insulin receptor inhibitor and its synergy with an EGFR inhibitor in glucose-driven glioblastoma”. Molecular Oncology, 2026. doi.org/10.1002/1878-0261.70274.

IF_{2026} = 4.5; MNiSW: 140

Total IF score = 12.9

Total MNiSW score = 380

2. List of Abbreviations

WHO – World Health Organization

GBM – glioblastoma

SOC – Standard of Care

OS – overall survival

CNS – central nervous system

MMR – Mismatch Repair

TMZ – temozolomide

Gy – Gray

BBB – blood-brain Barrier

FDA – Food and Drug Administration

EGFR - epidermal growth factor receptor

mTOR - mammalian target of rapamycin

RTK - receptor tyrosine kinase

MGMT - o6-methylguanine-DNA methyltransferase

PDGFR - platelet-derived growth factor receptor

PTEN - phosphatase and tensin homolog

IGF1R - insulin-like growth factor 1 receptor

InsR - insulin receptor

MT – tumor microtubes

MTAs - microtubule-targeting agents

ER - endoplasmic reticulum

ADME - Absorption, Distribution, Metabolism and Excretion

PDX - patient-derived xenograft

ROS – reactive oxygen species

qRT-PCR - Quantitative Reverse Transcription Polymerase Chain Reaction

TI – therapeutic index

IC_{50} - half-maximal inhibitory concentration

SD - standard deviation

NHA - normal human astrocytes

3. Streszczenie

Glejak jest najbardziej agresywnym i najczęstszym pierwotnym złośliwym nowotworem mózgu u dorosłych. Charakteryzuje się szybką proliferacją, heterogennością molekularną i opornością na leczenie. Pomimo obecnego wielopoziomowego standardu leczenia, pięcioletnia przeżywalność wciąż wynosi poniżej 10%. Niepowodzenie konwencjonalnego protokołu leczenia wynika z nadmiernej sygnalizacji sieci kinaz tyrozynowych, takich jak EGFR i IGF1R/InsR, a także ze zmian genetycznych, takich jak utrata PTEN i mutacje w genie *TP53*. Dodatkowymi czynnikami ograniczającymi skuteczność terapii są obecność bariery krew–mózg oraz adaptacje metaboliczne komórek nowotworowych.

Niniejsza rozprawa doktorska oceniła potencjał przeciwnowotworowy nowych pochodnych styrylochinazoliny i styrylochinazolonu oraz wyjaśniła ich wielopłaszczyznowy mechanizm działania na modelu 2D komórek ludzkiego glejaka. Zbadano trzy grupy związków: pochodną IS20 zawierającą grupę benzodioksolową, sulfonowane styrylochinazoliny (TS1–TS6) i styrylochinazolinony (W1A, W1B, W1C, W2B). Wyniki wskazują na trójpłaszczyznowy mechanizm działania badanych pochodnych. Po pierwsze, pochodna IS20 wykorzystuje podatność komórek glejaka na stres oksydacyjny, działając jako wewnątrzkomórkowy chelator żelaza, który indukuje generowanie reaktywnych form tlenu, zatrzymuje cykl komórkowy i ostatecznie wywołuje śmierć komórek. Po drugie, sulfonowane pochodne z serii TS zaburzają dynamikę polimeryzacji i depolimeryzacji mikrotubul, prowadząc do zatrzymania cyklu komórkowego w fazie G2/M, oraz osłabiając sygnalizację osi EGFR/mTOR. Po trzecie, najbardziej aktywna pochodna z grupy styrylochinazolonów - W1B hamuje aktywność IGF1R oraz EGFR, obniżając fosforylację Akt na szlaku PI3K/Akt/mTOR. W warunkach podwyższonego stężenia glukozy W1B zachowuje aktywność hamującą tylko wobec IGF1R, jednak skojarzenie z inhibitorem EGFR – dakomitynibem przywraca hamowanie EGFR przy zachowaniu inhibicji IGF1R i prowadzi do zwiększonego efektu terapeutycznego.

Zidentyfikowano trzy główne związki wiodące: IS20 do terapii ukierunkowanej na stres oksydacyjny; TS5 jako antymitotyczny inhibitor sygnalizacji EGFR/mTOR; oraz W1B do terapii skojarzonej ukierunkowanej na szlaki kompensacji metabolicznej. Otrzymane wyniki wskazują, że styrylochinazoliny i styrylochinazolinony stanowią obiecujące związki wiodące do dalszych badań przedklinicznych, wykazujące przewagę nad podejściami terapeutycznymi ukierunkowanymi na pojedynczy cel molekularny w leczeniu glejaka.

4. Abstract

Glioblastoma is the most aggressive and most common primary malignant brain tumor in adults. It is characterized by rapid proliferation, molecular heterogeneity, and resistance to therapy. Despite the current multi-level standard of care, the five-year survival rate remains below 10%. The failure of the conventional treatment protocol results from excessive signaling through tyrosine kinase networks, such as EGFR and IGF1R/InsR, as well as from genetic alterations, including PTEN loss and *TP53* mutations. Additional factors limiting therapeutic efficacy include the blood–brain barrier and metabolic adaptations of cancer cells.

This doctoral dissertation evaluated the anticancer potential of novel styrylquinazoline and styrylquinazolinone derivatives and elucidated their multifaceted mechanism of action in 2D models of human glioblastoma cells. Three groups of compounds were investigated: the IS20 derivative containing a benzodioxole group, sulfonated styrylquinazolines (TS1–TS6), and styrylquinazolinones (W1A, W1B, W1C, W2B). The results indicate a three-pronged mechanism of action for the studied derivatives. First, the IS20 derivative exploits glioblastoma cells' vulnerability to oxidative stress by acting as an intracellular iron chelator that induces reactive oxygen species generation, cell cycle arrest, and, ultimately, cell death. Second, the sulfonated TS-series derivatives disrupt microtubule polymerization/depolymerization dynamics, leading to G2/M cell cycle arrest and attenuating EGFR/mTOR axis signaling. Third, the most active derivative of the styrylquinazolinone group – W1B – inhibits IGF1R and EGFR activity, reducing Akt phosphorylation along the PI3K/Akt/mTOR pathway. Under high-glucose conditions, W1B retains inhibitory activity only against IGF1R; however, its combination with the EGFR inhibitor dacomitinib restores EGFR inhibition while maintaining IGF1R suppression, leading to an enhanced therapeutic effect.

Three main lead compounds have been identified: IS20 for oxidative stress-targeted therapy; TS5 as an antimitotic inhibitor of EGFR/mTOR signaling; and W1B for combination therapy targeting metabolic compensation pathways. The results indicate that styrylquinazolines and styrylquinazolinones are promising lead compounds for further preclinical studies and demonstrate superiority over single-target agents in glioblastoma treatment.

5. Introduction

5.1 Glioblastoma: Characteristics

According to the World Health Organization (WHO), cancer is one of the leading causes of death worldwide. Some types of malignant neoplasms have an exceptionally low 5-year survival rate; among them are pancreatic cancer, stage IV esophageal cancer with metastases, and grade 4 gliomas.

Gliomas are one of the most prevalent primary brain neoplasms arising from glial cells or neural stem and progenitor cells through genetic alterations. Currently, the glioma family can be divided into several subtypes, including pediatric-type diffuse low-grade gliomas, pediatric-type diffuse high-grade gliomas, glioneuronal and neuronal tumors, circumscribed astrocytic gliomas, and adult-type diffuse gliomas, which include glioblastoma (GBM). According to the fifth edition of the WHO classification from 2021, central nervous system (CNS) tumors are graded on a scale of 1 to 4. Malignant gliomas are distinguished from benign tumors by their advanced histological grade: the higher the grade, the more aggressive the clinical course and the poorer the prognosis. Grading is based on an integrated diagnosis combining histological features with molecular markers, with the molecular features given higher importance [1]. For adult-type diffuse gliomas, this classification relies primarily on IDH1/2 mutation, 1p/19q codeletion, and CDKN2A/B deletion status, along with histological criteria such as necrosis and microvascular proliferation.

Glioblastoma is graded as a WHO Grade 4 glioma with IDH-wildtype, and harbors one or more of the following genetic markers: *TERT* promoter mutation, epidermal growth factor receptor (*EGFR)* gene amplification, and chromosome +7/-10 alteration. GBM represents the most aggressive and prevalent form of primary malignant brain tumor in adults, characterized by rapid cellular proliferation, intense mitotic activity, infiltration into surrounding brain tissue, and poor clinical prognosis. The histological characteristics of GBM include cytological atypia, anaplasia, pseudopalisading necrosis, areas of necrosis, microvascular changes, and microscopic extension beyond the tumor border. In addition, the exceptional aggressiveness of glioblastoma and the challenges of treating it stem from a highly immunosuppressive tumor microenvironment, the accumulation of numerous genetic mutations in the major signaling pathways that regulate cell proliferation, growth, and survival, the blood-brain barrier (BBB), and subpopulation heterogeneity. The most common genetic mutations that occur in GBM are listed in Table 1 below.

Gene/Chromosome	Alteration	Prevalence (%)
Chromosome 10	Complete arm deletion	70-90
PTEN	Mutation/deletion	40
EGFR	Amplification	30-80
TP53	Mutation	25
TERT promoter	Mutation	80
CDKN2A	Homozygous deletion	10-20
MGMT promoter	Methylation	30-50

Table 1. Common genetic alteration in glioblastoma [2-12].

Glioblastoma appears in two ways: as primary tumors that arise de novo or as tumors that arise from lower-grade gliomas. This historical primary/secondary distinction has been superseded by the 2021 WHO report, in which glioblastoma is defined exclusively as an IDH-wildtype diffuse astrocytic glioma in adults; tumors formerly designated "secondary" or "IDH-mutant" glioblastoma, i.e., those progressing from lower-grade lesions, are now classified separately as astrocytoma, IDH-mutant, WHO Grade 4 [13, 14]. The two entities differ markedly in their clinical and molecular profiles. IDH-wildtype, which constitutes the large majority of cases historically diagnosed as glioblastoma, predominantly affects older adults (median age at diagnosis of 65), with a slight male predominance, and carries a median overall survival of less than two years despite aggressive therapy [15, 16]. By contrast, IDH-mutant astrocytomas arise in younger patients (median around 45 years) and are associated with substantially longer survival [15, 16]. At the molecular level, IDH-wildtype is characterized by TERT promoter mutation (over 80% of cases), EGFR amplification, which occurs in 30–80% of tumors and is associated with shortened survival, as well as a loss of PTEN (via mutation or chromosome 10 loss), which is identified in 15–40% of cases [17]. Homozygous deletion of CDKN2A/B is now recognized as a key molecular grading criterion. *TP53* mutations are found in approximately 25% of IDH-wildtype GBM [18]. In contrast, IDH-mutant astrocytomas carry the defining IDH1/2 hotspot mutation, together with TP53 mutation and loss of ATRX expression, the latter serving as a diagnostic marker of astrocytic lineage. EGFR amplification and TERT promoter mutations are uncommon [19, 20]. Recurrent glioblastoma, which survives standard of care (SOC), also displays distinct biomarkers. Genomic profiling reveals that while TERT promoter mutations and chromosome 7 gain/10 loss are typically maintained at clonal events [21]. Genetic alterations in EGFR, PTEN, and NF1 frequently emerge via evolution

under therapeutic pressure [22]. Recurrence is also driven by dynamic shifts in the tumor microenvironment, including the activation of microglia/macrophages, and by transcriptional reprogramming that upregulates DNA damage response pathways, ultimately giving resistance to alkylating chemotherapy [23]. The status of O6-methylguanine-DNA methyltransferase *(MGMT)* promoter methylation remains the strongest predictive biomarker for temozolomide response in IDH-wildtype glioblastoma, with methylated tumors demonstrating significantly prolonged survival compared to unmethylated counterparts. This genetic alteration is of particular clinical value as its presence is associated with a more favorable prognosis and an increased response to certain therapies, which will be discussed in greater detail in the section on therapeutic approaches.

5.2 Glioblastoma: Standard of care

Despite the current SOC, which includes maximal surgical resection followed by radiotherapy and chemotherapy with temozolomide, as depicted in Figure 1, patient outcomes remain profoundly poor, with a median overall survival (OS) of approximately 14 to 16 months and a five-year survival rate of less than 5–10% [24]. Notably, GBM is mostly common in patients between 60–80 years of age, with a median age of diagnosis of 64–66, and is more common among men than women [25]. Glioblastoma detection and removal are exceptionally challenging due to its highly infiltrative growth pattern along deep white matter tracts, making true, complete surgical eradication anatomically impossible in many cases. Despite billions of research dollars, innumerable clinical trials, and an aggressively high death rate, the prognosis of patients diagnosed with GBM has remained extremely low and practically unchanged for decades.

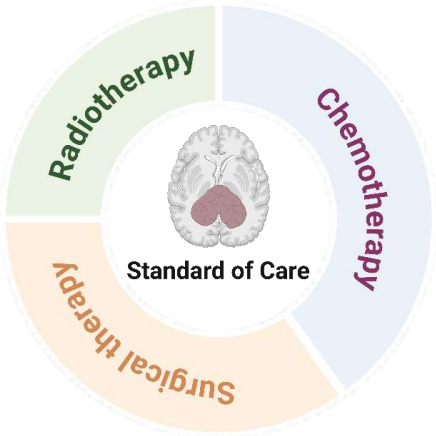

Figure 1. Glioblastoma therapeutic approach always includes radiotherapy, chemotherapy and surgical therapy.

The current foundational SOC for patients with newly diagnosed GBM, widely known as the Stupp protocol, is a highly coordinated, multimodal approach established by the pivotal joint EORTC-NCIC phase III trial (EORTC 26981-22981/NCIC CE.3) [26]. Management typically begins with maximal safe surgical resection. Surgery in the GBM is particularly challenging because the tumor must be removed while preserving the immediately adjacent healthy, functionally eloquent brain tissue to avoid permanent neurological deficits. To maximize the extent of resection, a critical prognostic factor, neurosurgeons increasingly utilize advanced intraoperative adjuncts, such as fluorescence-guided surgery with the prodrug 5-aminolevulinic acid (5-ALA) [27, 28]. 5-ALA exploits the preferential accumulation of fluorescent protoporphyrin IX in malignant tissue, enabling the real-time visual differentiation of neoplastic tissue from healthy brain parenchyma [29]. Following surgical intervention, the Stupp protocol prescribes fractionated focal radiotherapy. The standard regimen delivers a total dose of 60 Gray (Gy), divided into 30 daily fractions of two Gy over six weeks. Because radiotherapy can also injure the adjacent healthy brain and cause neurotoxicity, precise techniques, such as intensity-modulated radiation therapy or volumetric-modulated arc therapy, are used to spare functional tissue. Concurrent with this six-week radiotherapy phase, the primary response drug, temozolomide (TMZ), is administered orally at a daily dose of 75 mg/m^2 [30]. After a four-week treatment break, patients enter the adjuvant maintenance phase, receiving up to six cycles of TMZ administered for five consecutive days every 28 days at an escalated dose of 150 to 200 mg/m^2 [31]. The original Stupp trial demonstrated that the addition of concurrent and adjuvant TMZ to radiotherapy extended the median OS from 12.1 months to 14.6 months and increased the two-year survival rate from 10.4% to 26.5% [32].

TMZ is approved by the Food and Drug Administration (FDA) and is regarded as the gold standard of GBM therapy. It is a small (194 Da), lipophilic, DNA-alkylating agent that effectively crosses the restrictive BBB [33]. TMZ spontaneously hydrolyzes to its active metabolite MTIC, which decomposes into a reactive methyldiazonium cation, which alkylates DNA to form lesions such as N7-methylguanine, 3-methyladenine, and the highly cytotoxic O6-methylguanine [34]. During DNA replication, these O6-methylguanine adducts mispair with thymine. The mismatch repair (MMR) system recognizes the mispair but cannot remove the modified guanine, leading to a futile repair cycle that ultimately generates DNA double-strand breaks, cell cycle arrest at the G2/M phase, and apoptosis. TMZ is, nonetheless,

associated with serious adverse effects, including severe myelosuppression, lymphopenia, and gastrointestinal toxicity, and may drive adaptive hypermutations in surviving GBM cells [35].

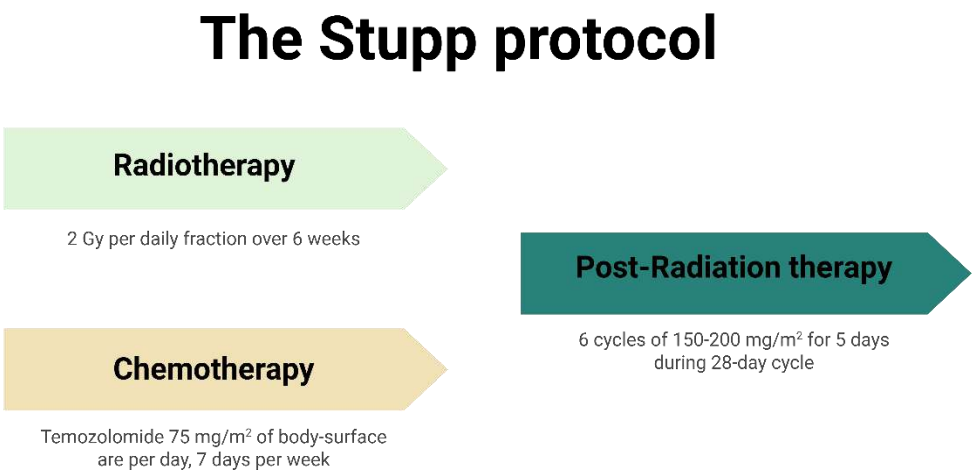

Figure 2. Original Stupp protocol used in GBM treatment [36].

The efficacy of the Stupp protocol showcased in Figure 2 depends strongly on the epigenetic status of the *MGMT* gene, the principal predictive and prognostic biomarker [37]. *MGMT* encodes a DNA repair enzyme that removes alkyl groups from the O6 position of guanine, directly neutralizing the cytotoxic lesions induced by TMZ. In approximately 40% of IDH-wildtype GBMs, the *MGMT* promoter is hypermethylated DNA [38], which silences the gene, abolishes enzyme synthesis and renders cancer cells highly susceptible to TMZ-induced apoptosis. Consequently, patients with a methylated *MGMT* promoter survive substantially longer than those with an unmethylated promoter, the latter conferring intrinsic resistance to alkylating chemotherapy.

Despite this multimodal SOC, GBM remains essentially incurable, and recurrence is nearly universal. The limited efficacy of these standard regimens reflects a deeper obstacle, which is the profound genetic, epigenetic, and cellular heterogeneity of GBM, which sustains resistant subpopulations and drives recurrence.

5.3 Glioblastoma: Heterogeneity and therapeutic challenges

The development of new therapeutic compounds for GBM is constrained by several intrinsic obstacles: extreme inter- and intratumoral heterogeneity, the limited drug access imposed by the BBB, and aggressive genomic alterations in critical signal transduction networks, most notably the EGFR and mammalian target of rapamycin (mTOR) pathways [39].

The *EGFR* gene encodes a transmembrane receptor tyrosine kinase (RTK), which is the most frequently altered RTK in GBM, with mutation or amplification occurring in approximately 40%-60% of primary tumors. Under physiological conditions, EGFR regulates cell survival, migration, and proliferation. In GBM, however, it undergoes profound structural aberrations, the most prevalent of which is the EGFRvIII mutation—an in-frame deletion of exons 2 through 7 (an 801 base-pair deletion). This truncation removes the extracellular ligand-binding domain, rendering the receptor unable to bind EGF or other ligands. Notably, EGFRvIII retains continuous, ligand-independent constitutive kinase activity that persistently drives downstream oncogenic signaling. In addition, the EGFRvIII variant almost invariably arises in the combination of wild-type EGFR amplification, generating a pathogenic paracrine loop and promoting transactivation of other RTKs, such as c-MET, PDGFRA, and EPHA2 [40]. Its expression also enhances signaling through downstream effectors, including the STAT3 and PI3K/AKT axes, which promote cell survival, increase invasiveness, drive angiogenesis, and contribute to resistance to radio- and chemotherapy in GBM [41]. When EGFR is pharmacologically suppressed, GBM cells rapidly co-activate functionally redundant RTKs—most prominently the insulin-like growth factor 1 receptor (IGF1R) and the insulin receptor (InsR)—which bypass the EGFR blockade to sustain downstream PI3K/Akt/mTOR signaling. In EGFR-dependent GBM cells expressing these receptors, the InsR/IGF1R axis acts as the dominant regulator of AKT: insulin or IGF1 can restore AKT phosphorylation even in the presence of EGFR inhibitors, whereas STAT3 and MEK/ERK remain suppressed [42].

IGF1R overexpression is a recognized poor prognostic factor in GBM that actively protects tumor cells against apoptosis [43]. Crucially, IGF1R signaling maintains the activation of downstream PI3K and AKT pathways even in the presence of potent EGFR or PDGFR inhibitors, thereby neutralizing the therapeutic efficacy of monotherapies [44, 45]. Consequently, effective targeted therapy in GBM is unlikely to succeed with single-target agents and instead requires polypharmacological or synergistic compounds capable of simultaneously extinguishing multiple nodes of this redundant oncogenic network.

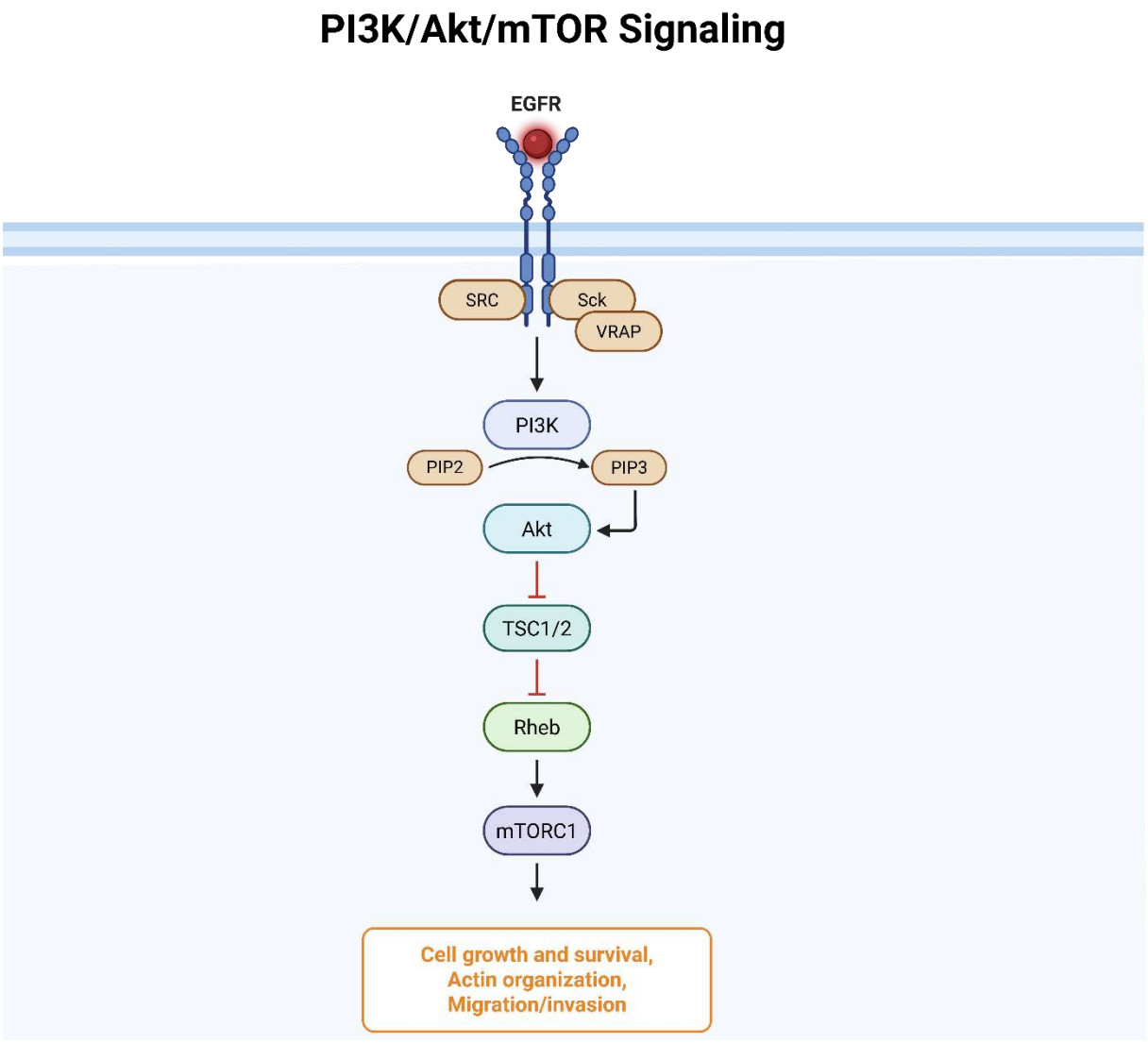

Figure 3. Simplified PI3K/Akt/mTOR signaling pathway (created by Biorender).

The PI3K/AKT/mTOR pathway is central to the pathogenesis of GBM; genetic alterations that activate this pathway have been reported in approximately 90% of tumors. The pathway regulates cell growth, proliferation, angiogenesis, DNA repair, apoptosis, autophagy, and nutrient sensing [46]. It is typically initiated by active RTKs (such as EGFR or PDGFR), which stimulate phosphoinositide 3-kinase (PI3K) to convert PIP2 into PIP3, as shown in Figure 3. PIP3, in turn, recruits AKT to the plasma membrane, where it undergoes full activation (a process partially mediated by mTORC2). Once activated, AKT phosphorylates numerous downstream targets, thereby suppressing apoptosis and activating mTORC1. Sustained signaling through this pathway is one of the principal reasons why targeted therapies fail in GBM. Beyond upstream RTK amplification, the pathway is frequently hyperactivated by the

loss or mutation of the tumor suppressor PTEN (phosphatase and tensin homolog) [47]. PTEN normally dephosphorylates PIP3 back to PIP2, acting as a critical brake on the cascade; its loss removes this constraint, leading to unchecked AKT and mTOR activity that drives tumor growth, lipogenesis, and therapy resistance. In addition, mTORC2 signaling contributes to alkylating agent resistance because the mTORC2/SGK1 axis induces N-Myc downstream-regulated gene 1 (NDRG1), a protein that binds and stabilizes the MGMT enzyme, thereby protecting tumor cells against TMZ [48, 49].

The clinical management of GBM is persistently challenged by an almost inevitable recurrence, a phenomenon fundamentally driven by the persistence of glioblastoma stem-like cells (GSCs) [50, 51]. These highly plastic cells serve as a reservoir for tumor regrowth, as they can survive initial radio- and chemotherapy, only to reconstitute the heterogeneous tumor bulk post-treatment [52]. GSCs represent a rare subpopulation at the apex of the tumor hierarchy, possessing robust self-renewal capacity and the ability to differentiate into the complex cellular lineages that comprise the tumor mass. They reside in specialized microanatomical niches—specifically the perivascular, invasive, and hypoxic regions—which offer sanctuary from conventional therapies. In the hypoxic necrotic core, for instance, oxygen deprivation stabilizes hypoxia-inducible factors (HIFs), which simultaneously promote aberrant angiogenesis and shift GSCs into a dormant, quiescent state that renders them virtually invisible to treatments targeting rapidly dividing cells [53].

Another factor is the tumor microenvironment (TME), which further contributes to treatment failure. GBM is characterized as an immunologically "cold" tumor, replete with a dense infiltration of non-neoplastic stromal and immune cells that the tumor hijacks to support its survival [54]. Up to 40% of the tumor mass can consist of tumor-associated macrophages (TAMs) and microglia [55]. Through the secretion of cytokines, such as transforming growth factor-beta (TGF-β), interleukin-10 (IL-10), and prostaglandin E2 (PGE2), GSCs polarize myeloid cells toward an immunosuppressive, protumorigenic M2-like phenotype. IGF1R, frequently overexpressed on GSCs, reinforces this paracrine network by enhancing TGF-β and IL-10 production and further suppressing innate immune surveillance [56, 57]. These M2-TAMs actively paralyze local anti-tumor immunity by inhibiting the infiltration and cytotoxic functions of CD8+ T cells and natural killer cells, while promoting the expansion of regulatory T cells (Tregs).

Given the hyperactivation of specific molecular nodes like EGFR and PDGFR, early therapeutic paradigms focused on single-point inhibition. However, first-generation tyrosine

kinase inhibitors (TKIs) targeting EGFR, such as gefitinib and erlotinib, completely failed to provide survival benefits in phase II and III GBM clinical trials despite their success in non-small cell lung cancer (NSCLC) [58, 59]. This failure stems from several factors. Primarily, gefitinib and erlotinib were designed to target the intracellular ATP-binding domain of activating mutations common in lung cancer. In contrast, the dominant driver in GBM (EGFRvIII) is an extracellular domain truncation that does not alter the kinase domain itself, rendering these specific inhibitors highly ineffective. Additionally, although these TKIs are lipophilic, they are highly susceptible to P-glycoprotein-mediated efflux at the BBB, resulting in sub-therapeutic accumulation within the CNS [60].

More critically, the profound intratumoral heterogeneity and extensive signaling redundancy in GBM severely undermine the efficacy of monotherapies. When a single molecular node (e.g., EGFR) is inhibited, cells rapidly engage compensatory receptor tyrosine kinases (e.g., c-MET, PDGFR, or IGF1R) to bypass the blockade and reactivate downstream PI3K or MAPK survival cascades [61, 62]. Consequently, overcoming the redundant resistance of GBM necessitates a paradigm shift from single-agent monotherapies toward rational, multifaceted, combinatorial targeted therapies. Effective future treatments must simultaneously address the complex signaling web, the immunosuppressive TME, and the physical constraints of the BBB. One primary approach involves multi-kinase inhibition to preemptively block compensatory RTK signaling [63]. Regorafenib, an oral multi-kinase inhibitor that simultaneously targets angiogenic (VEGFR1-3, TIE2), stromal (PDGFR-β), and oncogenic (RAF, RET, KIT) kinases, has shown encouraging efficacy. In the phase II REGOMA trial, regorafenib significantly improved OS in patients with relapsed GBM compared to lomustine chemotherapy, validating this multi-targeted blockade approach [64, 65]. Another strategy combines TKIs with inhibitors of downstream nodes, such as dual EGFR and mTOR inhibition, to sever the escape routes utilized by highly plastic GSCs [66].

As highlighted earlier, the formidable nature of the BBB critically limits the efficacy of targeted therapies, restricting the passage of approximately 98% of small-molecule drugs [67, 68]. To fully comprehend the challenge, one must consider the spatial heterogeneity of the BBB during tumor progression. In the healthy brain, the dynamic neurovascular unit utilizes multi-protein tight junctions (such as claudin-5, occludin, and zonula occludens-1) to stringently restrict paracellular diffusion [69]. During GBM development, hypoxia triggers the massive secretion of pro-angiogenic signals like VEGF and matrix metalloproteinases (MMPs). These enzymes degrade the endothelial basement membrane and tight junctions, forming a leaky,

dysfunctional blood-tumor barrier (BTB) [70]. Crucially, this disruption is highly localized. While the hypoxic tumor core exhibits a hyperpermeable BTB, the infiltrative margins of the tumor—where recurrence inevitably arises—are shielded by an intact and functionally "closed" BBB [71, 72]. Consequently, systemic therapies fail to reach these infiltrating glioblastoma cells. Furthermore, the BBB remains a formidable obstacle due to its aggressive biochemical defenses. Even in regions where the physical barrier is partially disrupted, the luminal membrane of capillary endothelial cells expresses a high density of ATP-binding cassette (ABC) efflux transporters, particularly P-glycoprotein (P-gp/ABCB1) and breast cancer resistance protein (BCRP/ABCG2) [73]. As noted with early TKIs, these active pumps continuously recognize and expel lipophilic small molecules back into the systemic circulation. To overcome these restrictive physiological barriers and achieve therapeutic concentrations in the brain, several advanced strategies are currently under investigation:

1. Drug design: Next-generation small molecules are being rationally engineered (MW < 500 Da, optimized lipophilicity) to evade recognition by ABC efflux transporters. For example, GNE-317 (a PI3K/mTOR inhibitor) and AZD3759 (an EGFR inhibitor) have been structurally modified to reduce their affinity for P-gp and BCRP, resulting in significantly greater BBB penetration than first-generation compounds [74].
2. Pharmacological Efflux Pump Inhibition: The co-administration of competitive dual efflux pump inhibitors, such as elacridar, aims to temporarily paralyze the BBB's active transport machinery and dramatically increase drug accumulation in the tumor core and surrounding healthy brain tissue [75, 76].
3. Engineered Nanocarriers: Lipid-based or polymeric nanoparticles can protect chemotherapeutics from systemic degradation and efflux pump clearance. By functionalizing the surface of these nanocarriers with targeting ligands (such as transferrin or angiopep-2), researchers can exploit receptor-mediated transcytosis to actively shuttle the drug across intact endothelial cells [77].
4. Physical Disruption and Delivery Modalities: Magnetic resonance-guided focused ultrasound combined with intravenous microbubbles applies acoustic energy to mechanically stretch tight junctions, creating a safe, reversible window for systemic drugs to enter the brain. Alternatively, convection-enhanced delivery bypasses the BBB entirely by infusing small molecules directly into the tumor interstitial space via stereotactically placed microcatheters [78].

5.4 Intracellular vulnerabilities in GBM: Microtubule dynamics and redox homeostasis

Beyond signaling cascades, the cytoskeleton, particularly the microtubule network, is indispensable for maintaining cellular architecture, executing mitosis, and facilitating the continuous intracellular trafficking of critical receptors (e.g., EGFR) to the plasma membrane. Microtubules are highly dynamic, cylindrical polymers composed of heterodimers of α- and β-tubulin subunits, as shown in Figure 4.

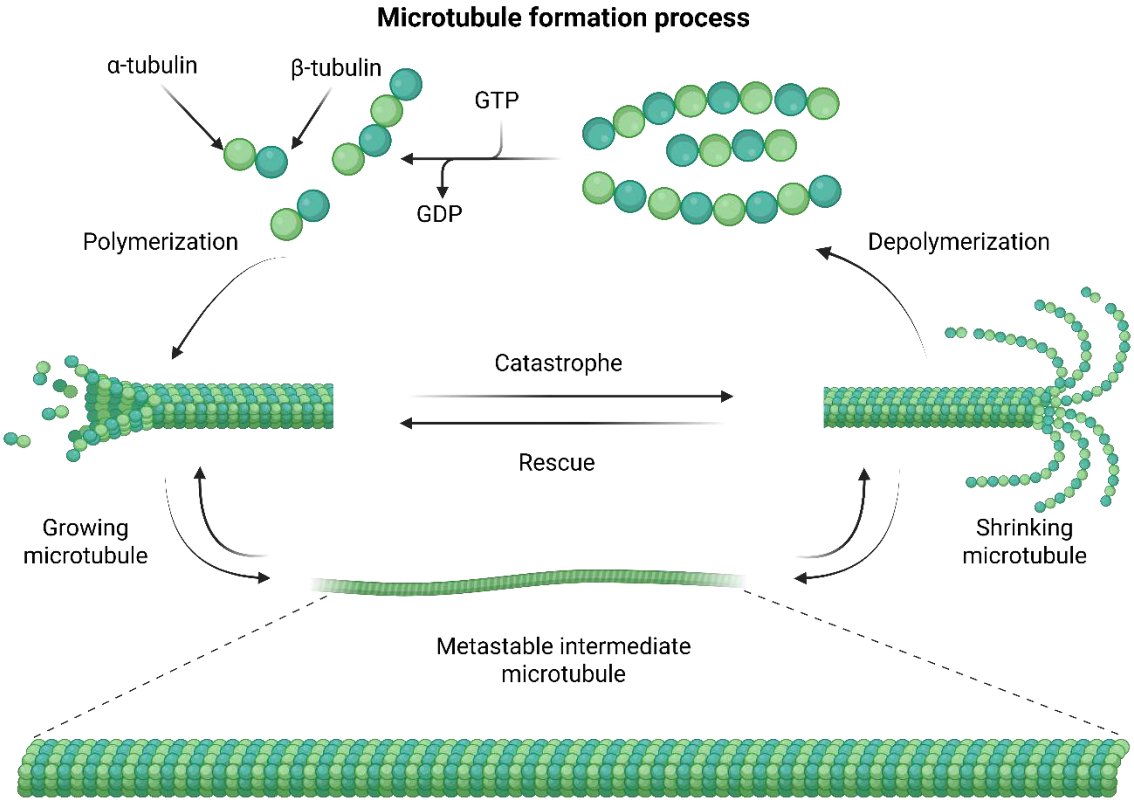

Figure 4. Dynamic microtubule formation process occurring inside living cells (created by Biorender).

Microtubules serve as tracks for the kinesin and dynein motor proteins, which direct the intracellular transport of cargo, including signaling endosomes, mitochondria, lysosomes, and mRNA–protein complexes. During mitosis, the microtubule network reorganizes into the mitotic spindle, in which kinetochore fibers capture and segregate chromosomes to maintain genomic stability [69]. In interphase glioma cells, this motor-driven transport supports the asymmetric distribution of growth factor receptors and integrins, thereby promoting invasion and intercellular crosstalk [79], and it contributes to asymmetric cell division in glioma stem cells, which underlies tumor heterogeneity [80]. In GBM, this transport machinery is frequently co-opted: tumor microtubes actively shuttle mitochondria and resistance factors between connected cells, thereby enhancing tumor cell survival against therapy [81]. In addition, in

GBM, microtubule dynamics are frequently hijacked to support uncontrolled cellular proliferation, aggressive invasion into the healthy brain parenchyma, and the formation of tumor microtubules (MTs). These are specialized network structures that facilitate long-range intercellular communication, calcium signaling, and the distribution of therapeutic resistance factors. Furthermore, the rapid segregation and anterograde transport of pro-tumoral components along these cytoskeletal highways are vital for maintaining the aggressive GBM phenotype. Consequently, microtubule-targeting agents (MTAs) represent a highly potent class of antineoplastic drugs [82, 83]. MTAs disrupt the delicate balance between tubulin polymerization and depolymerization, leading to failure of the proper chromosome alignment, activation of the spindle assembly checkpoint, cell cycle arrest at the G2/M phase, and, ultimately, mitotic catastrophe.

MTAs are broadly classified into microtubule-stabilizing agents (e.g., taxanes) and microtubule-destabilizing agents (e.g., vinca alkaloids, colchicine-site binders). Historically, the clinical translation of MTAs for GBM has been severely hindered by two major obstacles: dose-limiting neurotoxicity and the restrictive properties of the BBB, as discussed in the previous section. Because mature, post-mitotic neurons rely heavily on microtubule networks for axonal transport and synaptic function, systemic administration of MTAs frequently results in severe peripheral neuropathies [84, 85]. Additionally, classical bulky, lipophilic MTAs (like paclitaxel and vincristine) are rapidly expelled from the CNS by the previously described P-gp and BCRP efflux pumps [86, 87]. To overcome these limitations, next-generation small-molecule tubulin destabilizers have been rationally designed to evade efflux pumps. Compounds targeting the colchicine binding site—which is generally insensitive to P-gp-mediated resistance—have shown remarkable preclinical promise. For instance, RGN3067 is a highly BBB-penetrant small molecule that binds the colchicine site of β-tubulin [88]. *In vitro*, it demonstrates nanomolar potency against human GBM cells (including temozolomide-resistant LN-18 cells), inducing profound G2/M arrest and apoptosis [88]. Similarly, PTC596 is an orally bioavailable tubulin-binding agent that lacks the traditional trimethoxyphenyl moiety, allowing it to evade standard resistance mechanisms, achieve high CNS penetration, and prolong survival in orthotopic GBM models [89]. As an alternative to directly targeting tubulin, emerging therapeutic strategies focus on inhibiting proteins that tightly regulate microtubule dynamics exclusively during cell division.

The primary hereditary microcephaly genes—including KNL1, ASPM, CENPE, CITK, and KIF14—are ubiquitously expressed in proliferating cells but are selectively required for spindle

assembly and chromosome segregation in neural progenitors and malignant glial brain tumor cells [90].

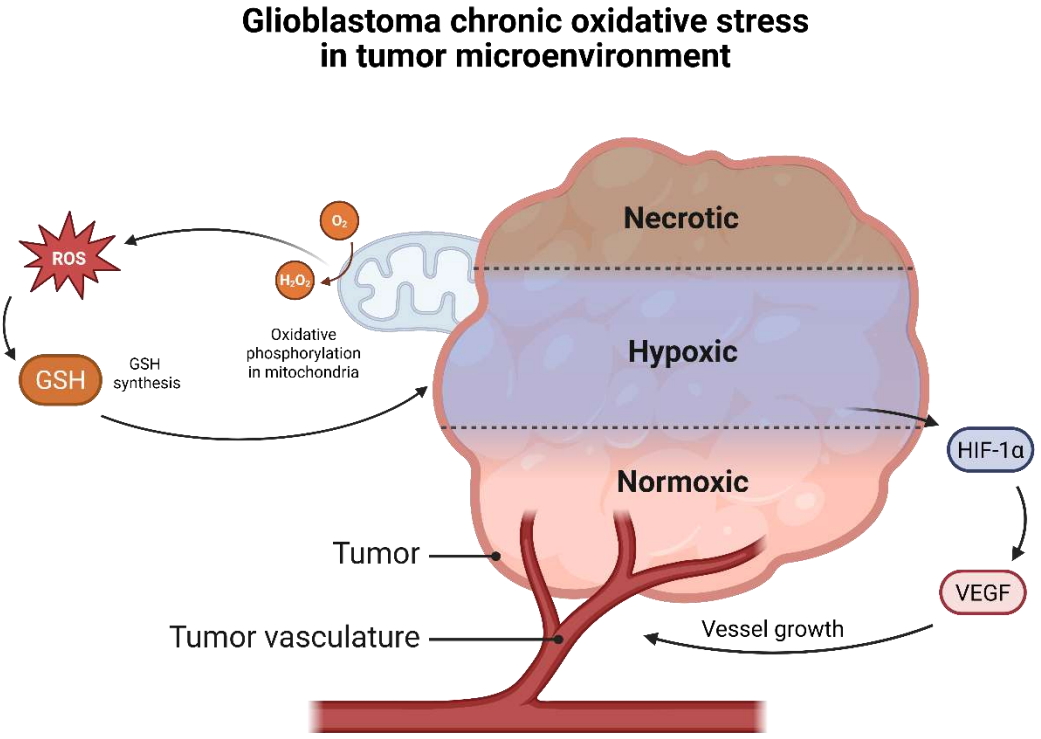

Figure 5. Glioblastoma tumor chronic oxidative stress (created by Biorender).

The metabolic reprogramming required to sustain the rapid proliferation of GBM inherently disturbs cellular redox homeostasis [91]. Glioblastoma cells function under chronic oxidative stress, characterized by elevated baseline levels of reactive oxygen species (ROS) generated by intense glycolytic and mitochondrial oxidative phosphorylation, as well as the hypoxic tumor microenvironment [92]. According to the principle of hormesis, this moderate elevation in ROS acts as a signaling mechanism that promotes cellular survival, tumor invasion, and angiogenesis (via HIF-1α stabilization), as shown in Figure 5. To survive this inherently hostile environment without suffering lethal lipid peroxidation and DNA damage, GBM cells become exquisitely dependent on a robust antioxidant defense network, such as glutathione (GSH) synthesis, and the thioredoxin system [93]. Crucially, redox homeostasis also dictates the therapeutic response. Standard treatments like radiation and temozolomide (TMZ) exert significant cytotoxicity primarily by generating lethal levels of ROS [94]. In response, GBM cells rapidly undergo metabolic reprogramming, upregulating the nuclear factor erythroid 2-related factor 2 (Nrf2)/Keap1 signaling axis [95]. Upon escaping Keap1-mediated degradation under oxidative

stress, the master transcription factor Nrf2 translocates to the nucleus to activate a vast array of antioxidant defense genes, including superoxide dismutase (SOD), catalase (CAT), and heme oxygenase-1 (HO-1) [96]. Consequently, high Nrf2 expression effectively neutralizes therapy-induced oxidative stress, strongly correlates with profound chemoresistance, and is associated with a shorter time to tumor recurrence.

This reliance on a fragile redox balance exposes a critical vulnerability: intentionally disrupting it by generating excessive ROS can overwhelm the tumor's antioxidant buffering capacity, triggering apoptosis or ferroptosis. Iron metabolism is fundamentally intertwined with this redox landscape. While GBM cells possess a heightened demand for intracellular iron to support DNA synthesis and energy production, an excess of labile ferrous iron (Fe^{2+}) can catalyze the Fenton reaction, interacting with hydrogen peroxide to produce highly toxic hydroxyl radicals that initiate catastrophic lipid peroxidation [96]. Exploiting this iron-dependent redox axis, agents that chelate iron and generate extreme ROS levels are emerging as powerful therapeutic tools. Iron chelators such as deferoxamine, thiosemicarbazones (Dp44mT), or terpyridine ligands systematically deplete intracellular iron pools [97, 98]. This targeted iron starvation, combined with massive oxidative stress, serves as a primary trigger for the profound upregulation of the N-myc downstream-regulated gene 1 (Ndrg1), an iron-regulated metastasis suppressor [99]. Upon activation, Ndrg1 robustly stimulates the expression of the cyclin-dependent kinase inhibitor p21 (CIP1/WAF1). The dramatic accumulation of p21 halts cell cycle progression, effectively arresting the rapidly dividing GBM cells in the G2/M phase [100]. Simultaneously, the severe disruption of redox homeostasis and the depletion of endoplasmic reticulum (ER) calcium stores induce profound ER stress [101]. Under these conditions, NDRG1 suppresses protective autophagy, forcing the critically damaged tumor cells into caspase-dependent apoptosis [102].

To sum up, by strategically targeting the structural vulnerabilities of the cytoskeleton, dismantling redundant oncogenic kinase networks, and weaponizing the tumor's precarious redox balance, this multifaceted pharmacological approach aims to definitively overcome the profound adaptability, heterogeneity, and therapeutic resistance of glioblastoma multiforme.

5.5 Quinazoline as a promising scaffold for targeted therapy

Advances in medicinal chemistry and rational drug design have driven the development of new anticancer agents and more effective treatment regimens. In recent years, alongside

conventional chemotherapy, which remains one of the mainstays of cancer therapy, targeted approaches have been increasingly adopted [103]. In particular, the quinazoline ring has emerged as a privileged scaffold in medicinal chemistry, serving as the structural core for numerous FDA-approved TKIs, such as gefitinib, afatinib, and dacomitinib, used in oncological therapy.

Afatinib is an irreversible second-generation EGFR/HER2 tyrosine kinase inhibitor that demonstrates clinical activity against brain metastases in EGFR-mutant NSLC [104]. However, its penetration across an intact BBB is severely restricted by active efflux via P-glycoprotein and breast cancer resistance protein, leading to cerebrospinal fluid concentrations far below plasma levels. Similarly, dacomitinib exhibits limited brain distribution in preclinical models due to efficient efflux transporter recognition, confining its CNS exposure under physiological conditions [105]. Both drugs achieve meaningful intracranial concentrations primarily when the BBB is disrupted by tumor growth. This inconsistent bioavailability highlights the need for novel quinazoline derivatives that are designed to evade efflux transporters and passively diffuse into the CNS.

The structural evolution of this core through the addition of a styryl moiety has yielded the 2-styrylquinazoline class. As with CP-31398, it is a compound able to stabilize the p53 protein. Recent pharmacological investigations have demonstrated that specific chemical modifications to this scaffold, such as the incorporation of sulfonic groups, tosyl moieties, or benzodioxole rings, can alter its biological activity profile. These structural variations enable styrylquinazolines to function as multitarget agents, capable of interacting with multiple molecular targets simultaneously. This versatility allows them to inhibit both receptor and non-receptor tyrosine kinases, intercalate into DNA, or disrupt cytoskeletal organization, depending on their specific substitution pattern. Due to their generally lipophilic nature and tunable physicochemical properties, styrylquinazoline derivatives possess significant potential for CNS penetration, making them highly attractive candidates for the development of next-generation therapies against complex and resistant malignancies, such as GBM.

5.6 Objectives and hypotheses

The overall aim of this doctoral dissertation was to evaluate the anticancer potential of novel styrylquinazoline and styrylquinazolinone scaffolds and to elucidate their mechanisms of action in cellular models of cancer, with particular emphasis on glioblastoma. The central hypothesis

was that styrylquinazoline and styrylquinazolinone derivatives act as multitarget anticancer agents whose activity arises from the simultaneous engagement of several oncogenic processes—microtubule dynamics, EGFR/IGF1R-driven PI3K/AKT/mTOR survival signaling, and cellular redox and metabolic homeostasis—and that such a multitarget profile offers an advantage over single-target inhibition in counteracting the therapeutic resistance characteristics of GBM. To test this hypothesis, the following specific objectives were defined across the four constituent studies:

1. to characterize the *in vitro* antiproliferative and cytotoxic activity of the derivatives in a panel of cancer cell lines, including GBM models;
2. to determine their effect on microtubule organization, mitotic progression, and cell-cycle distribution;
3. to assess their influence on EGFR/IGF1R/AKT/mTOR signaling using immunoassays and Western blotting;
4. to investigate their impact on cellular redox and metabolic homeostasis and to identify the resulting mode of cell death.

6. Materials and methods

6.1 Chemical synthesis

The series of styrylquinazoline derivatives subjected to biological evaluation in this work was designed and synthesized in the Drug Design and Nanopharmacology group, led by Prof. Robert Musioł, at the Institute of Chemistry, University of Silesia. The styrylquinazoline derivative coded IS20, investigated in Paper 1, and the sulfonated styrylquinazolines coded TS1–TS6, investigated in Paper 2, were synthesized by Dr. Eng. Jacek Mularski. A series of styrylquinazolinone derivatives, coded W1A, W1B, W1C, and W2B, were designed and synthesized by Dr. Wioleta Cieślik. The structures of the tested compounds are shown in Fig. 6.

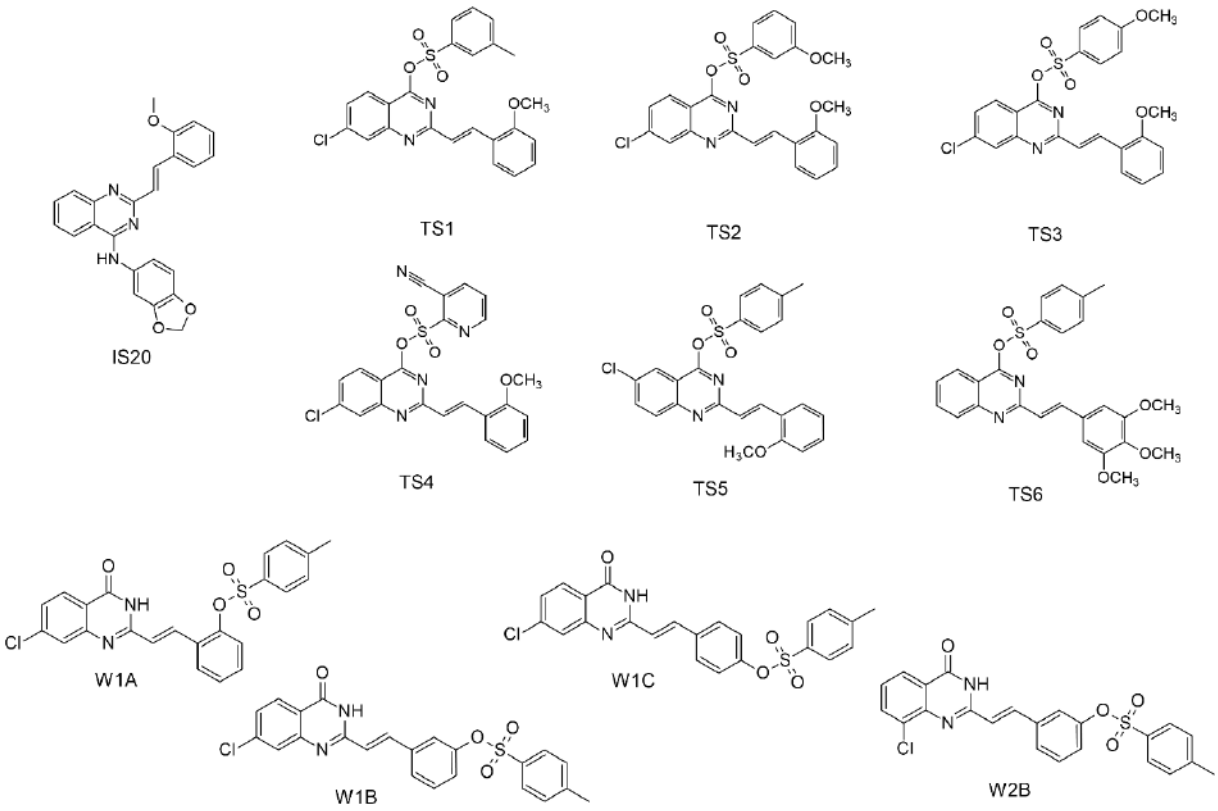

Figure 6. Tested compounds showcased in the papers.

6.2 Cell culture models

A panel of human cancer and normal cell lines was utilized to assess cytotoxicity and target selectivity, which were chosen to reflect different genetic landscapes. The *in vitro* models included wild-type p53 glioblastoma (U-87MG), mutated p53 glioblastoma (U-251, T98G, LN-18, LN-229), colon cancer (HCT 116 and HCT $116^{p53-\backslash-}$) and p53-null chronic myelogenous

leukemia (K562) cells. To evaluate safety, normal human astrocytes (NHA), human liver cells (HepG2), and normal human dermal fibroblasts (NHDF) were selected. Adherent cancer cell lines were cultured in Dulbecco's Modified Eagle's Medium supplemented with 10% heat-inactivated fetal bovine serum, while K562 cells were maintained in RPMI-1640 medium with 10% FBS. NHA cells were grown in a specialized astrocyte medium supplemented with N-2 and epidermal growth factor. NHDF cells were grown in fibroblast growth medium with low-serum content. All cultures were maintained at 37 °C in a humidified atmosphere containing 5% CO2 and routinely subjected to PCR-based mycoplasma testing to ensure the absence of contamination. Different cell cultures were present in paper 1 (K562, U-251, T98G, LN-18, LN-229, U-87MG, HCT-116, HCT 116$^{p53-\backslash-}$), paper 2 (U-251, U-87MG, K562, NHA, HepG2) and paper 3 (U-87MG, T98G, LN-18, LN-229, U-251, NHDF).

6.3 Cytotoxicity, cell cycle, and cell death assays

Antiproliferative activity was measured using the colorimetric MTS assay (CellTiter 96 AQueous One Solution). Cells were seeded at 5,000 cells per well in 96-well plates (except NHA and NHDF that were seeded at 4,000 cells per well), incubated for 24 hours and were treated with varying concentrations of the compounds (paper 1: IS20; paper 2: TS1-TS8; paper 3: W1A, W1B, W1C, W2B) for 72 hours, after which there were incubated for 1 hour with 100 µL of DMEM without phenol red and 20 µL of the CellTiter 96®AQueous One Solution-MTS (Promega). Optical densities were measured at 490 nm utilizing a Varioskan LUX multi-plate reader to calculate the half-maximal inhibitory concentration (IC_{50}).

To assess cell cycle, cells were seeded at a density of 250,000 cells per 3 cm Petri dish and then incubated for 24 hours. The next day, the medium was removed, and treated cells were incubated for 24 hours with the desired compounds (paper 1: IS20 K562 with 6 & 12 µM, U-251 with 10 µM; paper 2: U-251 TS1 2.5 & 5 µM, TS2 2.2 & 4.4 µM, TS3 1.8 & 3.6 µM, TS4 1.7 & 3.4 µM, TS5 0.2 & 0.4 µM, K552: TS1 1.45 µM, TS2 1.65 µM, TS3 3.75 µM, TS4 1.3 µM, TS5 10.75 µM). Collected cells were analyzed by flow cytometry using the Muse Cell Cycle (Millipore) kit according to the manufacturer's instructions to detect compound-induced cell cycle arrest.

Cells for apoptosis were seeded in the same manner as for the cell cycle and incubated with the compounds for 48 hours (paper 1: IS20 K562 with 12 µM & U-251 with 15 µM; paper 2: same concentration as in cell cycle assay). Cells for autophagy were seeded at 20,000 (24 hours) and 10,000 (48 hours) in 96-well plates, incubated for 24 hours, and treated with IS20 at 12 µM

(K562) and 10 μM (U-251), respectively. Apoptosis and autophagy were validated using detection of specific fluorescent markers, including Annexin V/7-AAD staining for apoptosis and fluorescence with the LC3-antibody-based kit (Millipore) tracking of autophagosome formation in treated cells.

6. Microtubule dynamics

Evaluation the mechanical disruption of the cytoskeleton was evaluated using *in vitro* tubulin polymerization assays, which utilized fluorescent reporters to monitor the assembly of tubulin heterodimers, comparing the kinetics of the novel styrylquinazolines against classical stabilizers like paclitaxel. This was presented visually at the cellular level using high-resolution immunofluorescence imaging of the microtubule network.

6.5 Redox homeostasis and metal complexation

U-251 and K562 cells were seeded in 96-well plates at a density of 9,000 cells per well and incubated for 24 hours for ROS generation. The medium was then replaced with freshly prepared IS20 solutions and incubated for selected time points (3, 6, 9, 12, and 24 hours). For combination studies, cells were co-incubated with the compound and 100 μM ascorbic acid for 24 hours. The same cells were seeded in 3 cm Petri dishes at a density of 500,000 cells per well and incubated for 24 hours for GSH depletion. To investigate the compounds' impact on redox homeostasis, intracellular ROS generation was quantified using CellROX, while the depletion of intracellular antioxidants like GSH was measured via colorimetric assays. ROS levels were calculated as a percentage relative to untreated controls, with normalization to Hoechst-stained cell number. GSH concentrations were normalized to untreated control.

Furthermore, UV-Vis spectrophotometric titrations were conducted by dr Patrycja Rawicka to confirm the direct metal-chelating properties of the benzodioxole-functionalized derivatives on Fe^{3+}.To evaluate the ability of IS20 to chelate metal ions, UV-Vis absorption titrations were performed with $FeCl_3 \cdot 6H_2O$ and $CuSO_4 \cdot 5H_2O$. Absorption spectra were recorded from 275 to 450 nm in 5 nm steps using a multi-well plate reader (Varioskan LUX). All spectra were normalized using vector normalization to identify hidden isosbestic points.

6.6 Protein and gene expression profiling

Intracellular signaling was measured using immunoblotting (Western blot) and Lumit immunoassays. Cells were lysed in RIPA buffer supplemented with protease and phosphatase inhibitor cocktails, and total protein was quantified using a BCA assay. After blocking in 5% non-fat milk or BSA in TBST for 1 hour at room temperature, membranes were incubated

overnight at 4 °C with primary antibodies (typically diluted 1:1000), followed by washing and incubation with secondary antibodies for 1 hour at room temperature. Chemiluminescent signals were developed using SuperSignal™ West Pico or West Atto substrates (Thermo Scientific) and captured with a ChemiDoc™ XRS+ System (Bio-Rad). Densitometric analysis was performed using ImageJ software with normalization to reference proteins. In the Lumit immunoassay, cells were lysed in a digitonin-containing buffer, incubated with primary antibodies against phosphorylated targets together with Lumit secondary antibodies for 90 min at 23°C and then furimazine substrate was added to generate a bioluminescent signal. Luminescence was measured using a multi-plate reader (Varioskan LUX) at time of 1 s per well. The protein targets are presented in Table 2.

Transcriptomic factors were measured using quantitative Real-Time PCR (qRT-PCR). Total RNA was isolated using TRIzol reagent, reverse-transcribed into cDNA, and amplified on a QuantStudio 5 Real-Time PCR System. Amplification was performed under the following conditions: initial denaturation at 95 ° C for 30 s, followed by 40 cycles of denaturation at 95 °C for 15 s, annealing at 60 °C for 30 s, and extension at 72 °C for 30–60 s. A melt curve analysis was performed to confirm single-product specificity and the absence of primer-dimers or nonspecific amplicons. The relative mRNA expression of key stress and cell cycle genes (including Ndrg1, GADD45, CCNE2, LC3, and calreticulin) was normalized against the GAPDH reference gene using the 2^-ΔΔCT method. The gene targets are presented in Table 3.

Targeted proteins in individual papers.		
Paper 1	**Paper 2**	**Paper 3**
cyclin E1	$p27^{Kip1}$	EGFR
cdc2	$p21^{Waf1/Cip1}$	IGF-I Receptor β
$p21^{Waf1/Cip1}$	p53	Akt
PARP-1	Cyclin A2	p-Akt (Ser473)
AIF	Cyclin B1	p70 S6 Kinase
caspase-9	cdc2	p-S6 Ribosomal Protein (Ser240/244)
cathepsin B	Aurora A	RAS
BID	EGFR	vinculin
p53	p-EGFR (Tyr1068)	GAPDH
HO-1	p-Akt (Ser473)	cyclophilin β

HIF-1α	PTEN	cofillin
EGFR	p-STAT5 (Tyr694)	
p-EGFR (Tyr1068)	PARP-1	
mTOR	caspase-9	
p-mTOR (Ser2448)	BID	
p-Akt (Ser473)	GADPH	
p-p44/42 MAPK (Erk1/2) (Thr202/Tyr204)	β-actin	
GAPDH	RAS	
β-actin	vinculin	
vinculin	mTOR	
	p-mTOR (Ser2448)	

Table 2. Protein targets showcased in studies.

Targeted genes in individual papers.	
Paper 1	**Paper 2**
MnSOD	*CCNE2*
CAT	*GADD45*
HO-1	*IDH-1*
Ndrg1	*TUBB3*
Calreticulin	*Calreticulin*
IDH-1	*LC3*
GADD45	
LC3	
p62	

Table 3. Gene expression targets showcased in studies.

6.7 Statistical analysis

Results were presented as the mean ± standard deviation from at least three independent experiments, each performed with technical replicates. The statistical analysis included: the one-way ANOVA with a Bonferroni post-hoc test, one-way ANOVA with a Dunn–Šidák correction test or unpaired t-test. A p-value of 0.05 or less was considered statistically significant. All statistical tests were performed using GraphPad Prism 9 software (GraphPad Software, USA).

7. Results and discussion

7.1 Cytotoxicity effect of tested compounds

The management of GBM is complicated by its pronounced heterogeneity, which underlies intrinsic and acquired resistance to conventional chemotherapeutics. In the search for novel therapeutic modalities to circumvent these resistance mechanisms, quinazoline-based scaffolds were investigated. The primary objective of this first phase of the study was to systematically evaluate the antiproliferative activity, structure-activity relationships, and cellular selectivity of three groups of derivatives: the benzodioxole-functionalized lead compound IS20 (Paper 1), the sulfonated styrylquinazolines (the TS series: Paper 2), and the related styrylquinazolinone derivatives (the W series: Paper 3).

The biological studies focused primarily on glioblastoma cell lines with diverse gene expression profiles: U-251 and U87MG (Papers 1, 2, and 3) and LN-18, LN-229, and T98G (Papers 1 and 3). In addition, the chronic myeloid leukemia model K562 was used for the biological evaluation of IS20 and the sulfonated derivative series. The biological evaluation showed that IS20 had a highly specific antiproliferative profile. GBM lines harboring point missense mutations in the *TP53* gene—U-251, LN-18, LN-229, and T98G, all TP53-mutant—were sensitive to IS20, with half-maximal inhibitory concentrations: IC_{50} of 5.45 μM (U-251), 5.99 μM (LN-18), 7.22 μM (LN-229), and 8.15 μM (T98G). IS20 was also cytotoxic toward the p53-null leukemia line K562, with an IC_{50} of 6.01 μM. These results suggest that, unlike classic alkylating agents, IS20 preferentially affects tumor cells carrying defective p53/apoptotic machinery.

In the W series, the quinazoline ring is replaced by a 2-styryl-quinazolin-4(3*H*)-one scaffold carrying a chlorine atom on the quinazolinone core and a tosyl group (OTs on the styryl phenyl ring). The series comprises three 7-chloro derivatives differing in the position of the tosyl group—W1A (7-Cl, 2-OTs), W1B (7-Cl, 3-OTs), and W1C (7-Cl, 4-OTs)—together with the 8-chloro analog W2B (8-Cl, 3-OTs). In the 7-chloro with 3-tosyl fragment derivative, W1B was the most active compound of the group, with IC_{50} values of 5.43 μM (U-251), 5.88 μM (U87MG), 21.01 μM (T98G), 11.06 μM (LN-18), and 3.57 μM (LN-229). Notably, its activity was not restricted to *TP53*-mutant lines, comparable potency being observed in the *TP53*-wild-type line U87MG. By contrast, W1A, W1C, and W2B were inactive against all tested GBM lines (IC_{50} > 15–25 μM). This pattern defines a strict structure-activity requirement: among the 7-chloro derivatives, only the meta-tosyl substitution (W1B, 3-OTs) retained activity, while both the ortho- (W1A, 2-OTs) and para-isomers (W1C, 4-OTs) lost it entirely; relocation of the

chlorine from C-7 to C-8 with retention of the optimal 3-OTs group (W2B) also abolished activity. Activity, thus, requires the combined presence of a 7-chloro substituent on the quinazolinone core and a 3-tosyl group on the styryl phenyl ring.

The next group of compounds comprised the sulfonated styrylquinazolines, in which a chlorine atom was attached to the quinazoline ring. *In vitro* screening showed that the presence and position of this chlorine substituent strongly determined cytotoxic activity, producing markedly different antiproliferative profiles against U-251 and U87MG cells. The 6-chloro-substituted derivative, TS5, displayed broad-spectrum, sub-micromolar cytotoxicity, with an IC_{50} of 0.17 μM against the U87MG and 0.21 μM against the U-251 cells, and retained potency against the non-adherent line K562 (IC_{50} of 0.26 μM). Conversely, shifting the chlorine atom to the 7-position on the quinazoline ring (TS1, TS2, and TS3) produced selectivity toward K562 while reducing efficacy against glioblastoma. The 7-chloro derivatives possessing methyl or methoxy groups attached to the benzenesulfonate moiety (TS1, TS2, TS3) were active against K562 (IC_{50} values ranging from 0.29 μM to 0.75 μM) but considerably weaker against U87MG (IC_{50} values of 3.53 μM for TS2, 6.88 μM for TS3, and a total lack of activity for TS1 at concentrations up to 25 μM). The 7-chloro derivative bearing a 3-cyanobenzenesulfonate group (TS4) was inactive against K562 (>25 μM), but moderately active against both U87MG (1.78 μM) and U-251 (1.76 μM) cell lines. In turn, the unsubstituted quinazoline cores (TS6-TS8) were inactive against most of the tested lines, confirming a stringent structure-activity relationship in which cytotoxicity depends on halogenation at the 6- or 7-positions.

Cellular selectivity, defined by its capacity to eradicate neoplastic cells while preserving healthy cells, is the most critical determinant of therapeutic potential. In addition, it is worth noting that hepatotoxicity and neurotoxicity profiling indicated a favorable safety profile for the sulfonated styrylquinazolines. Against the hepatocellular line (HepG2), the entire TS series showed no measurable effects on proliferation or viability at concentrations exceeding 25 μM, and the compounds exhibited negligible cytotoxicity toward NHA. The *in vitro* therapeutic index (TI) reached nearly 23 for the TS1 in K562, while TS5 achieved TI values of 10.3 and 8.5 in the U87MG and U-251, respectively. For comparison, Osimertinib demonstrated a TI below 0.58, and the microtubule-targeting agent paclitaxel exhibited indiscriminate cytotoxicity toward NHA.

Part of the *in vivo* studies on the *Danio rerio* (zebrafish) model was performed by Prof. Anna Boguszewska-Czubara at the Department of Medical Chemistry, Medical University of Lublin. Importantly, fish embryo toxicity testing showed that IS20 was neither cardiotoxic nor

associated with developmental malformations at a sub-LC_{50} dose. Similarly, cardiotoxicity assessment of the TS series in zebrafish yielded LC_{50} values of 2.9 μM (TS1), 3.5 μM (TS3), and 3.6 μM (TS5), with cardiotoxic effects occurring in a dose-dependent manner. In Paper 2, the anti-tumor efficacy of the TS series was evaluated in a *Danio rerio* larva xenograft model using U-251 cells, in which TS5 produced the greatest tumor burden reduction at concentrations below its LC_{50}. For W1B (Paper 3), zebrafish embryo toxicity testing yielded an LC_{50} of 25.29 μM, indicating a more favorable safety profile than the EGFR/ErbB inhibitors osimertinib (LC_{50} = 10.73 μM) and dacomitinib (LC_{50} = 10.03 μM). In the LN229 zebrafish xenograft model, W1B reduced tumor size to 76.09% in the untreated control at 10 μM, and its combination with dacomitinib at 7.5 μM exceeded the effect of either monotherapy, consistent with the synergy observed *in vitro* under high-glucose conditions.

7.2 Disruption of microtubule dynamics and G2/M cell cycle arrest

The integrity and maintained dynamic instability of the microtubule network at equilibrium are essential for proper cellular division, intracellular trafficking, and signal transduction. Microtubules, α- and β-tubulin heterodimers, play a central role in the cell cycle. In the context of GBM, characterized by intense mitotic activity and a high proliferation index, disturbances in microtubule dynamics represent a critical point of vulnerability. The mechanism of action studies of the styrylquinazoline derivatives—the TS series and IS20—focused on cell-cycle perturbation and showed that both groups induce a pronounced G2/M arrest in cancer cell lines, albeit through partially distinct molecular pathways.

The capacity of these derivatives to induce selective cell cycle arrest at the G2 to M transition has been confirmed by flow cytometry, particularly in U-251 cells. The most active compound from the TS series, TS5, increased in the G2/M phase of the cell cycle. U-251 treatment with TS5 increased the accumulation of cells in the G2/M phase, from 32.5% in untreated controls to 86%. In addition, the cell cycle arrest potential of TS5 was further corroborated in K562 cells, where TS5 induced a 34.7% increase in the G2/M population. Similarly, although not to the same extent, a G2/M cell cycle arrest has been observed with IS20. It is worth noting that this derivative involves intracellular iron chelation and the generation of ROS into its mechanism of action, identically halting cell cycle progression at the G2/M checkpoint. These results confirmed that the styrylquinazoline core affects cell cycle progression across different oncological lineages and several cell-cycle proteins.

In vitro tubulin polymerization assays showed that TS1, TS3, and TS5 are potent enhancers of microtubule polymerization. TS5 promoted tubulin assembly like paclitaxel, hyper-stabilizing the network and suppressing the dynamic instability required for mitotic spindle formation. Consistently, U-251 cells treated with these compounds showed marked reorganization of the microtubule network, which became densely condensed, disordered, and predominantly peripheral. qRT-PCR analyses confirmed that the TS derivatives disrupted microtubule dynamics. In addition, immunoblotting analyses revealed a pattern of cell cycle protein regulation by TS and IS20 derivatives, consistent with a blockade at the G2/M transition. The expression of the *CCNE2* gene, which encodes Cyclin E, essential for entry into the DNA synthesis phase, was downregulated across the treated glioblastoma cells. Expression of key CDK inhibitors was upregulated. The p27 protein, which binds to and inactivates the Cyclin E-CDK2 complex, experienced a nearly 3-fold increase following exposure to TS5. Another protein investigated in U-251 cells was p21, which was upregulated 14-fold by IS20 and also threefold by compounds in the TS series. The increased accumulation of p21 serves as a major biochemical roadblock, confirming that the cells are responding to cytoskeletal rearrangements that lead to stress and halts cell cycle progression. Because the cells are forcefully prevented from navigating the G2/M transition, the regulatory proteins responsible for spindle assembly and chromosomal alignment accumulate to highly pathological levels. Moreover, the expression of Cyclin B1 and CDK1, the core components of the mitosis-promoting factor, was significantly elevated in the GBM cells treated with a series of TS. Similarly, Aurora A kinase, an essential regulator of centrosome maturation, exhibited a staggering 10-fold overexpression in U-251 cells following incubation with TS5. The accumulation of Aurora A traps glioblastoma cells in an irreversible, hyperpolymerized mitotic state, ultimately leading to apoptosis.

Beyond arresting cell division, microtubule disruption intersects with oncogenic survival-kinase signaling. The cytoskeleton is not merely a static scaffold, but a dynamic infrastructure required for endosomal trafficking, receptor recycling, and the spatial organization of signaling complexes. By simultaneously arresting mitosis and perturbing this trafficking-dependent signaling, the styrylquinazolines may limit the compensatory mechanisms that contribute to resistance under conventional therapy.

7.3 Inhibition of crucial GBM signaling pathways (EGFR, Akt/mTOR, and IGF1R)

The hyperactivation and redundancy of RTK signaling networks remain principal drivers of oncogenesis and therapeutic resistance in GBM. Despite the central roles of the

PI3K/Akt/mTOR and the RAS/MAPK/ERK pathways, single-agent TKIs, such as erlotinib, gefitinib, or lapatinib, have failed to improve OS in GBM patients, an observation that motivated the multitarget evaluation of the styrylquinazoline derivatives in this work.

Biochemical and cellular evaluations showed that both the TS series and IS20 attenuate EGFR signaling. In cell-free enzymatic kinase profiling, TS1, TS3, and TS5 inhibited the kinase activity of EGFR and of the related HER2 and HER4 receptors, with inhibition reaching approximately 20%–25%. The cellular suppression of EGFR signaling was more pronounced than this enzymatic inhibition alone would predict, suggesting that direct kinase inhibition is reinforced in cells by additional mechanisms, such as the cytoskeletal disruption. Phosphorylation of EGFR at Tyr1068 was quantified. While standard immunoblotting revealed a moderate reduction in p-EGFR (Tyr1068) following exposure to the compounds, highly sensitive Lumit immunoassay uncovered a significant suppression. In U-251 cells, TS5 and TS3 produced an approximately 1.5-fold reduction in activated EGFR, and IS20 produced a comparable ~1.5-fold reduction in both U-251 and K562. By preventing the mitogenic signal at the plasma membrane, styrylquinazolines effectively blocked the primary oncogenic pathways mentioned above.

Blocking the receptor signal inhibits signaling downstream of the receptor, causing the PI3K/Akt/mTOR signaling cascade to collapse and effectively depriving cancer cells of the metabolic advantage necessary to sustain proliferation, growth, and survival. Western blot analyses demonstrated that the reduced EGFR activation by the styrylquinazoline derivatives resulted in reduced phosphorylation of downstream Akt. In K562, TS5 lowered p-Akt (Ser473) levels approximately 7-fold, TS1 and TS3 reduced phosphorylated Akt nearly 3-fold, while IS20 caused a 1.5-fold decrease in p-Akt expression. This observation confirmed that the styrylquinazoline core acts as a universal disruptor of this pathway. In U-251 cells, however, the absolute levels of p-Akt (Ser473) remained largely unchanged despite the EGFR blockade—an observation consistent with the loss of PTEN in this line, which sustains constitutive PI3K/Akt activity upstream independently. However, these compounds successfully bypassed this PTEN-mediated resistance by directly impacting the terminal node of the mTOR cascade. This suggests that the combined effects of the styrylquinazolines—on receptor-level kinase activity, on receptor trafficking, and on cytoskeletal organization—can inactivate mTOR from its canonical upstream regulators even when Akt remains constitutively active. Such action may effectively disable the glioblastoma's translational machinery, leading to apoptosis.

The metabolic phenotype of GBM, dominated by the Warburg effect, makes glucose-driven survival signaling a relevant therapeutic target. Therefore, targeted circumvention of the metabolic adaptations highlights the critical synergy achieved by a novel quinazolinone insulin receptor/IGF1R inhibitor (W1B from the W series of tested compounds) within the glucose-driven tumor microenvironment. W1B inhibited IGF1R by 74% and InsR by 60%, with only moderate activity against EGFR (35%) and HER2 (41%), and a negligible effect on non-receptor tyrosine kinases in cell-free enzymatic assays. At the cellular level, immunoblotting of LN229 cells showed that W1B reduced both IGF1R and EGFR protein levels by more than two-fold and suppressed Akt (Ser473) phosphorylation. Under high-glucose conditions, EGFR levels remained essentially unchanged, and, despite continued IGF1R suppression, the Akt/mTOR axis was paradoxically upregulated, with elevated p-Akt, p70 S6K, and RAS. This pattern reflects activation of the glucose-driven compensatory survival cascade, in which EGFR-mediated signaling sustains Akt phosphorylation even when IGF1R is inhibited. To overcome this adaptive resistance, a synergistic, multifaceted combination strategy was employed, combining the drug W1B with the irreversible EGFR/ErbB inhibitor dacomitinib. The dual treatment in LN229 HG cells preserved IGF1R suppression and restored the marked EGFR inhibition that was lost with W1B alone, producing a clearly synergistic cytotoxic effect. The dual blockade simultaneously inhibits the IGF1R/InsR–driven survival axis—operative under high-glucose conditions—and the EGFR–driven compensatory arm is activated when IGF1R is engaged alone. By targeting both receptors simultaneously, the combination addresses the redundancy of the survival network, which limits the efficacy of single-target RTK inhibitors in GBM.

7.4 ROS generation, oxidative stress, and cell death pathways

As mentioned above, GBM inherently operates under chronic, elevated levels of oxidative stress driven by hyperactive oncogenic metabolism and hypoxia. While moderate concentrations of ROS fuel tumor proliferation and therapeutic resistance, pushing intracellular ROS levels beyond a critical threshold triggers catastrophic oxidative damage to lipids, proteins, and genomic DNA, culminating in cell death. Exploiting this redox vulnerability by deploying compounds that simultaneously generate ROS and deprive the cell of its antioxidant buffering capacity provides a bypass to resistance mechanisms. Evaluation of tested styrylquinazolines in Papers 1 and 2 unveiled a capacity to destroy cancer cells by a disruption of redox homeostasis, followed by the dual induction of apoptosis and autophagy.

The genesis of styrylquinazoline-induced oxidative stress is linked to the chelating properties of the scaffold. Extensive spectroscopic titrations definitively established that the IS20 derivative acts as a potent intracellular metal chelator, exhibiting a particularly high affinity for ferric iron. The formation of a stable IS20-Fe^{3+} complex was confirmed by the emergence of two distinct isosbestic points at 320 nm and 370 nm, indicating a well-defined equilibrium between the free ligand and the IS20–Fe^{3+} complex with no detectable intermediates. This causes IS20 to directly disrupt mitochondrial respiration and triggers a surge in ROS. Quantitative fluorescence analyses have demonstrated that exposure to IS20 incites a rapid and sustained accumulation of ROS within the first 12 to 24 hours of treatment. The cytotoxicity of IS20 has been shown to rely on oxidative stress, as validated by co-incubation experiments with the antioxidant ascorbic acid, which quenches the compound-induced ROS generation. This oxidative burden rapidly depletes the antioxidant reserves of glioblastoma cells, with measurable shifts in intracellular GSH levels reflecting active scavenging of the elevated ROS.

As the redox imbalance intensifies, the primary enzymatic antioxidant defenses of glioblastoma cells undergo transcriptomic remodeling. Initial exposure to the styrylquinazoline derivatives induces upregulation of the *MnSOD* gene, consistent with a response to superoxide accumulation. However, catalase expression is concurrently downregulated, allowing H_2O_2 to accumulate and prolonging the oxidative stress. In parallel, the redox imbalance triggers overexpression of HO-1, leading to a 25-fold increase in mRNA within nine hours of IS20 treatment. Because HO-1 catalyzes heme degradation and enriches the mitochondrial iron pool, it catalyzes further lipid peroxidation and accelerates mitochondrial damage.

Therapeutically significant consequences of this iron depletion and oxidative stress include activation of HIF-1α and increased expression of the metastasis suppressor Ndrg1. Transcriptomic data revealed that IS20 induced a greater than 3.7-fold upregulation of Ndrg1 expression in U-251.

Ultimately, the collapse of redox and metabolic homeostasis triggers cell death, characterized by the co-activation of both intrinsic apoptosis and autophagy. The ER stress provides the primary bridge to autophagy. In our research, IS20 induced a more than 2.5-fold increase in the expression of the *calreticulin* gene in GBM. Flow cytometric analyses confirmed a greater than 4-fold induction of autophagy in U-251 cells (increase in the autophagy index compared to untreated control), accompanied by a 6-fold upregulation of the *p62* (SQSTM1) gene and a 2.5-fold increase in *LC3* mRNA. Sustained autophagic stress together with ROS

accumulation damages the mitochondria and engages the intrinsic apoptotic cascade. Flow cytometry analyses confirmed that the TS5 and IS20 compounds increased the GBM cell population by 60%-75 % at the early and late stages of apoptosis. At the molecular level, a hallmark of this response in our experiments is the engagement of the lysosomal–mitochondrial apoptotic axis: IS20 induced an 8-fold increase in procathepsin B, suggesting altered lysosomal proteolytic capacity, with downstream activation of BID. The resulting cascade leads to caspase-9 activation and the terminal cleavage of PARP-1.

By acting as intracellular metal chelators and ROS inducers, these compounds activate multiple distinct cell death pathways-autophagic, caspase-dependent, and caspase-independent pathways, thereby limiting the ability of cancer cells to evade cytotoxic effects through single resistance mechanisms.

8. Conclusions

8.1 Multifaceted mechanism of action

The overarching thesis of this dissertation, that the successful eradication of GBM strictly necessitates a multifaceted mechanism of action, has been validated through a comprehensive biological evaluation of styrylquinazoline and styrylquinazolinone derivatives. Historically, management of GBM has been hampered by the tumor's genomic instability, its immunosuppressive microenvironment, and the plasticity of its kinome. The 1st pillar relies on disrupting the tumor’s cytoskeletal architecture. Styrylquinazolines enhance tubulin polymerization, stabilizing the microtubule network and providing an irreversible G2/M phase cell cycle arrest. The 2nd pillar is attenuation of receptor tyrosine kinase signaling. Microtubule integrity is required for proper clustering, internalization, and recycling of RTKs. Therefore, cytoskeleton disruption complements the direct kinase-inhibitory activity of the tested scaffolds. As demonstrated, these compounds suppress EGFR signaling and the IGF1R axes. By concurrently blocking both EGFR and survival signals of IGF1R, these compounds induce a collapse of the downstream PI3K/Akt/mTOR cascade. The downregulation of activated Akt (Ser473) and mTOR (Ser2448) deprives the GBMs of their ability to sustain the Warburg effect. The 3rd pillar is the targeted use of the tumor's intrinsic oxidative stress as a weapon. Styrylquinazolines with benzodioxole groups exploit this by acting as potent intracellular iron chelators. By depleting the labile iron pool, these derivatives disrupt mitochondrial respiration and trigger a rapid increase in intracellular ROS that overwhelms the compensatory antioxidant enzymes. The accompanying oxidative damage and ER stress engage a combined cell death

program with simultaneous induction of caspase-dependent apoptosis and autophagy. In conclusion, the styrylquinazoline and quinazolinone derivatives represent a class of polypharmacological therapeutics. By fusing mitotic arrest, metabolic/kinase starvation, and fatal redox destabilization into a single molecular point, they lead to the destruction of glioblastoma cells.

8.2 Identification of lead candidates

The principal outcome of this work is the identification, from a broader library of synthesized compounds, of three lead candidates that satisfy a set of preclinical criteria extending beyond simple *in vitro* cytotoxicity, a favorable TI, the presence of physicochemical properties necessary for CNS penetration, and a multifaceted mechanism of action capable of overcoming the tumor's intrinsic genomic heterogeneity and metabolic plasticity. On this basis, three leads were selected: IS20 (Paper 1), TS5 (from the TS series: Paper 2), and W1B (from the W series: Paper 3).

IS20 was identified as the lead candidate for redox-directed therapy. It acts as a potent intracellular iron chelator, producing a sustained oxidative and ER stress that exceeds the compensatory capacity of the cellular antioxidant system. IS20 induces upregulation of the *Ndrg1* gene, which, in turn, degrades compensatory RTK signaling networks. Predictive AMDE modeling on IS20 revealed a highly favorable permeability that mirrors or exceeds the predicted BBB penetrability of several FDA-approved, CNS-active drugs, such as afatinib and erlotinib. Furthermore, prolonged *in vivo* toxicological assessments in zebrafish embryos confirmed that IS20 does not induce severe cardiotoxicity or lethal developmental malformations at therapeutic doses. Linking iron chelation, Ndrg1 activation, and dual autophagic-apoptotic cell death together in IS20 represents a pharmacological tool for eradicating chemotherapy-resistant glioblastoma with a *TP53* mutation.

TS5, the 6-chloro-substituted sulfonated styrylquinazoline, was identified as the lead antimitotic and multi-kinase agent. Within the TS series, the 7-chloro analogs (TS1 and TS3) showed selective sub-micromolar activity against leukemic (K562) cells but were considerably less active against the GBM panel. TS5 (6-Cl) extended this potency to a broad GBM panel, with sub-micromolar efficacy against both wild-type and p53-mutated GBM cells. The TI of TS5 against NHA compares favorably with the reference FDA-approved TKIs. *In vivo* validation in the *Danio rerio* xenograft model showed a reduction in glioblastoma tumor with a safety profile that vastly outperformed the third-generation clinical reference drug, osimertinib. ADME profiling indicated that TS5's high lipophilicity may limit BBB penetration

in its current form. TS4 demonstrated that the integration of a 3-cyanobenzenesulfonate group significantly improves theoretical BBB permeability. Therefore, TS5 serves as the definitive structural template for the next generation of brain-penetrant antimitotic kinase inhibitors.

W1B, the styrylquinazolinone with a 7-chloro substituent on the quinazolinone ring, was identified as the lead candidate for combination therapy targeting metabolic-compensation pathways. Glioblastoma cells rely on the Warburg effect, heavily utilizing the insulin and IGF1R signaling axes to maintain PI3K/Akt activation. Enzymatic profiling confirmed W1B as a selective inhibitor of the IGF1R/InsR axis, indicating the ability to reduce expression of IGF1R, EGFR, and downstream activation by Akt in normal GBM conditions. Under high-glucose conditions, EGFR remained largely unaffected, and Akt/mTOR was paradoxically upregulated, indicating a glucose-driven compensatory escape. Co-administration of W1B with the EGFR/ErbB inhibitor dacomitinib restored EGFR suppression and produced a synergistic cytotoxic effect. Therefore, W1B represents a rationally selected partner for combination strategies addressing metabolic-compensation resistance in GBM.

Together, these three lead candidates validate the therapeutic versatility of the styrylquinazoline and quinazolinone scaffolds. They demonstrate that it is entirely possible to develop highly selective, multi-targeted agents that simultaneously target the main areas of GBM resistance—mitotic, redox, and metabolic.

8.3 Clinical relevance and future directions

The findings presented in this dissertation contribute a polypharmacological framework based on the styrylquinazoline and quinazolinone scaffolds, and identify three lead candidates (TS5, IS20, and W1B) for further development against GBM. The clinically relevant attribute of these leads is their capacity to engage several axes of tumor resilience in parallel while, in the most sensitive models, maintaining a favorable selectivity over normal cells. SOC alkylating agents frequently fail due to indiscriminate dose-limiting toxicities and an inability to selectively target the tumor over healthy neural parenchyma. In contrast, sulfonated derivatives demonstrate exceptional *in vitro* selectivity, sparing normal human astrocytes and fibroblasts. This high selectivity was successfully translated to *in vivo* systems, where the lead compounds exhibited a wide safety profile and minimal cardiotoxicity in *Danio rerio* embryo models at sublethal doses, inducing tumor regression in xenografts.

Despite these highly promising preclinical outcomes, the successful clinical translation of these compounds requires decisive future directions, particularly concerning pharmacokinetics,

BBB penetration, and advanced *in vivo* validation. While predictive ADME profiling indicates that these styrylquinazolines may possess sufficient lipophilicity and structural features to cross the BBB, in parallel with structural modifications, future efforts must place greater emphasis on advanced nanomedicine formulations. The encapsulation of these lipophilic styrylquinazolines into lipid-based nanocarriers, such as liposomes or extracellular vesicle-derived structural droplet drugs, presents a sophisticated strategy to bypass the BBB.

Biological validation must transition to rodent and mammalian preclinical models. While the zebrafish xenograft model provided an excellent, high-throughput platform for initial *in vivo* toxicity and efficacy screening, the next logical step is to evaluate these compounds in patient-derived xenograft (PDX) models in mice. Using PDX models accurately preserves heterogeneity, specific genetic lesions, and the complex, immunosuppressive tumor microenvironment inherent to human glioblastoma. These mammalian studies will be crucial for confirming target engagement *in situ*, quantifying actual drug concentrations, assessing hepatotoxicity, and assessing long-term systemic toxicities. Similarly, the synergistic combination of IGF1R/InsR metabolic inhibitors with established EGFR inhibitors (such as dacomitinib or osimertinib) should be evaluated in *in vivo* models of glucose-driven metabolic stress to confirm the elimination of collateral resistance pathways. By pursuing these comprehensive future directions, the multifaceted targeted therapies developed in this dissertation can be systematically advanced from promising molecular entities into viable, transformative clinical candidates for the treatment of glioblastoma.

9. References

[1] D.N. Louis, A. Perry, P. Wesseling, D.J. Brat, I.A. Cree, D. Figarella-Branger, C. Hawkins, H.K. Ng, S.M. Pfister, G. Reifenberger, R. Soffietti, A. von Deimling, D.W. Ellison, The 2021 WHO Classification of Tumors of the Central Nervous System: a summary, Neuro Oncol 23(8) (2021) 1231-1251. https://doi.org/10.1093/neuonc/noab106.

[2] Rezaei Nima, Hanaei Sara, Human Brain and Spinal Cord Tumors: From Bench to Bedside., 2023. https://doi.org/10.1007/978-3-031-23705-8.

[3] A. Pouyan, M. Ghorbanlo, M. Eslami, M. Jahanshahi, E. Ziaei, A. Salami, K. Mokhtari, K. Shahpasand, N. Farahani, T.E. Meybodi, M. Entezari, A. Taheriazam, K. Hushmandi, M. Hashemi, Glioblastoma multiforme: insights into pathogenesis, key signaling pathways, and therapeutic strategies, Molecular Cancer 24(1) (2025) 58. https://doi.org/10.1186/s12943-025-02267-0.

[4] J.A. Benitez, J. Ma, M. D'Antonio, A. Boyer, M.F. Camargo, C. Zanca, S. Kelly, A. Khodadadi-Jamayran, N.M. Jameson, M. Andersen, H. Miletic, S. Saberi, K.A. Frazer, W.K. Cavenee, F.B. Furnari, PTEN regulates glioblastoma oncogenesis through chromatin-associated complexes of DAXX and histone H3.3, Nature Communications 8(1) (2017) 15223. https://doi.org/10.1038/ncomms15223.

[5] Z. An, O. Aksoy, T. Zheng, Q.W. Fan, W.A. Weiss, Epidermal growth factor receptor and EGFRvIII in glioblastoma: signaling pathways and targeted therapies, Oncogene 37(12) (2018) 1561-1575. https://doi.org/10.1038/s41388-017-0045-7.

[6] H. Wang, X. Zhang, J. Liu, W. Chen, X. Guo, Y. Wang, Y. Wang, H. Xing, T. Liang, Y. Shi, D. Liu, T. Yang, Y. Xia, J. Li, J. Wu, Q. Liu, T. Qu, S. Guo, H. Li, K. Zhang, Y. Li, S. Jin, D. Zhao, Y. Wang, W. Ma, Clinical roles of EGFR amplification in diffuse gliomas: a real-world study using the 2021 WHO classification of CNS tumors, Frontiers in Neuroscience Volume 18 - 2024 (2024). https://doi.org/10.3389/fnins.2024.1308627.

[7] Y.-J. Lee, H.W. Seo, J.-H. Baek, S.H. Lim, S.-G. Hwang, E.H. Kim, Gene expression profiling of glioblastoma cell lines depending on TP53 status after tumor-treating fields (TTFields) treatment, Scientific Reports 10(1) (2020) 12272. https://doi.org/10.1038/s41598-020-68473-6.

[8] S.S. Khalil, A. Salihi, Mutations in the TP53, VEGFA, and CTH Genes as Key Molecular Markers for the Diagnosis of Glioblastoma, Cureus 16(5) (2024) e61165. https://doi.org/10.7759/cureus.61165.

[9] Z. Sun, M. Du, X. Wu, R. Tao, P. Sun, S. Zheng, Z. Zhang, D. Zhou, X. Zhao, P. Yang, Rapid diagnosis of TERT promoter mutation using Terahertz absorption spectroscopy in glioblastoma, Scientific Reports 15(1) (2025) 18480. https://doi.org/10.1038/s41598-025-03161-x.

[10] D. Noack, J. Wach, A. Barrantes-Freer, N.H. Nicolay, E. Güresir, C. Seidel, Homozygous CDKN2A/B deletions in low- and high-grade glioma: a meta-analysis of individual patient data and predictive values of p16 immunohistochemistry testing, Acta Neuropathol Commun 12(1) (2024) 180. https://doi.org/10.1186/s40478-024-01889-7.

[11] M. Szylberg, P. Sokal, P. Śledzińska, M. Bebyn, S. Krajewski, Ł. Szylberg, A. Szylberg, T. Szylberg, K. Krystkiewicz, M. Birski, M. Harat, R. Włodarski, J. Furtak, MGMT Promoter Methylation as a Prognostic Factor in Primary Glioblastoma: A Single-Institution Observational Study, Biomedicines 10(8) (2022). https://doi.org/10.3390/biomedicines10082030.

[12] L. Li, F. Xiao, S. Wang, S. Kuang, Z. Li, Y. Zhong, D. Xu, Y. Cai, S. Li, J. Chen, Y. Liu, J. Li, H. Li, H. Xu, Preoperative prediction of MGMT promoter methylation in glioblastoma

based on multiregional and multi-sequence MRI radiomics analysis, Scientific Reports 14(1) (2024) 16031. https://doi.org/10.1038/s41598-024-66653-2.
[13] A.F.P. Aldana, O. Echeverría, A.M. Chinchilla, N. Contreras, C. Peralta, N. Caballero, H.V. Tovar, J.M. Palacio, V. Uribe, M. Mineo, F. Velandia, D. Silgado, W.M.R. Castillo, A.O.O. Méndez, D.J.F. Mendoza, Integrating Molecular Profiling into Glioma Diagnosis: Implications of the WHO-CNS5-2021 Classification (P4-6.008), Neurology 104(7_Supplement_1) (2025) 5675. https://doi.org/doi:10.1212/WNL.0000000000212520.
[14] W.C.o.T.E. Board, Central nervous system tumours. WHO classification of tumours series, International Agency for Research on Cancer2021.
[15] Q.T. Ostrom, L. Bauchet, F.G. Davis, I. Deltour, J.L. Fisher, C.E. Langer, M. Pekmezci, J.A. Schwartzbaum, M.C. Turner, K.M. Walsh, M.R. Wrensch, J.S. Barnholtz-Sloan, The epidemiology of glioma in adults: a "state of the science" review, Neuro Oncol 16(7) (2014) 896-913. https://doi.org/10.1093/neuonc/nou087.
[16] J.M. Melhem, J. Detsky, M.J. Lim-Fat, J.R. Perry, Updates in IDH-Wildtype Glioblastoma, Neurotherapeutics 19(6) (2022) 1705-1723. https://doi.org/10.1007/s13311-022-01251-6.
[17] L. Du, Q. Zhang, Y. Li, T. Li, Q. Deng, Y. Jia, K. Lei, D. Kan, F. Xie, S. Huang, Research progress on the role of PTEN deletion or mutation in the immune microenvironment of glioblastoma, Front Oncol 14 (2024) 1409519. https://doi.org/10.3389/fonc.2024.1409519.
[18] V. Di Nunno, L. Gatto, A. Tosoni, M. Aprile, L. Galvani, A. Zappi, M.P. Foschini, S. Asioli, G. Tallini, D. De Biase, T. Maloberti, S. Bartolini, C. Giannini, E. Franceschi, TP53 mutations and survival in patients with histologically defined Glioblastoma, IDH-wildtype, Pathol Res Pract 262 (2024) 155516. https://doi.org/10.1016/j.prp.2024.155516.
[19] D.F. Marker, S. Agnihotri, N. Amankulor, G.H. Murdoch, T.M. Pearce, The dominant TP53 hotspot mutation in IDH -mutant astrocytoma, R273C, has distinctive pathologic features and sex-specific prognostic implications, Neurooncol Adv 4(1) (2022) vdab182. https://doi.org/10.1093/noajnl/vdab182.
[20] C. Hu, K. Wang, C. Damon, Y. Fu, T. Ma, L. Kratz, B. Lal, M. Ying, S. Xia, D.P. Cahill, C.M. Jackson, M. Lim, J. Laterra, Y. Li, ATRX loss promotes immunosuppressive mechanisms in IDH1 mutant glioma, Neuro Oncol 24(6) (2022) 888-900. https://doi.org/10.1093/neuonc/noab292.
[21] E.G. Ordóñez-Rubiano, A. Ramos-Márquez, R.F. Vega-Alvear, C. Ruiz-Forero, A. Cadavid-Cobo, S. Fuentes-Tapias, P. Andrade-Andrade, A.L. Cómbita, C. Payán-Gómez, R. Parra-Medina, D.F. Gómez, J.F. Ramón, F. Hakim, Deciphering the Clinical Implications of Concurrent Chromosome 7 Gain and Chromosome 10 Loss in Glioblastoma: A Scoping Review, Brain Sci 16(1) (2025). https://doi.org/10.3390/brainsci16010060.
[22] J. Tang, N. Karbhari, J.L. Campian, Therapeutic Targets in Glioblastoma: Molecular Pathways, Emerging Strategies, and Future Directions, Cells 14(7) (2025). https://doi.org/10.3390/cells14070494.
[23] J. White, M.P.J. White, A. Wickremesekera, L. Peng, C. Gray, The tumour microenvironment, treatment resistance and recurrence in glioblastoma, J Transl Med 22(1) (2024) 540. https://doi.org/10.1186/s12967-024-05301-9.
[24] D. Sipos, B.L. Raposa, O. Freihat, M. Simon, N. Mekis, P. Cornacchione, Á. Kovács, Glioblastoma: Clinical Presentation, Multidisciplinary Management, and Long-Term Outcomes, Cancers (Basel) 17(1) (2025). https://doi.org/10.3390/cancers17010146.

[25] M. Kim, E. Ladomersky, A. Mozny, M. Kocherginsky, K. O'Shea, Z.Z. Reinstein, L. Zhai, A. Bell, K.L. Lauing, L. Bollu, E. Rabin, K. Dixit, P. Kumthekar, L.C. Platanias, L. Hou, Y. Zheng, J. Wu, B. Zhang, M. Hrachova, S.A. Merrill, M.M. Mrugala, V.C. Prabhu, C. Horbinski, C.D. James, B. Yamini, Q.T. Ostrom, M.O. Johnson, D.A. Reardon, R.V. Lukas, D.A. Wainwright, Glioblastoma as an age-related neurological disorder in adults, Neuro-Oncology Advances 3(1) (2021). https://doi.org/10.1093/noajnl/vdab125.
[26] R.O. Mirimanoff, T. Gorlia, W. Mason, M.J. Van den Bent, R.D. Kortmann, B. Fisher, M. Reni, A.A. Brandes, J. Curschmann, S. Villa, G. Cairncross, A. Allgeier, D. Lacombe, R. Stupp, Radiotherapy and temozolomide for newly diagnosed glioblastoma: recursive partitioning analysis of the EORTC 26981/22981-NCIC CE3 phase III randomized trial, J Clin Oncol 24(16) (2006) 2563-9. https://doi.org/10.1200/jco.2005.04.5963.
[27] J.S. Chen, J.S. Young, M.S. Berger, Current and Future Applications of 5-Aminolevulinic Acid in Neurosurgical Oncology, Cancers (Basel) 17(8) (2025). https://doi.org/10.3390/cancers17081332.
[28] J.E. Valerio, G. de Jesús Aguirre Vera, J. Zumaeta, N.S. Rea, M.P. Fernandez Gomez, P. Mantilla-Farfan, L. Valente, A.M. Alvarez-Pinzon, Comparative Analysis of 5-ALA and Fluorescent Techniques in High-Grade Glioma Treatment, Biomedicines 13(5) (2025). https://doi.org/10.3390/biomedicines13051161.
[29] C.G. Hadjipanayis, G. Widhalm, W. Stummer, What is the Surgical Benefit of Utilizing 5-Aminolevulinic Acid for Fluorescence-Guided Surgery of Malignant Gliomas?, Neurosurgery 77(5) (2015) 663-73. https://doi.org/10.1227/neu.0000000000000929.
[30] J.D. Joo, J.H. Chang, J.H. Kim, Y.K. Hong, Y.H. Kim, C.Y. Kim, Temozolomide during and after Radiotherapy for Newly Diagnosed Glioblastomas : A Prospective Multicenter Study of Korean Patients, J Korean Neurosurg Soc 52(2) (2012) 92-7. https://doi.org/10.3340/jkns.2012.52.2.92.
[31] D.G. Brachman, S.L. Pugh, L.S. Ashby, T.A. Thomas, E.M. Dunbar, S. Narayan, H.I. Robins, J.A. Bovi, J.K. Rockhill, M. Won, W.P. Curran, Phase 1/2 trials of Temozolomide, Motexafin Gadolinium, and 60-Gy fractionated radiation for newly diagnosed supratentorial glioblastoma multiforme: final results of RTOG 0513, Int J Radiat Oncol Biol Phys 91(5) (2015) 961-7. https://doi.org/10.1016/j.ijrobp.2014.12.050.
[32] R. Stupp, W.P. Mason, M.J. van den Bent, M. Weller, B. Fisher, M.J. Taphoorn, K. Belanger, A.A. Brandes, C. Marosi, U. Bogdahn, J. Curschmann, R.C. Janzer, S.K. Ludwin, T. Gorlia, A. Allgeier, D. Lacombe, J.G. Cairncross, E. Eisenhauer, R.O. Mirimanoff, Radiotherapy plus concomitant and adjuvant temozolomide for glioblastoma, N Engl J Med 352(10) (2005) 987-96. https://doi.org/10.1056/NEJMoa043330.
[33] N. Iturrioz-Rodríguez, N. Sampron, A. Matheu, Current advances in temozolomide encapsulation for the enhancement of glioblastoma treatment, Theranostics 13(9) (2023) 2734-2756. https://doi.org/10.7150/thno.82005.
[34] M. Fresnais, S. Turcan, D. Theile, J. Ungermann, Y. Abou Zeed, J.R. Lindner, M. Breitkopf, J. Burhenne, W.E. Haefeli, R. Longuespée, Approaching Sites of Action of Temozolomide for Pharmacological and Clinical Studies in Glioblastoma, Biomedicines 10(1) (2022) 1.
[35] R. Ortiz, G. Perazzoli, L. Cabeza, C. Jiménez-Luna, R. Luque, J. Prados, C. Melguizo, Temozolomide: An Updated Overview of Resistance Mechanisms, Nanotechnology Advances and Clinical Applications, Curr Neuropharmacol 19(4) (2021) 513-537. https://doi.org/10.2174/1570159x18666200626204005.

[36] R. Stupp, P. Mason Warren, J. van den Bent Martin, M. Weller, B. Fisher, J.B. Taphoorn Martin, K. Belanger, A. Brandes Alba, C. Marosi, U. Bogdahn, J. Curschmann, C. Janzer Robert, K. Ludwin Samuel, T. Gorlia, A. Allgeier, D. Lacombe, J.G. Cairncross, E. Eisenhauer, O. Mirimanoff René, Radiotherapy plus Concomitant and Adjuvant Temozolomide for Glioblastoma, New England Journal of Medicine 352(10) 987-996. https://doi.org/10.1056/NEJMoa043330.
[37] R. Rosas-Alonso, J. Colmenarejo-Fernández, O. Pernía, M. Burdiel, C. Rodríguez-Antolín, I. Losantos-García, T. Rubio, R. Moreno-Velasco, I. Esteban-Rodríguez, V. Martínez-Marín, P. Yubero, N. Costa-Fraga, A. Díaz-Lagares, R. López-López, E. Díaz-Martin, J.F. García, C.V. Sánchez, M.L. Gandía-González, G. Moreno-Bueno, J. de Castro, I.I. de Cáceres, Evaluation of the clinical use of MGMT methylation in extracellular vesicle-based liquid biopsy as a tool for glioblastoma patient management, Scientific Reports 14(1) (2024) 11398. https://doi.org/10.1038/s41598-024-62061-8.
[38] M. Torre, P.Y. Wen, J.B. Iorgulescu, The predictive value of partial MGMT promoter methylation for IDH-wild-type glioblastoma patients, Neurooncol Pract 10(2) (2023) 126-131. https://doi.org/10.1093/nop/npac070.
[39] S.S.K. Yalamarty, N. Filipczak, X. Li, M.A. Subhan, F. Parveen, J.A. Ataide, B.A. Rajmalani, V.P. Torchilin, Mechanisms of Resistance and Current Treatment Options for Glioblastoma Multiforme (GBM), Cancers (Basel) 15(7) (2023). https://doi.org/10.3390/cancers15072116.
[40] S.M.B. Rodriguez, A. Kamel, G.V. Ciubotaru, G. Onose, A.S. Sevastre, V. Sfredel, S. Danoiu, A. Dricu, L.G. Tataranu, An Overview of EGFR Mechanisms and Their Implications in Targeted Therapies for Glioblastoma, Int J Mol Sci 24(13) (2023). https://doi.org/10.3390/ijms241311110.
[41] M. Jiang, K. Zhang, Z. Zhang, X. Zeng, Z. Huang, P. Qin, Z. Xie, X. Cai, M. Ashrafizadeh, Y. Tian, R. Wei, PI3K/AKT/mTOR Axis in Cancer: From Pathogenesis to Treatment, MedComm (2020) 6(8) (2025) e70295. https://doi.org/10.1002/mco2.70295.
[42] Y. Ma, N. Tang, R.C. Thompson, B.C. Mobley, S.W. Clark, J.N. Sarkaria, J. Wang, InsR/IGF1R Pathway Mediates Resistance to EGFR Inhibitors in Glioblastoma, Clinical Cancer Research 22(7) (2016) 1767-1776. https://doi.org/10.1158/1078-0432.Ccr-15-1677.
[43] M. Zhang, J. Liu, M. Li, S. Zhang, Y. Lu, Y. Liang, K. Zhao, Y. Li, Insulin-like growth factor 1/insulin-like growth factor 1 receptor signaling protects against cell apoptosis through the PI3K/AKT pathway in glioblastoma cells, Exp Ther Med 16(2) (2018) 1477-1482. https://doi.org/10.3892/etm.2018.6336.
[44] A. Simpson, W. Petnga, V.M. Macaulay, U. Weyer-Czernilofsky, T. Bogenrieder, Insulin-Like Growth Factor (IGF) Pathway Targeting in Cancer: Role of the IGF Axis and Opportunities for Future Combination Studies, Target Oncol 12(5) (2017) 571-597. https://doi.org/10.1007/s11523-017-0514-5.
[45] R. Li, A. Pourpak, S.W. Morris, Inhibition of the insulin-like growth factor-1 receptor (IGF1R) tyrosine kinase as a novel cancer therapy approach, J Med Chem 52(16) (2009) 4981-5004. https://doi.org/10.1021/jm9002395.
[46] A. Barzegar Behrooz, Z. Talaie, F. Jusheghani, M.J. Łos, T. Klonisch, S. Ghavami, Wnt and PI3K/Akt/mTOR Survival Pathways as Therapeutic Targets in Glioblastoma, Int J Mol Sci 23(3) (2022). https://doi.org/10.3390/ijms23031353.
[47] A. Papa, P.P. Pandolfi, The PTEN⁻PI3K Axis in Cancer, Biomolecules 9(4) (2019). https://doi.org/10.3390/biom9040153.

[48] M. Weiler, J. Blaes, S. Pusch, F. Sahm, M. Czabanka, S. Luger, L. Bunse, G. Solecki, V. Eichwald, M. Jugold, S. Hodecker, M. Osswald, C. Meisner, T. Hielscher, P. Rübmann, P.N. Pfenning, M. Ronellenfitsch, T. Kempf, M. Schnölzer, A. Abdollahi, F. Lang, M. Bendszus, A. von Deimling, F. Winkler, M. Weller, P. Vajkoczy, M. Platten, W. Wick, mTOR target NDRG1 confers MGMT-dependent resistance to alkylating chemotherapy, Proc Natl Acad Sci U S A 111(1) (2014) 409-14. https://doi.org/10.1073/pnas.1314469111.
[49] M. Jezierzański, N. Nafalska, M. Stopyra, T. Furgoł, M. Miciak, J. Kabut, I. Gisterek-Grocholska, Temozolomide (TMZ) in the Treatment of Glioblastoma Multiforme-A Literature Review and Clinical Outcomes, Curr Oncol 31(7) (2024) 3994-4002. https://doi.org/10.3390/curroncol31070296.
[50] J.Y. Sung, K. Hwang, The Nexus of Stemness, Telomere Stability, and Metabolic Reprogramming in Glioblastoma: Foundations of Tumor Persistence and Targets for Intervention, MedComm (2020) 7(4) (2026) e70693. https://doi.org/10.1002/mco2.70693.
[51] J.-Y. Sung, K. Hwang, Glioblastoma: epidemiology, molecular pathogenesis, diagnosis, management, and therapeutic resistance, Molecular Biomedicine 7(1) (2026) 63. https://doi.org/10.1186/s43556-026-00467-8.
[52] A. Pérez-González, K. Bévant, C. Blanpain, Cancer cell plasticity during tumor progression, metastasis and response to therapy, Nat Cancer 4(8) (2023) 1063-1082. https://doi.org/10.1038/s43018-023-00595-y.
[53] Z. Li, S. Bao, Q. Wu, H. Wang, C. Eyler, S. Sathornsumetee, Q. Shi, Y. Cao, J. Lathia, R.E. McLendon, A.B. Hjelmeland, J.N. Rich, Hypoxia-inducible factors regulate tumorigenic capacity of glioma stem cells, Cancer Cell 15(6) (2009) 501-13. https://doi.org/10.1016/j.ccr.2009.03.018.
[54] J. Cvitković, W.L. Tan, T. Jiang, Z. Zhao, Glioma tumor microenvironment and immunotherapy: past, present, and future, Biomark Res 13(1) (2025) 150. https://doi.org/10.1186/s40364-025-00863-2.
[55] A. Buonfiglioli, D. Hambardzumyan, Macrophages and microglia: the cerberus of glioblastoma, Acta Neuropathol Commun 9(1) (2021) 54. https://doi.org/10.1186/s40478-021-01156-z.
[56] A.H. Nwabo Kamdje, P.F. Seke Etet, M.J. Kipanyula, L. Vecchio, R. Tagne Simo, A.K. Njamnshi, K.E. Lukong, P.N. Mimche, Insulin-like growth factor-1 signaling in the tumor microenvironment: Carcinogenesis, cancer drug resistance, and therapeutic potential, Front Endocrinol (Lausanne) 13 (2022) 927390. https://doi.org/10.3389/fendo.2022.927390.
[57] S. Singh, D.S. Kapkoti, G. Singh, Translating Molecular Insights into Effective Targeting of Glioblastoma Stem Cells, Cancers 18(5) (2026) 860.
[58] S.M.B. Rodriguez, A. Kamel, G.V. Ciubotaru, G. Onose, A.-S. Sevastre, V. Sfredel, S. Danoiu, A. Dricu, L.G. Tataranu, An Overview of EGFR Mechanisms and Their Implications in Targeted Therapies for Glioblastoma, International Journal of Molecular Sciences 24(13) (2023) 11110.
[59] H. Saleem, U. Kulsoom Abdul, A. Küçükosmanoglu, M. Houweling, F.M.G. Cornelissen, D.H. Heiland, M.E. Hegi, M.C.M. Kouwenhoven, D. Bailey, T. Würdinger, B.A. Westerman, The TICking clock of EGFR therapy resistance in glioblastoma: Target Independence or target Compensation, Drug Resistance Updates 43 (2019) 29-37. https://doi.org/https://doi.org/10.1016/j.drup.2019.04.002.
[60] A.B. Chai, R. Callaghan, I.C. Gelissen, Regulation of P-Glycoprotein in the Brain, Int J Mol Sci 23(23) (2022). https://doi.org/10.3390/ijms232314667.

[61] T.F. Day, B.V.S. Kallakury, J.S. Ross, O. Voronel, S. Vaidya, C.E. Sheehan, U.N. Kasid, Dual Targeting of EGFR and IGF1R in the TNFAIP8 Knockdown Non-Small Cell Lung Cancer Cells, Mol Cancer Res 17(5) (2019) 1207-1219. https://doi.org/10.1158/1541-7786.Mcr-18-0731.
[62] Q. Liu, S. Yu, W. Zhao, S. Qin, Q. Chu, K. Wu, EGFR-TKIs resistance via EGFR-independent signaling pathways, Molecular Cancer 17(1) (2018) 53. https://doi.org/10.1186/s12943-018-0793-1.
[63] A.E. Yesilkanal, G.L. Johnson, A.F. Ramos, M.R. Rosner, New strategies for targeting kinase networks in cancer, J Biol Chem 297(4) (2021) 101128. https://doi.org/10.1016/j.jbc.2021.101128.
[64] G. Lombardi, G.L. De Salvo, A.A. Brandes, M. Eoli, R. Rudà, M. Faedi, I. Lolli, A. Pace, B. Daniele, F. Pasqualetti, S. Rizzato, L. Bellu, A. Pambuku, M. Farina, G. Magni, S. Indraccolo, M.P. Gardiman, R. Soffietti, V. Zagonel, Regorafenib compared with lomustine in patients with relapsed glioblastoma (REGOMA): a multicentre, open-label, randomised, controlled, phase 2 trial, Lancet Oncol 20(1) (2019) 110-119. https://doi.org/10.1016/s1470-2045(18)30675-2.
[65] G. Lombardi, P. Del Bianco, A.A. Brandes, M. Eoli, R. Rudà, T. Ibrahim, I. Lolli, S. Rizzato, B. Daniele, A. Pace, F. Pasqualetti, M. Caccesse, E. Bergo, G. Magni, G.L. De Salvo, V. Zagonel, Patient-reported outcomes in a phase II randomised study of regorafenib compared with lomustine in patients with relapsed glioblastoma (the REGOMA trial), Eur J Cancer 155 (2021) 179-190. https://doi.org/10.1016/j.ejca.2021.06.055.
[66] M. Sidorov, P. Dighe, R.W.L. Woo, A. Rodriguez-Brotons, M. Chen, R.J. Ice, E. Vaquero, D. Jian, P.Y. Desprez, M. Nosrati, L. Galvez, L. Leng, L. Dickinson, M. Kashani-Sabet, S.D. McAllister, L. Soroceanu, Dual Targeting of EGFR and MTOR Pathways Inhibits Glioblastoma Growth by Modulating the Tumor Microenvironment, Cells 12(4) (2023). https://doi.org/10.3390/cells12040547.
[67] W.M. Pardridge, The blood-brain barrier: bottleneck in brain drug development, NeuroRx 2(1) (2005) 3-14. https://doi.org/10.1602/neurorx.2.1.3.
[68] I. Pediaditakis, S. Tsakali, M.R. Lemieux, M. Brennan, W.H. Robinson, S. Papapetropoulos, A. Papapetropoulos, Pharmacological modulation of the blood-brain barrier: Mechanisms, therapeutic strategies, and emerging technologies, Pharmacological Reviews 78(2) (2026) 100118. https://doi.org/https://doi.org/10.1016/j.pharmr.2026.100118.
[69] P. Berndt, L. Winkler, J. Cording, O. Breitkreuz-Korff, A. Rex, S. Dithmer, V. Rausch, R. Blasig, M. Richter, A. Sporbert, H. Wolburg, I.E. Blasig, R.F. Haseloff, Tight junction proteins at the blood-brain barrier: far more than claudin-5, Cell Mol Life Sci 76(10) (2019) 1987-2002. https://doi.org/10.1007/s00018-019-03030-7.
[70] C.D. Arvanitis, G.B. Ferraro, R.K. Jain, The blood-brain barrier and blood-tumour barrier in brain tumours and metastases, Nat Rev Cancer 20(1) (2020) 26-41. https://doi.org/10.1038/s41568-019-0205-x.
[71] M. Lim, S. Puttick, Z.H. Houston, K.J. Thurecht, P. Kalita-de Croft, S. Mahler, S.E. Rose, R.L. Jeffree, R. Mazzieri, R. Dolcetti, S.R. Lakhani, J.M. Saunus, Innovative Therapeutic Strategies for Effective Treatment of Brain Metastases, International Journal of Molecular Sciences 20(6) (2019) 1280.
[72] J.N. Sarkaria, L.S. Hu, I.F. Parney, D.H. Pafundi, D.H. Brinkmann, N.N. Laack, C. Giannini, T.C. Burns, S.H. Kizilbash, J.K. Laramy, K.R. Swanson, T.J. Kaufmann, P.D. Brown, N.Y.R. Agar, E. Galanis, J.C. Buckner, W.F. Elmquist, Is the blood–brain barrier really

disrupted in all glioblastomas? A critical assessment of existing clinical data, Neuro-Oncology 20(2) (2018) 184-191. https://doi.org/10.1093/neuonc/nox175.
[73] B. Poller, J. Drewe, S. Krähenbühl, J. Huwyler, H. Gutmann, Regulation of BCRP (ABCG2) and P-glycoprotein (ABCB1) by cytokines in a model of the human blood-brain barrier, Cell Mol Neurobiol 30(1) (2010) 63-70. https://doi.org/10.1007/s10571-009-9431-1.
[74] L. Zinzi, E. Capparelli, M. Cantore, M. Contino, M. Leopoldo, N.A. Colabufo, Small and Innovative Molecules as New Strategy to Revert MDR, Front Oncol 4 (2014) 2. https://doi.org/10.3389/fonc.2014.00002.
[75] J. Wang, M.M. Susam, C. Gan, R.W. Sparidans, M.C. Lebre, J.H. Beijnen, A.H. Schinkel, P-Glycoprotein (MDR1/ABCB1) Restricts Brain Accumulation of the Novel EGFR Inhibitor EAI045 and Oral Elacridar Coadministration Enhances Its Brain Accumulation and Oral Exposure, Pharmaceuticals (Basel) 15(9) (2022). https://doi.org/10.3390/ph15091124.
[76] P. Stasiak, J. Sopel, J.M. Lipowicz, A.A. Rawłuszko-Wieczorek, K. Sterzyńska, J. Korbecki, R. Januchowski, Elacridar Reverses P-gp-Mediated Drug Resistance in Ovarian Cancer Cells in 2D and 3D Culture Models, Int J Mol Sci 26(24) (2025). https://doi.org/10.3390/ijms262412105.
[77] S. Habib, M. Singh, Angiopep-2-Modified Nanoparticles for Brain-Directed Delivery of Therapeutics: A Review, Polymers (Basel) 14(4) (2022). https://doi.org/10.3390/polym14040712.
[78] A.I. Mehta, B.D. Choi, D. Ajay, R. Raghavan, M. Brady, A.H. Friedman, I. Pastan, D.D. Bigner, J.H. Sampson, Convection enhanced delivery of macromolecules for brain tumors, Curr Drug Discov Technol 9(4) (2012) 305-10. https://doi.org/10.2174/157016312803305951.
[79] N. Hirokawa, Y. Noda, Y. Tanaka, S. Niwa, Kinesin superfamily motor proteins and intracellular transport, Nat Rev Mol Cell Biol 10(10) (2009) 682-96. https://doi.org/10.1038/nrm2774.
[80] J.D. Lathia, M. Hitomi, J. Gallagher, S.P. Gadani, J. Adkins, A. Vasanji, L. Liu, C.E. Eyler, J.M. Heddleston, Q. Wu, S. Minhas, A. Soeda, D.J. Hoeppner, R. Ravin, R.D.G. McKay, R.E. McLendon, D. Corbeil, A. Chenn, A.B. Hjelmeland, D.M. Park, J.N. Rich, Distribution of CD133 reveals glioma stem cells self-renew through symmetric and asymmetric cell divisions, Cell Death & Disease 2(9) (2011) e200-e200. https://doi.org/10.1038/cddis.2011.80.
[81] M. Osswald, E. Jung, F. Sahm, G. Solecki, V. Venkataramani, J. Blaes, S. Weil, H. Horstmann, B. Wiestler, M. Syed, L. Huang, M. Ratliff, K. Karimian Jazi, F.T. Kurz, T. Schmenger, D. Lemke, M. Gömmel, M. Pauli, Y. Liao, P. Häring, S. Pusch, V. Herl, C. Steinhäuser, D. Krunic, M. Jarahian, H. Miletic, A.S. Berghoff, O. Griesbeck, G. Kalamakis, O. Garaschuk, M. Preusser, S. Weiss, H. Liu, S. Heiland, M. Platten, P.E. Huber, T. Kuner, A. von Deimling, W. Wick, F. Winkler, Brain tumour cells interconnect to a functional and resistant network, Nature 528(7580) (2015) 93-8. https://doi.org/10.1038/nature16071.
[82] A.F. Serpico, R. Visconti, D. Grieco, Exploiting immune-dependent effects of microtubule-targeting agents to improve efficacy and tolerability of cancer treatment, Cell Death & Disease 11(5) (2020) 361. https://doi.org/10.1038/s41419-020-2567-0.
[83] H.C. Assunção, P.M.A. Silva, H. Bousbaa, H. Cidade, Recent Advances in Microtubule Targeting Agents for Cancer Therapy, Molecules 30(16) (2025) 3314.

[84] E. Mukhtar, V.M. Adhami, H. Mukhtar, Targeting microtubules by natural agents for cancer therapy, Mol Cancer Ther 13(2) (2014) 275-84. https://doi.org/10.1158/1535-7163.Mct-13-0791.
[85] M.E. Pero, F. Chowdhury, F. Bartolini, Role of tubulin post-translational modifications in peripheral neuropathy, Exp Neurol 360 (2023) 114274. https://doi.org/10.1016/j.expneurol.2022.114274.
[86] C. Mortensen, K.C. Chua, H.S. Hammer, F. Nielsen, O. Pötz, Å.F. Svenningsen, D.L. Kroetz, T.B. Stage, Paclitaxel- and vincristine-induced neurotoxicity and drug transport in sensory neurons, bioRxiv (2023) 2023.02.07.527432. https://doi.org/10.1101/2023.02.07.527432.
[87] W. Löscher, H. Potschka, Blood-brain barrier active efflux transporters: ATP-binding cassette gene family, NeuroRx 2(1) (2005) 86-98. https://doi.org/10.1602/neurorx.2.1.86.
[88] L.A. Patron, H. Yeoman, S. Wilson, N. Tang, M.E. Berens, V. Gokhale, T.C. Suzuki, Novel Brain-Penetrant, Small-Molecule Tubulin Destabilizers for the Treatment of Glioblastoma, Biomedicines 12(2) (2024). https://doi.org/10.3390/biomedicines12020406.
[89] F. Jernigan, A. Branstrom, J.D. Baird, L. Cao, M. Dali, B. Furia, M.J. Kim, K. O'Keefe, R. Kong, O.L. Laskin, J.M. Colacino, M. Pykett, A. Mollin, J. Sheedy, M. Dumble, Y.C. Moon, R. Sheridan, T. Mühlethaler, R.J. Spiegel, A.E. Prota, M.O. Steinmetz, M. Weetall, Preclinical and Early Clinical Development of PTC596, a Novel Small-Molecule Tubulin-Binding Agent, Mol Cancer Ther 20(10) (2021) 1846-1857. https://doi.org/10.1158/1535-7163.Mct-20-0774.
[90] G. Iegiani, F. Di Cunto, G. Pallavicini, Inhibiting microcephaly genes as alternative to microtubule targeting agents to treat brain tumors, Cell Death & Disease 12(11) (2021) 956. https://doi.org/10.1038/s41419-021-04259-6.
[91] S. Agnihotri, G. Zadeh, Metabolic reprogramming in glioblastoma: the influence of cancer metabolism on epigenetics and unanswered questions, Neuro Oncol 18(2) (2016) 160-72. https://doi.org/10.1093/neuonc/nov125.
[92] C. Olivier, L. Oliver, L. Lalier, F.M. Vallette, Drug Resistance in Glioblastoma: The Two Faces of Oxidative Stress, Front Mol Biosci 7 (2020) 620677. https://doi.org/10.3389/fmolb.2020.620677.
[93] A. Nowacka, M. Śniegocki, E. Ziółkowska, Oxidative Stress and Antioxidants in Glioblastoma: Mechanisms of Action, Therapeutic Effects and Future Directions, Antioxidants (Basel) 14(9) (2025). https://doi.org/10.3390/antiox14091121.
[94] S.H. Tai, Y.W. Lin, T.Y. Huang, C.C. Chang, L.C. Chao, T.S. Wu, E.J. Lee, Cinnamophilin enhances temozolomide-induced cytotoxicity against malignant glioma: the roles of ROS and cell cycle arrest, Transl Cancer Res 10(9) (2021) 3906-3920. https://doi.org/10.21037/tcr-20-3426.
[95] W.A. Awuah, A.R. Toufik, R. Yarlagadda, T. Mikhailova, A. Mehta, H. Huang, M. Kundu, L. Lopes, S. Benson, L. Mykola, S. Vladyslav, A. Alexiou, B.S. Alghamdi, A.M. Hashem, G. Md Ashraf, Exploring the role of Nrf2 signaling in glioblastoma multiforme, Discov Oncol 13(1) (2022) 94. https://doi.org/10.1007/s12672-022-00556-4.
[96] S. Singh, I. Mohapatra, D. Barik, H. Zheng, S. Kim, M. Sharma, C.C. Chen, G. Singh, Harnessing ferroptosis to transform glioblastoma therapy and surmount treatment resistance, Cell Death Discovery 11(1) (2025) 448. https://doi.org/10.1038/s41420-025-02744-x.

[97] D.S. Kalinowski, P.J. Jansson, Z. Kovacevic, D.R. Richardson, The redox-active, anti-cancer drug Dp44mT inhibits T-cell activation and CD25 through a copper-dependent mechanism, Redox Rep 18(2) (2013) 48-50. https://doi.org/10.1179/1351000213y.0000000041.
[98] A.R. Bogdan, M. Miyazawa, K. Hashimoto, Y. Tsuji, Regulators of Iron Homeostasis: New Players in Metabolism, Cell Death, and Disease, Trends Biochem Sci 41(3) (2016) 274-286. https://doi.org/10.1016/j.tibs.2015.11.012.
[99] K.C. Park, J. Paluncic, Z. Kovacevic, D.R. Richardson, Pharmacological targeting and the diverse functions of the metastasis suppressor, NDRG1, in cancer, Free Radic Biol Med 157 (2020) 154-175. https://doi.org/10.1016/j.freeradbiomed.2019.05.020.
[100] T. Abbas, A. Dutta, p21 in cancer: intricate networks and multiple activities, Nat Rev Cancer 9(6) (2009) 400-14. https://doi.org/10.1038/nrc2657.
[101] L. Daverkausen-Fischer, F. Pröls, Regulation of calcium homeostasis and flux between the endoplasmic reticulum and the cytosol, Journal of Biological Chemistry 298(7) (2022) 102061. https://doi.org/https://doi.org/10.1016/j.jbc.2022.102061.
[102] M.G. Azad, T.M. Russell, X. Gu, X. Zhao, V. Richardson, T.P. Wijesinghe, G. Babu, X. Guo, B. Kaya, M. Dharmasivam, Z. Deng, D.R. Richardson, NDRG1 and its family members: More than just metastasis suppressor proteins and targets of thiosemicarbazones, Journal of Biological Chemistry 301(7) (2025) 110230. https://doi.org/https://doi.org/10.1016/j.jbc.2025.110230.
[103] D. Galmarini, C.M. Galmarini, F.C. Galmarini, Cancer chemotherapy: a critical analysis of its 60 years of history, Crit Rev Oncol Hematol 84(2) (2012) 181-99. https://doi.org/10.1016/j.critrevonc.2012.03.002.
[104] S. Watanabe, H. Hayashi, K. Nakagawa, Is afatinib a treatment option for brain metastases in patients with EGFR mutation-positive non-small cell lung cancer?, Ann Transl Med 4(11) (2016) 225. https://doi.org/10.21037/atm.2016.05.48.
[105] K. Kudo, K. Kawakado, T. Kawajiri, T. Nishi, G. Makimoto, T. Tamura, S. Kuyama, M. Tanimoto, Dramatic Response of Brain Metastasis from EGFR-mutation-positive NSCLC to Dacomitinib, Intern Med 59(14) (2020) 1739-1740. https://doi.org/10.2169/internalmedicine.4449-20.

10. Author declarations of the publications included in the doctoral thesis

mgr Patryk Rurka
Instytut Fizyki
Uniwersytet Śląski
ul. 75 Pułku Piechoty 1a
41-500 Chorzów

Chorzów, 31.05.2026

OŚWIADCZENIE

Oświadczam, że w pracy **Malarz K., Kuczak M., Rurka P., Rawicka P., Boguszewska-Czubara A., Jampilek J., Mularski J., Musiol R., Mrozek-Wilczkiewicz A.: "Unveiling the role of Ndrg1 gene on the oxidative stress induction behind the anticancer potential of styrylquinazoline derivatives", Scientific Reports 2025, 15, 16081** mój udział polegał na ocenie poziomu białek szlaku EGFR-mTOR z wykorzystaniem metody Western Blot, wykonaniu oznaczeń metodą Lumit Immunoassay.

Podpis

Dr Katarzyna Malarz, prof. UŚ
Instytut Fizyki
Uniwersytet Śląski
ul. 75 Pułku Piechoty 1a
41-500 Chorzów

Chorzów, 09.06.2026

OŚWIADCZENIE

Oświadczam, że w pracy **Malarz K., Kuczak M., Rurka P., Rawicka P., Boguszewska-Czubara A., Jampilek J., Mularski J., Musiol R., Mrozek-Wilczkiewicz A.: "Unveiling the role of Ndrg1 gene on the oxidative stress induction behind the anticancer potential of styrylquinazoline derivatives", Scientific Reports 2025, 15, 16081** mój udział polegał na sformułowaniu hipotezy badawczej, zaprojektowaniu eksperymentów, przeprowadzeniu badań cytotoksyczności, cyklu komórkowego, apoptozy oraz części badań qRT-PCR, dyskusji wyników oraz napisaniu manuskryptu.

Podpis

dr inż. Jacek Mularski
Instytut Chemii
Uniwersytet Śląski
ul. 75 Pułku Piechoty 1a
41-500 Chorzów

Katowice, 05.05.2026

OŚWIADCZENIE

Oświadczam, że w pracy **Malarz K., Kuczak M., Rurka P., Rawicka P., Boguszewska-Czubara A., Jampilek J., Mularski J., Musiol R., Mrozek-Wilczkiewicz A.: "Unveiling the role of Ndrg1 gene on the oxidative stress induction behind the anticancer potential of styrylquinazoline derivatives", Scientific Reports 2025, 15, 16081** mój udział polegał na dostarczeniu związku IS20 do pogłębionych badań biologicznych.

Podpis

dr Patrycja Rawicka
Instytut Fizyki
Uniwersytet Śląski
ul. 75 Pułku Piechoty 1a
41-500 Chorzów

Chorzów, 06.05.2026

OŚWIADCZENIE

Oświadczam, że w pracy **Malarz K., Kuczak M., Rurka P., Rawicka P., Boguszewska-Czubara A., Jampilek J., Mularski J., Musiol R., Mrozek-Wilczkiewicz A.: "Unveiling the role of Ndrg1 gene on the oxidative stress induction behind the anticancer potential of styrylquinazoline derivatives", Scientific Reports 2025, 15, 16081** mój udział polegał na wykonaniu eksperymentu i interpretacji widm UV/Vis dotyczących chelatacji metali.

Podpis
Patrycja Rawicka

Dr hab. Anna Mrozek-Wilczkiewicz, prof. UŚ
Instytut Fizyki
Uniwersytet Śląski
ul. 75 Pułku Piechoty 1a
41-500 Chorzów

Chorzów, 02.06.2026

OŚWIADCZENIE

Oświadczam, że w pracy **Malarz K., Kuczak M., Rurka P., Rawicka P., Boguszewska-Czubara A., Jampilek J., Mularski J., Musiol R., Mrozek-Wilczkiewicz A.: "Unveiling the role of Ndrg1 gene on the oxidative stress induction behind the anticancer potential of styrylquinazoline derivatives", Scientific Reports 2025, 15, 16081** mój udział polegał na przeprowadzeniu badań nad indukcją autofagii oraz przygotowaniu i edycji końcowej wersji manuskryptu.

Podpis

Prof. PharmDr. Josef Jampilek, Ph.D.
Department of Chemical Biology
Palacky University Olomouc
Slechtitelu 27
Olomouc 779 00
Czech Republic

Olomouc, 11.05.2026

DECLARATION

I hereby declare that my contribution to the publication **Malarz K., Kuczak M., Rurka P., Rawicka P., Boguszewska-Czubara A., Jampilek J., Mularski J., Musiol R., Mrozek-Wilczkiewicz A.: "Unveiling the role of Ndrg1 gene on the oxidative stress induction behind the anticancer potential of styrylquinazoline derivatives", Scientific Reports 2025, 15, 16081** consisted of performing the ADME calculations.

Signature

Zakład Chemii Medycznej
Katedry Nauk Podstawowych
Uniwersytetu Medycznego w Lublinie
ul. Chodźki 4a, 20-093 Lublin
tel. 81 448 61 90

Dr hab. Anna Boguszewska-Czubara, prof. UML
Zakład Chemii Medycznej
Uniwersytet Medyczny w Lublinie
ul. Chodźki 4a
20-093 Lublin

Lublin, 29.05.2026

OŚWIADCZENIE

Oświadczam, że w pracy **Rurka P., Cieślik W., Płaziński W., Stępnik K., Boguszewska-Czubara A., Kot E., Musioł R., Jasica M., Mrozek-Wilczkiewicz A., Malarz K.; „A novel quinazolinone insulin receptor inhibitor and its synergy with an EGFR inhibitor in glucose-driven glioblastoma", Molecular Oncology, 2026, https://doi.org/10.1002/1878-0261.70274** mój udział polegał na wykonaniu badań toksykologicznych i ocenie efektywności terapeutycznej *in vivo* na modelu *Danio rerio*, a także na analizie otrzymanych wyników.

Anna Boguszewska-Czubara

Podpis

Zakład Chemii Medycznej
Katedry Nauk Podstawowych
Uniwersytetu Medycznego w Lublinie
ul. Chodźki 4a, 20-093 Lublin
tel. 81 448 61 90

Dr hab. Anna Boguszewska-Czubara, prof. UML
Zakład Chemii Medycznej
Uniwersytet Medyczny w Lublinie
ul. Chodźki 4a
20-093 Lublin

Lublin, 29.05.2026

OŚWIADCZENIE

Oświadczam, że w pracy **Malarz K., Kuczak M., Rurka P., Rawicka P., Boguszewska-Czubara A., Jampilek J., Mularski J., Musiol R., Mrozek-Wilczkiewicz A.: "Unveiling the role of Ndrg1 gene on the oxidative stress induction behind the anticancer potential of styrylquinazoline derivatives", Scientific Reports 2025, 15, 16081** mój udział polegał na wykonaniu badań toksykologicznych *in vivo* na modelu *Danio rerio* oraz analizie otrzymanych wyników.

Anna Boguszewska-Czubara

Podpis

Prof. dr hab. Robert Musioł
Instytut Chemii
Uniwersytet Śląski
ul. 75 Pułku Piechoty 1a
41-500 Chorzów

Katowice, 18.05.2026

OŚWIADCZENIE

Oświadczam, że w pracy **Malarz K., Kuczak M., Rurka P., Rawicka P., Boguszewska-Czubara A., Jampilek J., Mularski J., Musiol R., Mrozek-Wilczkiewicz A.: "Unveiling the role of Ndrg1 gene on the oxidative stress induction behind the anticancer potential of styrylquinazoline derivatives", Scientific Reports 2025, 15, 16081** mój udział polegał na edycji końcowej wersji manuskryptu.

Podpis

mgr Patryk Rurka
Instytut Fizyki
Uniwersytet Śląski
ul. 75 Pułku Piechoty 1a
41-500 Chorzów

Chorzów, 31.05.2026

OŚWIADCZENIE

Oświadczam, że w pracy **Rurka P., Mularski J., Zioła P., Boguszewska-Czubara A., Jampilek J., Mrozek-Wilczkiewicz A., Malarz K.; „An insight into the anticancer potential of sulfonated styrylquinazolines as multifunctional agents targeting microtubules", Bioorganic Chemistry, 2026, 109517** mój udział polegał na przeprowadzeniu badań cytotoksyczności, analizie cyklu komórkowego i apoptozy metodą cytometrii przepływowej, wykonaniu badań poziomu ekspresji białek metodą Western Blot oraz Lumit Immunoassay oraz na edycji tekstu.

Podpis

Dr Katarzyna Malarz, prof. UŚ
Instytut Fizyki
Uniwersytet Śląski
ul. 75 Pułku Piechoty 1a
41-500 Chorzów

Chorzów, 09.06.2026

OŚWIADCZENIE

Oświadczam, że w pracy **Rurka P., Mularski J., Zioła P., Boguszewska-Czubara A., Jampilek J., Mrozek-Wilczkiewicz A., Malarz K.; „An insight into the anticancer potential of sulfonated styrylquinazolines as multifunctional agents targeting microtubules", Bioorganic Chemistry, 2026, 109517** mój udział polegał na sformułowaniu hipotezy badawczej, zaprojektowaniu eksperymentów biologicznych, przeprowadzeniu testów polimeryzacji tubuliny oraz testów kinazowych, dyskusji wyników oraz napisaniu manuskryptu.

Podpis

Zakład Chemii Medycznej
Katedry Nauk Podstawowych
Uniwersytetu Medycznego w Lublinie
ul. Chodźki 4a, 20-093 Lublin
tel. 81 448 61 90

Dr hab. Anna Boguszewska-Czubara, prof. UML
Zakład Chemii Medycznej
Uniwersytet Medyczny w Lublinie
ul. Chodźki 4a
20-093 Lublin

Lublin, 29.05.2026

OŚWIADCZENIE

Oświadczam, że w pracy **Rurka P., Mularski J., Zioła P., Boguszewska-Czubara A., Jampilek J., Mrozek-Wilczkiewicz A., Malarz K.; „An insight into the anticancer potential of sulfonated styrylquinazolines as multifunctional agents targeting microtubules", Bioorganic Chemistry, 2026, 109517** mój udział polegał na wykonaniu badań toksykologicznych i ocenie efektywności terapeutycznej *in vivo* na modelu *Danio rerio*, a także na analizie otrzymanych wyników.

Anna Boguszewska - Czubara

Podpis

Zakład Chemii Medycznej
Katedry Nauk Podstawowych
Uniwersytetu Medycznego w Lublinie
ul. Chodźki 4a, 20-093 Lublin
tel. 81 448 61 90

Dr hab. Anna Boguszewska-Czubara, prof. UML
Zakład Chemii Medycznej
Uniwersytet Medyczny w Lublinie
ul. Chodźki 4a
20-093 Lublin

Lublin, 29.05.2026

OŚWIADCZENIE

Oświadczam, że w pracy **Rurka P., Cieślik W., Płaziński W., Stępnik K., Boguszewska-Czubara A., Kot E., Musioł R., Jasica M., Mrozek-Wilczkiewicz A., Malarz K.; „A novel quinazolinone insulin receptor inhibitor and its synergy with an EGFR inhibitor in glucose-driven glioblastoma", Molecular Oncology, 2026, https://doi.org/10.1002/1878-0261.70274** mój udział polegał na wykonaniu badań toksykologicznych i ocenie efektywności terapeutycznej *in vivo* na modelu *Danio rerio*, a także na analizie otrzymanych wyników.

Anna Boguszewska-Czubara

Podpis

dr inż. Jacek Mularski
Instytut Chemii
Uniwersytet Śląski
ul. 75 Pułku Piechoty 1a
41-500 Chorzów

Katowice, 05.05.2026

OŚWIADCZENIE

Oświadczam, że w pracy **Rurka P., Mularski J., Zioła P., Boguszewska-Czubara A., Jampilek J., Mrozek-Wilczkiewicz A., Malarz K.; „An insight into the anticancer potential of sulfonated styrylquinazolines as multifunctional agents targeting microtubules". Bioorganic Chemistry, 2026, 109517** mój udział polegał na zaprojektowaniu oraz zsyntezowaniu związków, a także na przeprowadzeniu analiz *in silico* dotyczących ustalenia sposobu wiązania związków z tubuliną.

Podpis

Dr hab. Anna Mrozek-Wilczkiewicz, prof. UŚ
Instytut Fizyki
Uniwersytet Śląski
ul. 75 Pułku Piechoty 1a
41-500 Chorzów

Chorzów, 02.06.2026

OŚWIADCZENIE

Oświadczam, że w pracy **Rurka P., Mularski J., Zioła P., Boguszewska-Czubara A., Jampilek J., Mrozek-Wilczkiewicz A., Malarz K.; „An insight into the anticancer potential of sulfonated styrylquinazolines as multifunctional agents targeting microtubules", Bioorganic Chemistry, 2026, 109517** mój udział polegał na przygotowaniu i edycji końcowej wersji manuskryptu.

Podpis

Prof. PharmDr. Josef Jampilek, Ph.D.
Department of Chemical Biology
Palacky University Olomouc
Slechtitelu 27
Olomouc 779 00
Czech Republic

Olomouc, 11.05.2026

DECLARATION

I hereby declare that my contribution to the publication **Rurka P., Mularski J., Zioła P., Boguszewska-Czubara A., Jampilek J., Mrozek-Wilczkiewicz A., Malarz K.; „An insight into the anticancer potential of sulfonated styrylquinazolines as multifunctional agents targeting microtubules". Bioorganic Chemistry, 2026, 109517** consisted of calculating and interpreting the ADME properties.

Signature

mgr Patryk Zioła
Instytut Fizyki
Uniwersytet Śląski
ul. 75 Pułku Piechoty 1a
41-500 Chorzów

Chorzów, 08.05.2026

OŚWIADCZENIE

Oświadczam, że w pracy **Rurka P., Mularski J., Zioła P., Boguszewska-Czubara A., Jampilek J., Mrozek-Wilczkiewicz A., Malarz K.: „An insight into the anticancer potential of sulfonated styrylquinazolines as multifunctional agents targeting microtubules", Bioorganic Chemistry, 2026, 109517** mój udział polegał na wykonaniu eksperymentów qRT-PCR oraz obrazowania tubuliny w komórkach.

Podpis

Zioła Patryk

mgr Patryk Rurka
Instytut Fizyki
Uniwersytet Śląski
ul. 75 Pułku Piechoty 1a
41-500 Chorzów

Chorzów, 31.05.2026

OŚWIADCZENIE

Oświadczam, że w pracy **Rurka P., Cieślik W., Płaziński W., Stępnik K., Boguszewska-Czubara A., Kot E., Musioł R., Jasica M., Mrozek-Wilczkiewicz A., Malarz K.; „A novel quinazolinone insulin receptor inhibitor and its synergy with an EGFR inhibitor in glucose-driven glioblastoma", Molecular Oncology, 2026, https://doi.org/10.1002/1878-0261.70274** mój udział polegał na przeprowadzeniu pomiarów metodą termoforezy mikroskalowej (MST), badaniu skuteczności terapii skojarzonej, ocenie poziomu białek metodą Western Blot oraz na przygotowaniu pierwszej wersji manuskryptu.

Podpis

Dr Katarzyna Malarz, prof. UŚ
Instytut Fizyki
Uniwersytet Śląski
ul. 75 Pułku Piechoty 1a
41-500 Chorzów

Chorzów, 09.06.2026

OŚWIADCZENIE

Oświadczam, że w pracy **Rurka P., Cieślik W., Plaziński W., Stępnik K., Boguszewska-Czubara A., Kot E., Musioł R., Jasica M., Mrozek-Wilczkiewicz A., Malarz K.; „A novel quinazolinone insulin receptor inhibitor and its synergy with an EGFR inhibitor in glucose-driven glioblastoma", Molecular Oncology, 2026, https://doi.org/10.1002/1878-0261.70274** mój udział polegał na sformułowaniu hipotezy badawczej, zaprojektowaniu eksperymentów biologicznych, przeprowadzeniu badań cytotoksyczności oraz badań hamowania aktywności kinaz, dyskusji wyników oraz napisaniu manuskryptu.

Podpis

Zakład Chemii Medycznej
Katedry Nauk Podstawowych
Uniwersytetu Medycznego w Lublinie
ul. Chodźki 4a, 20-093 Lublin
tel. 81 448 61 90

Dr hab. Anna Boguszewska-Czubara, prof. UML
Zakład Chemii Medycznej
Uniwersytet Medyczny w Lublinie
ul. Chodźki 4a
20-093 Lublin

Lublin, 29.05.2026

OŚWIADCZENIE

Oświadczam, że w pracy **Rurka P., Cieślik W., Płaziński W., Stępnik K., Boguszewska-Czubara A., Kot E., Musioł R., Jasica M., Mrozek-Wilczkiewicz A., Malarz K.; „A novel quinazolinone insulin receptor inhibitor and its synergy with an EGFR inhibitor in glucose-driven glioblastoma", Molecular Oncology, 2026, https://doi.org/10.1002/1878-0261.70274** mój udział polegał na wykonaniu badań toksykologicznych i ocenie efektywności terapeutycznej *in vivo* na modelu *Danio rerio*, a także na analizie otrzymanych wyników.

Anna Boguszewska-Czubara

Podpis

dr hab. Katarzyna Stępnik
Katedra Chemii Fizycznej
Uniwersytet Marii Curie-Skłodowskiej w Lublinie
Pl. M. Curie-Skłodowskiej 3
20-031 Lublin

Lublin, 29.05.2026

OŚWIADCZENIE

Oświadczam, że w pracy **Rurka P., Cieślik W., Płaziński W., Stępnik K., Boguszewska-Czubara A., Kot E., Musioł R., Jasica M., Mrozek-Wilczkiewicz A., Malarz K.; „A novel quinazolinone insulin receptor inhibitor and its synergy with an EGFR inhibitor in glucose-driven glioblastoma", Molecular Oncology, 2026, https://doi.org/10.1002/1878-0261.70274** mój udział polegał na określeniu zdolności przenikania przez barierę krew-mózg (BBB) metodami *in silico* oraz na wykonaniu analiz biomimetycznych z wykorzystaniem chromatografii.

Katarzyna Stępnik

Podpis

dr Wioleta Cieślik
Instytut Chemii
Uniwersytet Śląski
ul. 75 Pułku Piechoty 1a
41-500 Chorzów

Katowice, 02.06.2026

OŚWIADCZENIE

Oświadczam, że w pracy **Rurka P., Cieślik W., Płaziński W., Stępnik K., Boguszewska-Czubara A., Kot E., Musiol R., Jasica M., Mrozek-Wilczkiewicz A., Malarz K.; „A novel quinazolinone insulin receptor inhibitor and its synergy with an EGFR inhibitor in glucose-driven glioblastoma", Molecular Oncology, 2026, https://doi.org/10.1002/1878-0261.70274** mój udział polegał na zaprojektowaniu oraz syntezie badanych związków wraz z ich pełną charakterystyką fizykochemiczną. Ponadto byłam odpowiedzialna za przygotowanie części chemicznej manuskryptu, obejmującej opis syntezy, charakterystyki otrzymanych związków oraz interpretację uzyskanych wyników.

Wioleta Cieślik
Podpis

Dr hab. Anna Mrozek-Wilczkiewicz, prof. UŚ
Instytut Fizyki
Uniwersytet Śląski
ul. 75 Pułku Piechoty 1a
41-500 Chorzów

Chorzów, 02.06.2026

OŚWIADCZENIE

Oświadczam, że w pracy **Rurka P., Cieślik W., Płaziński W., Stępnik K., Boguszewska-Czubara A., Kot E., Musioł R., Jasica M., Mrozek-Wilczkiewicz A., Malarz K.; „A novel quinazolinone insulin receptor inhibitor and its synergy with an EGFR inhibitor in glucose-driven glioblastoma", Molecular Oncology, 2026, https://doi.org/10.1002/1878-0261.70274** mój udział polegał na przygotowaniu i edycji końcowej wersji manuskryptu.

Podpis

Prof. dr hab. Robert Musioł
Instytut Chemii
Uniwersytet Śląski
ul. 75 Pułku Piechoty 1a
41-500 Chorzów

Katowice, 08.06.2026

OŚWIADCZENIE

Oświadczam, że w pracy **Rurka P., Cieślik W., Płaziński W., Stępnik K., Boguszewska-Czubara A., Kot E., Musioł R., Jasica M., Mrozek-Wilczkiewicz A., Malarz K.; „A novel quinazolinone insulin receptor inhibitor and its synergy with an EGFR inhibitor in glucose-driven glioblastoma", Molecular Oncology, 2026, https://doi.org/10.1002/1878-0261.70274** mój udział polegał na edycji końcowej wersji manuskryptu.

Podpis

lic. Elżbieta Kot
Zakład Chemii Medycznej
Uniwersytet Medyczny w Lublinie
ul. Chodźki 4a
20-093 Lublin

Lublin, 02.06.2026

OŚWIADCZENIE

Oświadczam, że w pracy **Rurka P., Cieślik W., Płaziński W., Stępnik K., Boguszewska-Czubara A., Kot E., Musioł R., Jasica M., Mrozek-Wilczkiewicz A., Malarz K.; „A novel quinazolinone insulin receptor inhibitor and its synergy with an EGFR inhibitor in glucose-driven glioblastoma", Molecular Oncology, 2026, accepted** mój udział polegał na wykonaniu badań *in vivo* na modelu *Danio rerio*.

Podpis

Zakład Chemii Medycznej
Katedry Nauk Podstawowych
Uniwersytetu Medycznego w Lublinie
ul. Chodźki 4a, 20-093 Lublin
tel. 81 448 61 90

Dr hab. Anna Boguszewska-Czubara, prof. UML
Zakład Chemii Medycznej
Uniwersytet Medyczny w Lublinie
ul. Chodźki 4a
20-093 Lublin

Lublin, 29.05.2026

OŚWIADCZENIE

Oświadczam, że w pracy **Rurka P., Cieślik W., Płaziński W., Stępnik K., Boguszewska-Czubara A., Kot E., Musioł R., Jasica M., Mrozek-Wilczkiewicz A., Malarz K.; „A novel quinazolinone insulin receptor inhibitor and its synergy with an EGFR inhibitor in glucose-driven glioblastoma", Molecular Oncology, 2026, https://doi.org/10.1002/1878-0261.70274** mój udział polegał na wykonaniu badań toksykologicznych i ocenie efektywności terapeutycznej *in vivo* na modelu *Danio rerio*, a także na analizie otrzymanych wyników.

Anna Boguszewska-Czubara

Podpis

inż. Mateusz Jasica
Instytut Chemii
Uniwersytet Śląski
ul. 75 Pułku Piechoty 1a
41-500 Chorzów

Katowice, 02.06.2026

OŚWIADCZENIE

Oświadczam, że w pracy **Rurka P., Cieślik W., Płaziński W., Stępnik K., Boguszewska-Czubara A., Kot E., Musioł R., Jasica M., Mrozek-Wilczkiewicz A., Malarz K.; „A novel quinazolinone insulin receptor inhibitor and its synergy with an EGFR inhibitor in glucose-driven glioblastoma", Molecular Oncology, 2026, https://doi.org/10.1002/1878-0261.70274** mój udział polegał na syntezie części badanych związków zgodnie z opracowanymi procedurami syntetycznymi.

Podpis

Prof. dr hab. Wojciech Płaziński
Instytut Katalizy i Fizykochemii Powierzchni im. Jerzego Habera PAN
ul. Niezapominajek 8
30-239 Kraków

Lublin, 29.05.2026

OŚWIADCZENIE

Oświadczam, że w pracy **Rurka P., Cieślik W., Płaziński W., Stępnik K., Boguszewska-Czubara A., Kot E., Musioł R., Jasica M., Mrozek-Wilczkiewicz A., Malarz K.; „A novel quinazolinone insulin receptor inhibitor and its synergy with an EGFR inhibitor in glucose-driven glioblastoma", Molecular Oncology, 2026, https://doi.org/10.1002/1878-0261.70274** mój udział polegał na przeprowadzeniu badań z wykorzystaniem dokowania molekularnego oraz analizie uzyskanych wyników.

Podpis

Wojciech Płaziński

11. Supplement

www.nature.com/scientificreports

scientific reports

Check for updates

OPEN

Unveiling the role of *Ndrg1* gene on the oxidative stress induction behind the anticancer potential of styrylquinazoline derivatives

Katarzyna Malarz[1,2✉], Michał Kuczak[3], Patryk Rurka[2], Patrycja Rawicka[2], Anna Boguszewska-Czubara[4], Josef Jampilek[5], Jacek Mularski[3], Robert Musiol[3] & Anna Mrozek-Wilczkiewicz[1,2]

This work presents a multifaceted mechanism of the anticancer action of a 2-styrylquinazoline derivative. Extensive analysis of various aspects related to tyrosine kinase inhibition and effects on cellular targets at both the gene and protein levels revealed the potential of this IS20 compound for future research. This study presents a detailed analysis of the relationship between ABL and SRC kinase affecting the inhibition of the EGFR/mTOR signaling pathway in a non-obvious manner. The study was supported by experiments using various molecular biology techniques to confirm the induction of oxidative stress, inhibition of the cell cycle in the G2/M phase and the triggering of cell death via both the apoptosis and autophagy pathways. The cell models included those with different p53 protein status, which affected the cellular response in the form of altered *Ndrg1* expression. Finally, the appropriate physicochemical properties of IS20 for adequate bioavailability and toxicity to the body were observed in an *in vivo* model.

Keywords Anticancer drug, Styrylquinazoline, Oxidative stress, Iron chelator, *Ndrg1*, p53 protein, Autophagy, Apoptosis

The quinazoline scaffold is a versatile and unique motif, which has proved beneficial in drug design and discovery. Compounds containing quinazoline rings have a wide range of biological activities, including therapeutic effects such as antitumor[1–3], antibacterial[4], anti-inflammatory[5], antiviral[6,7], and antifungal[8,9]. Importantly, this privileged structure is commonly present in many FDA-approved EGFR inhibitors, particularly gefitinib, erlotinib, lapatinib, and afatinib[10]. In recent years, quinazoline compounds containing a styryl moiety have become increasingly popular in medicinal chemistry. It has been possible to identify compounds with interesting antitumor activity, which, despite some common features, are characterized by a diverse molecular mechanism of action (see Fig. 1), some of which show clinical relevance. The first example of a promising compound in the preclinical studies is CP-31398. This small molecule is known to be a p53 reactivator and is characterized by both stabilization of the active conformation of wild-type p53 protein and the ability to activate it in some types of cancers harboring a mutation of this protein[11]. Studies on CP-31398 have revealed a more complex mechanism of apoptosis induction in both a p53-dependent and -independent manner via Bax induction[12]. Our team recently identified an interesting enzymatic inhibition profile for CP-31398 against several proteins belonging to the non-receptor tyrosine kinase family[13]. Another structurally very similar compound is KIN-281, described as a MELK, BMX and STAT3 inhibitor[14]. Conversely, its analog KIN-236 can interact with and effectively diminish the activity of a wide range of tumor-related kinase proteins, including the Ca^{2+}/calmodulin-dependent protein kinase (CAMK) family, ERBB4 and Lyn B[15]. Diversification and design of novel compounds based on the CP-31398 core led to the discovery and synthesis of a 2-styryl-4-aminoquinazoline (10ah). Its anticancer activity against several cancer cell lines was greater than that of the output p53 reactivator and was shown to be most potent against gastric cancer cells (IC_{50} value below 2 μM). Similarly, the molecular mechanism of its anticancer

[1]Department of Systems Biology and Engineering, Silesian University of Technology, Akademicka 16, Gliwice 44-100, Poland. [2]Institute of Physics, University of Silesia in Katowice, 75 Pułku Piechoty 1a, Chorzów 41-500, Poland. [3]Institute of Chemistry, University of Silesia in Katowice, 75 Pułku Piechoty 1a, Chorzów 41-500, Poland. [4]Department of Medical Chemistry, Medical University of Lublin, Chodźki 4a, Lublin 20-093, Poland. [5]Department of Chemical Biology, Palacky University Olomouc, Slechtitelu 27, Olomouc 779 00, Czech Republic. ✉email: katarzyna.malarz@us.edu.pl

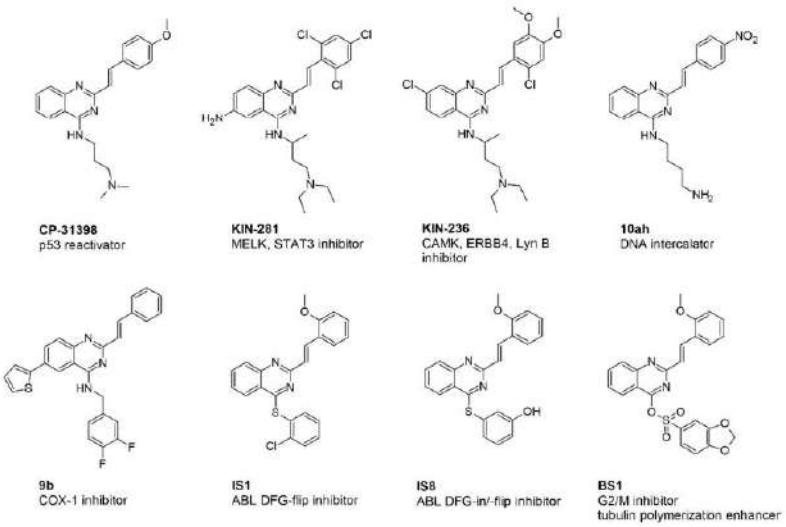

Fig. 1. Diversity of 2-styrylquinazoline-core compounds and their biological signature in cancer cells.

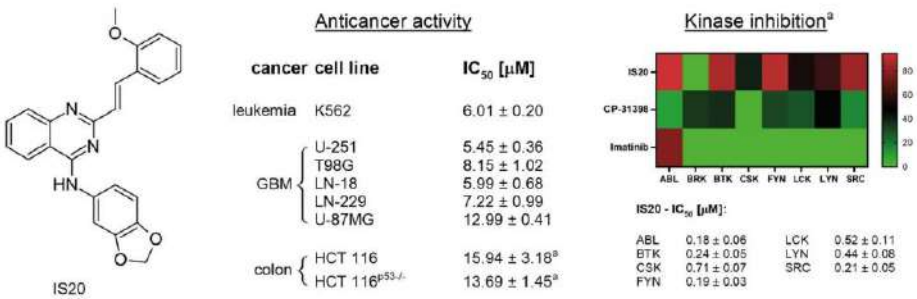

Fig. 2. The chemical structure of IS20 (6b) styrylquinazoline, along with its anticancer activity on a panel of cancer cell lines with different *TP53* gene status and kinase inhibition profiles. [a]Values for anticancer activity of IS20 against HCT 116 cells, as well as kinase inhibition activity by IS20, CP-31398, and imatinib, were taken from our previous work[13].

activity was different and focused on DNA intercalation and upregulation of p53 and p21 to cause G2/M cell cycle arrest, as well as regulation of pro- and anti-apoptotic molecules that led to caspase-dependent apoptosis[16]. Some structural modifications involving the attachment of a thiophene ring can be found in compound 9b, which was an effective and selective COX-1 inhibitor, with possible indications of activity in skin, breast, colorectal and ovarian cancers where COX-1 is overexpressed[17]. Recently, we designed and investigated a series of styrylquinazolines with a thioaryl moiety in the C4 position. Interestingly, we revealed two different binding modes for the IS1 and IS8 derivatives, indicating interaction with the DFG-flip and DFG-flip/DFG-in conformational states of ABL kinase[18]. In turn, the sulfonic styrylquinazoline (BS1) characterized by our team proved to be a potent antimitotic agent that enhanced tubulin polymerization much more than the currently utilized paclitaxel[19]. Notably, our earlier work described the anticancer activity of a series of styrylquinazolines based on a similar structural scaffold to CP-31398. Among them, we indicated molecule 6b (described in this work as IS20, structure in Fig. 2), with a benzodioxol group, could be a promising compound with more than 90% inhibitory potency against non-receptor tyrosine kinases, including ABL, and kinases of the SRC family[13]. It is also worth pointing out that its antiproliferative activity against several types of cancer, was significantly greater than CP-31398.

Despite the great interest in quinazoline derivatives, there are many gaps in fully understanding the action of these compounds on cell biochemistry and interactions with various molecular targets. In addition, the indicated examples show that despite the similar structural pattern, the molecular mechanism of action of the compounds at the cellular level is quite different. Considering this, we decided to explore this area of cellular biochemistry in-depth, focusing on the effect of IS20 derivatives on cellular metabolism, redox disruption, EGFR/mTOR signaling and cell cycle progression in glioblastoma and leukemia cells with altered p53 status. We also examined the mechanism of cell death through both autophagy and apoptosis. Notably, a comprehensive analysis of IS20 action, due to its superior ability to inhibit several tyrosine kinases, may reveal interesting interactions with other molecular targets. Indeed, this could be particularly important in outlining new therapeutic opportunities in designing compounds containing the styrylquinazoline scaffold.

The tumor suppressor protein p53 is a crucial molecule that regulates cell cycle progression, DNA repair, apoptosis, autophagy, and senescence. Under physiological conditions, p53 is typically maintained at low levels, but with increased cellular stress, its levels can upregulate, and it becomes activated, which modulates various cellular events[20,21]. The behavior of p53 may differ under low and high oxidative stress. For example, in response to low levels of oxidative stress, p53 may have an antioxidant function, unlike the occurrence of high oxidative stress, in which p53 exhibits pro-oxidative activities and suppresses antioxidant genes to enhance the level of oxidative status, leading to apoptosis[22]. The frequency of *TP53* gene mutations and p53 protein aberrations is very high in many types of tumors, at approximately 50% of cases. In glioblastoma (GBM), deregulation of p53 signaling occurs in up to 84% of patients. Together with the heterogeneity within the tumor, the multiplicity of genetic abnormalities among the most important signaling pathways (such as EGFR, PI3K, Ras, IDH-1), and the recurrence due to the presence of stem cells makes GBM the most aggressive brain tumor with poor prognosis, and thus difficult to treat[23,24].

One of the more important downstream targets of p53 is the ABL protein, encoded by the proto-oncogene of the same name, which is involved in cell proliferation, differentiation, and migration. Of note, the *BCR-ABL1* fusion transcript is a characteristic lesion of leukemia, but its active form has also been found in some cases of GBM[25,26]. Surprisingly, in recent years, more similarities have been found in leukemic cells among sets of mutations involving signaling pathways and gene expression abnormalities detected in GBM[27]. While p53 has been shown to directly regulate the activity of ABL in response to DNA damage, ABL also interacts with p53, enhancing its transcription and increasing the expression of p21, which can decide cell fate in two ways[28]. Thus, the interplay between p53 and ABL is particularly important for regulating processes leading to cell cycle arrest, suppression of tumor growth and in triggering apoptosis.

Results and discussion

Activity landscape of IS20 against cell lines with different *TP53* status

Understanding the molecular mechanism of action of the 2-styrylquinazoline derivative IS20 began by evaluating its antiproliferative profile on five GBM cell lines, including U-251, T98G, LN-18, LN-229, and U87-MG, and a leukemia cell line K562. It is worth noting that both leukemia and GBM cell lines, except U87-MG, were characterized by altered *TP53* expression levels and heterogeneity of p53 mutants. The GBM cells (U-251, T98G, LN-18 and LN-229) carry a point missense mutation resulting in a one amino acid substitution in the codon, which may cause the p53 protein to acquire a gain-of-function feature. Each of these GBM cell lines produces a different version of the final protein due to different amino acid exchange sites in the codons[29] (Table S1). Conversely, in K562 cells, the p53 protein is inactivated by the loss of one allele and an insertion mutation in exon 5 of the second allele, resulting in the production of a truncated protein of 148 amino acids in length[30]. The loss of wild-type p53 activity is often attributed to the development of chemoresistance. Moreover, altered expression and mutations of this protein result in the acquisition of oncogenic functions, which has a key impact on the regulation of proliferation, growth, survival, transduction and redox signaling in cancer cells[31].

In general, IS20 exhibited adequate antiproliferative activity levels against cells with p53 mutation. As shown in Fig. 2, the most susceptible cell line to the compound was U-251, for which the calculated IC_{50} value was 5.45 µM. Also, in the case of LN-18 and K562 cells, the biological activity of IS20 was equally high (IC_{50} was around 6 µM). For the remaining GBM cells with a mutation in p53, the IC_{50} value was 7.22 and 8.15 µM. Interestingly, the most resistant cell line was found to be U87-MG, in which the antiproliferative activity of IS20 was reduced more than 2-fold (IC_{50} 12.99 µM). We have juxtaposed our results with previous data from colon cancer cell lines: HCT 116 p53 wild-type and HCT 116 with $p53^{-/-}$[13] and found that IS20 was not effective, regardless of the cellular p53 protein status. Such a difference could be due not only to the expression of the *TP53* gene and p53 protein in these lines but also to interactions with other targets and metabolic reprogramming. In addition, the diverse expression landscape present in cells may significantly impact the activity of multi-targeted inhibitors[32]. In this regard, we decided to unravel the mechanism of action of IS20 on two different cell lines, K562 and U-251, with altered p53 status. We further wanted to examine the regulation of metabolism, cell cycle and redox signaling in p53 mutant cells in which the similarity between ABL and IDH-1 enzymes was discovered[32].

Destabilization of the cellular redox balance

Maintaining redox homeostasis is an essential process for normal growth, proliferation, survival and regulation of cell signaling pathways. However, if equilibrium is being disrupted, the elevated reactive oxygen species (ROS) drives cellular metabolism, promoting uncontrolled cell growth, tumor progression and metastasis. Hence, cancer cells adapt to increased levels of intrinsic ROS and exhibit an altered capacity of the ROS-scavenging system[33]. Therefore, an approach targeting the disruption of redox homeostasis may be an effective strategy for eradicating cancer cells[34]. Thus, ROS is perceived as a double-edged sword or Trojan horse[35]. It has been shown to facilitate cancer cells' vulnerability to damage and the effects of oxidative stress due to the excessive increase in ROS concentrations induced by anticancer drugs, and metal chelators[36–39]. It should be noted that excessive ROS

can completely deplete the capacity of antioxidant systems, leading to oxidative damage to lipids, proteins, and DNA, and ultimately triggering cell death through apoptosis[35]. In a therapeutic context, modulation of redox equilibrium and the associated cellular signaling is an effective and selective approach due to the significant differences in ROS levels between cancer and normal cells[34].

Changes in the level of ROS in leukemia and GBM cells were monitored using a fluorescence CellROX dye assay. Experiments were conducted over 3 to 24 h following treatment with IS20. Our analysis revealed a significant increase in ROS levels in both cell lines (Fig. 3A–navy blue bars), and in particular, a clear trend of growing ROS levels was observed in K562 cells. Elevated ROS levels were observed as early as 3 h following compound administration, after which they continued to increase at subsequent time points, reaching their highest level after 12 h (an increase of more than 135%). Smaller changes were observed in U-251 cells, with the highest level of ROS detected 24 h after exposure to IS20 (over 110%). The observed differences may be due to cellular vulnerability and the ability of the antioxidant system to eliminate ROS. As mentioned above, even small changes in the ROS levels and prolonging this condition can be sufficient to disrupt redox homeostasis, which leads to the induction of oxidative stress. It is noteworthy that the potential of IS20 to generate ROS after 24 h was drastically suppressed after incubation with the antioxidant ascorbic acid (Fig. S1A). Similarly, higher viability of K562 and U-251 cells was observed after incubation with IS20 in combination with ascorbic acid (Fig. S1B). In the literature, it has been shown that CP-31398 can also induce ROS production in cancer cells, which can trigger cell death by apoptosis[40,41]. However, how this p53 reactivator can directly increase ROS levels while also affecting the cellular antioxidant defense system has not been clarified. Moreover, the quinazoline core can exhibit a high affinity for metal ions, which are also present in coordination compounds with transition metals, such as copper[42,43].

With this in mind, we explored whether 2-styrylquinazoline derivative is capable of chelating ions and forming active redox complexes, as this could explain the disruption of redox homeostasis. Thus, we performed spectroscopic titration of the IS20 solution with iron (III) and copper (II) (Fig. S2). In general, adding both metal ions caused a decrease in absorption intensity at 345 nm. After titration with Fe^{3+}, two marked isosbestic points were located at 320 and 370 nm, while for Cu^{2+}, only one was observed at 320 nm. These isosbestic points indicate the existence of equilibrium in this region and the occurrence of at least two molecular forms of the compound (free and ion-bound). The isosbestic point located at shorter wavelengths is likely responsible for the electron transitions in the molecule from the ground state to the excited state in the presence of metal ions. In turn, an isosbestic point shifted toward longer wavelengths is associated with the charge transfer mechanism between the ligand and the metal ion[44]. Thus, two well-identified isosbestic points may confirm the presence of a stable complex between the IS20 ligand and the Fe^{3+} ion in the solution. In contrast, only one isosbestic point was observed when titrated with Cu^{2+} ions, which may suggest a weak affinity for these ions and a lower chelating ability by IS20.

Next, the response of the antioxidative defense system to the elevation of ROS levels in both cell lines was evaluated. For this purpose, we performed a series of GSH concentration measurements in a similar kinetic

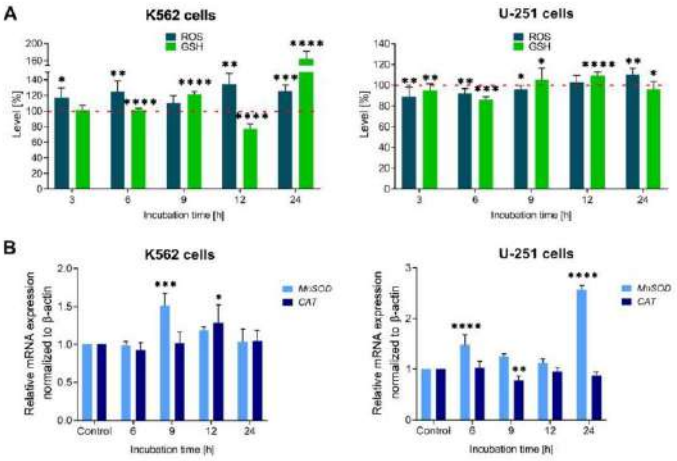

Fig. 3. The time-dependent impact of the tested IS20 derivative on ROS (navy blue bars) and GSH (green bars) levels in the K562 and U-251 cells (**A**). The mRNA expression of *MnSOD*, and *CAT* genes in the K562 and U-251 cells after incubation with IS20 in kinetic experiments (**B**). The data were normalized to the control–untreated cells and analyzed using the unpaired t-test: $^{*}p<0.05$, $^{**}p<0.01$, $^{***}p<0.001$, $^{****}p<0.0001$ compared to the control. The results are presented as the mean ± SD of several independent experiments ($n=5$). The red dashed lines indicate the standardized levels of ROS and GSH in the control, which is taken to be 100%.

manner. We detected many fluctuations in GSH concentration in K562 and U-251 cells (Fig. 3A-green bars), which may indicate that the cellular defense program was activated upon ROS production by IS20. The largest depletion of GSH levels (about 20%) was observed after a 12 h incubation in leukemia cells. It seems that a decrease in antioxidant potential may correlate with the highest ROS concentration. Surprisingly, the GSH levels increased over the following 12 h. Smaller fluctuations were noticed in U-251 cells, in which GSH levels finally decreased after a 24 h incubation with IS20. The reduction of GSH levels can trigger early apoptotic events such as mitochondrial damage followed by cytochrome c release, and a cascade of caspase activation[45]. However, it should be noted, that the GSH system, together with thioredoxin, is not a large detoxification system, but a second-line defense against ROS[46]. Therefore, insight into other antioxidant effectors involved in free-radical leveling is crucial. Antioxidant disruption and loss of potential to nullify ROS may encompass a multifaceted mechanism that involves the regulation of a set of different factors and signaling pathways. Such regulation may result from differential susceptibility to ROS-based therapy.

For this reason, our attention focused on the impact of IS20 on the regulation of superoxide dismutase (*MnSOD*) and catalase (*CAT*) gene expression as elements of the first line of cellular defense, which are responsible for scavenging radicals, such as superoxide (O_2^-) or hydrogen peroxide (H_2O_2). Gene expression analysis indicated fluctuations in *MnSOD* and *CAT* levels in both cell lines (Fig. 3B). We noticed a significant upregulation of *MnSOD* and *CAT* expression after 9 h and 12 h of treatment with IS20 in K562 cells, respectively. In GBM cells, *MnSOD* levels increased after 6 h and 24 h of treatment, in contrast to the expression of *CAT*, which decreased after 9 h of incubation with IS20. The sustained reduction in *CAT* expression appears to be a response to the prolonged oxidative state, that weakens and depletes resources for nullifying radicals. Moreover, the differences in *MnSOD* responses appear to correspond to a steady increase in ROS levels in both tested cell lines.

Modulation of oxidative stress-related and iron-regulated proteins

To comprehensively assess the induction of oxidative stress by IS20, we examined changes in heme oxygenase-1 (HO-1) at the gene and protein levels. This molecule has a pro- and antioxidant role in cells depending on the status of redox homeostasis and the fate of iron distribution[47]. HO-1 is responsible for heme degradation to biliverdin, releasing carbon monoxide and ferrous iron (Fe^{2+}). Biliverdin and its transformation product, bilirubin, can act as powerful antioxidants. However, increased HO-1 expression may lead to an enrichment of iron availability in the mitochondrial pool[48,49], thereby increasing iron accumulation and inducing cell damage[50]. We found an almost 1.5-fold increase in *HO-1* gene expression was registered in K562 cells after a 9 h incubation with IS20 (Fig. 4A). Conversely, remarkable changes were found in U-251, where *HO-1* gene expression increased at least more than 5-fold during the entire incubation (Fig. 4B). Of note, a strong, more than 25-fold, increase in *HO-1* levels was recorded in a 9 h incubation with IS20. At the protein level, we also confirmed significant upregulation of HO-1 expression in U-251 cells (Fig. 4C). It should be noted that another protein associated with the destabilization of redox balance, and an increase of oxygen levels in the cellular environment is HIF-1α. Therefore, it is not surprising that IS20 caused a 5-fold increase in HIF-1α protein levels in the GBM cells. Unfortunately, both mentioned proteins were undetectable in leukemia cells using the Western Blot technique.

Another crucial molecule in the cellular stress response is the iron-regulated metastasis suppressor N-myc downstream-regulated gene 1 (Ndrg1). This molecule negatively regulates cancer cell growth, differentiation, invasion and migration[51]. It is also a powerful target for anticancer therapy due to its role in many significant cellular processes, and its reduced expression is found in several types of cancer, such as brain, breast, and pancreatic[51,52]. For example, Sun et al. revealed that decreased *Ndrg1* gene expression in gliomas could contribute to carcinogenesis, cancer progression and survival[53]. Most importantly, several studies by Richardson's group have shown that Ndrg1 expression can be regulated by factors that induce hypoxia, DNA damage and changes in intracellular iron[54]. Indeed, the iron chelators from the thiosemicarbazone group (i.e., Dp44mT), as well as deferoxamine (DFO), can induce strong upregulation of Ndrg1 expression at the gene and protein levels by decreasing iron levels in cells[55,56]. Moreover, Ndrg1 expression can be augmented by HIF-1α–dependent and –independent mechanisms[56]. The qRT-PCR analysis showed that *Ndrg1* gene expression was strongly increased following treatment with IS20 in both cell lines (Fig. 4 A, B), with a more than 3.7-fold upregulation of *Ndrg1* in the U-251 cell line. Notably, the effect was slightly stronger in K562 cells. Moreover, this regulatory mechanism appears to depend on HIF-1α, which was elevated in GBM cells. Interestingly, both molecules may also promote endoplasmic reticulum stress (ER stress), which can exist and crosstalk with oxidative stress[57,58]. Elevated ROS levels can deregulate redox homeostasis at several sites in cells, such as the mitochondria, cytosol and ER. The ER is responsible for protein synthesis, folding, post-translational modifications, as well as maintaining calcium homeostasis. However, it is sensitive to any changes in the cellular environment. Thus, if the antioxidant defense is ineffective, several cellular events occur that have multilevel effects on the regulation of signaling pathways, including Ca^{2+} influx, energy demand, hypoxia, ER stress, or autophagy[57]. These findings prompted us to investigate the impact of IS20 on the *calreticulin* expression, a gatekeeper of the Ca^{2+} pool in the ER. Indeed, we detected a greater than 2.5-fold increase in the expression of this gene in GBM cells (Fig. 4B). This is consistent with previous data, in which Waser et al. suggested that depletion of intracellular Ca^{2+} stores in the ER induces *calreticulin* gene activation in both *in vitro* and *in vivo* models[59]. Moreover, recent reports have shown that overexpression of calreticulin can enhance autophagosome formation and autophagy-related cell death under ER stress[60]. The mechanism of this activation focused on interactions with LC3 protein through the LC3-interacting region (LIR) motif conserved in the calreticulin protein[60]. Metal chelator studies demonstrated enhanced Ndrg1, calreticulin and LC3-II expression[58]. Yet, surprisingly, detailed analysis showed that endogenous overexpression of Ndrg1 in cells may act as a suppressor of autophagy and an enhancer of apoptosis[61]. Interestingly, no significant changes in *calreticulin* expression were observed in leukemia cells. These

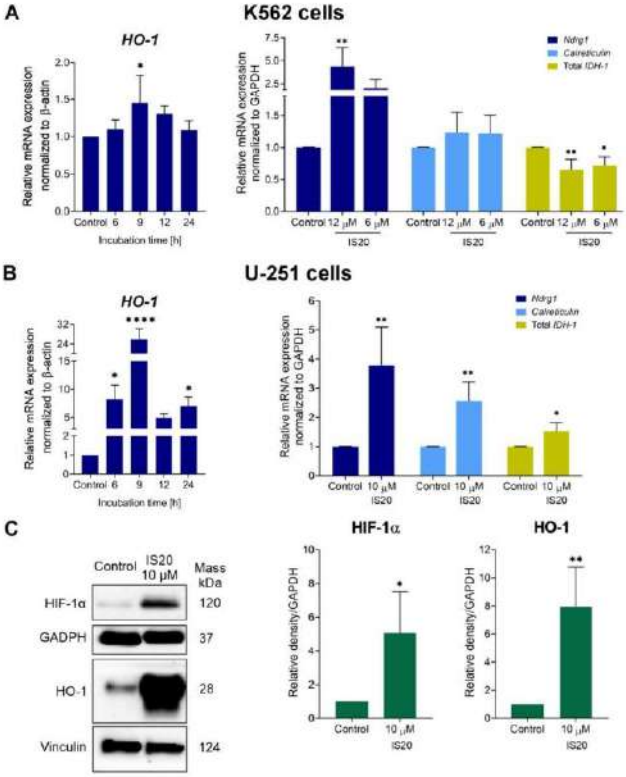

Fig. 4. The impact of IS20 on the expression of selected genes and proteins associated with oxidative stress and iron regulation in the K562 (**A**) and U-251 cells (**B**,**C**). The *HO-1* expression was determined in kinetic experiments, while *Ndrg1*, *calreticulin*, and *IDH-1* gene expression after 24-hour incubation. The levels of HO-1 and HIF-1α proteins were determined after 24-h treatment with IS20 in U-251 cells. The results of gene and protein expression are presented as the mean ± SD of several independent experiments ($n = 5$). Immunoblots shown are representative of five independent experiments. The displayed blots were cropped, and the full-length blots are shown in Fig. S6. The statistical analysis was performed using a t-test or one-way ANOVA with Bonferroni's posthoc test: $^{*}p < 0.05$, $^{**}p < 0.01$, $^{***}p < 0.001$, $^{****}p < 0.0001$ compared to the untreated controls.

data reinforce our belief that the two types of p53-mutated cancers have different susceptibility to IS20-induced oxidative stress. The indicated changes are also of interest due to the impact of styrylquinazoline on induced cell death through pathways related to both autophagy and apoptosis.

Furthermore, we evaluated the impact of IS20 on cellular metabolism under stress conditions by determining *IDH-1* expression in both tested cell lines. The IDH-1 protein is involved in the tricarboxylic acid (TCA) cycle, one of the most essential cellular reactions. During the TCA cycle, reduced nicotinamide adenine dinucleotide phosphate (NADPH) co-enzyme is produced, which is essential for cellular processes that maintain redox balance and facilitate the production of lipids and nucleotides[62]. Notably, a reduction in NADPH availability has implications for the induction of oxidative stress due to the depletion of the GSH pool and the thioredoxin system[63]. Shi et al. have indicated that the overexpression of IDH-1-R132H in glioma cells caused a decrease in NADPH levels, resulting in an increase in ROS levels and a decrease in GSH levels[64]. Our analysis indicated that IS20 applied at a dose of 10 μM caused a significant, almost 1.5-fold increase in the *IDH-1* levels in U-251 cells (Fig. 4B). Notably, gene analysis showed the total mRNA expression, while IDH1 protein is often mutated in GBM cells at the arginine site at position 132. Importantly, the opposite effect was registered in leukemia cells, where an almost 1.5-fold downregulation was detected (Fig. 4A). Considering the literature, this change is favourable and may lead to an increase in total ROS levels and oxidative stress. Interestingly, the different behaviour of IS20 in these cellular environments may be related to stimulating alternative pathways due to different basal levels of *IDH-1* in both tested cell lines, as well as existing mutant forms of IDH1 protein[32].

Inhibition of EGFR/mTOR signaling pathway

As mentioned above, we showed that the IS20 compound can inhibit several non-receptor tyrosine kinases, such as ABL and SRC. We then checked the possibility of blocking receptor tyrosine kinases from the ErbB and insulin-related families. As depicted in Table S2, the styrylquinazoline at 1 µM concentration demonstrated moderate potential to inhibit the activity of EGFR and HER2 receptor kinase (approximately 25 to 30% inhibition of activity). We registered slightly higher values for insulin-like growth factor 1 receptor (IGF1R), whose activity was blocked by 40% following IS20 administration. Nevertheless, we also examined the possibility of inhibiting the EGFR signaling pathway with its downstream targets at the cellular level. Our assumptions about the impact of the tested compound on this signaling pathway were based on the knowledge that Ndrg1 can interact with and suppress many oncogenic signaling pathways by downregulating EGFR expression[65]. An important example of this may be the inhibition of SRC kinase activation through upregulation of Ndrg1 and interaction with EGFR, which may translate into downregulation of signaling pathways like $p130^{Cas}$ substrate and Abl[66]. For this purpose, we determined the expression of EGFR, phosho-EGFR at Tyr1068, phospho-Akt at Ser473, phospho-ERK1/2 (p44/42) at Thr202 and Tyr204, mTOR and p-mTOR at Ser2448 after exposure to IS20 using the Western Blot method. We found that IS20 caused a significant reduction in the EGFR activation in GBM cells (Fig. 5). In addition, some fluctuations in the phosphorylation of EGFR protein in both cell lines were observed. It appears that IS20 caused a slight decrease in the expression of EGFR phosphorylated at Tyr1068. However, to clarify, we performed additional experiments to determine the p-EGFR levels using the Lumit Immunoassay, which gives more linear read-outs for the level of protein phosphorylation, making it more suitable to discover more minute changes (Fig. S3)[67]. The data from this assay showed that IS20 caused a significant, greater than

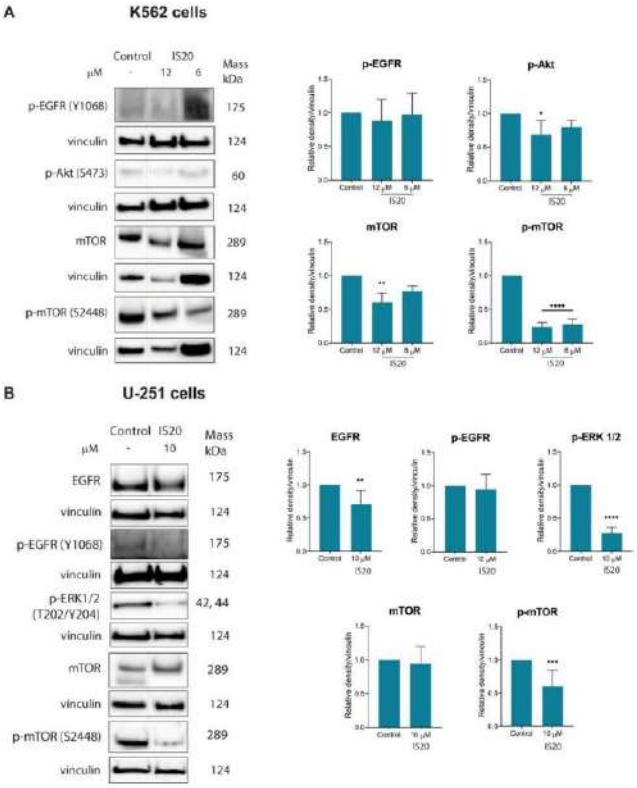

Fig. 5. The impact of IS20 on the expression of EGFR and its downstream signaling proteins in K562 (**A**) and U-251 (**B**) cells. The results of protein expression are presented as the mean ± SD of six independent experiments ($n = 6$). Immunoblots shown are representatives from these independent experiments. The displayed blots were cropped, and the full-length blots are shown in Fig. S6. Statistical significance is presented above as $^{*}p < 0.05$, $^{**}p < 0.01$, $^{***}p < 0.001$, $^{****}p < 0.0001$ relative to the respective control, statistical analysis was done using one-way ANOVA with Bonferroni's posthoc test (for Western Blot) or Dunn–Šidák correction test (for Lumit Immunoassay).

1.5-fold decrease in p-EGFR levels in both K562 and U-251 cells. These findings suggest that IS20 may interfere with EGFR activation and phosphorylation, which may affect the transduction of the signaling cascade in cells. Moreover, further analysis of Western Blot results confirmed EGFR pathway inhibition through reducing levels of downstream targets, such as p-Akt and p-ERK1/2. Moreover, IS20 at 12 µM caused a significant, almost 1.5-fold decrease in the expression of Akt phosphorylated at Ser473 in leukemia cells. It should be noted that this protein is a crucial effector of cell proliferation, metabolism, survival and migration. In addition, literature revealed that overexpression of Ndrg1 can regulate PI3K/Akt signaling and GSK3ß protein in GBM cells, resulting in inhibition of cell proliferation and invasion[68,69]. Similarly, the ERK1/2 protein, which belongs to the MAPK protein family, regulates cancer growth and proliferation. By upregulating Ndrg1, iron chelators may deactivate the MEK/ERK signaling cascade, that is stimulated by EGFR[65]. Hence, we detected a significant, greater than 3.6-fold downregulation of p-ERK1/2 after exposure to IS20 in GBM cells. Unfortunately, the level of this protein in leukemia cells was undetectable.

Finally, we evaluated the expression of mTOR signaling after incubation with IS20. The mTOR protein regulates metabolism, activates cell survival, and suppresses autophagy. Thus, insights into the altered expression of this protein may be important given the stimulation of ER stress by IS20 through the calreticulin activation, which affects autophagosome formation. Generally, expression of mTOR phosphorylated at Ser2448 was inhibited after exposure to IS20 in both cell lines. The increased effect was observed in K562 cells, in which IS20 caused a significant 3.5-fold decrease in the expression, while we detected an almost 1.5-fold reduction in the expression of p-mTOR levels in GBM cells. These results were also confirmed by Lumit immunoassay, as depicted in Fig. S3. In summary, these data suggest that IS20 can induce autophagy as a result of oxidative and ER stress occurring in the cells. To confirm this hypothesis, we further verified the induction of autophagy using flow cytometry and determined the expression of two autophagy-related genes (*LC3* and *p62*).

Cell cycle arrest and regulation of cell cycle-related proteins

To more deeply evaluate IS20, we determined its effect on the cell cycle progression and the change in expression of cell cycle-related genes and proteins. The earlier described changes regarding redox disturbance and iron homeostasis can result in cell cycle inhibition and apoptosis induction. Therefore, we performed a series of flow cytometry, qRT-PCR, and Western Blot experiments on K562 and U-251 cells (Fig. 6). Analysis of the flow cytometry data showed that IS20 causes a significant increase in the cell population in the G2/M phase in both cell lines. Simultaneously, the cell number in the G0/G1 and S phases is reduced. Detailed histograms and a table with the percentage of cells in each phase of the cell cycle are shown in Fig. S4. These findings indicate cell cycle arrest in the G2/M phase by IS20. Despite the similar inhibition of the cell cycle induced by IS20 on both cancer cells, interesting changes were noticed at the molecular level, including a significant 1.8-fold decrease in the expression of *GADD45* after exposure to IS20 at 12 µM in K562 cells (Fig. 6A). The opposite effect was registered in GBM cells, in which a more than 4.5-fold rise in *GADD45* mRNA levels was observed (Fig. 6B). Interestingly, the similar trend was observed in our earlier studies on sulfonic styrylquinazolines[19]. *GADD45* plays a crucial role in G2/M checkpoints, and its stimulation is often associated with DNA damage and stress signal responses, causing cell cycle arrest and the induction of apoptosis. Notably, this gene can be regulated by both p53-dependent and p53-independent pathways. In addition, upregulation of *GADD45* can recruit and activate p38 and JNK kinases, which can mediate the oxidative stress response depending on the potency of the effector/ligand[70]. In the context of cell death induction, *GADD45* may also act together with *CDKN1A* encodes $p21^{CIP1/WAF1}$ protein, and our analysis indicated that IS20 caused significant activation of $p21^{CIP1/WAF1}$ in both cell lines. A greater effect was observed in GBM cells, where we noted an almost 14-fold increase in the level of this protein. These data are consistent with our previous reports on iron chelators, in which the activation of the protein was associated with early hallmarks of apoptosis[36,39]. Moreover, it was observed that p21 was an important stimulator of different cellular responses concerning the destabilization of redox homeostasis, which correlated with different cellular susceptibility to changes in ROS concentrations[39]. It is worth mentioning that Ndrg1 can also upregulate p21 through transcriptional and post-transcriptional mechanisms[71]. In the case of styrylquinazolines, Zhong et al. found that CP-31398 arrested the cell cycle in the G2/M phase, which can be assigned to the enhancement of the p21 protein[41]. Similarly, KIN-281 increased p21 expression in a p53-dependent manner, contributing to cell growth inhibition[14].

Other proteins examined were cyclin E1 and cdc2, which are responsible for the transition from G0/G1 to S phase and from G2 to mitosis of the cell cycle, respectively. Interestingly, we observed a different pattern of IS20 action on tested cancer cell lines. The cyclin E1 and cdc2 were slightly downregulated after exposure to IS20 at 12 µM in the K562 cells (Fig. 6A), while in U-251 cells, the opposite effect was observed where IS20 induced a more than 1.5-fold increase in these proteins (Fig. 6B). An explanation for the different activation of these cell cycle proteins may be the involvement of p53 in the network of interactions and responses to the breakdown of cellular homeostasis and the induction of multilineage oxidative stress. Indeed, the leukemia cells studied were devoid of p53 protein, while the GBM cells harbored a mutated form of it.

Dual cell death activation by autophagy and apoptosis

To summarize and verify previously obtained results, we conducted experiments to determine the type of cell death induced by IS20. For this purpose, we conducted an experiment using flow cytometry, measuring the fluorescence of an anti-LC3 mouse monoclonal antibody conjugated to Alexa Fluor 555 (Fig. 7 and Fig. S5). This assay allows quantitative measurement of autophagy level. These results indicate a significant increase in autophagy induction ratios in both tested cell lines following incubation with IS20. The largest increase of more than 4 times was recorded for the U-251 cell line after just 24 h of incubation (Fig. 7B). A 2.5-fold increase was registered for the K562 cell line, however, this occurred after a longer 48-hour incubation time (Fig. 7A). Notably, these levels are higher than those of the reference Imatinib. In addition, experiments were performed

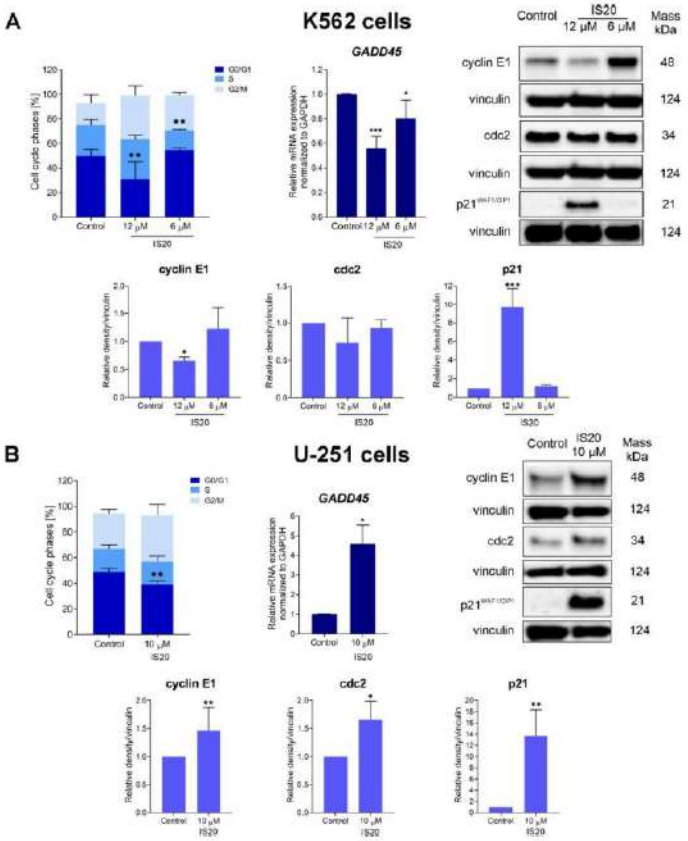

Fig. 6. The impact of IS20 on the progression of the cell cycle and related molecules in the K562 (**A**) and U-251 (**B**) cells. The chart presents the percentage of cells in the G0/G1, S and the G2/M phases of the cell cycle. The mRNA expression of *GADD45* in the cells and immunoblotting results with densitometric analysis of cyclin E1, cdc2 and p21 $^{CIP1/WAF1}$ protein expression after 24-hour treatment with IS20. Results were normalized to the reference gene/protein and are from five independent experiments ($n = 5$). Immunoblots shown are representative from these independent experiments. The displayed blots were cropped, and the full-length blots are shown in Fig. S6. All presented data were analyzed using a one-way ANOVA with Bonferroni's post-hoc test: $^{*}p < 0.05$, $^{**}p < 0.01$, $^{***}p < 0.001$, $^{****}p < 0.0001$ compared to the control.

using qRT-PCR to determine the levels of *LC3* and *p62* genes, which are considered markers of autophagy[72,73]. For *LC3*, the increase in mRNA levels was greatest for the U-251 cell line (more than 2.5-fold), while for the leukemia cells, it increased 1.5-fold. Significant increases in the *p62* gene were registered for both cell lines, with the largest (6-fold) for glioblastoma and about 3-fold for the leukemia cells. The elevated level of both genes indicates the presence of autophagy. These results are consistent with those obtained previously and demonstrate that iron binding by chelators increases the expression of Ndrg1, which in turn affects the activation of HIF-1α[54]. Another example is the interrelation of autophagy with an increase in calreticulin[60], the occurrence of oxidative stress[74] and inhibition of the mTOR pathway[75].

The termination of cell proliferation is often associated with the triggering of several cell death pathways, therefore, experiments measuring the fluorescence of apoptotic cells were performed. These results are consistent for both cell lines and show a clear increase in both early and late apoptosis at approximately 60% after incubation with IS20 (Fig. 8). These results indicate a strong activation of apoptotic processes by IS20.

The next step was to analyze apoptotic-related proteins (Fig. 9). One of the indicators of the apoptosis process is the presence of cleaved PARP and caspase-9 proteins. Densitometric analysis indicated a 10-fold increase in the concentration of the PARP cleavage fragment with a molecular weight of 89 kDa following administration with 12 μM of IS20 incubated with the K562 cell line. The U-251 cell line showed a more than 3-fold increase

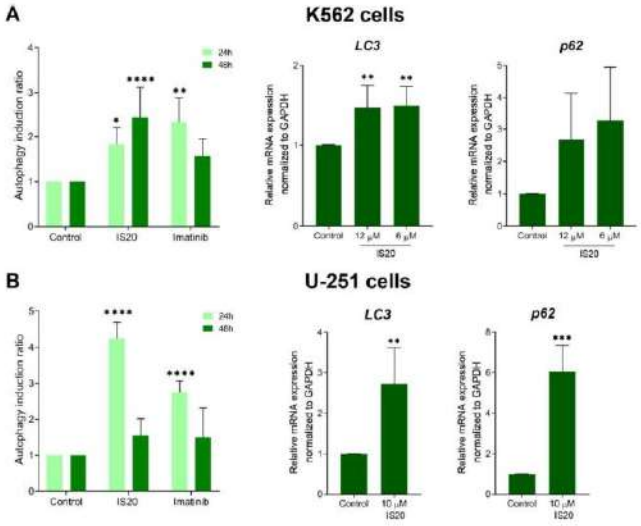

Fig. 7. The influence of IS20 on the autophagy induction and expression of autophagy-related genes in the K562 (**A**) and U-251 (**B**) cells. The expression of *LC3* and *p62* genes was determined in both cell lines after a 24 h incubation with IS20. The results are presented as the mean ± SD from five independent experiments ($n = 5$). The statistical analyses were carried out using a one-way ANOVA with Bonferroni's post-hoc test: $^{*}p < 0.05$, $^{**}p < 0.01$, $^{***}p < 0.001$, $^{****}p < 0.0001$ compared to the untreated cells (control).

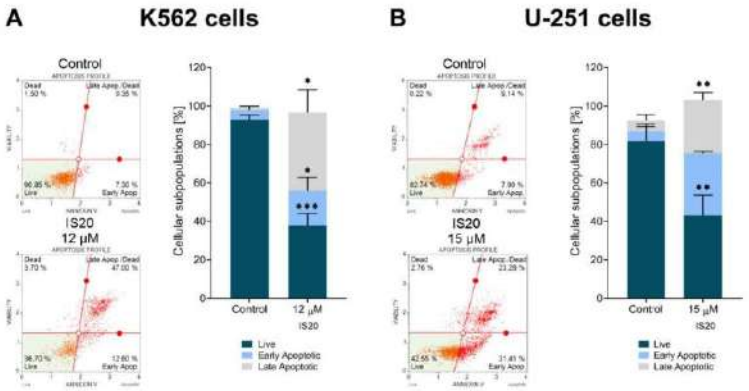

Fig. 8. The impact of IS20 on the induction of apoptosis in the K562 (**A**) and U-251 (**B**) cells. The histograms display the percentage of live, early, and late independent experiments. The statistical analysis of the data was performed using a one-way ANOVA with Bonferroni's post-hoc test: $^{*}p < 0.05$, $^{**}p < 0.01$, $^{***}p < 0.001$, $^{****}p < 0.0001$ compared to the untreated cells (control).

in the concentration of this cleavage product. Moreover, IS20 also influenced the activation of the cell death pathway through caspase-9 cleavage. In both cell lines, an approximately 2-fold increase in the 37 – 35 kDa molecular weight caspase-9 cleavage product was observed compared to control cells. Apoptosis-inducing factor (AIF) protein is involved in triggering a caspase-independent apoptotic pathway[76]. Therefore, we decided to test if the mechanism of IS20 action also occurs through a pathway independent of caspase involvement. Western Blot results indicate that this protein was activated more than 3-fold in the leukemia line for an IS20 concentration of 6 μM. This indicated a multifaceted action of the tested derivative. Interestingly, the AIF protein was undetected in the glioblastoma line. While for the K562 cell line, p53 was undetected due to the loss of one

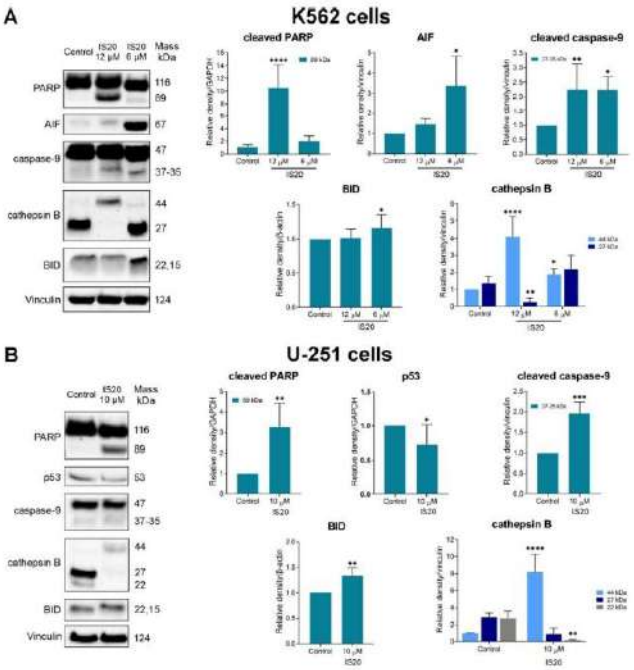

Fig. 9. The impact of IS20 on the induction of expression of apoptosis-related proteins in the K562 (**A**) and U-251 (**B**) cells. Results were normalized to the reference protein and are from five independent experiments ($n = 5$). Immunoblots shown are representative from these independent experiments. The displayed blots were cropped, and the full-length blots are shown in Fig. S6. The statistical analysis of the data was performed using a one-way ANOVA with Bonferroni's post-hoc test: $^{*}p < 0.05$, $^{**}p < 0.01$, $^{***}p < 0.001$, $^{****}p < 0.0001$ compared to the untreated cells (control).

allele and insert mutation in the second allele[30,77], the U-251 cell line gave an unusual response. Many papers on 2-styrylquinazolines, including CP-31398, showed overexpression of p53 protein[11], while our study shows a decrease in activity. This is noteworthy because of the elevated p21 level in both lines and indicates an important role for the p53 protein in the cell's response to treatment. Cathepsin B is a lysosomal cysteine peptidase involved in programmed cell death. This protein is initially synthesized as an inactive proenzyme form (44 kDa), and modified into an active two-chain form (27 and 24 kDa)[78]. The intrinsic apoptotic pathway activated by increased ROS levels initiates leakage of cathepsin B from the lysosome, resulting in BID activation[79]. A marked (8-fold for U-251 and 4-fold for K562) increase of procathepsin B (44 kDa) was observed for both cell lines incubated with IS20. Additionally, the heavy chain form of cathepsin B demonstrated a marked decrease. BID belongs to a pro-apoptotic member of the Bcl-2 protein family, and its expression is upregulated by the tumor suppressor p53[80]. Upregulation of BID was observed in both leukemia and glioblastoma cell lines, which confirms the pro-apoptotic mechanism of IS20.

ADME properties

In the early stage of the drug discovery process, especially orally administered drugs, it is important to perform at least indicative absorption, distribution, metabolism, and excretion (ADME) profiling to provide critical information about the basic physiologic behavior of a potential drug. ADME screening is generally performed using software-based approaches, and ADME profiling is subsequently verified for selected drug candidates in preclinical and clinical studies[81,82].

The Lipinski Rule of Five (Ro5) is one of the most accepted recommendations concerning the physicochemical parameters of biologically active compounds, and all medicinal chemists try to follow it when designing molecules[83]. Ro5 contains the limits of specific molecular descriptors (MW < 500, logP < 5, HBD < 5, HBA < 10) set based on experimentally and statistically obtained results so that a compound that meets this recommendation has a higher chance of becoming a drug. However, a good drug-like score does not make a molecule a drug, and vice versa[84,85]. It is clear that ADME-friendly properties, such as lipophilicity, polar surface area, etc., are important in the context of specific ligand-receptor interactions.

The following table (Table 1) shows the predicted ADME-influencing properties of IS20 compared to those of the model tyrosine kinase inhibitors (TKIs) presented in the paper, i.e., gefitinib, erlotinib, lapatinib, afatinib, KIN-281, KIN-236 and CP-31398 with an *N*-phenylquinazolin-4-amine scaffold. Also, imatinib was chosen as the comparator drug due to its ability to inhibit ABL, although the *N*-[4-(pyridin-3-yl)pyrimidin-2-yl]benzene-1,3-diamine fragment is in its molecule. TKIs are known to have limited bioavailability, tend to be extensively metabolized, and are substrates of P-glycoprotein[86], therefore, in addition to Ro5 parameters, intestinal absorption and permeation into the brain were also characterized.

IS20 has a molecular weight (MW) close to erlotinib (MW approx. 400). Lipinski's recommendation of MW < 500 is not met by lapatinib and KIN-236. Limit values also have imatinib, KIN-281 and afatinib. The compounds KIN-281, KIN-236, and lapatinib do not meet the recommendation of Ro5 for lipophilicity (logP < 5). IS20 has a logP value of ca. 4.6, so it is the fourth most lipophilic molecule from Table 1. All the compounds meet the criteria for the number of H-bond donors (HBD) and acceptors (HBA), and in this regard, IS20 is close to KIN-236, gefitinib and erlotinib. The number of rotatable bonds (RB) of IS20 is close to imatinib, while the topological polar surface area (TPSA) of IS20 is close to KIN-281 and gefitinib, and parachor is close to its parent CP-31398. TPSA has been recognized as a good indicator of intestinal drug absorption, with the acceptable limit for good absorption being a TPSA value < 120 Å^2[87]. In addition, for orally administered compounds, which are intended to cross the blood-brain barrier (BBB), the TPSA value should be lower than 70 Å^2[88]. The TPSA value of IS20 is 65.50 Å^2, which suggests that the compound should have good intestinal absorption. The predicted value of the rate of absorption in the jejunum (k_a = 0.051 min^{-1}) of IS20 is closest to erlotinib and is the highest of all the evaluated compounds.

A remarkable prediction was made by ACD/Percepta for BBB permeation. In general, logBB ≥ 0.3 is for BBB permeable drugs and logBB ≤ -0.3 is for impermeable drugs[89], the value of logBB = -0.33 for IS20 is borderline and lies between the predicted values for imatinib (logBB = -0.16) and lapatinib (logBB = -0.50). More informative are the values of the permeability surface-area product (expressed as logPS)[90], which for IS20 is logPS = -1.1 and thus close to lapatinib and gefitinib (logPS = -1.4). For all three drugs (imatinib, lapatinib, and gefitinib), the probability of penetration through the BBB into the brain ranges from 0.62 to 0.97 (values are taken from the DrugBank database). IS20 has some parameters similar to erlotinib, whose BBB permeation probability is 0.93 (value from DrugBank), and the brain plasma equilibrium rate predicted by ACD/Percepta for IS20 is -3.1 and is equal to the rate predicted for imatinib. However, the ABL inhibitor is a strong substrate for efflux via P-glycoprotein and has limited effect on the brain. Conversely, the value for IS20 is quite close to afatinib (-3.3), which can penetrate the BBB in preclinical models and is sufficient for action in the central nervous system (CNS). Therefore, IS20 may also be predicted to be able to reach therapeutic levels in the CNS. However, more detailed studies on relevant cellular models[91] are needed.

In vivo studies

To elucidate the toxicological reactions of organisms to IS20, the *Danio rerio* experimental model was employed as a reliable and rapid *in vivo* tool for toxicity assessment. Zebrafish possess several advantageous characteristics, including economical housing requirements, diminutive size reducing space and test agent consumption, and a high fecundity rate, with individual females capable of generating approximately 300 eggs, thereby supporting their efficiency as a model organism. Moreover, zebrafish and humans share an approximate 70% genomic similarity. Notably, there exists considerable conservation of critical developmental and physiological processes, such as those governing the digestive, nervous, and cardiovascular systems, when compared to humans. This conservation largely underpins the robust parallels in response to pharmacological agents between the two species, with numerous zebrafish models accurately recapitulating human diseases both genetically and phenotypically[92]. Indeed, zebrafish have attained widespread recognition as a primary model organism within the domain of high-throughput screening for biological investigations, akin to conventional models such as mice and rats[93].

Comp.	MW	logP	HBD	HBA	RB	TPSA [Å^2]	Parachor [cm^3]	k_a [min^{-1}]	logBB	logPS	Brain plasma equilibrim rate
Imatinib	493.60	3.10	2	8	7	86.28	1110.03	0.043	-0.16	-2.0	-3.1
Gefitinib	446.90	3.70	1	7	8	68.74	921.04	0.049	0.12	-1.4	-2.9
Erlotinib	393.44	3.05	1	7	11	74.73	877.68	0.050	-0.84	-1.5	-2.6
Lapatinib	581.06	5.22	2	8	11	114.73	1159.20	0.046	-0.50	-1.4	-3.5
Afatinib	485.94	3.44	2	8	8	88.61	980.17	0.044	-0.46	-2.0	-3.3
KIN-281	492.87	6.01	3	5	9	67.07	1027.98	0.047	0.31	-2.3	-4.4
KIN-236	503.46	5.99	1	6	11	59.51	1079.62	0.047	0.41	-2.0	-4.2
CP-31398	362.47	3.72	1	5	8	50.28	834.47	0.048	0.00	-1.7	-3.2
IS20	397.43	4.59	1	6	5	65.50	839.46	0.051	-0.33	-1.1	-3.1

Table 1. Values of parameters characterizing physicochemical properties of discussed TKIs predicted using ACD/Percepta ver. 2012. Molecular weight (MW), lipophilicity (log P), number of H-bond donors (HBD), number of H-bond acceptors (HBA), number of rotatable bonds (RB), topological polar surface area (TPSA), absorption rate in human jejunum at pH 6.5 (k_a), permeability across BBB (logBB - concentration of drug in brain divided by concentration in blood), rate of brain penetration (logPS - permeability surface-area product).

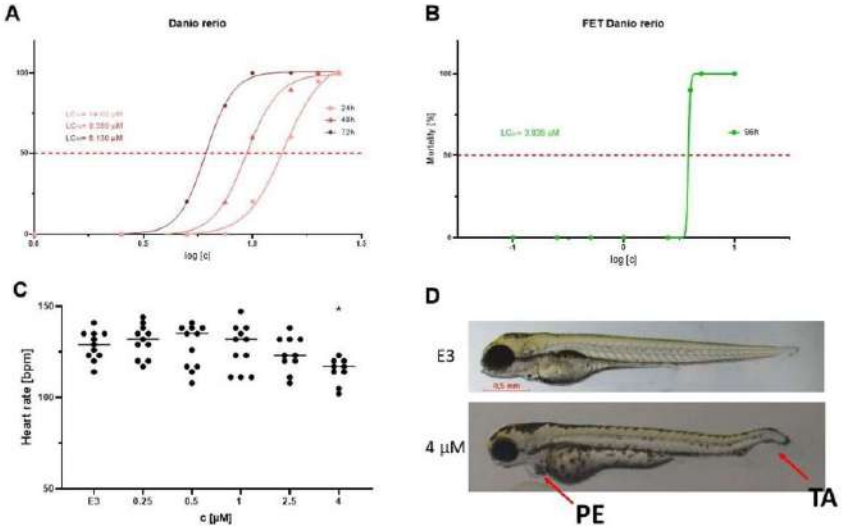

Fig. 10. The toxicity of IS20 in *Danio rerio* experimental model. **(A)** Toxicity (expressed as LC_{50}) after 24, 48 and 72 h of incubation with IS20; **(B)** Toxicity (expressed as LC_{50}) of IS20 in FET after 96 h of incubation; **(C)** Cardiotoxicity, measured as heart rate [beats per minute], the statistical analysis of the data was performed using a one-way ANOVA with Tukey's post-hoc test: $^{*}p < 0.05$ compared to the untreated control (E3) fish; **(D)** Example of malformations stated for the incubation with IS20 versus untreated control (E3) fish; *PE* pericardial edema, *TA* tail autophagy.

The toxicological evaluation of IS20 was performed according to the OECD 236 test. The freshly fertilized zebrafish eggs were exposed to different concentrations of IS20. Every 24 h, the embryos were observed for visual indicators of lethality like the coagulation of fertilized eggs, lack of somite formation, lack of detachment of the tailbud from the yolk sac and lack of heartbeat. The obtained outcomes showed that the toxicity of IS20 increased with time of incubation from 14.02 µM (24 h: Fig. 10A) to 3.85 µM (96 h: Fig. 10B).

Zebrafish present an attractive platform for cardiovascular risk assessment post-treatment due to the straightforward nature of heart rate measurement. Notably, zebrafish exhibit remarkable resilience, as they can persist without cardiac output and despite major vascular anomalies for extended periods, a feat not commonly observed in larger animal models. These attributes have collectively propelled *Danio rerio* into the spotlight for evaluating cardiotoxicity and cardiovascular developmental effects following drug administration[94].

As an indicator of normal heart functions, heartbeats were measured after incubation of 96 h. Interestingly, a small decrease in heart rate was observed only at the highest dose (Fig. 10C). Additionally, at that dose of IS20, we observed developmental malformations, which are a consequence of some heart dysfunctions (Fig. 10D). Pericardial edema (PE) is commonly observed in zebrafish embryo-based chemical toxicity screens, with the underlying mechanism potentially related to disruption of embryonic osmoregulation. Tail autophagy (TA) is closely related to the disruption of circulation related to deregulation of heart functions.

Conclusions

Unlike our previous investigations in which we presented large libraries of compounds searching for a privileged structure, in this paper, we present IS20, which is attractive in terms of its multi-target mechanism of action. The selected cell model included cell lines with different p53 status, which allowed us to analyze the effect of this protein on different molecular targets. This work aimed to conduct a detailed analysis of the mechanism of action of the antiproliferative activity of the IS20 derivative based on previous results showing interesting inhibitory potential for tyrosine kinases, particularly ABL and SRC. Notably, this is the first report to indicate that a 2-styrylquinazoline compound can bind to iron and exhibit chelating properties, thereby affecting the generation of ROS. Disruption of cellular homeostasis by IS20 triggered several factors, including antioxidants such as GSH, *MnSOD* and *CAT*, associated with cellular defense against the induction of oxidative stress. This, in turn, affected the activation of HO-1 and HIF-1α proteins. Interestingly, the *Ndrg1* gene was overexpressed and inhibited the EGFR/mTOR signaling pathway. The final effect of IS20 was the activation of coexisting cell death pathways apoptosis and autophagy, which was confirmed by the activation of the cascade of proteins responsible for these processes. Based on the prediction from the primary ADME screening using the commercially available ACD/Percepta software, it could be assumed that the investigated compound may have suitable physicochemical parameters for sufficient bioavailability. The *in vivo* studies on the *Danio rerio* model evaluated the toxicological

responses of IS20 on living organisms. The lethal doses were decreased with incubation time, receiving an LC_{50} value of approximately 3.85 µM at the end of the exposure period, i.e., at 96 hpf. The compound was not found to be cardiotoxic up to the LD_{50} dose. Moreover, no lethal malformations were observed, only those connected with lower heart rates at the highest survived dose (4 µM), namely PE and TA. Further chemical modifications should be considered to fully avoid or at least diminish the cardiotoxicity. Based on the structure of the IS20 as well as its profile of activity, ROS generation and excessive oxidation stress can be regarded as factors connected with cardiotoxicity. According to our former study the chelation of iron may be a key feature for oxidative toxicity. This is connected with higher lipophilicity, which can strengthen the toxicity against circulatory system and also with ionophoric activity[37,38]. From[13], some less lipophilic styrylquinazolines are known to still possess good multitarget anti-kinase activity. Particularly, exchange the benzodioxole to methoxylated phenyl group would be beneficial. On the other hand, in[19], we presented less lipophilic sulfonates of C4 quinazoline core with good activity, which may suggest a possible route. Further modifications that will be considered are the bioisosteric exchange of the 4-amine-quinazoline group that may be involved in the chelation of divalent metal ions and may therefore participate in oxidizing stress.

Materials and methods

Chemicals

The metal salts, such as iron(III) chloride hexahydrate and copper(II) sulfate pentahydrate, were purchased from POCH and Chempur, respectively. DMSO (99.9% purity) for spectroscopy studies was obtained from Thermo Scientific. Imatinib was acquired from Sigma-Aldrich. The IS20 compound (*N*-(1,3-benzodioxol-5-yl)-2-[(*E*)-2-(2-methoxyphenyl)vinyl] quinazolin-4-amine) was synthesized and characterized as described previously[13].

Cell culture

The human glioblastoma cell lines T98G, LN-18, LN-229, and U-87MG were purchased from ATCC. The glioblastoma cell line U-251 was kindly provided by Prof. G. Kramer-Marek from the Institute of Cancer Research in London, United Kingdom. The human suspension chronic myelogenous leukemia cell line K562 was purchased from Sigma-Aldrich. All adherent cancer cell lines were cultured in Dulbecco's modified Eagle's medium (DMEM) that had been supplemented with 10% heat-inactivated fetal bovine serum (FBS) (all from Sigma-Aldrich) in 75 cm^2 flasks (Nunc). The suspension cell line K562 was cultured in an RPMI-1640 medium (Sigma-Aldrich), which contained 10% heat-inactivated FBS. Each medium contained a combination of penicillin and streptomycin (1% v/v; Gibco). All cell lines were cultured under standard conditions at 37 °C with a 5% CO_2 humidified atmosphere. Moreover, all cell lines were routinely tested for mycoplasma using the PCR technique with specific *Mycoplasma* primers to confirm that there was no contamination.

Cell treatments

The IS20 compound was dissolved in DMSO at a concentration of 8.35 mM, then diluted in medium (DMEM or RPMI-1640) to a concentration of 25 µM (final DMSO concentration did not exceed 0.3%). For cytotoxicity assays, cells were incubated with IS20 in various concentrations (0–25 µM). For the remaining assays, K562 cells were incubated with IS20 at 12 µM and 6 µM, and the U-251 cells were exposed to IS20 at 10 µM. The doses of IS20 for these experiments were selected based on the results of antiproliferative activity and calculated IC_{50} values. Imatinib was used for autophagy assays, which was dissolved in DMSO at a concentration of 8.35 mM, then diluted in DMEM or RPMI-1640 medium to concentrations of 25 µM or 0.4 µM, respectively.

Cytotoxicity studies

The cells were seeded in 96-well plates (Nunc) at a density of 5,000 cells per well and incubated under standard conditions at 37 °C for 24 h. The assay was performed following a 72 h incubation with IS20, according to standard methodology as described previously[13,19]. Briefly, 100 µL of DMEM without phenol red containing 20 µL of the CellTiter 96® AQueous One Solution-MTS (Promega) solution was added to each well and incubated for 40 min–1 h at 37 °C. The optical densities of the samples were measured at 490 nm using a multi-well plate reader (Varioskan LUX, Thermo Scientific). The results were compared to the control and were estimated as the inhibitory concentration (IC_{50}) values (using GraphPad Prism 9). Each compound was tested in triplicate in a single experiment, with each experiment being performed at least four times.

Intracellular measurement of ROS levels

The U-251 and K562 cells were seeded in 96-well plates at a density of 9,000 per well and incubated with the freshly prepared solutions of IS20 for 3, 6, 9, 12 and 24 h. Additionally, the cells were incubated for 24 h with a solution of IS20 with ascorbic acid (100 µM). The ROS levels were measured immediately using the CellROX® Green Reagent assay procedure. In addition, Hoechst 33,342 (Molecular Probes™) staining was used to determine the number of cells in each well. Briefly, after treatment, the medium was removed (plates with K562 cells had been previously centrifuged), and a 100 µL mixture of CellROX Green Reagent (5 µM) and Hoechst 33,342 (6 µM) was added to each well. The samples were incubated for 30 min under standard conditions in the dark. The fluorescence was measured using a multi-plate reader (Synergy 4, Bio Tek), and readings were performed at 485 nm excitation and 520 nm emission, and 345 nm excitation and a 485 nm emission for CellROX Green Reagent and Hoechst 33,342, respectively. ROS levels were calculated as the percentage relative to the untreated controls. The experiments were performed at five times.

Time-dependent measurement of GSH level

The U-251 and K562 cells were seeded in 3 cm Petri dishes (Nunc) at a density of 500,000 cells per well. The next day, the medium was replaced by freshly prepared solutions of IS20. The cells were incubated with this derivate

at the same times as the levels of intracellular ROS measurement. Preparation of the lysates and intracellular glutathione levels were determined by the method described by Rahman et al.[95]. In short, the lysates in a volume of 20 µL were transferred into 96-well plates. Then, freshly prepared DNTB (0.67 mg/mL) and glutathione reductase (1.67 units/mL) solutions in KPE buffer were added to each well and incubated for 30 s. Immediately afterward, a solution of β-NADPH (0.67 mg/mL) prepared in KPE buffer was added to each well. The samples were mixed, and the absorbance was measured immediately at 412 nm in a Synergy4 multi-well plate reader. Data were compared to the levels of GSH in untreated cells (control). The experiments were repeated at five times.

Cell cycle assay

The K562 and U-251 cells were seeded in 3 cm Petri dishes at a density of 250,000 cells per well and incubated under standard conditions. After a day, the medium was removed and replaced by freshly prepared solutions of IS20. After a 24-hour incubation, the assays were performed using a Muse Cell-Cycle Kit (Millipore) according to the manufacturer's instructions. In short, cells were collected, washed with cold PBS and centrifuged at 300 g for 5 min. Next, the cells were fixed in ice-cold 70% ethanol and stored at -20 °C overnight. The following day, the cells were washed with cold PBS and centrifuged. Then, the cell pellets were resuspended in 200 µL of Muse™ Cell Cycle Reagent. Samples were incubated for 30 min at room temperature in the dark. The analysis of cellular subpopulation values in individual cell cycle phases was estimated using a Muse Cell Analyzer (Millipore). The experiments were performed at least four times.

Apoptosis assay

The K562 and U-251 cells were seeded in the same manner as for the cell cycle assay. After a day, the medium was removed and replaced by freshly prepared solutions of the tested compound IS20. The samples were incubated for 48 h. Next, the assays were performed using the FITC-Annexin V Apoptosis Detection KIT with 7-AAD (Bio-Legend) according to the manufacturer's instructions. In short, the cells were collected, washed twice with cold PBS and centrifuged at 300 g for 5 min. Then, the pellets of cells were resuspended in 100 µL Annexin V Binding Buffer. Next step, 5 µL of FITC-Annexin V and 5 µL 7-AAD Viability Staining Solution were added to each sample and incubated for 15 min at room temperature in the dark. After immunostaining, the number of events for live, early and late apoptotic cells was determined using a Muse Cell Analyzer. The experiments were performed at least four times.

Autophagy assay

The K562 and U-251 cells were seeded in 96-well plates and incubated at 37 °C for 24 h. The cell density was 20,000 cells per well (for the 24 h assay) and 10,000 per well (for the 48 h assay). Next, the medium was changed for freshly prepared solutions of IS20 and the cells were incubated for 24–48 h. Additionally, the cells were treated with imatinib as the positive control. After treatment, the assays were performed using a Muse™ Autophagy LC3-antibody-based kit (Millipore) according to the manufacturer's instructions. Briefly, the cells were collected, washed with cold Hank's Balanced Salt Solution and centrifuged at 300 g for 5 min. Then, the cells were resuspended in a mixture of 95 µL 1X Autophagy Reagent B and 5 µL Anti-LC3 Alexa Fluor®555 antibody. The samples were incubated on ice for 30 min in the dark. After incubation, the cells were centrifuged and resuspended in 200 µL of a 1X Assay Buffer. Then, the samples were directly processed to analyze the autophagy induction using a Muse Cell Analyzer. The autophagy induction ratio was calculated based on the ratio between the target's fluorescence versus the control sample. The experiments were performed at five times.

qRT-PCR studies

The total RNA was isolated from the K562 and U-251 cells after 24-h treatment with IS20 according to the TRIzol Reagent procedure (Ambion). Reverse transcription was performed with 5 µg of total RNA using a GoScript™ Reverse Transcriptase kit (Promega) and Oligo$(dT)_{23}$ Primers (Sigma). The Real-Time PCR was carried out in a 10 µL reaction volume using CTX96 Touch™ Real-Time PCR Detection System (Biorad). Each sample contained SsoAdvanced™ Universal SYBR® Green Supermix (Biorad), a specific primer pair mix (0.5 µM each) and 1 µL of cDNA. The reaction was performed under the following conditions: initial denaturation at 95 °C for 30 s; followed by 40 denaturation cycles at 95 °C for 15 s; annealing (primer-specific temperature for 30 s) and extension at 72 °C for 60 s. The results were analyzed based on a comparison of the expression of the target genes to a reference gene (*GAPDH*) using the $2^{-\Delta\Delta CT}$ method. The experiments were performed at least four times.

Immunoblotting studies

The K562 and U-251 were seeded in 3 cm Petri dishes at a density of 500,000 cells per well and incubated under standard conditions for 24 h. Next, the cells were incubated with freshly prepared solutions of IS20 for one day. After this time, the U-251 cells were detached by trypsinization. In turn, K562 were immediately collected into Eppendorf tubes. All samples were centrifuged at 2,000 rpm. Next, the cell pellets were resuspended in a RIPA buffer containing Halt Protease Inhibitor Cocktail, Halt Phosphatase Inhibitor Cocktail along with 0.5 M EDTA (all from Thermo Scientific) and lysed on ice for 20 min. The obtained lysates were sonicated and centrifuged at 10,000 rpm for 10 min at 4 °C. The supernatants were transferred to new tubes and used in further studies. The protein concentration was measured using a Micro BCA™ Protein Assay Kit (Thermo Scientific) according to the manufacturer's instructions. 16 µg of the proteins were electrophoresed on SDS-Page gels and transferred onto nitrocellulose membranes. The membranes were blocked in 5% non-fat milk prepared in TBST (containing 0.1% Tween-20) for 1 h. After this time, the membranes were incubated with specific primary antibodies (all from Cell Signalling Technology) at 1:1000 dilution for target proteins: cyclin E1 (#4129), cdc2 (#9116), $p21^{Waf1/Cip1}$ (#2947), PARP (#9542), AIF (#5318), caspase-9 (#9508), cathepsin B (#31718), BID (#2002), p53 (#2524),

HO-1 (#5853), HIF-1α (#14179), EGFR (#4267), phospho-EGFR (Tyr1068) (#2236), mTOR (#2983), phospho-mTOR (Ser2448) (#5536), phospho-Akt (Ser473) (#4060), phospho-p44/42 MAPK (Erk1/2) (Thr202/Tyr204) (#9101), as well as at 1:2000 dilution for reference proteins: GAPDH (#2118), β-actin (#3700) and vinculin (#13901) overnight at 4° C. The following day, membranes were washed in TBST and incubated with horseradish peroxidase (HRP)-conjugated secondary antibodies for 1 h at room temperature. Then, the membranes were washed in TBST and incubated with a SuperSignal™ West Pico Chemiluminescent Substrate (Thermo Scientific). The chemiluminescence signals were captured using a ChemiDoc™ XRS + System (BioRad). The experiments were repeated at least five times. The densitometric analysis was performed using ImageJ software (Wayne Rasband, National Institutes of Health, USA).

Lumit immunoassay

The U-251 and K562 cells were seeded into 96-well plates at a density of 50,000 for 24 h before the treatment. Next, the medium was changed for freshly prepared solutions of IS20 and the cells were incubated for 24 h. At the same time, Fluorogenic Live Cell Substrate (GF-AFC Substrate) was added for the final concentration in each well of 50 µM. Lumit immunoassay was done following the manufacturer's instructions. In brief, lysis buffer containing digitonin was mixed with the immunoassay reaction buffer and added to the wells. The plates were then mixed for 20 min. After that, primary antibodies against p-EGFR (Tyr1068), mTOR, p-mTOR (Ser2448) and Lumit secondary antibodies were added to the wells. The plates were then incubated at 23 °C for 90 min, followed by adding furimazine substrate. Luminescence and fluorescence were measured after 2 min using a multi-plate reader Varioskan LUX. The instrument was set to 1 s time. Tests were done at least three times with duplicate repeats on each plate.

In vivo toxicity

The fish embryo toxicity (FET) test was performed on zebrafish - *Danio rerio* (Experimental Medicine Centre, Medical University of Lublin, Poland) according to OECD Test Guideline 236 to determine the toxicity of IS20. According to the procedure, newly fertilized zebrafish eggs were exposed to the solution of IS20 for a period of 96 h at concentrations ranging from 1 to 25 µM. The system applied in the experiment was static, as the changes in solution concentrations did not exceed the range of 20% of nominal concentration values. The solutions were prepared in normal embryo culture medium - E3 solution (5 mmol/L NaCl, 0.17 mmol/L KCl, 0.33 mmol/L $CaCl_2$, and 0.33 mmol/L $MgSO_4$, containing no methylene blue, with a pH value of about 7.2). The experiment was performed in 24-well plates, with five embryos per well, and ten per group. Each plate was covered and kept in an incubator set at 28 ± 0.5 °C under a light/dark period of 12/12 h. Every 24 h, acute toxicity was determined based on a positive outcome in any of the four visual indicators of lethality, including the coagulation of fertilized eggs, lack of somite formation, lack of detachment of the tailbud from the yolk sac and lack of heartbeat. The values of LC_{50} for each timepoint (24, 48, 72 and 96 h) were calculated using GraphPad Prism 10. The final value of toxicity is the one measured at the end of the exposure period (96 hpf - hours post fertilization). Cardiotoxicity, as defined by heart rate, was also evaluated at that time point.

Experiments using the *Danio rerio* model were carried out on larvae up to 96 h post-fertilization, and therefore the approval of Ethics Committees was not required (according to Polish law and EU directives). All experiments using the *in vivo* model were carried out respecting the 3Rs principle and other guidelines (e.g. ARRIVE) for working with animals.

Tyrosine kinase assay

To determine the inhibition of non-receptor tyrosine kinases, assays were performed using the kinase selectivity system TK-1 and the ADP-Glo Kinase Assay (both from Promega). The protocol was developed by our group and previously described[13,32]. Experiments were performed at least four times. Data are expressed as a percentage of tyrosine kinase inhibitory activity after treatment with the derivatives tested.

Studies of the complexing properties of IS20 with metal ions

The tested compound and metal ions (Fe (III) and Cu (II)) were dissolved in DMSO to obtain an initial stock solution of 100 µM. Then, solutions of the tested IS20 derivative and ions were prepared by transferring the appropriate volume into individual wells of a 96-well black plate with a transparent bottom (Nunc). Finally, each well contained 200 µL of solution containing: the IS20 derivative at a concentration of 50 µM and various concentrations of ions to obtain the following ligand-to-metal molar ratios: 1:0; 10:1; 5:1; 3.3:1; 2.5:1; 2:1; 1.67:1; 1.43:1; 1.25:1; 1.11:1; 1:1. The prepared plates were then incubated for 4 h at room temperature. Absorption spectra in the range of 275 to 450 nm (in 5 nm steps) were measured using a multi-well plate reader Varioskan LUX. All spectra were normalized using vector normalization to reveal the hidden isosbestic point (HIP). Absorption spectra were processed by OriginPro 2023 software.

ADME calculations

All parameters were predicted using the commercially available program ACD/Percepta ver. 2012 (Advanced Chemistry Development, Inc., Toronto, ON, Canada, 2012).

Statistical analysis

The obtained results are presented as the mean ± standard deviation (SD) from 3 to 6 independent experiments. Depending on the type of experiment, the statistical analysis was carried out using the one-way ANOVA with a Bonferroni post-hoc test or unpaired t-test. Lumit Immunoassay statistical analysis was done with the usage of one-way ANOVA with a Dunn–Šidák correction test. A p-value of 0.05 or less was considered statistically significant. All statistical tests were performed using GraphPad Prism 9 software (GraphPad Software, USA).

Data availability

Data supporting the findings of this study are available within the article. Source data are available from the corresponding author on request.

Received: 9 October 2024; Accepted: 18 April 2025
Published online: 08 May 2025

References

1. Mrozek-Wilczkiewicz, A. et al. Investigating the anti-proliferative activity of styrylazanaphthalenes and azanaphthalenediones. *Bioorg. Med. Chem.* **18**, 2664–2671 (2010).
2. Das, D. & Hong, J. Recent advancements of 4-aminoquinazoline derivatives as kinase inhibitors and their applications in medicinal chemistry. *Eur. J. Med. Chem.* **170**, 55–72 (2019).
3. Musiol, R. et al. Investigating the Activity Spectrum for Ring-Substituted 8-Hydroxyquinolines.*Molecules***15**, 288–304. (2010).
4. Bedi, P. M., Kumar, V. & Mahajan, M. P. Synthesis and biological activity of novel antibacterial Quinazolines. *Bioorg. Med. Chem. Lett.* **14**, 5211–5213 (2004).
5. Alagarsamy, V. et al. Synthesis of novel 3-butyl-2-substituted amino-3H-quinazolin-4-ones as analgesic and anti-inflammatory agents. *Chem. Biol. Drug Des.* **70**, 254–260 (2007).
6. Held, F. E. et al. Facile access to potent antiviral Quinazoline heterocycles with fluorescence properties via merging metal-free domino reactions. *Nat. Commun.* **8**, 15071 (2017).
7. Lee, J. Y., Park, J. H., Lee, S. J., Park, H. & Lee, Y. S. Styrylquinazoline derivatives as HIV-1 integrase inhibitors. *Arch. Pharm.*, **335** (2002).
8. Hricoviniova, J., Hricoviniova, Z. & Kozics, K. Antioxidant, cytotoxic, genotoxic, and DNA-Protective potential of 2,3-Substituted Quinazolinones: Structure-Activity relationship study. *Int. J. Mol. Sci.*, **22** (2021).
9. Jampilek, J. et al. Investigating biological activity spectrum for novel styrylquinazoline analogues. *Molecules* **14**, 4246–4265 (2009).
10. Shagufta, S. & Ahmad, I. An insight into the therapeutic potential of Quinazoline derivatives as anticancer agents. *MedChemComm* **8**, 871–885 (2017).
11. Wischhusen, J., Naumann, U., Ohgaki, H., Rastinejad, F. & Weller, M. CP-31398, a novel p53-stabilizing agent, induces p53-dependent and p53-independent glioma cell death. *Oncogene* **22**, 8233–8245 (2003).
12. Rippin, T. M. et al. Characterization of the p53-rescue drug CP-31398 in vitro and in living cells. *Oncogene* **21**, 2119–2129 (2002).
13. Mularski, J., Malarz, K., Pacholczyk, M. & Musiol, R. The p53 stabilizing agent CP-31398 and multi-kinase inhibitors. Designing, synthesizing and screening of styrylquinazoline series. *Eur. J. Med. Chem.* **163**, 610–625 (2019).
14. Zhou, D. et al. Small molecules inhibit STAT3 activation, autophagy, and cancer cell anchorage-independent growth. *Bioorg. Med. Chem.* **25**, 2995–3005 (2017).
15. Xu, D. et al. Structure-Based Target-Specific screening leads to Small-Molecule camkii inhibitors. *ChemMedChem* **12**, 660–677 (2017).
16. Wei, X. W. et al. Su, 2-Styryl-4-aminoquinazoline derivatives as potent DNA-cleavage, p53-activation and in vivo effective anticancer agents. *Eur. J. Med. Chem.* **186**, 111851 (2020).
17. Dvorakova, M. et al. Synthesis, inhibitory activity, and in Silico modeling of selective COX-1 inhibitors with a Quinazoline core. *ACS Med. Chem. Lett.* **12**, 610–616 (2021).
18. Malarz, K., Mularski, J., Pacholczyk, M. & Musiol, R. Styrylquinazoline derivatives as ABL inhibitors selective for different DFG orientations. *J. Enzyme Inhib. Med. Chem.* **38**, 2201410 (2023).
19. Malarz, K., Mularski, J., Kuczak, M., Mrozek-Wilczkiewicz, A. & Musiol, R. Novel benzenesulfonate scaffolds with a high anticancer activity and G2/M cell cycle arrest. *Cancers.* **13**, 1790 (2021).
20. Simabuco, F. M. et al. p53 and metabolism: from mechanism to therapeutics. *Oncotarget* **9**, 23780–23823 (2018).
21. Rivlin, N., Brosh, R., Oren, M. & Rotter, V. Mutations in the p53 tumor suppressor gene: important milestones at the various steps of tumorigenesis. *Genes Cancer.* **2**, 466–474 (2011).
22. Liu, D., Xu, Y. & Aging p53, Oxidative Stress, and *Antioxid. Redox. Signal.*, 15 1669–1678. (2011).
23. Niedbala, M., Malarz, K., Sharma, G., Kramer-Marek, G. & Kaspera, W. Glioblastoma: pitfalls and opportunities of immunotherapeutic combinations. *Onco Targets Ther.* **15**, 437–468 (2022).
24. Cancer Genome Atlas Research. Comprehensive genomic characterization defines human glioblastoma genes and core pathways. *Nature* **455**, 1061–1068 (2008).
25. Pang, Y. et al. Report of canonical BCR-ABL1 fusion in glioblastoma. *JCO Precis. Oncol.* **5**, 1348–1353 (2021).
26. Palande, V. et al. Detection of gene mutations and gene–gene fusions in Circulating cell-free DNA of glioblastoma patients: an avenue for clinically relevant diagnostic analysis. *Mol. Oncol.* **16**, 2098–2114 (2022).
27. Goethe, E., Carter, B. Z., Rao, G. & Pemmaraju, N. Glioblastoma and acute myeloid leukemia: malignancies with striking similarities. *J. Neurooncol.* **136**, 223–231 (2018).
28. Nie, Y., Li, H. H., Bula, C. M. & Liu, X. Stimulation of p53 DNA binding by c-Abl requires the p53 C terminus and tetramerization. *Mol. Cell. Biol.* **20** 741–748. (2000).
29. Weller, M. et al. Predicting chemoresistance in human malignant glioma cells: the role of molecular genetic analyses. *Int. J. Cancer.* **79**, 640–644 (1998).
30. Law, J. C., Ritke, M. K., Yalowich, J. C., Leder, G. H. & Ferrell, R. E. Mutational inactivation of the p53 gene in the human erythroid leukemic K562 cell line. *Leuk. Res.* **17**, 1045–1050 (1993).
31. Freed-Pastor, W. A. & Prives, C. Mutant p53: one name, many proteins. *Genes Dev.* **26**, 1268–1286 (2012).
32. Malarz, K., Mularski, J., Pacholczyk, M. & Musiol, R. The landscape of the Anti-Kinase activity of the IDH1 inhibitors. *Cancers.* **12**, 536 (2020).
33. Trachootham, D., Alexandre, J. & Huang, P. Targeting cancer cells by ROS-mediated mechanisms: a radical therapeutic approach? *Nat. Rev. Drug Discov.* **8**, 579–591 (2009).
34. Zou, Z., Chang, H., Li, H. & Wang, S. Induction of reactive oxygen species: an emerging approach for cancer therapy. *Apoptosis* **22**, 1321–1335 (2017).
35. Perillo, B. et al. ROS in cancer therapy: the bright side of the Moon. *Exp. Mol. Med.* **52**, 192–203 (2020).
36. Malarz, K. et al. The role of oxidative stress in activity of anticancer thiosemicarbazones. *Oncotarget* **9**, 17689–17710 (2018).
37. Malarz, K., Zych, D., Gawecki, R., Kuczak, M. & Musiol, R. A. Mrozek-Wilczkiewicz, New derivatives of 4'-phenyl-2,2':6',2''-terpyridine as promising anticancer agents. *Eur. J. Med. Chem.*, 113032. (2020).
38. Malarz, K., Zych, D., Kuczak, M., Musiol, R. & Mrozek-Wilczkiewicz, A. Anticancer activity of 4'-phenyl-2,2':6',2''-terpyridines - behind the metal complexation. *Eur. J. Med. Chem.* **189**, 112039 (2020).
39. Mrozek-Wilczkiewicz, A., Malarz, K., Rejmund, M., Polanski, J. & Musiol, R. Anticancer activity of the thiosemicarbazones that are based on di-2-pyridine ketone and Quinoline moiety. *Eur. J. Med. Chem.* **171**, 180–194 (2019).
40. Arihara, Y. et al. Small molecule CP-31398 induces reactive oxygen species-dependent apoptosis in human multiple myeloma. *Oncotarget* **8**, 65889–65899 (2017).

41. Zhong, B. et al. A p53-stabilizing agent, CP-31398, induces p21 expression with increased G2/M phase through the YY1 transcription factor in esophageal carcinoma defective of the p53 pathway. *Am. J. Cancer Res.* **9**, 79–93 (2019).
42. Sivaraman, G. et al. Chemically diverse small molecule fluorescent chemosensors for copper ion. *Coord. Chem. Rev.* **357**, 50–104 (2018).
43. Chai, L. Q., Chai, Y. M., Li, C. G. & Zhou, L. Two mono- and dinuclear Cu (II) complexes derived from 3-ethoxy salicylaldehyde: X-ray structures, spectroscopic, electrochemical, antibacterial activities, Hirshfeld surfaces analyses, and time-dependent density functional theory studies. *Appl. Organomet. Chem.* **36**, e6475 (2022).
44. Sarkar, S. et al. A multi-responsive thiosemicarbazone-based probe for detection and discrimination of group 12 metal ions and its application in logic gates. *New. J. Chem.* **42**, 15157–15169 (2018).
45. Franco, R. & Cidlowski, J. A. Apoptosis and glutathione: beyond an antioxidant. *Cell. Death Differ.* **16**, 1303–1314 (2009).
46. Ighodaro, O. M. & Akinloye, O. A. First line defence antioxidants-superoxide dismutase (SOD), catalase (CAT) and glutathione peroxidase (GPX): their fundamental role in the entire antioxidant defence grid. *Alex. J. Med.* **54**, 287–293 (2018).
47. Ryter, S. W. & Tyrrell, R. M. The Heme synthesis and degradation pathways: role in oxidant sensitivity. Heme Oxygenase has both pro- and antioxidant properties. *Free Radic. Biol. Med.* **28**, 289–309 (2000).
48. Chau, L. Y. Heme oxygenase-1: emerging target of cancer therapy. *J. Biomed. Sci.*, 22 (2015).
49. Chiang, S. K., Chen, S. E. & Chang, L. C. The role of HO-1 and its crosstalk with oxidative stress in Cancer cell survival. *Cells* **10**, 2401 (2021).
50. Mrozek-Wilczkiewicz, A. et al. The synthesis and anticancer activity of 2-styrylquinoline derivatives. A p53 independent mechanism of action. *Eur. J. Med. Chem.* 177, 338–349 (2019).
51. Fang, B. A. et al. Molecular functions of the iron-regulated metastasis suppressor, NDRG1, and its potential as a molecular target for cancer therapy. *Biochim. Biophys. Acta.* **1845**, 1–19 (2014).
52. Nakahara, Y. et al. A tumor suppressor gene, N-myc Downstream-Regulated gene 1 (NDRG1), in gliomas and glioblastomas. *Brain Sci.* **12**, 473 (2022).
53. Sun, B. et al. Decreased expression of NDRG1 in glioma is related to tumor progression and survival of patients. *J. Neurooncol.* **94**, 213–219 (2009).
54. Menezes, S. V., Sahni, S., Kovacevic, Z. & Richardson, D. R. Interplay of the iron-regulated metastasis suppressor NDRG1 with epidermal growth factor receptor (EGFR) and oncogenic signaling. *J. Biol. Chem.* **292**, 12772–12782 (2017).
55. Chen, Z. et al. The Iron chelators Dp44mT and DFO inhibit TGF-β-induced Epithelial-Mesenchymal transition via Up-Regulation of N-Myc Downstream-regulated gene 1 (NDRG1). *J. Biol. Chem.* **287**, 17016–17028 (2012).
56. Le, N. T. V. & Richardson, D. R. Iron chelators with high antiproliferative activity up-regulate the expression of a growth inhibitory and metastasis suppressor gene: a link between iron metabolism and proliferation. *Blood* **104**, 2967–2975 (2004).
57. Cao, S. S. & Kaufman, R. J. Endoplasmic reticulum stress and oxidative stress in cell fate decision and human disease. *Antioxid. Redox Signal.* **21**, 396–413 (2014).
58. Merlot, A. M. et al. The metastasis suppressor, NDRG1, differentially modulates the Endoplasmic reticulum stress response. *Biochim. Biophys. Acta Mol. Basis Dis.* **1865**, 2094–2110 (2019).
59. Waser, M., Mesaeli, N., Spencer, C. & Michalak, M. Regulation of calreticulin gene expression by calcium. *J. Cell Biol.* **138**, 547–557 (1997).
60. Yang, Y. et al. The ER-localized Ca2+-binding protein calreticulin couples ER stress to autophagy by associating with microtubule-associated protein 1A/1B light chain 3. *J. Biol. Chem.* **294**, 772–782 (2019).
61. Sahni, S. et al. The metastasis suppressor, N-myc Downstream-regulated gene 1 (NDRG1), inhibits Stress-induced autophagy in Cancer cells. *J. Biol. Chem.* **289**, 9692–9709 (2014).
62. Pollak, N., Dolle, C. & Ziegler, M. The power to reduce: pyridine nucleotides–small molecules with a multitude of functions. *Biochem. J.* **402**, 205–218 (2007).
63. Parker, S. J. & Metallo, C. M. Metabolic consequences of oncogenic IDH mutations. *Pharmacol. Ther.* **152**, 54–62 (2015).
64. Shi, J. et al. An IDH1 mutation inhibits growth of glioma cells via GSH depletion and ROS generation. *Neurol. Sci.* **35**, 839–845 (2014).
65. Kovacevic, Z. et al. The metastasis suppressor, N-MYC downstream-regulated Gene-1 (NDRG1), Down-regulates the erbb family of receptors to inhibit downstream oncogenic signaling pathways. *J. Biol. Chem.* **291**, 1029–1052 (2016).
66. Liu, W. et al. *The proto-oncogene c-Src and its Downstream Signaling Pathways Are Inhibited by the Metastasis Suppressor, NDRG1 Oncotarget*, 68851–8874 (2015).
67. Hwang, B., Engel, L., Goueli, S. A. & Zegzouti, H. A homogeneous bioluminescent immunoassay to probe cellular signaling pathway regulation. *Commun. Biol.* **3** (2020).
68. Ito, H. et al. Bidirectional regulation between NDRG1 and GSK3β controls tumor growth and is targeted by differentiation inducing Factor-1 in glioblastoma. *Cancer Res.* **80**, 234–248 (2020).
69. Ma, W., Na, M., Tang, C., Wang, H. & Lin, Z. Overexpression of N-myc downstream-regulated gene 1 inhibits human glioma proliferation and invasion via phosphoinositide 3-kinase/AKT pathways. *Mol. Med. Rep.* **12**, 1050–1058 (2015).
70. Takekawa, M. & Saito, H. A family of stress-inducible GADD45-like proteins mediate activation of the stress-responsive MTK1/MEKK4 MAPKKK, *Cell.* **95**, 521–530. (1998).
71. Kovacevic, Z. et al. The metastasis suppressor, N-myc downstream regulated gene 1 (NDRG1), upregulates p21 via p53-independent mechanisms. *Carcinogenesis* **32**, 732–740 (2011).
72. Schlafli, A. M. et al. Prognostic value of the autophagy markers LC3 and p62/SQSTM1 in early-stage non-small cell lung cancer. *Oncotarget* **7**, 39544–39555 (2016).
73. Gomez-Sanchez, R. et al. Gonzalez-Polo, mRNA and protein dataset of autophagy markers (LC3 and p62) in several cell lines. *Data Brief.* **7**, 641–647 (2016).
74. Li, L., Tan, J., Miao, Y., Lei, P. & Zhang, Q. ROS and autophagy: interactions and molecular regulatory mechanisms. *Cell. Mol. Neurobiol.* **35**, 615–621 (2015).
75. Kim, Y. C. & Guan, K. L. mTOR: a Pharmacologic target for autophagy regulation. *J. Clin. Invest.* **125**, 25–32 (2015).
76. Cande, C. et al. Apoptosis-inducing factor (AIF): a novel caspase-independent death effector released from mitochondria. *Biochimie* **84**, 215–222 (2002).
77. Usuda, J. et al. Restoration of p53 gene function in 12-O-tetradecanoylphorbor 13-acetate-resistant human leukemia K562/TPA cells. *Int. J. Oncol.* **22**, 81–86 (2003).
78. Ni, J., Lan, F., Xu, Y., Nakanishi, H. & Li, X. Extralysosomal cathepsin B in central nervous system: mechanisms and therapeutic implications. *Brain Pathol.* **32**, e13071 (2022).
79. Xie, Z. et al. Cathepsin B in programmed cell death machinery: mechanisms of execution and regulatory pathways. *Cell. Death Dis.* **14**, 255 (2023).
80. Sax, J. K., Fei, P., Murphy, M. E., Bernhard, E. & Korsmeyer, S. J. El-Deiry, BID regulation by p53 contributes to chemosensitivity. *Nat. Cell. Biol.* **4**, 842–849 (2002).
81. Kerns, E. H., Di, L. & Properties, D. L. *Concepts. Structure Design and Methods: from ADME To Toxicity Optimization* (Academic, 2008).
82. Krüger, A., Gonçalves Maltarollo, V., Wrenger, C. & Kronenberger, T. *ADME Profiling in Drug Discovery and a New Path Paved on Silicia* (In: Drug Discovery and Development - New Advances, 2020).

83. Lipinski, C. A., Lombardo, F., Dominy, B. W. & Feeney, P. J. Experimental and computational approaches to estimate solubility and permeability in drug discovery and development settingsIPII of original article: S0169-409X(96)00423-1. *Adv. Drug Deliv. Rev.* **46** (2001) 3–26. (1997).
84. Jimenez, D. G. et al. Molecular properties, including chameleonicity, as essential tools for designing the next generation of oral beyond rule of five drugs. *ADMET DMPK.* **12**, 721–736 (2024).
85. Avdeef, A. Often neglected steps in transforming drug solubility from single measurement in pure water to physiologically-appropriate solubility-pH. *ADMET DMPK*, **13** (2025).
86. Jampilek, J. & Kralova, K. Insights into Lipid-Based Delivery Nanosystems of Protein-Tyrosine Kinase Inhibitors for Cancer Therapy. *Pharmaceutics* **14**, 2706. (2022).
87. Lipinski, C. A. Compound properties and drug quality. In: (ed Wermuth, C. G.) *The Practice of Medicinal Chemistry*. Academic, New York, 481–490. (2008).
88. Veber, D. F., Johnson, S. R., Cheng, H. Y., Smith, B. R. & Ward, K. W. Kopple, molecular properties that influence the oral bioavailability of drug candidates. *J. Med. Chem.* **45**, 2615–2623 (2002).
89. Muehlbacher, M., Spitzer, G. M., Liedl, K. R. & Kornhuber, J. Qualitative prediction of blood–brain barrier permeability on a large and refined dataset. *J. Comput. Aided Mol. Des.* **25**, 1095–1106 (2011).
90. Carpenter, S. et al. Felice, A method to predict Blood-Brain barrier permeability of Drug-Like compounds using molecular dynamics simulations. *Biophys. J.* **107**, 630–641 (2014).
91. Chunduri, V. & Maddi, S. Role of in vitro two-dimensional (2D) and three-dimensional (3D) cell culture systems for ADME-Tox screening in drug discovery and development: a comprehensive review. *ADMET DMPK.* **11**, 1–32 (2023).
92. Shen, C. & Zuo, Z. Zebrafish (Danio rerio) as an excellent vertebrate model for the development, reproductive, cardiovascular, and neural and ocular development toxicity study of hazardous chemicals. *Environ. Sci. Pollut. Res. Int.* **27**, 43599–43614 (2020).
93. Zhao, W., Chen, Y., Hu, N., Long, D. & Cao, Y. The uses of zebrafish (Danio rerio) as an in vivo model for toxicological studies: A review based on bibliometrics. *Ecotoxicol. Environ. Saf.* **272**, 116023 (2024).
94. Caballero, M. V. & Candiracci, M. Zebrafish as toxicological model for screening and recapitulate human diseases. *J. Unexplored Med. Data.* **3**, 4 (2018).
95. Rahman, I., Kode, A. & Biswas, S. K. Assay for quantitative determination of glutathione and glutathione disulfide levels using enzymatic recycling method. *Nat. Protoc.* **1**, 3159–3165 (2006).

Acknowledgements
This study was financed by a National Science Centre grant no. 2019/35/B/NZ5/04208 (KM). The publication was co-financed by the funds granted under the Research Excellence Initiative of the University of Silesia in Katowice (KM). Synthesis of IS20 was supported with grant 2018/31/B/NZ7/02122 (RM).

Author contributions
KM created the research hypothesis, designed experiments, performed cytotoxicity, cell cycle, apoptosis and part of qRT-PCR studies, discussed the results, and wrote the manuscript; MK performed ROS and GSH assays, qRT-PCR and immunoblotting studies; PRU performed immunoblotting of EGFR-mTOR pathway and Lumit Immunoassay; PRA conducted UV-Vis studies; ABC performed *in vivo* studies; JJ calculated ADME properties; JM delivered the IS20 compound; RM reviewed the manuscript; AMW performed autophagy assay, analyzed the data, wrote the manuscript. All the authors read and approved the final manuscript.

Declarations

Competing interests
The authors declare no competing interests.

Additional information
Supplementary Information The online version contains supplementary material available at https://doi.org/10.1038/s41598-025-99277-1.

Correspondence and requests for materials should be addressed to K.M.

Bioorganic Chemistry 170 (2026) 109517

Contents lists available at ScienceDirect

Bioorganic Chemistry

journal homepage: www.elsevier.com/locate/bioorg

An insight into the anticancer potential of sulfonated styrylquinazolines as multifunctional agents targeting microtubules.

Patryk Rurka [a], Jacek Mularski [b], Patryk Ziola [a], Anna Boguszewska-Czubara [c], Josef Jampilek [b,d], Anna Mrozek-Wilczkiewicz [a,e], Katarzyna Malarz [a,*]

[a] Institute of Physics, University of Silesia in Katowice, 75 Pułku Piechoty 1a, 41-500 Chorzów, Poland
[b] Institute of Chemistry, University of Silesia in Katowice, Szkolna 9, 40-006 Katowice, Poland
[c] Department of Medical Chemistry, Medical University of Lublin, Chodźki 4a, 20-093 Lublin, Poland
[d] Department of Chemical Biology, Faculty of Science, Palacky University Olomouc, Slechtitelu 27, 779 00 Olomouc, Czech Republic
[e] Department of Systems Biology and Engineering, Silesian University of Technology, Akademicka 16, 44-100 Gliwice, Poland

ARTICLE INFO

Keywords:
Sulfonic styrylquinazolines
Cell cycle arrest
Microtubule
Tubulin polymerization
Antimitotic activity
Apoptosis

ABSTRACT

Developing new microtubule-targeting agents is extremely important for cancer treatment. One of the goals is to overcome drug resistance, since these agents can cause mitotic arrest and thus cause impairment to cell signaling. Despite this, there are many gaps in our understanding of the complex actions of such agents. In this study, we report the synthesis and biological evaluation of a novel series of sulfonic styrylquinazoline derivatives, featuring three quinazoline core variants: unsubstituted, 6-chloro, and 7-chloro. Antiproliferative assays revealed that the 6-chloro derivative exhibited potent sub-micromolar activity against glioblastoma (GBM) and leukemia cell lines, while the 7-chloro analogs showed selective activity against leukemia cells. Importantly, the compounds were selective against normal cells. Further detailed molecular studies revealed that the most active compounds caused cell cycle arrest in the G2/M phase and disrupted microtubule polymerization–depolymerization dynamics, thereby affecting intracellular signaling pathways. Mechanistic studies showed the influence of the derivatives on cell cycle-related proteins (Aurora A and cyclin B1) and the inhibition of EGFR/Akt/mTOR and EGFR/Ras cell signaling. Cell death was induced primarily through apoptosis and potentially *via* autophagy, depending on the type of cell line. In addition, detailed computational studies have established a plausible binding model for these derivatives at the cevipabulin site of tubulin. Finally, physicochemical properties were determined to ensure adequate bioavailability, also toxicity and therapeutic efficacy were studied on an *in vivo* model. Notably, the 6-Cl derivative showed significantly better therapeutic efficacy than osimertinib on the zebrafish GBM xenograft model.

1. Introduction

Microtubules (MTs) are highly dynamic cytoskeletal structures composed of multiple α−/β-tubulin heterodimers, which are functionalized by various post-translational modifications (PTMs), such as acetylation or phosphorylation. They play a central role in cytoskeleton formation and maintenance, the intracellular trafficking of proteins, and the regulation of cell motility, division, and apoptosis [1]. Various cellular functions are defined by the dynamic instability of MTs, which includes a gradual growth at the plus end followed by rapid depolymerization (known as "catastrophe") and subsequent rescue [2]. Moreover, tubulin diversity alters the dynamics and mechanics of MTs, as well as the recruitment and activity of motor proteins and MT-associated proteins (MAPs). The latter proteins significantly affect protein-MT interactions, cross-linking and overall MT stability, as well as susceptibility to chemotherapy and tumor growth [3].

Altered patterns of PTMs, MAPs, and the presence of different tubulin isotypes can significantly influence the intracellular movement of cytoplasmic components and oncogenic signaling [4]. An instance is the increased acetylation of α-tubulin, which promotes cell migration and maintains the active state of protein kinase B/Akt, thereby enhancing the epithelial-mesenchymal transition (EMT), causing cancer metastasis [5]. Similarly, elevated levels of β-tubulin isotypes have been observed in many tumors, which often correlate with their aggressive

* Corresponding author.
E-mail address: katarzyna.malarz@us.edu.pl (K. Malarz).

https://doi.org/10.1016/j.bioorg.2026.109517
Received 30 October 2025; Received in revised form 7 January 2026; Accepted 15 January 2026
Available online 17 January 2026

nature, and poor prognosis [6]. Also, mutations in tubulin genes, such as missense or truncating mutations, can affect therapeutic responses after the administration of microtubule-targeting agents (MTAs). Differences in the amino acid residues lining the drug-binding pocket can significantly alter the strength and specificity of drug-tubulin interactions [7]. Besides this, there are also several known mechanisms of drug resistance, including overexpression of P-glycoprotein or drug efflux pumps, reduced levels of ABCG2, and changes in the expression of the MAP protein [8]. In particular, the interaction between MTs and MAPs or motor proteins can influence the expression of mitogen-activated protein kinases (MAPKs), which have pivotal roles in cell survival, apoptosis, and cell proliferation. Considering the crucial role of MTs in maintaining cellular architecture and dynamics, they represent an attractive target for the development of new targeted therapeutic strategies against many types of cancer.

MTAs are currently among the most widely used chemotherapeutic drugs in clinical practice. Many of them, such as paclitaxel, docetaxel, vincristine, and vinblastine, being the most effective tubulin inhibitors, have been approved by the FDA and EMA for the treatment of solid tumors and hematological malignancies [9]. However, their use in monotherapy has revealed serious limitations related to the development of drug resistance, as well as the occurrence of adverse effects such as high toxicity to healthy tissues, neurotoxicity, and myelosuppression [10]. Therefore, new approaches are constantly being sought, including the use of combination therapy to overcome drug resistance and improve therapeutic efficacy. For example, paclitaxel is being studied in 1586 ongoing clinical trials for solid tumors. On the other hand, new MTAs with high anticancer potential are being intensively developed, which have the ability to overcome resistance mechanisms to previous-generation MTAs, cross the blood-brain barrier (BBB), and inhibit angiogenesis [11–13]. It is noteworthy that MTAs were traditionally classified as antimitotic drugs that inhibit cell division through the formation of aberrant mitotic spindles and blocking the metaphase-anaphase transition. However, this perception has changed and evolved in light of evidence indicating that the disruption of MT assembly can profoundly affect cellular signaling, protein-protein interactions, and metabolic activity [14]. Nowadays, MTAs are increasingly recognized as agents with a broader cellular mechanism of action that extends beyond their simple antimitotic activity associated with tubulin binding. However, the complex and multifaceted mechanism underlying their action has not yet been fully elucidated.

Many MTAs have been reported in the literature to activate the JNK, ERK, and p38 MAPK signaling pathways, triggering an apoptotic response [15,16]. These agents are divided into two groups, destabilizing and stabilizing, based on their interference with the dynamic balance of MTs. Hence, they regulate and alter the interactions between MTs and various MAPs, ultimately affecting the triggering of apoptosis through a p53-dependent or -independent pathway. Interestingly, compounds have recently been described that cause microtubule dysfunction, increase the effect of iron and calcium ions on mitochondrial damage, and induce both apoptotic and ferroptotic mechanisms of cell death [17]. Notably, disruption of MT dynamics can also cause downregulation of other important signaling pathways, including EGFR [18], HIF-1α-mediated angiogenesis [19], EMT [20], JAK2/STAT3 [21] and Wnt/β-catenin [22]. Therefore, dual EGFR/tubulin inhibitors based on furo[2,3-*d*]pyrimidine, pyrrolo[3,2-*d*]pyrimidine, 2-arylobenzofuran, or 1,2,4-triazole scaffolds are increasingly being developed [23]. There are also reports of compounds based on the quinazoline scaffold as MT-disrupting agents [24–26]. In our group, we have so far focused on developing novel non-receptor tyrosine kinase inhibitors containing the styrylquinazoline structural motif. We have characterized a group of p53 reactivator analogues, CP-31398 [27], and subsequently described in detail the mechanism of action of one of the molecules, IS20 (6b), demonstrating its ability to induce oxidative stress by affecting the expression of the *Ndrg1* gene and disrupting the EGFR signaling pathway [28]. Further work on the synthesis of thio-analogs of styrylquinazoline derivatives, with increased bioavailability and improved binding to different conformations in the DFG pocket of Abl kinase, has been performed [29]. In addition, our studies have also revealed a different mechanism of action of the compounds on cell cycle inhibition depending on how they bind to Abl kinase. Interestingly, the study of intermediates in the synthesis of these thio-aryl derivatives revealed interesting antiproliferative and antimitotic properties. Several benzenesulfonates enhanced tubulin polymerization similarly to paclitaxel but exhibited a significantly greater potential for inhibiting the cell cycle in the G2/M phase [30]. Analysis of the mechanism of action also revealed the possibility of activating two cell death pathways, depending on the status of p53. Nevertheless, the possible interaction of benzenesulfonates with tubulin and cell cycle proteins, as well as their impact on key signaling pathways regulated by EGFR, which are responsible for metabolism, growth, cell proliferation, and metastasis, has not been characterized. Accordingly, in the present study, we expanded this compound library by designing additional sulfonated styrylquinazolines and complemented the experimental work with *in silico* analyses on a large virtual compound library to provide additional support for hypotheses concerning their possible interaction with tubulin, together with multidimensional cellular and molecular studies. Ultimately, a deeper understanding of cellular biochemistry and the multidirectional action of antimitotic agents may lead to more effective and rational development of innovative therapeutic strategies.

2. Results and discussion

2.1. Synthesis of novel compounds

The new benzenesulfonates that are the subject of the following biological studies were synthesized according to known procedures [27,29,30]. The presented small series is an extension of our group's previous studies on new scaffolds responsible for high antiproliferative activity and having the potential to inhibit the cell cycle in the G2/M phase through interaction with tubulins, as mentioned above [30]. Hence, three series of sulfonated styrylquinazolines were obtained, which had chlorine substitution at position 7 of the quinazoline ring (TS1-TS4), chlorine at position 6 (TS5), and were unsubstituted (TS6-TS8). The structures of the final compounds (Fig. 1) were confirmed by ^{1}H and ^{13}C NMR spectroscopy and mass spectrometry, as displayed in the Supplementary Information **(Fig. S1-S16).**

2.2. Anticancer profiles of the tested sulfonic styrylquinazolines

The biological evaluation of the synthesized compounds began with an analysis of their antiproliferative activity profiles against a panel of cancer cells representing different types and genetic landscapes, particularly regarding the status of the *TP53* gene, known as the guardian of the genome. So far, several studies have shown that compounds containing styrylquinazoline [27] or styrylquinoline [31,32] scaffolds are extremely interesting and promising in the treatment of tumors with a mutated or absent p53 protein. Therefore, for this study, we selected cancer cells with a wild-type p53 protein: U87MG (glioblastoma), cancer cells with mutated p53: U-251 (glioblastoma) [33], and cancer cells devoid of p53: K562 (leukemia) [34]. The results are presented in Table 1.

In general, there was a clear difference in the antiproliferative activity of the tested compounds in which the quinazoline ring was substituted by 6-Cl or 7-Cl and those that were unsubstituted. Among the tested compounds, the TS5 derivative with chlorine in position 6 was the most active toward the tested cancer cells. The lowest IC_{50} for TS5 was registered against both glioblastoma cells, *i.e.* 0.17 μM and 0.21 μM for U87MG and U-251 cells, respectively. Interestingly, GBM may be particularly vulnerable to MTAs due to the high genome instability affecting MT dynamics, the abnormal activity of cell division regulators or chromosome instability [35]. On the other hand, Abbassi et al.

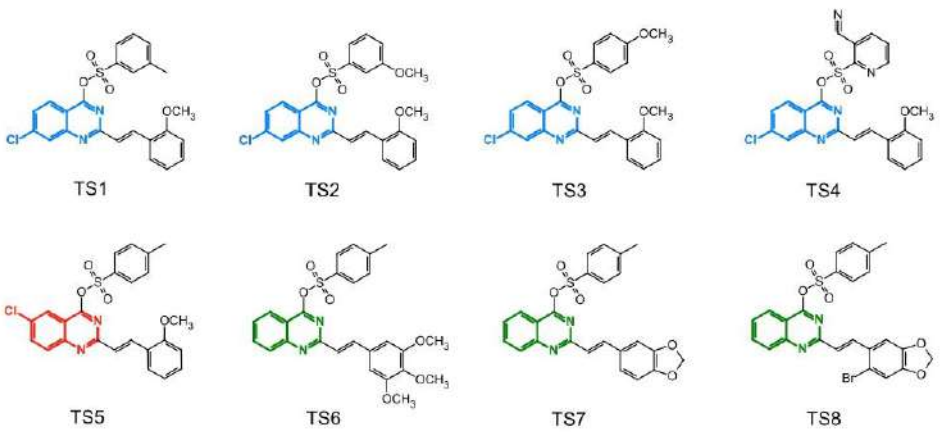

Fig. 1. Structures of tested sulfonic styrylquinazolines.

Table 1
Antiproliferative activity of tested compounds for a panel of cancer cells and normal astrocytes (NHA).

No.	Antiproliferative activity - IC_{50} values [μM]				
	U87MG	U-251	K562	HepG2	NHA
TS1	>25	2.53 ± 0.58	0.29 ± 0.06	>25	6.72 ± 0.47
TS2	3.53 ± 0.10	2.24 ± 0.20	0.34 ± 0.10	>25	3.06 ± 0.25
TS3	6.88 ± 0.14	1.80 ± 0.34	0.75 ± 0.08	>25	5.32 ± 0.37
TS4	1.785 ± 0.746	1.761 ± 0.338	>25	>25	2.70 ± 0.31
TS5	0.17 ± 0.02	0.21 ± 0.02	0.26 ± 0.08	>25	1.75 ± 0.14
TS6	7.25 ± 0.15	15.06 ± 3.83	2.15 ± 0.75	>25	24.88 ± 1.50
TS7	>25	>25	>25	NT	NT
TS8	>25	>25	>25	NT	NT
Osimertinib	11.24 ± 0.46	20.13 ± 0.34	NT	NT	6.55 ± 0.17
CP-31398	NT	18.77 ± 1.65	3.09 ± 0.36	NT	NT
Paclitaxel	NT	0.06 ± 0.02	NT	NT	0.03 ± 0.01
Nocodazole	NT	0.25 ± 0.10	NT	NT	NT

NT – not tested.

revealed that the isoform landscape of tubulin is unique to each glioblastoma cell line, and only the total expression level of α- and β-tubulin influences MTAs sensitivity [36]. Therefore, it is surprising that the rest of the chloroquinazolines displayed a worse activity profile on GBM cells. In U87MG cells, the two 7-Cl derivatives, TS4 with a cyano, and TS2 with methoxy group attached to the benzenesulfonate showed moderate activity (IC_{50} was 1.79 and 3.53 μM, respectively), while TS3 showed a weak level of activity and TS1 was inactive. Moreover, the antiproliferative activity profile of these compounds was slightly better in U-251 cells. The recorded IC_{50} values for the four derivatives were similar and ranged from 1.76 (TS4) to 2.53 μM (TS1). Such results may indicate a different mechanism or efficacy of tubulin binding in the case of 6- and 7-chloroquinazoline.

Similarly, the high activity level for TS5 was registered for K562 cells, where the calculated IC_{50} was 0.26 μM. Interestingly, the leukemia cell line was the most susceptible to the other tested compounds. The 7-chloroquinazolines, such as TS1, TS2, and TS3, with a methyl or methoxy group attached to the benzenesulfonate were characterized by a high activity level against K562, with an IC_{50} ranging from 0.29 to 0.75 μM. The situation was completely different for the TS4 derivative with a 3-cyanobenzenesulfonate group, which was inactive (>25 μM) only against these non-adhesive cells.

Interestingly, the unsubstituted quinazolines did not show antiproliferative activity against the tested cell lines with one exception. Namely, the TS6 derivative with 3,4,5-trimethoxy attached to the styryl group showed moderate activity against K562 cells, the calculated IC_{50} was 2.15 μM. For GBM cell lines, TS6 had a weak level of activity (IC_{50} from 7.25 to 15.06 μM). Surprisingly, taking into account our previous studies [27,29,30], compounds TS7 and TS8 containing a benzodioxol group were inactive against the cancer cells. However, it should be noted that the benzodioxol group in the novel compounds was substituted at a different position, on the styryl moiety side. This most likely resulted in an inability to interact with the critical amino acids of the proteins in the protein binding pocket and a loss of activity.

The hepatotoxicity profile of the tested compounds was analyzed for HepG2 cells, which are commonly used for these assays, as well as for studying drug metabolism through cytochrome P450 induction. As depicted in Table 1, none of the sulfonic styrylquinazolines had an effect on the proliferation and condition of liver cells (>25 μM). In addition, to determine the selectivity of the tested compounds, assays were performed on normal astrocyte (NHA) cells. The therapeutic index (TI) was calculated as the ratio of the IC_{50} of normal cells *versus* that of cancer cells (Fig. 2, **Table S1**). The higher the value of this parameter, the more selective the drug is toward tumor cells and the safer it is for healthy tissues. The highest TI of approximately 23 was recorded for TS1 on K562 cells. The other derivatives showed quite good selectivity toward leukemia cells, with TI values ranging from about 11.57 (TS6) to 6.69 (TS5). In contrast, one derivative (TS4) showed low selectivity. In the case of GBM cells, TS5 proved to be the most selective derivative. High TI values reaching 10.3 and 8.5 were recorded for U87MG and U-251, respectively. It is worth noting that the TIs for most anticancer drugs, including those approved for use by the FDA, are very low. As expected, the reference drug: osimertinib (3rd generation EGFR inhibitor) showed low selectivity (TIs were below 0.58) in our tests. Similarly, the clinically used chemotherapeutic drug paclitaxel, a well-known microtubule disruptor, exhibits high cytotoxicity toward normal astrocytes, resulting in low selectivity.

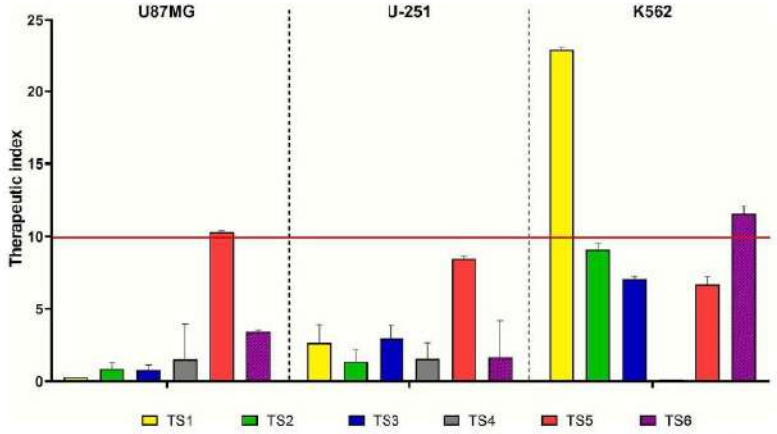

Fig. 2. *In vitro* therapeutic indexes of tested compounds that exhibited antiproliferative activity. The TI is the ratio of the IC_{50} values of normal *versus* cancer cells (*i.e.*, IC_{50} (NHA)/IC_{50} (U87MG)) with variance ratio.

2.3. *Influence on cell cycle arrest and destabilization of tubulin assembly*

The first step toward explaining the molecular mechanism of action of the tested derivatives was to determine their effect on cell cycle arrest. The effect of biologically active sulfonic derivatives on cell lines differing in p53 status (U-251 and K562) was evaluated (Fig. 3A). Representative histograms from one of the experiments with tables summarizing the results are provided in **Figs. S17** and **S18**. In general, the highest level of cell cycle arrest in the G2/M phase was observed in the U-251 cells. As our previous studies have shown, glioblastoma is particularly vulnerable to the effects of antimitotic compounds. It is worth noting that the most active derivative, **TS5** (with double the IC_{50}

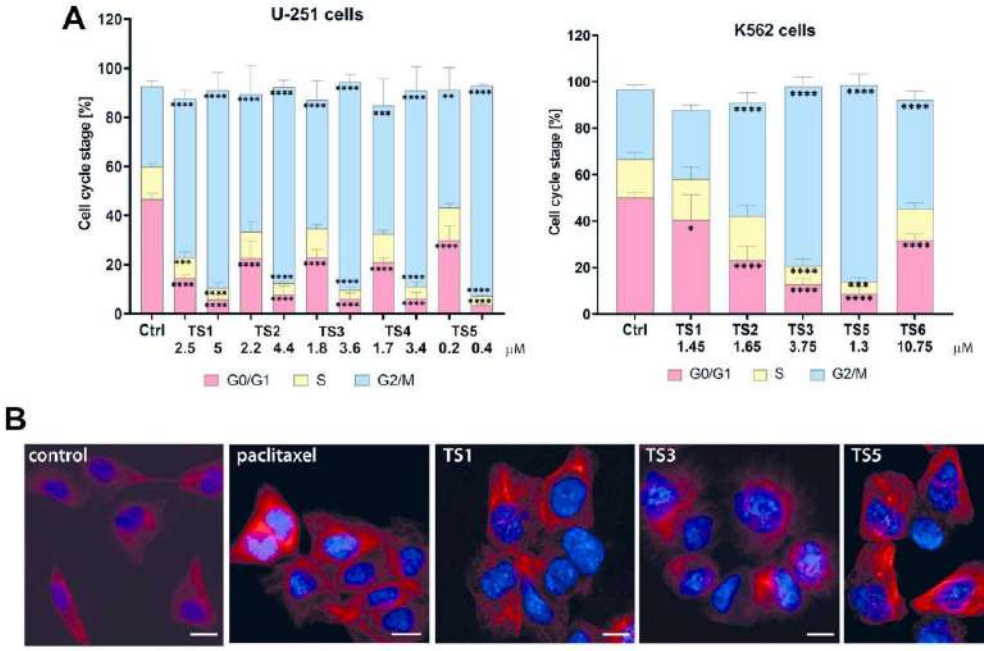

Fig. 3. Impact of the tested compounds on cell cycle arrest in U-251, and K562 cell lines (A) and destabilization of tubulin assembly dynamics in U-251 cells after 3 h of incubation (B). Statistical significance compared to the control was performed with one-way ANOVA and *post hoc* to Dunnett's correction from at least four independent experiments and presented on the charts as: * $p < 0.05$; ** $p < 0.01$; *** $p < 0.001$; **** $p < 0.0001$. The scale in the images was 10 μm.

concentration), caused the greatest inhibition of the cell cycle. A remarkable increase in the population of cells in the G2/M phase was recorded, reaching almost 86% (32.5% in untreated control) with a simultaneous decrease in the content of cells in the S and G1 phases. A significant effect was also observed with other derivatives, where the percentage of cells in the G2/M phase increased to 80%. Similarly, a high number of cells in the above mentioned phase of the cell cycle was observed for the IC_{50} concentration of the tested TS1-TS5 derivatives. In leukemia cells, the changes in cell cycle distribution were less impressive. The TS5 derivative triggered a 34.7% increase in the population of leukemia cells in the G2/M phase compared to the control (from 50% to 84.7%). In turn, for the TS3 compound, a 27% increase in cells was observed. The changes in the degree of sensitivity of the tested cells to sulfonic styrylquinazoline agents may be related to differences in the expression of key cell cycle-related proteins, such as CDK, cyclins, and Auroras. It is worth noting that the regulation of tubulin dynamics during mitosis is a highly complex process in which a number of regulatory proteins are involved, as many studies have shown [37]. In the following sections, we examine and describe in more detail the effects of the most active compounds on gene and protein expression using qRT-PCR and Western blot methods.

Moreover, the behavior of the tubulin assembly process in U-251 cells was monitored after treatment with the most active derivatives: TS1, TS3, and TS5. After 3 h of incubation, changes in MT dynamics were observed, as evidenced by more intense red tubulin bands compared to untreated cells (Fig. 3B). In addition, the cytoskeletal network of the MTs appeared to be more disordered and condensed at the cell periphery. This effect persisted during the 24 h incubation (**Fig. S19A**). Moreover, the pattern of increased microtubule networking after TS5 treatment seemed similar to the effect induced by paclitaxel. This was also confirmed by *in vitro* tubulin polymerization tests, in which an increase in the degree of polymerization was observed after incubation with TS5 (**Fig. S19B**). Thus, like the previous series of sulfonated styrylquinazolines [30] and another series of 2,4-bis substituted quinazolines [38], the tested compounds can increase tubulin polymerization, leading to a dynamic imbalance between MT assembly and disassembly. The observed effect can affect the retention of cellular metabolism, the impairment of cellular signaling, including that related to the EGFR and mTOR pathways, the disruption of intracellular transport, and cell cycle arrest in the G2/M phase.

2.4. *In silico analyses - binding modes to tubulin*

Cell-based and enzymatic assays demonstrated that treatment with the tested compounds alters tubulin dynamics. The observed effects are consistent with either enhanced microtubule polymerization or attenuation of depolymerization processes. These findings motivated a focused computational investigation aimed at identifying the most probable tubulin binding site(s) for the biologically active benzenesulfonates, assessing the stability and reproducibility of their binding modes, and determining whether the ligands can be rationalized as a coherent and tunable chemical family.

A primary objective of this analysis was to determine whether ligands based on a styrylquinazoline core functionalized with a benzenesulfonate moiety exhibit preferential positioning toward specific tubulin binding sites. The virtual library comprised quinazoline cores lacking halogen substitution as well as two additional variants bearing 6-chloro and 7-chloro substituents. Structural diversity was introduced through systematic variation of both the styryl and benzenesulfonate substituents. In addition to motifs present in experimentally tested compounds, 20 benzenesulfonate and 22 styryl variants were defined, yielding a total of 1320 unique structures ($20 \times 22 \times 3$). A complete list of SMILES for all screened compounds is provided in the SI (**section 3.1**). For each structure, up to 100 conformers were generated using the Conformator program [39], resulting in approximately 132,000 ligand instances per binding pocket. Initial ligand placement within each binding site was guided by a proprietary workflow component to ensure consistency with experimentally observed binding modes. Docking calculations were performed against 21 Protein Data Bank structures representing experimentally characterized tubulin binding sites. The corresponding binding pockets are summarized in **Table S4 (section 3.2 in the SI)**. For each ligand instance, the top three preliminarily aligned poses were retained, and all associated conformers were subsequently re-docked and rescored using the JAMDA protocol, yielding approximately 7.2 million evaluated ligand instances. Based on the docking performance of established reference ligands, a JAMDA score threshold of −3.5 was adopted to identify high-confidence binding solutions. Notably, only nine structures across the entire virtual library satisfied this criterion, and all were associated exclusively with docking to the cevipabulin binding site (PDB ID: 7CLD). Importantly, these top-ranking solutions also exhibited high internal shape similarity, indicating convergence toward a single, well-defined binding geometry (**section 3.3** in the SI). The combined selectivity and geometric coherence of these poses support the classification of the styrylquinazoline–benzenesulfonate scaffold as a coherent ligand family suitable for further optimization toward tubulin-stabilizing activity.

A two-tier docking strategy was employed to examine ligand preferences across several experimentally characterized tubulin pockets. Rather than relying exclusively on docking score ranking to infer binding relevance, we evaluated the structural consistency of docking outcomes using a shape-based similarity analysis that is independent of atom-by-atom correspondence or predefined reference poses (Fig. 4A). For the cevipabulin binding site (PDB ID: 7CLD), all significant docked poses (score cutoff: −2.5) were compared pairwise using the RDKit implementation of the Shape Tanimoto metric. This descriptor quantifies volumetric similarity after optimal spatial alignment and thus reports whether independent docking runs converge toward the same geometric region within the binding pocket. To quantify pose consistency, a consensus geometry (medoid) was defined as the pose exhibiting the highest average three-dimensional shape similarity to all other poses in the ensemble, rather than an averaged or artificial geometry. The shape similarity of each pose to this medoid was then used as a quantitative measure of binding-mode stability. High similarity values indicate convergence toward a single, well-defined, and reproducible binding geometry, whereas low similarity values reflect geometric dispersion and the absence of a dominant binding mode. Analysis of the relationship between within-site docking rank and shape similarity revealed a clear monotonic trend. Higher-ranking solutions consistently clustered around the consensus geometry, while progressively lower-ranked poses displayed reduced similarity and increased geometric dispersion. This relationship was supported by both rank-based and linear correlation analyses and further corroborated by binned statistics, which showed a systematic decline in median shape similarity accompanied by a broadening of the similarity distribution as docking rank deteriorated (Fig. 4B). Collectively, these observations indicate that top-ranked docking solutions correspond to a stable and reproducible binding space rather than isolated favorable configurations, whereas lower-ranked poses are characterized by conformational heterogeneity and diminished geometric coherence. Thus, docking rank and pose stability emerge as mutually reinforcing criteria, with shape-based similarity providing an orthogonal validation of favorable binding modes. The ligand library analyzed in this study was constructed as systematic permutations of substituents on a common chemical scaffold. Notably, despite substantial substituent diversity, the docked ligands converged toward a common, geometrically stable binding region. This behavior indicates that the cevipabulin pocket tolerates chemical variation within the explored substituent space without enforcing alternative global binding orientations. This observation reflects geometric robustness of the binding mode rather than fine-grained equivalence between individual substituents and should therefore not be interpreted as a quantitative structure–activity relationship. Consistent with this analysis, molecular docking revealed that the highest-ranking ligands

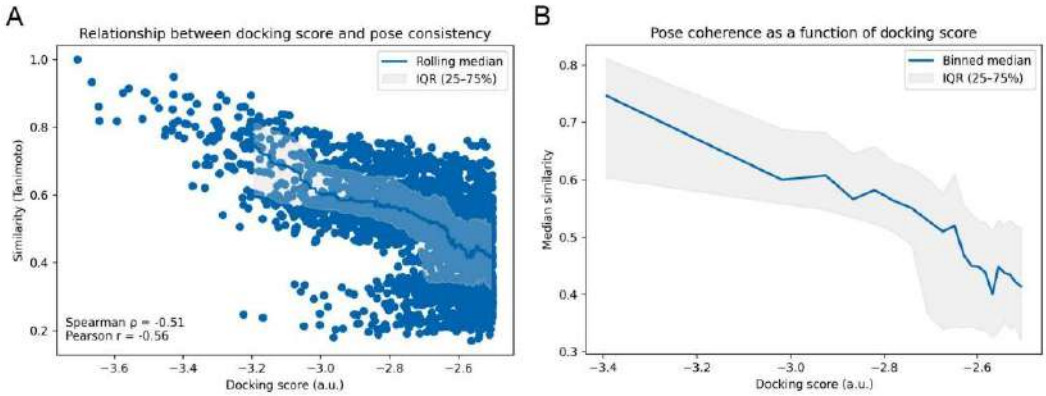

Fig. 4. Statistical analysis of docking score and pose consistency (A) and pose coherence (B).

adopt binding modes closely resembling that of cevipabulin, occupying the corresponding β-tubulin binding site (**section 3.4** in the SI). Importantly, the synthesized compounds also ranked highly for the cevipabulin binding site, with **TS5** showing the most favorable docking score (**section 3.5** in the SI).

2.5. *Influence on genes and proteins associated with cell cycle progression*

In a further step, we investigated the effects of the tested derivatives on cell cycle-related molecules at the gene and protein levels. The first of the proteins tested was the p27 molecule (Fig. 5A). There were high statistically significant levels of expression, ranging from an almost 3-fold increase for **TS5** and a 2.5-fold increase for TS1 and TS3 compared to the control for the U-251 cell line. More than a 3-fold overexpression of this protein was also observed in leukemia cells for TS1 and TS3, and 1.5-fold for TS5. The increase in p27 levels has the effect of inhibiting the cell cycle by affecting cyclin-kinases complexes. According to [40,41] p27 can bind to the cyclin *E*-CDK2 complex, suppressing its function and thereby blocking the progression from the G1 phase to DNA synthesis. Cyclin E, on the other hand, is encoded by the *CCNE2* gene, therefore a decrease in the expression of this gene explains the increase in p27 protein levels. As shown in Fig. 5B a decrease in *CCNE2* expression for line U-251 was recorded for all the derivatives tested. In contrast, for the leukemia cell line, a decrease was noted only for compound TS5, but by as much as 5.8-fold relative to the control. Another protein involved in the control of cell cycle processes at the G1 step is p21. As with the p27 protein, the expression of the p21 protein was also heightened for all three compounds for the U-251 cell line compared to the control, with about a 3-fold statistically significant increase in the case of TS5 and TS3, and 2.5-fold for TS1. The K562 cell

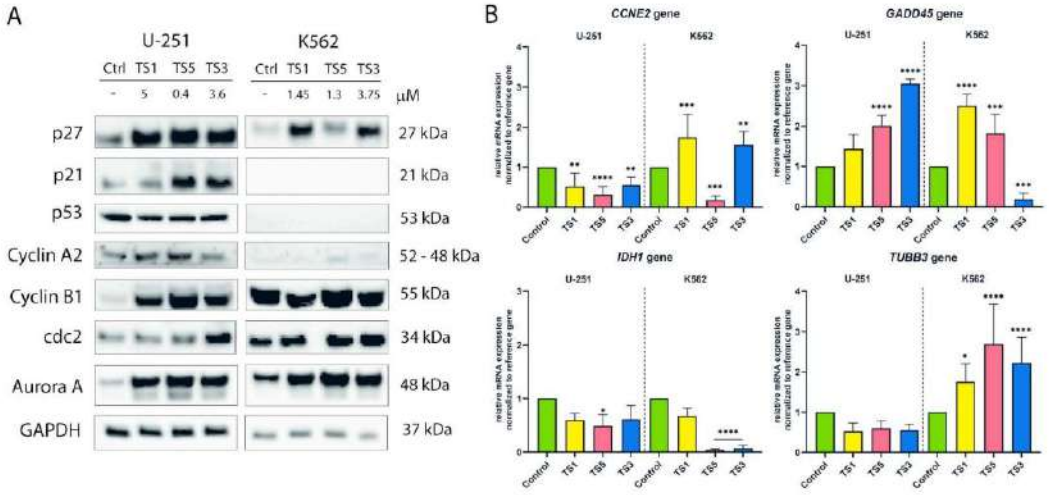

Fig. 5. Impact of the tested compounds on the expression of proteins and genes related to cell cycle progression in U-251, and K562 cells. Assessment of proteins expression using Western blot technique. The immunoblots shown are representative of at least four independent experiments. The displayed blots were cropped, and the full-length blots are shown in Fig. S24 (A). Determination of expression levels of cell cycle-related genes (*CCNE2*, *GADD45*, *IDH1*, *TUBB3*) using qRT-PCR (B). The gene expression values were normalized to a reference and compared to untreated cells ($n = 7$). Statistical significance compared to the control was performed with one-way ANOVA with *post hoc* to Šidák's correction and presented on the charts as: * $p < 0.05$; ** $p < 0.01$; *** $p < 0.001$; **** $p < 0.0001$.

line did not show any p21 protein expression. A similar situation occurred with the p53 protein, which was absent in the K562 cell line. The incubation of the U-251 cell line with the three studied derivatives resulted in a slight decrease in p53 levels.

In the case of the cyclin A2 protein, which is involved in S and G2-phase cell division, the observed fluctuations were not statistically significant. A high overexpression (around 4 times) of cyclin B1 was registered for the U-251 cell line after incubation with all the tested compounds. For the U-251 cell line, changes in cyclin B1 levels were not statistically significant. Cyclin B1 is involved in the G2 phase of cell division. The observed increase in its expression in line U-251 is consistent with the results of cell cycle inhibition by flow cytometry. Additionally, we registered a downregulation of the *IDH1* gene, which also confirmed cell cycle arrest in the G2/M phase. These changes may cause further fluctuations in the level of cyclin B1 [42]. The cdc2 protein is also involved in the G2 phase, forming a complex with cyclin B/A. A statistically significant increase in cdc2 levels was similarly recorded for line U-251, being approximately 1.5-fold for compounds TS3 and TS5. In addition, for line K562 we noted a similar increase (approximately 1.5-fold) in cdc2 concentration for the TS3 derivative. Confirmation that the tested compounds inhibited the cell cycle in the G2/M phase was also provided by *GADD45* gene expression analysis. *GADD45* may be regulated by the p53 protein and plays a crucial role in controlling the G2/M checkpoint following DNA damage [43,44]. The highest increase in *GADD45* expression was observed for the U-251 line for compound TS3, at almost 3-fold, followed by 2-fold for TS5 and 1.5-fold for TS1. For leukemia, a significant (2.5-fold) increase was also registered for TS1 and about 2-fold for TS5. This relationship did not apply to the TS3 compound.

The protein involved in the subsequent phases (M phase) of the cycle is Aurora A, for which the greatest increase in expression was observed. For the U-251 line, where inhibition of the cycle in the G2/M phase was the most evident in previous flow cytometry experiments, incubation with compound TS5 resulted in a more than 10-fold increase in Aurora A expression, while compounds TS1 and TS3 gave an approximately 8-fold increase in the concentration of the analyzed protein. Similarly, in the K562 line, all the derivatives tested resulted in an increase in Aurora A expression: TS5 by more than 6-fold, TS1 and TS3 by about 5-fold. In addition, Aurora A enhanced the polymerization of tubulins, confirming earlier studies [45,46].

The influence of the tested derivatives on the expression of the *TUBB3* gene encoding the βIII tubulin isotype was also examined. As previously mentioned, the βIII isotype may play a key role in the aggressive behavior of many tumors and may also be a key factor in response to therapy. As shown on Fig. 5B, all of tested sulfonic styrylquinazolines caused a significant increase in *TUBB3* expression for K562 cells. For TS3 and TS5, this increase was more than 2.2-fold. For U-251, some downward fluctuations in expression were observed. However, it is worth noting that the biosynthesis and regulation of tubulin levels are the result of post-transcriptional regulation as well as the influence of other cellular components. Gasic et al. have shown that PI3K activity modulates tubulin gene expression due to changes in MT stability, leading to autoregulation of tubulin mRNA [47]. On the other hand, MT can be regulators of the PI3K signaling cascade through direct participation in the recruitment of receptor substrates, the maintenance of activated AKT, and the spatial regulation of antagonists such as PTEN [48,49].

2.6. Regulation of EGFR cellular signaling

As mentioned above, MT can affect many major cell signaling pathways that transmit signals and control cell growth, proliferation, differentiation, migration and death. Indeed, the MT destabilizing agents can inactivate EGFR phosphorylation and suppress the signaling pathway [18]. Gao et al. also showed that histone deacetylase 6 (HDAC6), which is an MT-associated deacetylase, associates with endosomal compartments and controls the trafficking of EGFR and promotes its degradation [50]. Similarly, the nucleocytoplasmic protein TBC1D3 interacts with the MT network and is responsible for regulating the stability and signaling of EGFR [51]. Moreover, EGFR kinase itself can interact with the cytoskeleton, cell-cell junctions and MT motor proteins to promote cell growth and adhesion [52]. With this in mind, we decided to evaluate the ability of the tested compounds, as MT disrupting agents, to alter the expression of EGFR and its downstream targets in the signaling pathway. Protein expression studies using the Western blot method were performed, and the results are presented in Fig. 6A, with the densitometric analyses in **Fig. S23.**

Data analysis showed that EGFR activation by phosphorylation of tyrosine at position 1068 was almost halved after incubation with TS3 on leukemia cells. A slight reduction in p-EGFR levels was also observed after incubation with TS1 and TS5. To detect more subtle changes in the level of phosphorylated EGFR (Tyr1068), we performed additional experiments using the Lumit Immunoassay, which may be more suitable for this purpose [53]. As depicted in Fig. 6B, the EGFR activation was significantly inhibited (almost 1.5-fold) after exposure to TS3 and TS5 derivatives, which was not so well illustrated by the Western blot technique. It appears that the observed inhibition of the EGFR receptor may result from disturbances in microtubule assembly dynamics. Kinase assays showed approximately 20–25% inhibition of EGFR activity by TS1, TS3, and TS5 derivatives (data shown in **Table S2**).

Other components of the signaling pathway activated by EGFR are Akt and PI3K. In particular, Akt is the main mediator of cellular responses regulating glucose metabolism, cell proliferation and survival, transcription, and cell migration. This means that this enzyme is at the crossroads of many important cellular signaling pathways, including EGFR, IGFR1, VEGFR, and FGFR. As mentioned above, co-regulation between PI3K/Akt signaling and MT behavior has been observed. It should be noted that PI3K and Akt, together with GSK3, may regulate MT stability and organization [54]. For example, disassembly of MTs switches off PI3K/Akt signaling by dephosphorylation and inactivation of Akt [55]. Importantly, a significant decrease in the level of activated p-Akt (Ser473) was observed in K562 cells after incubation with all the tested derivatives (Fig. 6A). The highest effect, an almost 7-fold reduction in expression, was observed for TS5 in K562 cells. For TS1 and TS3, an almost 3-fold reduction in p-Akt level was observed. Surprisingly, we did not observe significant changes in U-251 cells. One explanation for this effect may be the status of PTEN, which is an antagonist of PI3K activity and signal transduction to Akt. Loss of PTEN has been observed in U-251 cells, which may exacerbate the overactivation of the PI3K/Akt pathway and sustain its high level. Despite this, an interesting effect was observed with mTOR, the last element of the EGFR signaling pathway. The mTOR complex is mainly responsible for launching the process of cell survival, as well as protein synthesis. Literature data also show that PI3K/Akt inhibition may increase the apoptotic effect induced by MTAs, as a result of the inhibition of the mTOR function [56]. For U-251 cells, a nearly two-fold decrease in the expression of phosphorylated mTOR at position 2448 serine was recorded after treatment with TS derivatives (Fig. 6B).

The protein STAT5 can regulate the processes of cell invasion, survival and migration, and it can also interact with PI3K/Akt signaling in this regard. Importantly, the activation and phosphorylation of this protein is particularly evident in leukemia cells due to the excessive oncogenic activity of BCR-Abl kinase [57]. Our analysis revealed an almost 3-fold downregulation of p-STAT5 expression after treatment with the TS5 derivative. This effect may correlate with the high inhibition of Akt kinase activity, which leads to a therapeutic effect.

Lastly, the effect of sulfonic styrylquinazolines on RAS expression was evaluated. This protein, together with RAF-MEK-ERK-MAPK, is another key mediator of the response after EGFR activation. In the RAS signaling pathway, mainly ERK and MAPK proteins react with substrates to regulate cellular responses by increasing cell proliferation and differentiation, as well as suppressing apoptosis. Importantly, the Ras

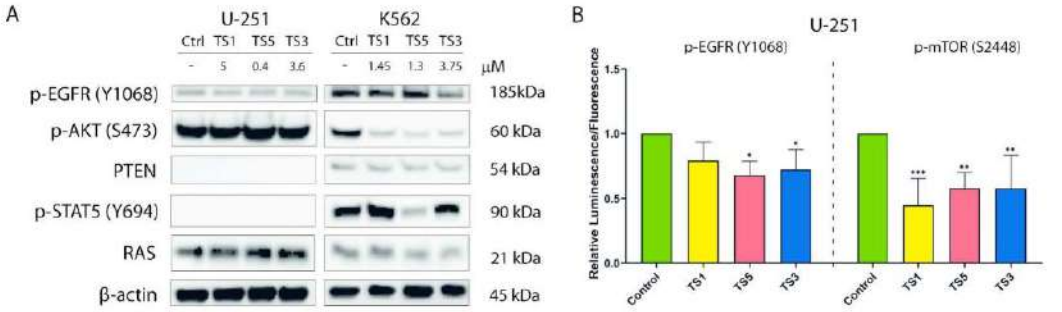

Fig. 6. Impact of the tested compounds on the expression of proteins related to the EGFR signaling pathway. Assessment of expression of EGFR and its downstream proteins on U-251, and K562 cells by Western blot. The immunoblots shown are representative of at least four independent experiments. The displayed blots were cropped, and the full-length blots are shown in Fig. S24 (A). Changes in p-EGFR (Y1068) and p-mTOR (S2448) proteins after treatment with TS1, TS3 and TS5 in U-251 cells (B). The presented protein luminescence values were first normalized to the cell count with fluorescence and then normalized to the luminescence of untreated control protein samples. Statistical significance compared to control was performed with one-way ANOVA with *post hoc* to Šidák's correction and presented on the charts as: * $p < 0.05$; ** $p < 0.01$; *** $p < 0.001$.

protein can interact with the p110 subunit of PI3K, mediating Akt activation [58]. An increase in RAS expression (almost 1.5-fold) was observed in the U-251 cells treated with the TS3 derivative, which also seemed to correlate with a slight upward fluctuation in Akt expression. In contrast, a decrease in RAS levels was observed in K562 cells, with the highest effect detected for TS3. Moreover, RAS can activate JNK/SAPK signaling, which is involved in the stress response and participates in the triggering of apoptosis. It has been shown that the effect of MTAs on the activation of this signaling cascade can lead to phosphorylation of the anti-apoptotic factor Bcl-2 [59]. It can therefore be assumed that, depending on the type of tumor and its proteomic profile, the RAS protein may play a dual role, either by inhibiting signal transduction through the PI3K/Akt/mTOR pathway or by enhancing the induction of apoptosis through JNK/SAPK signaling.

2.7. Cell death induction

Finally, the mode of cell death after exposure to the tested derivatives was determined. For this purpose, experiments were performed using a microcapillary flow cytometer and annexin V/7-ADD dual-cell staining, indicating the distribution of cells in the early and late apoptosis phases, as well as necrosis. It should be noted that annexin V is a specific protein that has a high affinity for phosphatidylserine. In undamaged cells, this phospholipid is located on the inner side of the plasma membrane and is therefore inaccessible to annexin V. However, one of the early events of apoptosis is the translocation of phosphatidylserine to the surface of the plasma membrane, which enables the interaction of the phospholipid with FITC-conjugated annexin V and the recording of a signal from damaged cells. Our analyses revealed that all of the tested compounds were able to induce apoptosis in U-251 and K562 cells. Graphs presenting detailed results are shown in Fig. 7. Also, representative histograms from one of the experiments with tables indicating the percentage of cells that were live, in early, or in late apoptosis are provided in Figs. S20 and S21. The highest number of cells in early and late apoptosis was recorded for TS5 in U-251 cells (almost 75% compared to 14.9% in the control). Similar values were observed for TS2 and TS4. In the case of K562 cells, the percentage of cells undergoing apoptosis was around 50% for the TS2, TS5, and TS6 derivatives.

Next, the influence of TS1, TS3 and TS5 derivatives on the expression

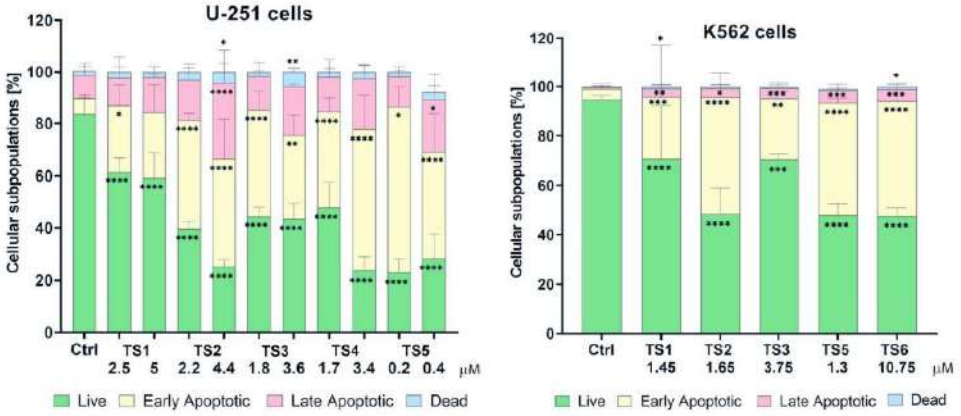

Fig. 7. Evaluation of apoptosis induction for U-251, and K562 cells after 48 h exposure to the tested compounds. Statistical significance compared to control was performed with one-way ANOVA and *post hoc* to Dunnett's correction from at least four independent experiments and presented on the charts as: * $p < 0.05$; ** $p < 0.01$; *** $p < 0.001$; **** $p < 0.0001$.

of proteins associated with apoptosis induction, such as caspase-9, PARP-1, and BID was evaluated. As shown in Fig. 8A, Western blot analyses confirmed that the tested compounds induce caspase-9 cleavage, which activates the executioner caspases that initiates apoptosis. The highest effects were registered for TS5 (almost 3.5-fold) in U-251 cells, and TS1 (almost 3-fold) in K562 cells. The last substrate that is proteolytically cleaved by the executioner caspases is the PARP-1 protein. It is responsible for DNA repair and transcriptional regulation, which is halted by the caspases, which is considered a characteristic feature of apoptosis. A significant increase in the expression of cleaved PARP-1 was observed for TS1 and TS3 in both U-251 and K562 cells. Moreover, the BID protein, which has a pro-apoptotic role in cells, was upregulated in U-251 and K562 cells. As with PARP, a significant increase in BID expression was observed after treatment with TS1 and TS3.

Finally, we decided to check the effect of the tested compounds on the expression of two genes, *calreticulin* and *LC3* related to autophagy and ER stress mechanisms (Fig. 8B). As indicated in the literature, both benzenesulfonates and sulfonamides, as well as other antimitotic agents that disrupt MT dynamics and organization, can induce autophagy [30,60,61]. Moreover, a dual mode of cell death has been proven for lexibulin, which can induce apoptosis and autophagy through the induction of ER stress and increased ROS concentration [62]. On the other hand, several reports for MTAs indicate that suppression of autophagy can enhance the apoptotic effect [63,64]. It is worth noting that many proteins involved in the response to apoptosis, autophagy, and oxidative stress, such as JNK and MAPK, are regulated by MTs [65]. These cytoskeleton elements can also be critical for the regulation of ER morphology, dynamics, and transport to the cell periphery [66]. Yang et al. have proven that calreticulin induced during ER stress can increase the production of autophagosomes through interaction with LC3 and intensify the induction of autophagy [67]. Our qRT-PCR analyses did not show any significant changes in the level of *calreticulin* expression on glioblastoma cells (Fig. 8B). In contrast to leukemia cells, in which an almost 2-fold increase in the expression of this gene was recorded after treatment with the TS3 derivative. Moreover, the other two derivatives caused a significant increase of almost 1.5-fold in K562 cells. This effect correlated with an over 1.5-fold increase in *LC3* gene expression in the leukemia cell line. Interestingly, in the case of the TS3 compound, no significant increase was observed in K562 cells. In contrast, a decrease in *LC3* expression was observed in U-251 cells after exposure to TS3. These results suggest that autophagy-related pathways may contribute to the response in K562 cells with p53 protein deficiency. Further protein-level analyses of autophagic markers are required to substantiate this mechanism. In contrast, apoptosis is the preferred type of cell death in GBM cells, which correlates with the observed augmented effect in the annexin V assay. On the other hand, the different isotypes occurred in GBM cells may contribute to more resistance to ER stress and autophagy induction. Like, the downregulation of the *TUBB3* gene (Fig. 5B), which has been proven to be an LC3-binding partner [68].

2.8. ADME properties

Styrylquinazolines, despite their widespread use in drug design and extensive biological activity attributed to the quinazoline scaffold, pose a challenge from an ADME perspective due to their generally problematic solubility and overall bioavailability [69–71]. Many quinazoline agents targeting various tyrosine kinases are characterized by limited bioavailability, undergo intensive metabolism, and their effect is hindered by the fact that they are substrates of the efflux transporter P-glycoprotein [71]. These reasons led to an attempt to predict at least approximate ADME properties in order to evaluate the possible behavior of our compounds in more advanced systems.

The gold standard in the design of drug-like molecules is the fulfillment of the criteria of the so-called Lipinski Rule of Five (Ro5), which contains the limits of specific molecular descriptors (MW <500, logP <5, HBD <5, HBA <10) determined on the basis of experimentally and statistically obtained results so that a compound meeting this recommendation has a higher chance of becoming a drug [72]. However, a good drug-like score does not make a molecule a drug, and *vice versa* [73,74]. It is clear that ADMET-friendly properties, such as lipophilicity, polar surface area, *etc.*, are important in the context of specific ligand-receptor interactions. The predicted properties affecting ADME (also other parameters, not only Ro5) of active compounds TS1–TS6 are shown in Table 2. It also presents the physicochemical properties and ADME profile of drugs that have been approved for the treatment of GBM (temozolomide, lomustine) or are in clinical trials (quinazoline tyrosine kinase inhibitors: tandutinib, cediranib, vandetanib) for the therapy of GBM. Additionally, values for lorlatinib, the 3rd generation non-quinazoline tyrosine kinase inhibitor that is able to cross the BBB, have been added to Table 2.

All the compounds TS1–TS6 meet the recommended Ro5 molecular weight value, with the exception of TS4 and TS6, the other derivatives have logP >5 (range 5.1–5.23). None of the compounds are H-bond donors (HBD), while TS1 and TS5 have six H-bond acceptors (HBA) and TS2–4 seven H-bond acceptors and TS6 eight H-bond acceptors, so the HBA meets the Ro5. Similarly, the number of rotational bonds (RB) is six for TS1 and TS5, while being seven for TS2–4 and eight for TS6. The topological polar surface area (TPSA) has been recognized as a good indicator of drug absorption in the intestine (TPSA <120 Å^2) and BBB penetration (TPSA <60 Å^2) [75,76]. The TPSA values of the discussed compounds ranged from 86.76 to 95.99 Å^2 (except for the less effective TS4 with TPSA = 110 Å^2), which suggested that the compounds should

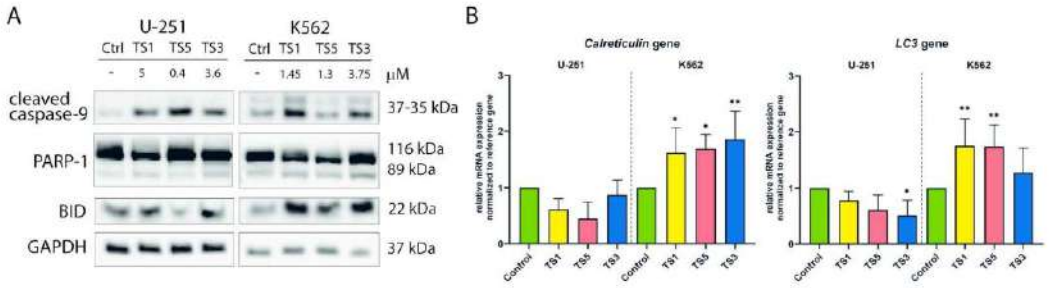

Fig. 8. Impact of tested compounds on the expression of proteins and genes related to cell death induction in U-251 and K562 cells. Assessment of expression of apoptotic proteins (cleaved caspase-9, PARP-1, and BID) using the Western blot technique. The immunoblots shown are representative of at least four independent experiments. The displayed blots were cropped, and the full-length blots are shown in **Fig. S24** (A). Determination of expression levels of autophagic genes (*calreticulin* and *LC3*) using qRT-PCR (B). The gene expression values were normalized to a reference gene and compared to untreated cells ($n = 7$). Statistical significance compared to control was performed with one-way ANOVA with *post hoc* to Šidák's correction and presented on the charts as:* $p < 0.05$; ** $p < 0.01$.

Table 2
Values of parameters characterizing physicochemical properties and ADME profiling of active compounds TS1–TS6 and selected medicines predicted using the commercially available program ACD/Percepta ver. 2025.

Comp.	MW	logP	HBD	HBA	RB	TPSA [Å²]	Parachor [cm³]	k_a [min⁻¹]	%PPB	logBB	logPS	Brain plasma equilibrium rate
TS1	466.94	5.28	0	6	6	86.76	947.28	0.049	99.73	−0.38	−1.1	−3.3
TS2	482.94	5.11	0	7	7	95.99	967.62	0.049	99.71	−0.38	−1.1	−3.3
TS3	482.94	5.09	0	7	7	95.99	967.62	0.049	99.64	−0.30	−1.1	−3.3
TS4	477.92	4.13	0	7	7	110.55	956.66	0.049	99.04	0.05	−1.2	−2.9
TS5	466.94	5.28	0	6	6	86.76	947.28	0.049	99.73	−0.38	−1.1	−3.3
TS6	492.55	4.45	0	8	8	105.22	1027.37	0.049	99.72	−0.64	−1.2	−3.1
Temozolomide	194.15	−0.98	2	8	1	105.94	314.93	0.007	17.80	−0.06	−3.5	−3.5
Lomustine	233.70	2.52	1	5	4	61.77	460.87	0.060	59.46	0.49	−1.5	−2.3
Tandutinib	562.72	3.99	1	10	10	92.29	1261.72	0.043	88.42	0.66	−2.1	−3.7
Cediranib	450.51	4.15	1	7	8	72.50	960.18	0.048	90.35	0.65	−1.8	−3.4
Vandetanib	475.36	4.64	1	6	6	59.51	912.57	0.049	97.29	0.33	−1.6	−3.4
Lorlatinib	406.42	1.38	2	8	1	110.06	770.54	0.044	76.59	−0.27	−2.4	−2.8

molecular weight (MW), lipophilicity (log P), number of H-bond donors (HBD), number of H-bond acceptors (HBA), number of rotatable bonds (RB), topological polar surface area (TPSA), absorption rate in human jejunum at pH 6.5 (k_a), drug binding to plasma proteins (%PPB), permeability across BBB (logBB – concentration of drug in brain divided by concentration in blood), rate of brain penetration (logPS - permeability surface-area product).

have good intestinal absorption, but the derivatives might not show adequate BBB penetration as the TPSA values were higher than 60 Å². Sufficient intestinal absorption was also confirmed by the rate of absorption in the human jejunum at pH 6.5 ($k_a = 0.049\ min^{-1}$), which was the same for all the molecules. In addition, the prediction indicated that all the compounds should be significantly (approx. 99%) bound to plasma proteins, mainly alpha(1)-acid glycoprotein and albumin.

Although the TS1–TS5 compounds were not predicted to be P-glycoprotein substrates, literature data [71], suggest that quinazoline-based scaffolds are often recognized by this efflux transporter, warranting cautious interpretation. LogBB values for TS1–3, TS5, TS6 ranged from −0.64 to −0.30 (logBB ≤ −0.3 is for impermeable drugs [77]), indicating that the compounds are likely to be CNS inactive due to low brain penetration, as already indicated by the magnitude of the TPSA values. The exception is TS4 with a logBB of 0.05.

Standard drugs used for GBM treatment temozolomide and lomustine are well absorbed, weakly or moderately bound to proteins, but according to modeling using ACD/Percepta 2025 temozolomide is CNS non-penetrating (total CNS score − 3.55) while lomustine is CNS well-penetrating (total CNS score − 1.85). All three clinically evaluated quinazolines for GBM treatment are well absorbed, tandutinib is weakly bound to proteins, while cediranib and vandetanib are strongly bound (similar to our studied compounds). In terms of BBB penetrability, tandutinib and vandetanib are CNS-poorly penetrative (total CNS score − 3.04 or − 3.12, respectively), while cediranib is CNS-penetrating (total CNC score − 2.79). Lorlanitib has specific values, see Table 2, but has a completely different (and extremely interesting) structure from quinazolines - its backbone is a 12-membered macrolactam. From the point of view of *in silico* physicochemical and ADME profiling, this is an almost perfect molecule.

Physicochemical profiling suggests that compounds TS1–TS6 generally show a good match with Ro5. In summary, preliminary ADME profiling predicts sufficient absorption after oral administration. However, as can be seen from the data presented in Table 2, the ability of the active derivatives to penetrate brain tissue appears to be limited without further structural modifications. It is expected, according to ACD/Percepta 2025, that only TS4 will have sufficient penetration for activity in the CNS. Therefore, further studies will be essential to substantiate these predictions [78,79].

Unfortunately, the findings from this meta-analysis are consistent with other published works [80], where the development of effective therapies based on quinazoline tyrosine kinase inhibitors for the treatment of GBM encounters low permeability of these agents across the BBB. General strategies for improving the delivery of anticancer drugs across the BBB for the treatment of GBM have been presented, for example, in reviews [81–83]. The chemical structure can be modified to prepare new generations of tyrosine kinase inhibitors, such as the aforementioned lorlatinib [84] or cediranib [85]. In the case of the discussed sulfonated styrylquinazolines, it would be possible to modify TS5 by replacing 4-methylbenzene-1-sulfonate with 3-cyanobenzene-1-sulfonate. This changes the overall CNC score from −3.68 to −2.89, which causes easy BBB permeability. In general, according to the ACD/Percepta 2025 prediction, the introduction of an N-heterocyclic group onto the sulfonate increases penetrability across the BBB. The penetrability of tyrosine kinase inhibitors across the BBB can be increased also by galenic modifications, as described, for example, by Jampilek and Kralova [86], *i.e.* by encapsulation into lipid-based nanoparticles, such as nanoemulsions, liposomes, solid lipid nanoparticles or nanostructured lipid carriers. Furthermore, surface-modified formulations with so-called Trojan horses, various molecules recognized by influx transport systems or, conversely, efflux inhibitors, can be applied. Physically-assisted methods can also be used to disrupt the BBB [87,88].

2.9. *In vivo studies in the zebrafish model*

To further explore the therapeutic potential of TS compounds, we employed the *Danio rerio* experimental model. Acute toxicity was first assessed following OECD Guideline 236 *Fish Embryo Acute Toxicity*, revealing LC_{50} values of 2.913 μM (TS1), 3.538 μM (TS3), 3.614 μM (TS5) and 10.72 μM (Osimertinib), indicating a comparable toxicity profile among TS derivatives and a substantially lower toxicity for Osimertinib, a known anticancer drug (Fig. 9). Moreover, heart function was evaluated by quantifying heart rate (beats per minute) in zebrafish larvae following 96 h exposure to increasing concentrations of TS1 (Fig. 9 **B**), TS3 (Fig. 9C) and TS5 (Fig. 9 **D**). All three compounds demonstrated a dose-dependent cardiotoxic potential, with a noticeable reduction in heart rate beginning at 3 μM. Statistical significance was observed for: TS1 at 3 μM ($p < 0.05$), 4 μM ($p < 0.05$); TS3 at 3 μM ($p < 0.05$), 4 μM ($p < 0.01$), 5 μM ($p < 0.005$) and TS5 at 3 μM ($p < 0.05$), 4 μM ($p < 0.005$), 5 μM ($p < 0.005$).

To better characterize and visualize the toxicity profiles of the TS compounds, representative images of zebrafish larvae exposed for 96 h to increasing concentrations (1–5 μM) of TS1, TS3 and TS5 compounds are presented on Fig. 10. Untreated embryos maintained in E3 medium served as controls and displayed normal morphology, including straight body axis, transparent abdominal region, and absence of cardiac or developmental abnormalities. Progressive morphological defects were observed upon exposure to TS compounds. Three major phenotypic categories are indicated on the images: scoliosis (body-axis curvature) which is bending or lateral deviation of the spine, indicative of neurotoxic or musculoskeletal developmental impairment; pericardial edema which is subtle to moderate swelling or loss of transparency around the

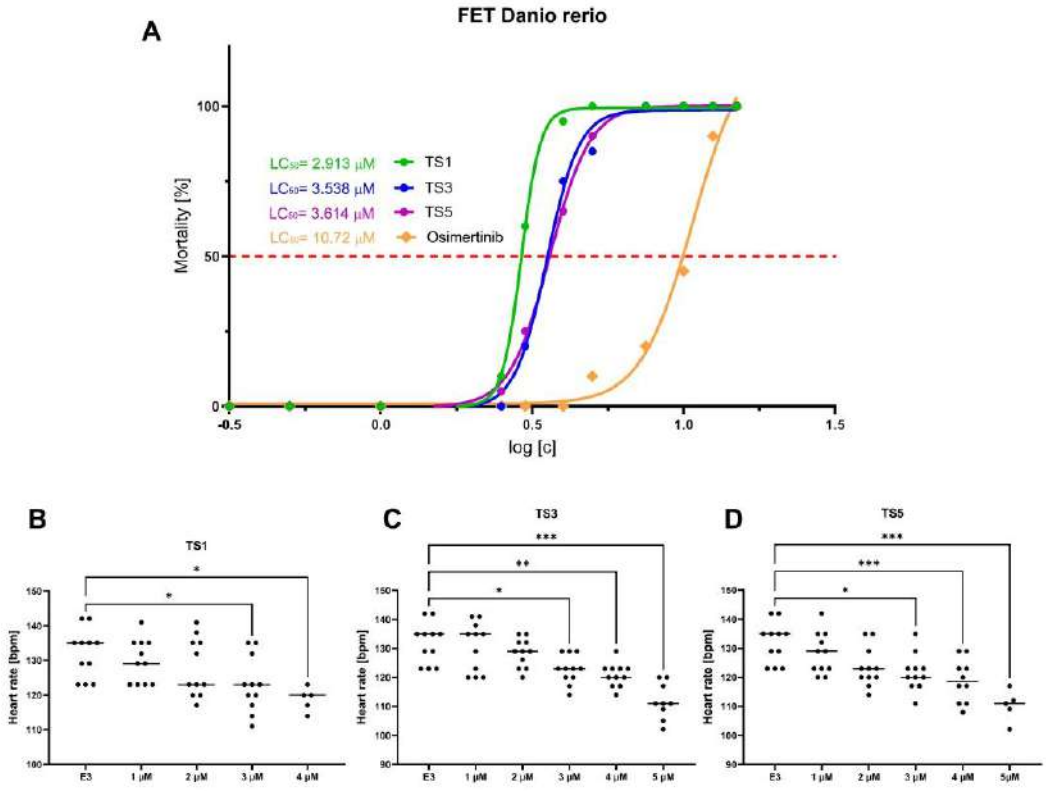

Fig. 9. Toxicity of TS1, TS3, TS5 and Osimertinib showed as (A) mortality rate [%] of zebrafish embryos (*Danio rerio*) exposed to various chemical compounds. Calculated values of LC_{50} for TS1, TS3, TS5 and Osimertinib: 2.913, 3.538, 3.614 and 10.72 µM, respectively. Cardiotoxicity of of (B) TS1, (C) TS3, (D) TS5 showed as heart rate per minute; one-way ANOVA, Tukey *post hoc*: *p < 0.05, **p < 0.01, ***p < 0.005.

cardiac region, consistent with early cardiotoxicity; abdominal opacity observed as cloudiness, yolk retention or swelling in the abdominal cavity, suggestive of disrupted metabolism, delayed yolk resorption or potential hepato-renal toxicity. The severity and frequency of these malformations increased in a concentration-dependent manner, with the highest prevalence occurring at 3–5 µM for all tested TS compounds. These phenotypes support the LC_{50} values obtained in zebrafish assays and provide visual confirmation of developmental and organ-specific toxicity associated with TS compound exposure.

Based on the FET results, cardiotoxicity measurements, and detailed phenotypic analysis of developmental malformations, sublethal concentrations (0.5, 1, and 2 µM) were selected for efficacy testing in xenografted zebrafish. The results aligned well with previous *in vitro* data, where TS5 demonstrated the strongest antiproliferative activity (IC_{50} = 0.21 µM) compared to TS1 (2.53 µM), TS3 (1.80 µM) and Osimertinib (20.13 µM). To assess the therapeutic potential of these compounds, 2-dpf zebrafish embryos were xenografted with human glioblastoma U-251 cells into yolk sac and subsequently exposed to TS compounds at concentrations of 0.5, 1, and 2 µM for 72 h. Osimertinib was used as a reference at concentrations of 5, 7.5 and 10 µM. The results were consistent with prior *in vitro* findings: TS5 demonstrated the highest antitumor activity, with the 2 µM dose showing the most pronounced therapeutic effect (Fig. 11), comparable to the results of Osimertinib at the dose of 10 µM. This suggests TS5 as a promising candidate for further preclinical evaluation in mouse models.

3. Conclusion

Our previous research focused on highly active benzenesulfonates, which are usually used as intermediates in synthesis. For the first time, we discovered the strong potential of these compounds to inhibit the cell cycle in the G2/M phase, to a greater extent than paclitaxel. Encouraged by these results, we synthesized and examined in depth a novel small series of sulfonic styrylquinazolines that had a chlorine substituent at position 7 of the quinazoline ring (TS1-TS4), chlorine at position 6 (TS5), and were unsubstituted (TS6-TS8). The biological assays revealed high antiproliferative activity for the TS5 derivative with chlorine in position 6 against GBM and leukemia cells (IC_{50} ranged from 0.17 to 0.26 µM). In turn, the 7-chloroquinazolines (TS1-TS3) exhibited a high activity profile for leukemia cells (IC_{50} ranged from 0.29 to 0.75 µM), while being characterized by lower levels of activity for GBM cells. Importantly, the tested compounds showed a lack of hepatoxicity, as well as high selectivity with respect to normal astrocyte cells. Further in-depth molecular studies uncovered the multifaceted mechanism of action of the most active compounds, TS1, TS3, and TS5, focusing on the disruption of MT assembly and disassembly dynamics. Studies were performed on cell cycle inhibition, tubulin polymerization in cells, and the effect of the compounds on the expression of genes and proteins

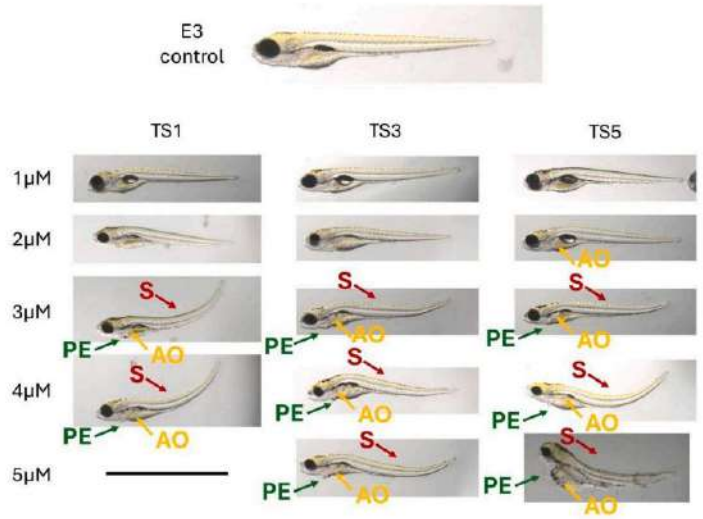

Fig. 10. Phenotypic documentation of zebrafish larvae after 96 h treatment with TS compounds. Representative images of zebrafish larvae exposed to increasing concentrations (1–5 μM) of TS1, TS3 and TS5 compared with the untreated E3 control group. Phenotypic abnormalities are indicated with colored arrows: S (red) – scoliosis; PE (green) – pericardial edema; AO (yellow) – abdominal opacity. (For interpretation of the references to color in this figure legend, the reader is referred to the web version of this article.)

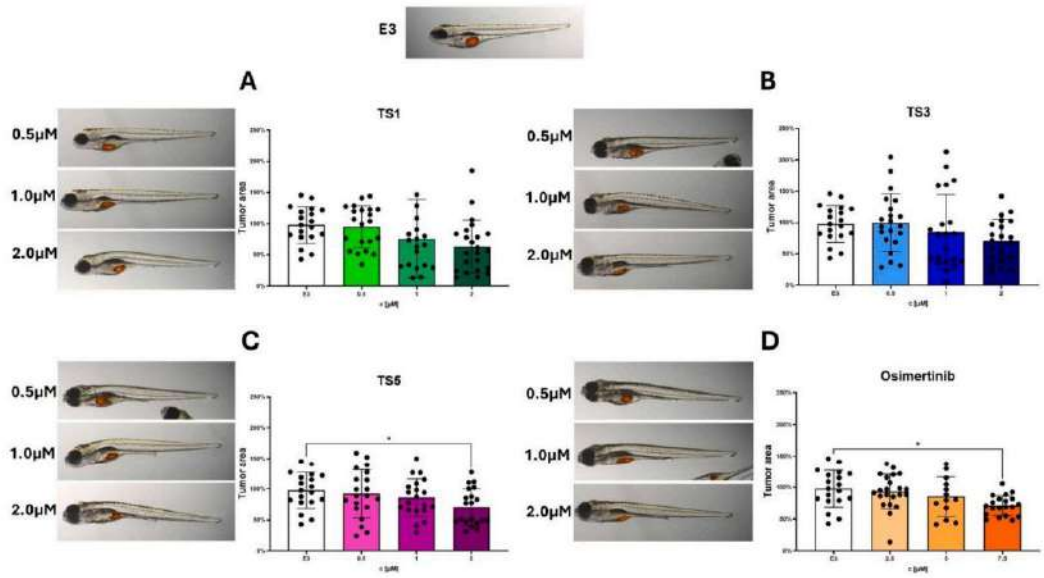

Fig. 11. Anti-tumor effectiveness of TS1, TS3 and TS5 in *Danio rerio* xenograft model evaluated as a percentage of tumor area measurements for the U-251 xenograft after 72 h of incubation with tested compounds: (A) TS1, (B) TS3 (C) TS5 and (D) Osimertinib at three different concentrations: 0.5, 1 and 2 μM, compared to 100% for the untreated control group (E3). One-way ANOVA; $^{*}p < 0.05$.

associated with the cell cycle and the EGFR/mTOR and Ras pathways. The results indicated that the tested derivatives, in particular TS5, caused a remarkable cell cycle arrest in the G2/M phase in both U-251 and K562 cells. Significant changes in tubulin status were also observed

in GBM cells. In addition, the tubulin polymerization test confirmed a similar enhancement of assembly as with paclitaxel. Cellular experiments showed that the tested derivatives caused upregulation of Aurora A, cyclin B, and *GADD45*, which correlated with cell cycle arrest. Importantly, for the first time in this class of compounds, inhibition of the EGFR/Akt/mTOR and Ras signaling pathways, which are involved in cell growth, proliferation, and survival, was discovered. Finally, the tested derivatives induced cell death through apoptosis in GBM cells and through a coexisting mechanism of apoptosis and autophagy in K562 cells. Based on ADME profiling, it can be assumed that the compounds studied have suitable physicochemical parameters for sufficient bioavailability. *In vivo* toxicity studies on zebrafish showed a similar toxicity profile for TS compounds as in *in vitro* studies (in the range of 2.9–3.6 μM). Meanwhile, therapeutic efficacy studies in zebrafish with xenografted U-251 tumors showed that TS5 at a dose of 2 μM was more effective than osimertinib at a dose of 10 μM. Therefore, TS5 appears to be a promising candidate for further preclinical evaluation.

4. Experimental section

The Fourier transform nuclear magnetic resonance spectra of the sample solutions were obtained using a Bruker Avance III 500 spectrometer (500 MHz for ^{1}H and 126 MHz for ^{13}C), and the chemical shifts are reported in δ units (parts per million) relative to tetramethylsilane, the residual solvent peaks being used as the reference. The NMR samples were prepared in concentrations in the range 5–10 mM. The high-resolution mass spectra were measured using an electrospray single-quad Agilent Infinity Lab LC/MSDXT mass spectrometer, equipped with an Agilent 1260 Infinity II HPLC system (Agilent Technologies). The chromatographic separations were performed on a Teledyne ISCO Combiflash Rf150+ system.

4.1. Synthesis

A novel method was devised for synthesizing the sulfone derivatives that are the focus of our research (see Scheme 1). Key features of this method are its high throughput and the simplicity with which pure substances can be isolated. A typical application involved preparing a suspension of 2-(*E*)-styrylquinazolin-4(*3H*)-one in dichloromethane (0.1 mmol in 5 mL), initiating stirring, and adding 100 μL of DIPEA, 0.2 mmol of sulfonyl chloride, and DMAP (6.0 mg, 0.05 mmol). The mixture was left in the dark. Over time, depending on the substrates' nature, the system homogenized. 25 mL of anhydrous 2-propanol was then added. The remaining sulfonyl chloride is converted into the corresponding propyl ester. The low solubility of the resulting product in 2-propanol leads to its precipitation from the reaction mixture. Filtration and washing with 2-propanol on the filter were sufficient to achieve 98% purity.

4.1.1. TS1: 7-Chloro-2-[(E)-2-(2-methoxyphenyl)ethenyl]quinazolin-4-yl 3-methylbenzene-1-sulfonate

^{1}H NMR (500 MHz, CD_2Cl_2) δ 8.28 (d, *J* = 16.2 Hz, 1H), 8.18–8.13 (m, 1H), 8.12 (dd, *J* = 8.9, 0.6 Hz, 1H), 8.10–8.07 (m, 1H), 7.95 (dd, *J* = 2.1, 0.7 Hz, 1H), 7.70 (dd, *J* = 7.6, 1.8 Hz, 1H), 7.58 (dd, *J* = 8.7, 2.0 Hz, 1H), 7.56–7.52 (m, 2H), 7.42 (ddd, *J* = 8.2, 7.4, 1.7 Hz, 1H), 7.26 (d, *J* = 16.0 Hz, 1H), 7.09–7.03 (m, 2H), 4.04 (s, 3H), 2.44 (s, 3H); ^{13}C NMR (126 MHz, CD_2Cl_2) δ 161.50, 161.38, 158.01, 153.88, 141.03, 139.82, 136.51, 135.52, 135.34, 130.85, 129.23, 128.93, 128.40, 127.99, 126.97, 126.97, 126.41, 124.79, 124.52, 120.78, 113.09, 111.18, 55.59, 20.94; MS (ESI) calcd for $C_{24}H_{19}ClN_2O_4S$ $[M + H]^+$ 467.08; found 467.2;

4.1.2. TS2: 7-Chloro-2-[(E)-2-(2-methoxyphenyl)phenylethenyl] quinazolin-4-yl 3-methoxybenzene-1-sulfonate

^{1}H NMR (500 MHz, CD_2Cl_2) δ 8.24 (d, *J* = 16.0 Hz, 1H), 8.12 (d, *J* = 8.8 Hz, 1H), 7.96 (d, *J* = 2.0 Hz, 1H), 7.93 (ddd, *J* = 7.8, 1.8, 0.9 Hz, 1H), 7.73 (dd, *J* = 2.6, 1.7 Hz, 1H), 7.69 (dd, *J* = 7.7, 1.7 Hz, 1H), 7.61–7.55 (m, 2H), 7.41 (ddd, *J* = 8.2, 7.4, 1.7 Hz, 1H), 7.28 (d, *J* = 16.0 Hz, 1H), 7.27 (ddd, *J* = 8.4, 2.6, 1.0 Hz, 1H), 7.06 (t, *J* = 7.5 Hz, 2H), 7.04 (d, *J* = 8.4 Hz, 1H), 4.03 (s, 3H), 3.85 (s, 3H); ^{13}C NMR (126 MHz, CD_2Cl_2) δ 161.55, 161.38, 159.99, 158.09, 153.93, 141.07, 137.78, 135.56, 130.84, 130.17, 128.43, 128.25, 127.06, 126.98, 124.78, 124.47, 121.39, 121.07, 120.74, 113.37, 113.14, 111.15, 55.79, 55.56; MS (ESI) calcd for $C_{24}H_{18}N_2O_5S$ $[M + H]^+$ 483.08; 483.2;

4.1.3. TS3: 7-Chloro-2-[(E)-2-(2-methoxyphenyl)phenylethenyl] quinazolin-4-yl 4-methoxybenzene-1-sulfonate

^{1}H NMR (500 MHz, CD_2Cl_2) δ 8.32 (d, *J* = 16.0 Hz, 1H), 8.29–8.23 (m, 2H), 8.12 (d, *J* = 8.8 Hz, 1H), 7.94 (d, *J* = 2.0 Hz, 1H), 7.72 (dd, *J* = 7.6, 1.7 Hz, 1H), 7.57 (dd, *J* = 8.7, 2.0 Hz, 1H), 7.42 (ddd, *J* = 8.1, 7.4, 1.7 Hz, 1H), 7.26 (d, *J* = 16.0 Hz, 1H), 7.14–7.09 (m, 2H), 7.09–7.04 (m, 2H), 4.05 (s, 3H), 3.88 (s, 3H); ^{13}C NMR (126 MHz, CD_2Cl_2) δ 161.51, 161.40, 158.04, 153.82, 146.30, 140.98, 135.27, 133.59, 130.85, 129.75, 129.75, 129.27, 129.27, 128.36, 127.91, 126.94, 126.92, 124.79, 124.51, 120.80, 113.05, 111.21, 55.65, 21.54; MS (ESI) calcd for $C_{24}H_{18}N_2O_5S$ $[M + H]^+$ 483.08; found 483.2;

4.1.4. TS4: 7-Chloro-2-[(E)-2-(2-methoxyphenyl)phenylethenyl] quinazolin-4-yl 3-cyanobenzene-1-sulfonate

^{1}H NMR (500 MHz, CD_2Cl_2) δ 8.60 (td, *J* = 1.8, 0.6 Hz, 1H), 8.58 (ddd, *J* = 8.0, 1.9, 1.2 Hz, 1H), 8.24 (d, *J* = 16.1 Hz, 1H), 8.13 (dd, *J* = 8.8, 0.6 Hz, 1H), 8.01 (ddd, *J* = 7.8, 1.6, 1.2 Hz, 1H), 7.98 (dd, *J* = 2.0, 0.5 Hz, 1H), 7.81 (td, *J* = 7.9, 0.7 Hz, 1H), 7.73 (dd, *J* = 7.6, 1.7 Hz, 1H), 7.61 (dd, *J* = 8.8, 2.0 Hz, 1H), 7.43 (ddd, *J* = 8.2, 7.4, 1.7 Hz, 1H), 7.24 (d, *J* = 16.1 Hz, 1H), 7.07 (t, *J* = 7.5 Hz, 1H), 7.06 (d, *J* = 8.3 Hz, 1H), 4.05 (s, 3H); ^{13}C NMR (126 MHz, CD_2Cl_2) δ 161.29, 161.18, 158.00, 153.99, 141.43, 138.37, 137.76, 135.31, 133.20, 132.68, 131.06, 130.27, 128.70, 127.77, 127.07, 126.40, 124.59, 124.23, 120.82,

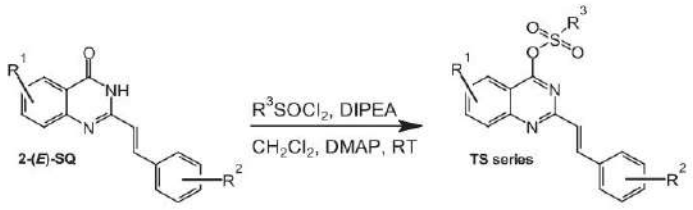

Scheme 1. The general chemical synthesis procedure of the target molecules. R^1: 6-H, 6-Cl, 7-H, 7-Cl; R^2: 2-OCH_3, 3,4,5-OCH_3, 1,3-benzodioxole, 6-Br-1,3-benzodioxole; R^3: various substituents.

116.65, 113.95, 112.72, 111.23, 55.69; MS (ESI) calcd for $C_{24}H_{16}ClN_3O_4S$ $[M+H]^+$ 478.06; found 478.2;

4.1.5. TS5: 6-Chloro-2-[(E)-2-(2-methoxyphenyl)phenylethenyl] quinazolin-4-yl 4-methylbenzene-1-sulfonate

^{1}H NMR (500 MHz, $(CD_3)_2CO$) δ 8.02 (d, J = 16.1 Hz, 1H), 7.98–7.94 (m, 2H), 7.84 (dd, J = 2.3, 0.7 Hz, 1H), 7.71 (dd, J = 9.0, 2.2 Hz, 1H), 7.67 (dd, J = 8.9, 0.7 Hz, 1H), 7.48 (dd, J = 7.7, 1.8 Hz, 1H), 7.33–7.25 (m, 2H) 7.14 (ddd, J = 8.3, 7.3, 1.7 Hz, 1H), 6.99 (d, J = 16.1 Hz, 1H), 6.87 (dd, J = 8.4, 1.0 Hz, 1H), 6.80–6.75 (m, 1H), 3.79 (s, 3H), 2.17 (s, 3H); ^{13}C NMR (126 MHz, CD_2Cl_2) δ 160.59, 160.58, 158.00, 151.68, 146.35, 135.59, 134.90, 133.53, 133.01, 130.77, 129.77, 129.51, 129.30, 127.84, 126.91, 124.56, 122.38, 120.79, 115.15, 111.21, 55.64, 21.55; MS (ESI) calcd for $C_{24}H_{19}ClN_2O_4S$ $[M+H]^+$ 467.08; found 467.2;

4.1.6. TS6: 7-Chloro-2-[(E)-2-(3,4,5-trimethoxyphenyl)phenylethenyl] quinazolin-4-yl 4-methylbenzene-1-sulfonate

^{1}H NMR (500 MHz, $(CD_3)_2CO$) δ 8.22–8.19 (m, 2H), 8.18 (ddd, J = 8.2, 1.5, 0.7 Hz, 1H), 8.05 (ddd, J = 8.4, 7.0, 1.5 Hz, 1H), 7.98 (ddd, J = 8.4, 0.7, 0.7 Hz, 1H), 7.76 (ddd, J = 8.1, 6.9, 1.1 Hz, 1H), 7.72 (d, J = 15.9 Hz, 1H), 7.67–7.59 (m, 2H), 7.23 (d, J = 15.8 Hz, 1H), 7.08 (s, 1H), 4.00 (s, 6H), 3.81 (s, 3H), 2.51 (s, 3H); ^{13}C NMR (126 MHz, CD_2Cl_2) δ 161.38, 160.57, 153.26, 151.80, 146.11, 143.61, 134.74, 133.90, 133.73, 129.68, 129.68129.23, 129.23, 127.62, 127.24, 124.43, 123.26, 116.20, 114.44, 110.24, 97.24, 56.49, 56.45, 56.00, 25.14, 21.53; MS (ESI) calcd for $C_{26}H_{24}N_2O_6S$ $[M+H]^+$ 493.14; found 493.4;

4.1.7. TS7: 2-[(E)-2-(2H-1,3-benzodioxol-4-yl)ethenyl]quinazolin-4-yl 4-methylbenzene-1-sulfonate

^{1}H NMR (500 MHz, $(CD_3)_2SO$) δ 8.15 (dd, J = 8.0, 1.5 Hz, 1H), 8.03 (d, J = 16.2 Hz, 1H), 7.88 (ddd, J = 8.5, 7.1, 1.6 Hz, 1H), 7.72 (dd, J = 8.3, 1.1 Hz, 1H), 7.56 (ddd, J = 8.2, 7.2, 1.1 Hz, 1H), 7.53–7.47 (m, 2H), 7.18 (d, J = 16.2 Hz, 1H), 7.14–7.10 (m, 2H), 7.09 (dd, J = 8.1, 1.1 Hz, 1H), 7.02 (dd, J = 7.7, 1.2 Hz, 1H), 6.96 (t, J = 7.8 Hz, 1H), 6.23 (s, 2H), 2.29 (s, 3H); ^{13}C NMR (126 MHz, CD_2Cl_2) δ 161.64, 159.79, 152.97, 148.02, 146.21, 146.13, 135.01, 133.99, 133.61, 129.84, 129.84129.18, 129.01, 129.01127.87, 127.74, 123.35, 121.82, 121.46, 118.70, 114.83, 108.90, 101.56, 21.56; MS (ESI) calcd for $C_{24}H_{18}N_2O_5S$ $[M+H]^+$ 447.10; found 447.20;

4.1.8. TS8: 2-[(E)-2-(6-bromo-2H-1,3-benzodioxol-5-yl)ethenyl] quinazolin-4-yl 4-methylbenzene-1-sulfonate

^{1}H NMR (500 MHz, CD_2Cl_2) δ 8.25 (d, J = 15.8 Hz, 1H), 8.23–8.20 (m, 2H), 8.18 (ddd, J = 8.2, 1.3, 0.8 Hz, 2H), 7.99–7.89 (m, 2H), 7.66 (ddd, J = 8.2, 6.3, 1.8 Hz, 1H), 7.47–7.43 (m, 2H), 7.31 (s, 1H), 7.17 (s, 1H), 7.07 (d, J = 15.7 Hz, 1H), 6.10 (s, 2H), 2.46 (s, 3H); ^{13}C NMR (126 MHz, CD_2Cl_2) δ 161.56, 159.53, 153.14, 149.50, 148.15, 146.16, 137.20, 134.91, 133.56, 129.84, 129.84129.13, 129.05, 129.05, 128.16, 127.87, 127.83, 123.32, 116.82, 114.80, 112.85, 106.29, 102.47, 21.45; MS (ESI) calcd for $C_{24}H_{17}BrN_2O_5S$ $[M+H]^+$ 525.01, 527.01; found 525.2, 527.2;

4.2. Cell culture

The human glioblastoma cell line U87MG was purchased from ATCC. The glioblastoma cell line U-251 was kindly provided by Prof. G. Kramer-Marek from the Institute of Cancer Research in London, United Kingdom. The human suspension chronic myelogenous leukemia cell line K562 and the human hepatoma cell line HepG2 were bought from Sigma-Aldrich. The normal human astrocytes NHA were purchased from Gibco. All of the adherent cancer cell lines were cultured in Dulbecco's modified Eagle's medium (DMEM) that had been supplemented with 10% heat-inactivated fetal bovine serum – FBS (all from Merck). The suspension cell line (K562) was cultured in RPMI-1640 medium (Merck), which contained 10% heat-inactivated FBS. The NHA cells were cultured in astrocyte medium with 10% FBS, N-2 supplement and EGF (20 ng/mL, Gibco). Each complete medium contained a mixture of two antibiotics - penicillin and streptomycin (1% v/v; Gibco). The cell lines were cultured at 37 °C with 5% CO_2 humidified atmosphere.

4.3. Cytotoxicity studies

The cells were seeded in 96-well plates (Nunc) at a density of 5,000 cells per well (U87MG, U-251, K562, and HepG2) or 4,000 cells per well (NHA) and incubated under standard conditions at 37 °C for 24 h. Assays were carried out following a 72 h incubation with the various concentrations of the tested compounds. DMEM without phenol red with CellTiter 96®AQueous One Solution-MTS (Promega) solution was then added to each well and incubated for 1 h at 37 °C. The optical densities of the samples were measured at 490 nm using a multi-plate reader (Varioskan LUX, Thermo Scientific). The obtained results were compared to the control and were estimated as the inhibitory concentration (IC_{50}) values using GraphPad Prism 9. Each individual compound was tested in triplicate in a single experiment with each experiment being performed three or four times.

4.4. Cell cycle assay

The U-251, and K562 cells were seeded in 3 cm Petri dishes (Nunc) at a density of 200,000 and incubated at 37 °C. After 24 h, the medium was removed and various concentrations of TS1-TS6 compounds were added to each cell line. The cells were then incubated for an additional 24 h and assays were performed using the Muse™ Cell Cycle Kit (Millipore) according to the supplier's information. Briefly, the cells were collected, washed with cold PBS and centrifuged. The cells were then fixed in ice-cold 70% ethanol and stored at −20 °C overnight. The next day, the cells were washed with cold PBS, centrifuged and resuspended in Muse™ Cell Cycle Reagent. The samples were incubated for 30 min at room temperature in the dark. After staining, the cellular subpopulation values in the individual cell cycle phases were assessed using a Muse Cell Analyzer (Millipore). The experiments were performed at least four times.

4.5. Annexin V binding assay

Cells were seeded, and compounds were applied in the same manner as previously described in Section 4.5. Assays were then performed after a 48-h treatment using the FITC Annexin V Apoptosis Detection kit with 7-AAD (Bio-Legend) according to the manufacturer's instructions. The cells were collected, washed with PBS and centrifuged. The cells were then resuspended in Annexin V Binding Buffer and incubated for 15 min at room temperature in the dark with FITC Annexin V and 7-AAD Viability Staining Solution. After staining, the samples were counted for live, early, and late apoptotic cells using the Muse Cell Analyzer. The experiments were performed at least four times.

4.6. Immunoblotting

The U-251 and K562 cells were seeded in 3 cm Petri dishes (Nunc) at a density of 500,000 and incubated for 24 h at 37 °C. After 24 h, the medium was removed, and various concentrations of TS1, TS3, and TS5 compounds were added to each cell line. The cells were then incubated for an additional 24 h and collected, centrifuged, and lysed on ice in complete RIPA buffer containing Halt Protease Inhibitor Cocktail, Halt Phosphatase Inhibitor Cocktail, and 0.5 M EDTA (all from Thermo Scientific). The amount of protein was determined using a BCA Protein Assay Kit (Thermo Scientific) according to the manufacturer's protocol. Equal amounts of the proteins were electrophoresed on SDS-Page gels and transferred onto nitrocellulose membranes. After blocking with 5% non-fat milk with TTBS, the membranes were cut and incubated overnight at 4 °C with one of the chosen primary antibodies (from Cell-Signaling, Abcam, or Fine Biotech): $p27^{Kip1}$ (#3688), $p21^{Waf1/Cip1}$

(#2947), p53 (#2524), Cyclin A2 (#4656), Cyclin B1 (#Fnab02122), cdc2 (#9116), Aurora A (#14475), EGFR (#4267), p-EGFR (Tyr1068) (#2236), p-Akt (Ser473) (#4060), PTEN (#ab32199), p-STAT5 (Tyr694) (#9359), PARP-1 (#9542), Caspase-9 (#9508), BID (#2002), GAPDH (#2118), β-actin (#3700), (all diluted 1:1000), RAS (#ab52939) (diluted 1:5000) and vinculin (#13901) (diluted 1:2000). The antibodies were diluted in 5% non-fat milk or BSA with TTBS. The membranes were then washed and incubated with horseradish peroxidase-conjugated secondary antibodies for 1 h at room temperature. Chemiluminescence signals were recorded after staining with a SuperSignal™ West Pico Chemiluminescent Substrate (Thermo Scientific) using a ChemiDoc™ XRS+ System (BioRad). The experiments were performed at least three times. The densitometric analysis for the Western blots was performed using ImageJ 1.41.

4.7. Lumit Immunoassay

The cells were seeded in a white flat-bottom 96-well plate at a density of 50,000 for U-251, and K562 and incubated under standard condition at 37 °C for 24 h. Afterward, the cells were treated with solutions of the tested compounds (TS1, TS3, and TS5). At the same time, fluorogenic Live Cell Substrate (GF-AFC Substrate) was added to give a final concentration 50 μM in each well. After 24 h, the lysis buffer containing digitonin was mixed with the immunoassay reaction buffer and added to the wells. The plate was then digested for 20 min on a plate shaker at 800 rpm. Subsequently, primary antibodies against EGFR (#4267), p-EGFR (Tyr1068) (#2236), mTOR (#2983 and #4517), and p-mTOR (Ser2448) (#5536), and Lumit secondary antibodies (Promega) were added to the lysates. The plates were then incubated at 23 °C for 90 min, followed by adding Lumit Detection Reagent. The luminescence and fluorescence were measured after 2 min using a multi-plate reader (Varioskan LUX). The instrument was set to a time of 1 s. Tests were performed at least three times, with at least duplicate repeats for each experiment.

4.8. Tyrosine kinase inhibition assay

The assays were conducted using the Kinase Selectivity TK-1 profiling system and the ADP-Glo Kinase Assay (both from Promega), following the manufacturer's instructions and protocols previously described by our group [89]. The inhibitory potential of compounds TS1, TS3, and TS5, as well as the reference drugs Osimertinib and Erlotinib, was assessed against EGFR, HER2, HER4, and IGF-1R kinases. The experiments were performed three times. The data expressed as the percentage of the inhibition of tyrosine kinase after treatment with the tested compounds.

4.9. Cell imaging

U-251 cells were seeded into 60 mm plates containing inside a microscope coverslip (approximately 120,000 cells) and incubated for 24 h at 37 °C under 5% CO_2 atmosphere. The medium was then removed, and the cells were treated with the solution of tested compounds, TS1, TS3, and TS5, at concentration equal to triple the value of the IC_{50}. After 180 min of incubation, the medium was removed, and the cells were incubated with a 1× solution of Tubulin Tracker™ Deep Red and 4 μg/mL solution of Hoechst 33342 (both from Invitrogen) in a medium without phenol red for 30 min. The cells were washed three times with PBS and mounted with a serum-free medium without phenol red. The cells were observed after excitation at 385 nm (for nuclei staining) and 650 nm (for tubulin) using a CellInsight CX7 High Content Analysis Platform (Thermo Scientific).

4.10. Tubulin polymerization assay

The impact of TS5 on tubulin polymerization was assessed using an *In Vitro* Tubulin Polymerization Kit (>99% pure bovine tubulin) from Millipore, in accordance with the manufacturer's protocol. Briefly, TS5, along with the reference agent paclitaxel (a polymerization enhancer), was applied at a concentration of 10 μM. The compounds were mixed with purified bovine tubulin (60 μM) and polymerization buffer containing 1 mM GTP in a 96-well plate maintained on ice. The plate was then transferred to a Synergy 4 multi-plate reader preheated to 37 °C, and turbidity changes were monitored at 350 nm every 30 s for 90 min. All experiments were performed in triplicate.

4.11. Analysis of mRNA expression

Approximately 500,000 cells of each of the tested cell lines (U-251 and K562) were seeded on 3 cm Petri dishes (Nunc) and incubated at 37 °C for 24 h. The next day, the culture medium was removed and replaced with medium solutions of TS1, TS3 and TS5. After 24 h treatment, the cells were lysed using TRIzol Reagent (Ambion) for about 30 min in room temperature. The obtained lysates were collected into sterile 1.5 mL Eppendorf tubes and kept in the freezer at a temperature of −80 °C. The isolation of RNA was performed according to the manufacturer's protocol (Ambion), followed by the synthesis of cDNA using a ProtoScript II First Strand cDNA Synthesis Kit (New England Biolabs), also according to the provided protocol. The obtained final product was used for quantitative Real-Time PCR (qRT-PCR) reaction carried out using a QuantStudio™ 5 Real-Time PCR System (Applied Biosystems). During the experiment, six target genes were measured (*calreticulin, CCNE2, GADD45, IDH1, LC3*, and *TUBB3*) and their results were compared to the results of the reference gene (*GAPDH*) (**Table S3**). Reaction mix was prepared in 10 μL volume, consisting of 5 μL of Luna® Universal qPCR Master Mix (New England BioLabs), 0.25 μL of forward and reverse primers, 1 μL of cDNA, and ddH_2O. The PCR reaction followed the protocol: 60 s of initial denaturation (95 °C), 40 cycles of 15 s denaturation (95 °C), 30 s extension (60 °C), and plate reading. The experiments were performed at least four times.

4.12. In vivo

Experiments using the *Danio rerio* model were carried out on larvae up to 96 h post-fertilization, and therefore the approval of Ethics Committees was not required (according to Polish law and EU directives). All experiments using the *in vivo* model were carried out respecting the 3Rs principle and other guidelines (*e.g.* ARRIVE) for working with animals.

4.12.1. Zebrafish toxicity studies

The evaluation of toxicity was performed according to modified OECD 236 procedure. Briefly, freshly obtained zebrafish (*Danio rerio*) embryos were distributed onto 24-well plates, with 5 embryos per well, two wells per group. The embryos were maintained in E3 medium and subjected the treatment with TS1, TS3, TS5 and Osimertinib at the doses ranging from 0 to 15 μM on separate plate each. Embryos were incubated in a controlled environment in an incubator at a constant temperature of 28 ± 0.5 °C and a day-night cycle of 14 h of light followed by 10 h of darkness. After 96 h of exposure, the following developmental endpoints were assessed: (1) coagulation of embryos, (2) absence of somite formation, (3) tail separation and (4) absence of cardiac activity.

4.12.2. Zebrafish xenograft experiments

Tumor U-251 cell lines were cultured until cells reached 70% of confluence, then washed with phosphate-buffered saline (PBS), detached and stained with Vybrant CM-DiI (ThermoFisher; 4 μL/mL in 1× PBS) for 10 min at 37 °C in darkness. The stained cell suspension was resuspended in PBS to a final concentration of 2.5×10^8 cells/mL. The number of 500–1000 cells od fluorescently labeled cancer cells were injected into the yolk sac of 2 days post-fertilization (dpf) zebrafish embryos. Successfully engrafted embryos were imaged (Zeiss Discovery V8) to assess tumor size and subsequently allocated into treatment

groups: E3, TS1–0.5, 1, 2 μM, TS3–0.5, 1, 2 μM, TS5–0.5, 1, 2 μM and Osimertinib – 5, 7.5, 10 μM. Then, the embryos were incubated at 31 °C for 72 h when tumor size was measured *via* image analysis. Fluorescence images were captured using a Zeiss Discovery V8 fluorescence microscope and analyzed with FIJI/ImageJ software to quantify tumor-derived fluorescence at injection point and 72 h post-injection. The difference was calculated as a percentage *versus* 100% for non-treated E3 control group.

4.13. ADME calculations

All the parameters were predicted using the commercially available program ACD/Percepta ver. 2025 (Advanced Chemistry Development, Inc., Toronto, ON, Canada, 2025).

4.14. In silico with statistical analysis of pose consistency

The docking results for the highest-ranking ligand were analyzed and visualized using UCSF ChimeraX. Pose consistency was quantified using RDKit shape-based similarity (Shape Tanimoto) computed relative to a consensus pose (a medoid). Scatter plots of shape similarity *versus* docking rank were complemented by rolling-window trend estimates (rolling median; window size defined as a fixed fraction of the dataset) to capture monotonic relationships under substantial point dispersion. The interquartile range (IQR; 25th–75th percentile) within each window was used as a robust measure of local geometric variability. Pearson's correlation coefficient (r) and Spearman's rank correlation coefficient (ρ) were reported to quantify linear association and monotonic dependence, respectively. These analyses assess geometric convergence and pose reproducibility and are not intended to establish quantitative structure–activity relationships.

4.15. Statistical analysis

The results are presented as the mean ± standard deviation (SD) from at least three independent experiments. The statistical analyses for the cell cycle, apoptosis, and gene and protein expression were performed using one-way ANOVA with multiple comparisons with post-hoc test correction (Dunnett's or Šidák's). All the samples were compared to their respective controls, a p-value of 0.05 or less being considered statistically significant. All statistical analyses were performed using GraphPad Prism 9.0.

Authors' contribution

PR performed cytotoxicity, cell cycle, apoptosis induction, Lumit immunoassays and Western Blot studies; JM designed, synthetized compounds and performed *in silico* studies; PZ performed tubulin imaging and qRT-PCR experiments; ABC conducted *in vivo* studies; JJ calculated ADME properties; AMW analyzed data and wrote the manuscript; KM created research hypothesis, designed biological experiments, performed the tubulin polymerization and kinase assays, discussed the results and wrote the manuscript. All of the authors read and approved the final version of the manuscript.

CRediT authorship contribution statement

Patryk Rurka: Visualization, Methodology, Investigation, Formal analysis. **Jacek Mularski:** Validation, Methodology, Investigation. **Patryk Ziola:** Visualization, Validation, Investigation. **Anna Boguszewska-Czubara:** Writing – review & editing, Methodology, Investigation. **Josef Jampilek:** Writing – review & editing, Software, Investigation. **Anna Mrozek-Wilczkiewicz:** Writing – review & editing, Writing – original draft, Supervision, Formal analysis, Data curation. **Katarzyna Malarz:** Writing – review & editing, Writing – original draft, Supervision, Project administration, Methodology, Investigation, Funding acquisition, Conceptualization.

Declaration of competing interest

The authors declare that they have no known competing financial interests or personal relationships that could have appeared to influence the work reported in this paper.

Acknowledgements

The study was supported by National Science Centre grant 2019/35/B/NZ5/04208 (KM). We thank BoostHigh for providing access to the workflow component and computational resources. JJ thanks the Slovak Research and Development Agency (APVV) for the financial support provided under project APVV-24-0242, which enabled the use of software applied in the ADME studies.

Appendix A. Supplementary data

Supplementary data to this article can be found online at https://doi.org/10.1016/j.bioorg.2026.109517.

Data availability statement

Data supporting the findings of this study are available within the article. Source data are available from the corresponding author on request (katarzyna.malarz@us.edu.pl).

References

[1] M.O. Steinmetz, A.E. Prota, Microtubule-targeting agents: strategies to hijack the cytoskeleton, Trends Cell Biol. 28 (10) (2018) 776–792, https://doi.org/10.1016/j.tcb.2018.05.001.
[2] K.M. Bhat, V. Setaluri, Microtubule-associated proteins as targets in cancer chemotherapy, Clin. Cancer Res. 13 (10) (2007) 2849–2854, https://doi.org/10.1158/1078-0432.CCR-06-3040.
[3] F. Mollinedo, C. Gajate, Microtubules, microtubule-interfering agents and apoptosis, Apoptosis 8 (5) (2003) 413–450, https://doi.org/10.1023/a:1025513106330.
[4] O. Wattanathamsan, V. Pongrakhananon, Emerging role of microtubule-associated proteins on cancer metastasis, Front. Pharmacol. 13 (2022) 935493, https://doi.org/10.3389/fphar.2022.935493.
[5] V. Pongrakhananon, O. Wattanathamsan, M. Takeichi, P. Chetprayoon, P. Chanvorachote, Loss of CAMSAP3 promotes EMT via the modification of microtubule-Akt machinery, J. Cell Sci. 131 (21) (2018), https://doi.org/10.1242/jcs.216168.
[6] A.L. Parker, W.S. Teo, J.A. McCarroll, M. Kavallaris, An emerging role for tubulin isotypes in modulating cancer biology and chemotherapy resistance, Int. J. Mol. Sci. 18 (7) (2017) 1434, https://doi.org/10.3390/ijms18071434.
[7] J.J. Field, J.F. Diaz, J.H. Miller, The binding sites of microtubule-stabilizing agents, Chem. Biol. 20 (3) (2013) 301–315, https://doi.org/10.1016/j.chembiol.2013.01.014.
[8] W. Krause, Resistance to anti-tubulin agents: from vinca alkaloids to epothilones, Cancer Drug Resist 2 (1) (2019) 82–106, https://doi.org/10.20517/cdr.2019.06.
[9] X. Wang, B. Gigant, X. Zheng, Q. Chen, Microtubule-targeting agents for cancer treatment: seven binding sites and three strategies, MedComm –Oncology 2 (3) (2023), https://doi.org/10.1002/mog2.46.
[10] R. Velasco, J. Bruna, Taxane-induced peripheral neurotoxicity, Toxics 3 (2) (2015) 152–169, https://doi.org/10.3390/toxics3020152.
[11] Y.Y. Hsieh, J.L. Du, P.M. Yang, Repositioning VU-0365114 as a novel microtubule-destabilizing agent for treating cancer and overcoming drug resistance, Mol. Oncol. 18 (2) (2024) 386–414, https://doi.org/10.1002/1878-0261.13536.
[12] M. Koutsioumpa, A.L. Carlson, T. DesRochers, P.Y.W. Chan, A.L. Risinger, R. Adams, C. Bardy, D. Thomas, H. Lelie, The microtubule-destabilizing agent AUS_001 as a candidate for glioblastoma therapy, J. Clin. Oncol. 42 (16_suppl) (2024) 3114, https://doi.org/10.1200/JCO.2024.42.16_suppl.3114.
[13] L.A. Patron, H. Yeoman, S. Wilson, N. Tang, M.E. Berens, V. Gokhale, T.C. Suzuki, Novel brain-penetrant, small-molecule tubulin destabilizers for the treatment of glioblastoma, Biomedicines 12 (2) (2024), https://doi.org/10.3390/biomedicines12020406.
[14] R. Kaul, A.L. Risinger, S.L. Mooberry, Microtubule-targeting drugs: more than antimitotics, J. Nat. Prod. 82 (3) (2019) 680–685, https://doi.org/10.1021/acs.jnatprod.9b00105.
[15] L.C. Husemann, A. Reese, C. Radine, R.P. Piekorz, W. Budach, D. Sohn, R. U. Janicke, The microtubule targeting agents eribulin and paclitaxel activate similar signaling pathways and induce cell death predominantly in a caspase-

independent manner, Cell Cycle 19 (4) (2020) 464–478, https://doi.org/10.1080/15384101.2020.1716144.
[16] C.R. Andersson, T. Selvin, K. Blom, J. Rubin, M. Berglund, M. Jarvius, L. Lenhammar, V. Parrow, A. Loskog, M. Fryknas, P. Nygren, R. Larsson, Mebendazole is unique among tubulin-active drugs in activating the MEK-ERK pathway, Sci. Rep. 10 (1) (2020) 13124, https://doi.org/10.1038/s41598-020-68986-0.
[17] L. Chen, Z. Lu, Y. Hu, L. Li, J.Q. Wu, W.H. Chen, J. Hu, Dual induction of ferroptosis and apoptosis by Triazolopyrimidinyl derivatives: design, synthesis, and biological evaluation for their anticancer efficacy via calcium/calmodulin Signaling and mitochondrial impairment, J. Med. Chem. 68 (21) (2025) 23024–23049, https://doi.org/10.1021/acs.jmedchem.5c01888.
[18] X. Wu, L. Sooman, J. Lennartsson, S. Bergstrom, M. Bergqvist, J. Gullbo, S. Ekman, Microtubule inhibition causes epidermal growth factor receptor inactivation in oesophageal cancer cells, Int. J. Oncol. 42 (1) (2013) 297–304, https://doi.org/10.3892/ijo.2012.1710.
[19] M. Carbonaro, A. O'Brate, P. Giannakakou, Microtubule disruption targets HIF-1α mRNA to cytoplasmic P-bodies for translational repression, J. Cell Biol. 192 (1) (2011) 83–99, https://doi.org/10.1083/jcb.201004145.
[20] T. Yoshida, Y. Ozawa, T. Kimura, Y. Sato, G. Kuznetsov, S. Xu, M. Uesugi, S. Agoulnik, N. Taylor, Y. Funahashi, J. Matsui, Eribulin mesilate suppresses experimental metastasis of breast cancer cells by reversing phenotype from epithelial–mesenchymal transition (EMT) to mesenchymal–epithelial transition (MET) states, Br. J. Cancer 110 (6) (2014) 1497–1505, https://doi.org/10.1038/bjc.2014.80.
[21] L. Chen, Y. Hu, Z. Lu, Z. Lin, L. Li, J.Q. Wu, Z.L. Yu, C. Wang, W.H. Chen, J. Hu, Design, synthesis, and antitumor efficacy of substituted 2-amino[1,2,4]triazolo-pyrimidines and related heterocycles as dual inhibitors for microtubule polymerization and Janus kinase 2, J. Med. Chem. 66 (21) (2023) 15006–15024, https://doi.org/10.1021/acs.jmedchem.3c01690.
[22] A. Kumari, O. Shriwas, S. Sisodiya, M.K. Santra, S.K. Guchhait, R. Dash, D. Panda, Microtubule-targeting agents impair kinesin-2-dependent nuclear transport of β-catenin: evidence of inhibition of Wnt/β-catenin signaling as an important antitumor mechanism of microtubule-targeting agents, FASEB J. 35 (4) (2021) e21539, https://doi.org/10.1096/fj.202002594R.
[23] L. Tan, J. Zhang, Y. Wang, X. Wang, Y. Wang, Z. Zhang, W. Shuai, G. Wang, J. Chen, C. Wang, L. Ouyang, W. Li, Development of dual inhibitors targeting epidermal growth factor receptor in cancer therapy, J. Med. Chem. 65 (7) (2022) 5149–5183, https://doi.org/10.1021/acs.jmedchem.1c01714.
[24] Y. Liu, Q. Ma, X. Kong, X. Huo, Z. Dong, Y. Ma, K. Yang, W. Niu, K. Zhang, Design of balanced dual-target inhibitors of EGFR and microtubule, Bioorg. Chem. 143 (2024) 107087, https://doi.org/10.1016/j.bioorg.2023.107087.
[25] L. Zhu, M. Zhang, J. Leng, B. Zhao, M. Ning, C. Zhang, L. Kong, Y. Yin, Discovery of novel quinazoline derivatives as tubulin polymerization inhibitors targeting the colchicine binding site with potential anti-colon cancer effects, Eur. J. Med. Chem. 280 (2024) 117000, https://doi.org/10.1016/j.ejmech.2024.117000.
[26] T.B. Shaik, M.S. Malik, S.R. Routhu, Z.S. Seddigi, A. Althagafi, Kamal, Evaluation of anticancer and anti-mitotic properties of quinazoline and quinazolino-benzothiadiazine derivatives, Anticancer Agents Med Chem. 20 (5) (2020) 599–611, https://doi.org/10.2174/1871520620666191224122204.
[27] J. Mularski, K. Malarz, M. Pacholczyk, R. Musiol, The p53 stabilizing agent CP-31398 and multi-kinase inhibitors, Designing, synthesizing and screening of styrylquinazoline series, Eur J Med Chem 163 (2019) 610–625, https://doi.org/10.1016/j.ejmech.2018.12.012.
[28] K. Malarz, M. Kuczak, P. Rurka, P. Rawicka, A. Boguszewska-Czubara, J. Jampilek, J. Mularski, R. Musiol, A. Mrozek-Wilczkiewicz, Unveiling the role of Ndrg1 gene on the oxidative stress induction behind the anticancer potential of styrylquinazoline derivatives, Sci. Rep. 15 (1) (2025) 16081, https://doi.org/10.1038/s41598-025-99277-1.
[29] K. Malarz, J. Mularski, M. Pacholczyk, R. Musiol, Styrylquinazoline derivatives as ABL inhibitors selective for different DFG orientations, J. Enzyme Inhib. Med. Chem. 38 (1) (2023) 2201410, https://doi.org/10.1080/14756366.2023.2201410.
[30] K. Malarz, J. Mularski, M. Kuczak, A. Mrozek-Wilczkiewicz, R. Musiol, Novel benzenesulfonate scaffolds with a high anticancer activity and G2/M cell cycle arrest, Cancers (Basel) 13 (8) (2021) 1790, https://doi.org/10.3390/cancers13081790.
[31] M. Kuczak, W. Cieslik, R. Musiol, A. Mrozek-Wilczkiewicz, 4-Furanylvinylquinoline derivative as a new scaffold for the design of oxidative stress initiator and glucose transporter inhibitor drugs, Sci. Rep. 14 (1) (2024) 28454, https://doi.org/10.1038/s41598-024-79698-0.
[32] A. Mrozek-Wilczkiewicz, M. Kuczak, K. Malarz, W. Cieslik, E. Spaczynska, R. Musiol, The synthesis and anticancer activity of 2-styrylquinoline derivatives. A p53 independent mechanism of action, Eur. J. Med. Chem. 177 (2019) 338–349, https://doi.org/10.1016/j.ejmech.2019.05.061.
[33] M. Brázdová, T. Quante, L. Tögel, K. Walter, C. Loscher, V. Tichý, L. Činčárová, W. Deppert, G.V. Tolstonog, Modulation of gene expression in U251 glioblastoma cells by binding of mutant p53 R273H to intronic and intergenic sequences, Nucleic Acids Res. 37 (5) (2009) 1486–1500, https://doi.org/10.1093/nar/gkn1085.
[34] J.C. Law, M.K. Ritke, J.C. Yalowich, G.H. Leder, R.E. Ferrell, Mutational inactivation of the p53 gene in the human erythroid leukemic K562 cell line, Leuk. Res. 17 (12) (1993) 1045–1050, https://doi.org/10.1016/0145-2126(93)90161-d.
[35] E.A. Horne, P. Diaz, P.J. Cimino, E. Jung, C. Xu, E. Hamel, M. Wagenbach, D. Kumasaka, N.B. Wageling, D.D. Azorin, F. Winkler, L.G. Wordeman, E. C. Holland, N. Stella, A brain-penetrant microtubule-targeting agent that disrupts hallmarks of glioma tumorigenesis, Neurooncol Adv 3 (1) (2021) vdaa165, https://doi.org/10.1093/noajnl/vdaa165.
[36] R.H. Abbassi, A. Reensens, D.C. Indurthi, T.G. Johns, B.W. Stringer, B.W. Day, L. Munoz, Lower tubulin expression in glioblastoma stem cells attenuates efficacy of microtubule-targeting agents, ACS Pharmacol Transl Sci 2 (6) (2019) 402–413, https://doi.org/10.1021/acsptsci.9b00045.
[37] G. Wang, Q. Jiang, C. Zhang, The role of mitotic kinases in coupling the centrosome cycle with the assembly of the mitotic spindle, J. Cell Sci. 127 (Pt 19) (2014) 4111–4122, https://doi.org/10.1242/jcs.151753.
[38] A.R. Dwivedi, V. Kumar, V. Prashar, K. Jangid, N. Kumar, B. Devi, J. Parkash, V. Kumar, Synthesis and screening of novel 2,4-bis substituted quinazolines as tubulin polymerization promoters and antiproliferative agents, RSC, Med. Chem. 16 (3) (2025), https://doi.org/10.1039/d4md00755g.
[39] N.-O. Friedrich, F. Flachsenberg, A. Meyder, K. Sommer, J. Kirchmair, M. Rarey, Conformator: a novel method for the generation of conformer ensembles, J. Chem. Inf. Model. 59 (2) (2019) 731–742, https://doi.org/10.1021/acs.jcim.8b00704.
[40] C. Sun, G. Wang, K.H. Wrighton, H. Lin, Z. Songyang, X.H. Feng, X. Lin, Regulation of p27(Kip1) phosphorylation and G1 cell cycle progression by protein phosphatase PPM1G, Am. J. Cancer Res. 6 (10) (2016) 2207–2220.
[41] G. He, J. Kuang, Z. Huang, J. Koomen, R. Kobayashi, A.R. Khokhar, Z.H. Siddik, Upregulation of p27 and its inhibition of CDK2/cyclin E activity following DNA damage by a novel platinum agent are dependent on the expression of p21, Br. J. Cancer 95 (11) (2006) 1514–1524, https://doi.org/10.1038/sj.bjc.6603448.
[42] Y. Gao, Y. Wu, N. Zhang, H. Yuan, F. Wang, H. Xu, J. Yu, J. Ma, S. Hou, X. Cao, IDH1 gene mutation activates Smad signaling molecules to regulate the expression levels of cell cycle and biological rhythm genes in human glioma U87-MG cells, Mol. Med. Rep. 23 (5) (2021), https://doi.org/10.3892/mmr.2021.11993.
[43] N. Han, F. Yuan, P. Xian, N. Liu, J. Liu, H. Zhang, H. Zhang, K. Yao, G. Yuan, GADD45a mediated cell cycle inhibition is regulated by p53 in bladder cancer, Onco. Targets. Ther. 12 (2019) 7591–7599, https://doi.org/10.2147/OTT.S222223.
[44] S. Jin, T. Tong, W. Fan, F. Fan, M.J. Antinore, X. Zhu, L. Mazzacurati, X. Li, K. L. Petrik, B. Rajasekaran, M. Wu, Q. Zhan, GADD45-induced cell cycle G2-M arrest associates with altered subcellular distribution of cyclin B1 and is independent of p38 kinase activity, Oncogene 21 (57) (2002) 8696–8704, https://doi.org/10.1038/sj.onc.1206034.
[45] L.H. Wang, M. Yan, D.Z. Xu, J.X. Cao, X.F. Zhu, Y.X. Zeng, Q. Liu, Requirement of aurora-a kinase in astral microtubule polymerization and spindle microtubule flux, Cell Cycle 7 (8) (2008) 1104–1111, https://doi.org/10.4161/cc.7.8.5738.
[46] J. Lyu, E.J. Yang, B. Zhang, C. Wu, L. Pardeshi, C. Shi, P.K. Mou, Y. Liu, K. Tan, J. S. Shim, Synthetic lethality of RB1 and aurora a is driven by stathmin-mediated disruption of microtubule dynamics, Nat. Commun. 11 (1) (2020) 5105, https://doi.org/10.1038/s41467-020-18872-0.
[47] L. Gasic, S.A. Boswell, T.J. Mitchison, Tubulin mRNA stability is sensitive to change in microtubule dynamics caused by multiple physiological and toxic cues, PLoS Biol. 17 (4) (2019) e3000225, https://doi.org/10.1371/journal.pbio.3000225.
[48] S. Deng, H.C. Leong, A. Datta, V. Gopal, A.P. Kumar, C.T. Yap, PI3K/AKT signaling tips the balance of cytoskeletal forces for cancer progression, Cancers (Basel) 14 (7) (2022), https://doi.org/10.3390/cancers14071652.
[49] J. Mercado-Matos, J.L. Clark, A.J. Piper, J. Janusis, L.M. Shaw, Differential involvement of the microtubule cytoskeleton in insulin receptor substrate 1 (IRS-1) and IRS-2 signaling to AKT determines the response to microtubule disruption in breast carcinoma cells, J. Biol. Chem. 292 (19) (2017) 7806–7816, https://doi.org/10.1074/jbc.M117.785832.
[50] Y.S. Gao, C.C. Hubbert, T.P. Yao, The microtubule-associated histone deacetylase 6 (HDAC6) regulates epidermal growth factor receptor (EGFR) endocytic trafficking and degradation, J. Biol. Chem. 285 (15) (2010) 11219–11226, https://doi.org/10.1074/jbc.M109.042754.
[51] Z. He, T. Tian, D. Guo, H. Wu, Y. Chen, Y. Zhang, Q. Wan, H. Zhao, C. Wang, H. Shen, L. Zhao, X. Bu, M. Wan, C. Shen, Cytoplasmic retention of a nucleocytoplasmic protein TBC1D3 by microtubule network is required for enhanced EGFR signaling, PloS One 9 (4) (2014) e94134, https://doi.org/10.1371/journal.pone.0094134.
[52] R. Pike, E. Ortiz-Zapater, B. Lumicisi, G. Santis, M. Parsons, KIF22 coordinates CAR and EGFR dynamics to promote cancer cell proliferation, Sci. Signal. 11 (515) (2018), https://doi.org/10.1126/scisignal.aaq1060.
[53] B. Hwang, L. Engel, S.A. Goueli, H. Zegzouti, A homogeneous bioluminescent immunoassay to probe cellular signaling pathway regulation, Communications Biology 3 (1) (2020), https://doi.org/10.1038/s42003-019-0723-9.
[54] G.J. Buttrick, J.G. Wakefield, PI3-K and GSK-3: Akt-ing together with microtubules, Cell Cycle 7 (17) (2008) 2621–2625, https://doi.org/10.4161/cc.7.17.6514.
[55] H. Jo, F. Loison, H.R. Luo, Microtubule dynamics regulates Akt signaling via dynactin p150, Cell. Signal. 26 (8) (2014) 1707–1716, https://doi.org/10.1016/j.cellsig.2014.04.007.
[56] Y. Fujiwara, Y. Hosokawa, K. Watanabe, S. Tanimura, K.-I. Ozaki, M. Kohno, Blockade of the phosphatidylinositol-3-kinase–Akt signaling pathway enhances the induction of apoptosis by microtubule-destabilizing agents in tumor cells in which the pathway is constitutively activated, Mol. Cancer Ther. 6 (3) (2007) 1133–1142, https://doi.org/10.1158/1535-7163.Mct-06-0639.
[57] S. Bibi, M.D. Arslanhan, F. Langenfeld, S. Jeanningros, S. Cerny-Reiterer, E. Hadzijusufovic, L. Tchertanov, R. Moriggl, P. Valent, M. Arock, Co-operating STAT5 and AKT signaling pathways in chronic myeloid leukemia and mastocytosis: possible new targets of therapy, Haematologica 99 (3) (2014) 417–429, https://doi.org/10.3324/haematol.2013.098442.

[58] A.A. Krygowska, E. Castellano, PI3K: a crucial piece in the RAS signaling puzzle, Cold Spring Harb. Perspect. Med. 8 (6) (2018) a031450, https://doi.org/10.1101/cshperspect.a031450.
[59] T.H. Wang, H.S. Wang, H. Ichijo, P. Giannakakou, J.S. Foster, T. Fojo, J. Wimalasena, Microtubule-interfering agents activate c-Jun N-terminal kinase/stress-activated protein kinase through both Ras and apoptosis signal-regulating kinase pathways, J. Biol. Chem. 273 (9) (1998) 4928–4936, https://doi.org/10.1074/jbc.273.9.4928.
[60] H.I. Gul, C. Yamali, M. Bulbuller, P.B. Kirmizibayrak, M. Gul, A. Angeli, S. Bua, C. T. Supuran, Anticancer effects of new dibenzenesulfonamides by inducing apoptosis and autophagy pathways and their carbonic anhydrase inhibitory effects on hCA I, hCA II, hCA IX, hCA XII isoenzymes, Bioorg. Chem. 78 (2018) 290–297, https://doi.org/10.1016/j.bioorg.2018.03.027.
[61] M. Gonzalez, M. Ovejero-Sanchez, A. Vicente-Blazquez, M. Medarde, R. Gonzalez-Sarmiento, R. Pelaez, Methoxy and bromo scans on N-(5-methoxyphenyl) methoxybenzenesulphonamides reveal potent cytotoxic compounds, especially against the human breast adenocarcinoma MCF7 cell line, J. Enzyme Inhib. Med. Chem. 36 (1) (2021) 1029–1047, https://doi.org/10.1080/14756366.2021.1925265.
[62] Z. Wang, F. Yin, J. Xu, T. Zhang, G. Wang, M. Mao, Z. Wang, W. Sun, J. Han, M. Yang, Y. Jiang, Y. Hua, Z. Cai, CYT997(Lexibulin) induces apoptosis and autophagy through the activation of mutually reinforced ER stress and ROS in osteosarcoma, J. Exp. Clin. Cancer Res. 38 (1) (2019) 44, https://doi.org/10.1186/s13046-019-1047-9.
[63] M. Hasanain, R. Sahai, P. Pandey, M. Maheshwari, K. Choyal, D. Gandhi, A. Singh, K. Singh, K. Mitra, D. Datta, J. Sarkar, Microtubule disrupting agent-mediated inhibition of cancer cell growth is associated with blockade of autophagic flux and simultaneous induction of apoptosis, Cell Prolif. 53 (4) (2020) e12749, https://doi.org/10.1111/cpr.12749.
[64] R.J. Wei, S.S. Lin, W.R. Wu, L.R. Chen, C.F. Li, H.D. Chen, C.T. Chou, Y.C. Chen, S. S. Liang, S.T. Chien, Y.L. Shiue, A microtubule inhibitor, ABT-751, induces autophagy and delays apoptosis in Huh-7 cells, Toxicol. Appl. Pharmacol. 311 (2016) 88–98, https://doi.org/10.1016/j.taap.2016.09.021.
[65] C. Geeraert, A. Ratier, S.G. Pfisterer, D. Perdiz, I. Cantaloube, A. Rouault, S. Pattingre, T. Proikas-Cezanne, P. Codogno, C. Pous, Starvation-induced hyperacetylation of tubulin is required for the stimulation of autophagy by nutrient deprivation, J. Biol. Chem. 285 (31) (2010) 24184–24194, https://doi.org/10.1074/jbc.M109.091553.
[66] M.S. Tikhomirova, A. Kadosh, A.J. Saukko-Paavola, T. Shemesh, R.W. Klemm, A role for endoplasmic reticulum dynamics in the cellular distribution of microtubules, Proc. Natl. Acad. Sci. U. S. A. 119 (15) (2022) e2104309119, https://doi.org/10.1073/pnas.2104309119.
[67] Y. Yang, F. Ma, Z. Liu, Q. Su, Y. Liu, Z. Liu, Y. Li, The ER-localized ca(2+)-binding protein calreticulin couples ER stress to autophagy by associating with microtubule-associated protein 1A/1B light chain 3, J. Biol. Chem. 294 (3) (2019) 772–782, https://doi.org/10.1074/jbc.RA118.005166.
[68] L.J. Kraft, P. Manral, J. Dowler, A.K. Kenworthy, Nuclear LC3 associates with slowly diffusing complexes that survey the nucleolus, Traffic 17 (4) (2016) 369–399, https://doi.org/10.1111/tra.12372.
[69] G.K.F. Baska, L. Őrfi, P. Bánhegyi, L. Kekesi, L. Zsakai, A. Sipos, C. Szántai-Kis, J. Dobos, T.D. Blaauwen, Styryl Quinazoline Derivatives As Pharmaceutically Active Agents, 2014.
[70] Y.A. Samir, 4(3H)-quinazolinone derivatives: Syntheses, physical properties, chemical reaction, and biological properties, in: A.-K. Ali Gamal (Ed.), Quinazolinone and Quinazoline Derivatives, IntechOpen, Rijeka, 2020, https://doi.org/10.5772/intechopen.90104 p. Ch. 4.
[71] M.F. Zayed, Medicinal chemistry of quinazolines as anticancer agents targeting tyrosine kinases, Sci. Pharm. 91 (2) (2023) 18.
[72] C.A. Lipinski, F. Lombardo, B.W. Dominy, P.J. Feeney, Experimental and computational approaches to estimate solubility and permeability in drug discovery and development settings1PII of original article: S0169-409X(96)00423–1. The article was originally published in Advanced Drug Delivery Reviews 23 (1997) 3–25.1, Advanced Drug Delivery Reviews 46(1), 2001, https://doi.org/10.1016/S0169-409X(00)00129-0, 3–26.
[73] L.Z. Benet, Solubility-permeability interplay in facilitating the prediction of drug disposition routes, extent of absorption, food effects, brain penetration and drug induced liver injury potential, J. Pharm. Sci. 112 (9) (2023) 2326–2331, https://doi.org/10.1016/j.xphs.2023.07.006.
[74] D.G. Jimenez, M. Vallaro, L. Vitagliano, L.L. Lopez, G. Apprato, G. Ermondi, G. Caron, Molecular properties, including chameleonicity, as essential tools for designing the next generation of oral beyond rule of five drugs, ADMET & DMPK 12 (5) (2024) 721–736, https://doi.org/10.5599/admet.2334.
[75] C.A. Lipinski, Chapter 22 - compound properties and drug quality, in: C. G. Wermuth (Ed.), The Practice of Medicinal Chemistry, Third edition, Academic Press, New York, 2008, pp. 481–490, https://doi.org/10.1016/B978-0-12-374194-3.00022-6.
[76] H. Van de Waterbeemd, 5.28 - in silico models to predict oral absorption, in: J. B. Taylor, D.J. Triggle (Eds.), Comprehensive Medicinal Chemistry II, Elsevier, Oxford, 2007, pp. 669–697, https://doi.org/10.1016/B0-08-045044-X/00145-0.
[77] M. Muehlbacher, G.M. Spitzer, K.R. Liedl, J. Kornhuber, Qualitative prediction of blood–brain barrier permeability on a large and refined dataset, J. Comput. Aided Mol. Des. 25 (12) (2011) 1095–1106, https://doi.org/10.1007/s10822-011-9478-1.
[78] V. Chunduri, S. Maddi, Role of in vitro two-dimensional (2D) and three-dimensional (3D) cell culture systems for ADME-tox screening in drug discovery and development: a comprehensive review, ADMET & DMPK 11 (1) (2023) 1–32, https://doi.org/10.5599/admet.1513.
[79] A. Avdeef, Often neglected steps in transforming drug solubility from single measurement in pure water to physiologically-appropriate solubility-pH, ADMET and DMPK 13 (1) (2025), https://doi.org/10.5599/admet.2626.
[80] J. Pinto-Fraga, C. García-Chico, S. Lista, P.M. Lacal, G. Carpenzano, M. Salvati, A. Santos-Lozano, G. Graziani, C. Ceci, Protein kinase inhibitors as targeted therapy for glioblastoma: a meta-analysis of randomized controlled clinical trials, Pharmacol. Res. 212 (2025) 107528, https://doi.org/10.1016/j.phrs.2024.107528.
[81] R.K. Oberoi, K.E. Parrish, T.T. Sio, R.K. Mittapalli, W.F. Elmquist, J.N. Sarkaria, Strategies to improve delivery of anticancer drugs across the blood-brain barrier to treat glioblastoma, Neuro Oncol. 18 (1) (2016) 27–36, https://doi.org/10.1093/neuonc/nov164.
[82] C. Ferraris, R. Cavalli, P.P. Panciani, L. Battaglia, Overcoming the blood-brain barrier: successes and challenges in developing nanoparticle-mediated drug delivery systems for the treatment of brain tumours, Int J Nanomedicine 15 (2020) 2999–3022, https://doi.org/10.2147/ijn.S231479.
[83] M. Pinkiewicz, A. Zaczyński, J. Walecki, M. Zawadzki, Beyond the walls of Troy: a scoping review on pharmacological strategies to enhance drug delivery across the blood–brain barrier and blood–tumor barrier, Int. J. Mol. Sci. 26 (15) (2025) 7050.
[84] W. Chen, D. Jin, Y. Shi, Y. Zhang, H. Zhou, G. Li, The underlying mechanisms of lorlatinib penetration across the blood-brain barrier and the distribution characteristics of lorlatinib in the brain, Cancer Med. 9 (12) (2020) 4350–4359, https://doi.org/10.1002/cam4.3061.
[85] M. Momeny, S. Shamsaiegahkani, B. Kashani, S. Hamzehlou, F. Esmaeili, H. Yousefi, S. Irani, S.A. Mousavi, S.H. Ghaffari, Cediranib, a pan-inhibitor of vascular endothelial growth factor receptors, inhibits proliferation and enhances therapeutic sensitivity in glioblastoma cells, Life Sci. 287 (2021) 120100, https://doi.org/10.1016/j.lfs.2021.120100.
[86] J. Jampilek, K. Kralova, Insights into lipid-based delivery nanosystems of protein-tyrosine kinase inhibitors for cancer therapy, Pharmaceutics 14 (12) (2022) 2706.
[87] E. Angeli, G. Bousquet, Brain metastasis treatment: the place of tyrosine kinase inhibitors and how to facilitate their diffusion across the blood–brain barrier, Pharmaceutics 13 (9) (2021) 1446.
[88] S. Feng, H. Liu, C. Yun, W. Zhu, Y. Pan, Application of EGFR-TKIs in brain tumors, a breakthrough in future? J. Transl. Med. 23 (1) (2025) 449, https://doi.org/10.1186/s12967-025-06448-9.
[89] P. Ziola, K. Malarz, P. Rawicka, M. Korzec, M. Serda, A. Boguszewska-Czubara, M. Pacholczyk, M. Książek, A. Mrozek-Wilczkiewicz, The multifaceted mechanism of action of quinoline thiosemicarbazone based on disruption of iron homeostasis and selective IGF1R inhibition leading to oxidative stress induction, Biomed. Pharmacother. 192 (2025) 118692, https://doi.org/10.1016/j.biopha.2025.118692.

Molecular Oncology

FEBS PRESS

A novel quinazolinone insulin receptor inhibitor and its synergy with an EGFR inhibitor in glucose-driven glioblastoma

Patryk Rurka[1], Wioleta Cieślik[2], Wojciech Płaziński[3,4], Katarzyna Stępnik[5], Anna Boguszewska-Czubara[6], Elżbieta Kot[6], Robert Musioł[2], Mateusz Jasica[2], Anna Mrozek-Wilczkiewicz[1,7] and Katarzyna Malarz[1]

1 Institute of Physics, University of Silesia in Katowice, Chorzów, Poland
2 Institute of Chemistry, University of Silesia in Katowice, Chorzów, Poland
3 Jerzy Haber Institute of Catalysis and Surface Chemistry, Polish Academy of Sciences, Kraków, Poland
4 Department of Biopharmacy, Medical University of Lublin, Poland
5 Department of Physical Chemistry, Institute of Chemical Sciences, Maria Curie–Skłodowska University in Lublin, Poland
6 Department of Medical Chemistry, Medical University of Lublin, Poland
7 Department of Systems Biology and Engineering, Silesian University of Technology, Gliwice, Poland

Keywords
anticancer activity; combination therapy; EGFR; glioblastoma; IGF1R kinase; insulin inhibitor; styrylquinazolinone

Correspondence
K. Malarz, Institute of Physics, University of Silesia in Katowice, 75 Pułku Piechoty 1a, 41-500 Chorzów, Poland
Tel: +48323497669
E-mail: katarzyna.malarz@us.edu.pl

(Received 3 November 2025, revised 27 March 2026, accepted 12 May 2026)

doi:10.1002/1878-0261.70274

Aberrant signaling through insulin-like growth factor 1 receptor (IGF1R) and epidermal growth factor receptor (EGFR) drives glioblastoma (GBM) progression and therapy resistance. Herein, we describe the synthesis and biological evaluation of W1B, a novel styrylquinazolinone-based small-molecule inhibitor. In antiproliferative assays, W1B exhibited potent submicromolar activity against a panel of GBM cell lines. Kinase assays and binding studies confirmed strong inhibition and high binding affinity toward IGF1R. Molecular docking suggested possible interactions with both IGF1R and EGFR, with W1B adopting distinct binding poses in each kinase domain. In cellular studies, W1B reduced IGF1R and EGFR protein levels in LN229 cells and suppressed Akt phosphorylation. Under high-glucose conditions, however, W1B only retained inhibitory activity toward IGF1R, resulting in attenuated effects on the Akt/mTOR axis and underscoring the influence of glucose-dependent signaling rewiring on drug efficacy. Combination studies revealed that W1B acts synergistically with the EGFR inhibitor dacomitinib, effectively overcoming compensatory activation of parallel pathways. Biomimetic lipophilicity and *in silico* pharmacokinetic analyses indicated that styrylquinazolinone has the potential to cross the blood–brain barrier (BBB). The *in vivo* studies on Danio rerio have shown a good safety profile, as well as strong antitumor potential of the tested compound. Therefore, these findings establish W1B as a promising derivative for the development of next-generation dual IGF1R/EGFR inhibitors in GBM.

Abbreviations
BBB, blood–brain barrier; EGFR, epidermal growth factor receptor; Fb, unbound fractions in brain tissue; Fu, unbound fractions in plasma; GBM, glioblastoma; HPLC, high-performance liquid chromatography; IAM, immobilized artificial membrane; IGF1R, insulin-like growth factor 1 receptor; InsR, insulin receptor; logBB, logarithm of blood–brain partitioning; logPcw, logarithm of the cyclohexane/water partition coefficient; logPow, logarithm of the octanol–water partition coefficient; logPS, logarithm of passive diffusion; logPS-fu, brain, logarithm of brain-plasma equilibrium; MST, microscale thermophoresis; NSCLC, non-small cell lung cancer; RTKs, receptor tyrosine kinases; TME, tumor microenvironment; TPSA, topological polar surface area.

1. Introduction

The insulin-like growth factor 1 receptor (IGF1R) is a key mediator of signaling pathways that regulate cell growth, proliferation, metabolism, and survival [1]. IGF1R is a transmembrane tyrosine kinase receptor activated by IGF1 and IGF2, which bind to its extracellular domain and initiate autophosphorylation of intracellular tyrosine residues [2]. This leads to the activation of multiple downstream pathways, most notably the PI3K/AKT/mTOR and RAS/RAF/MEK/ERK cascades, as well as Src and JAK/STAT, which are crucial for stimulating cell proliferation, migration and resistance to apoptosis [3]. IGF1R also influences the expression of drug transporters, DNA repair enzymes, and cell cycle regulators [4]. Overexpression or constitutive activation of IGF1R has been observed in various types of cancers, including glioblastoma (GBM), non-small cell lung cancer (NSCLC), breast cancer, colon cancer, and pancreatic cancer [5]. Beyond tumor cell-intrinsic mechanisms, IGF1R also shapes the immune landscape of the tumor microenvironment (TME) by driving immunosuppression through STAT3, MAPK, and PI3K signaling that attenuates cytotoxic T-cell activity [6,7]. These findings highlight IGF1R as a key driver of tumor progression and immune evasion, supporting the inhibition of this receptor as a therapeutic strategy.

Glioblastoma, the most aggressive and treatment-resistant primary brain tumor, is characterized by high IGF1R expression and correlates with poor prognosis, reduced survival, and limited responsiveness to standard-of-care therapies such as temozolomide [8,9]. Despite the use of intensive treatment modalities, the median overall survival for GBM patients is only about 10.2 months, and the five-year survival rate remains below 5% [10]. The development of novel therapeutic approaches has faced numerous obstacles, one of the most critical being efficient drug delivery across the highly selective blood–brain barrier (BBB), which restricts the efficacy of nearly 98% of therapeutic agents [11].

Although targeted therapies against receptor tyrosine kinases (RTKs), such as epidermal growth factor receptor (EGFR) and IGF1R, have shown promise in preclinical models, clinical translation has been largely unsuccessful [12,13]. This limited efficacy is mainly attributed to the pronounced molecular heterogeneity of GBM, particularly within the EGFR/PI3K/AKT/mTOR, CDK4/6–CDKN2A/B–RB1 and p53 signaling networks, as well as the emergence of resistance mechanisms, including loss of EGFR expression and activation of compensatory pathways (e.g., c-MET, IGF1R) [14,15]. Importantly, similar to other RTKs, IGF1R functions as a central hub within highly integrated signaling networks [16]. Its extensive crosstalk with EGFR [17], integrins [18], and insulin receptor (InsR) [19] has complicated the development of effective IGF1R-directed therapeutics, while simultaneously providing a rationale for cotargeting strategies. Ultimately, overcoming the resilience of such interconnected signaling systems may require the use of multi-agent or combination-based therapeutic approaches. Indeed, combination strategies with OSI-906 (Linsitinib) (Fig. 1), a dual inhibitor of IGF1R/InsR, and gefitinib, the EGFR inhibitor, showed greater efficacy in treating subcutaneous GBM xenograft tumors. However, this effect may have been counteracted by increased Akt kinase expression [20]. Despite more than 180 clinical trials involving IGF1R-targeting agents, none have been approved for oncology indications, and only a few have included patients with primary brain tumors [13]. Nonetheless, early clinical data suggest the potential of the small-molecule AXL1717 (Picropodophyllin) (Fig. 1), which induced a durable response in patients with astrocytoma in a phase I trial [21].

Significant efforts have been directed toward the development of IGF1R inhibitors, encompassing both monoclonal antibodies [22–25] and small-molecule tyrosine kinase inhibitors. Notable examples of the latter are NVP-AEW541 (a pyrrolopyrimidine derivative) [26] and BMS-754807 (a pyrrolotriazine derivative) [27,28] (Fig. 1). Quinazoline-based compounds, such as HMJ-30 [29] (Fig. 1), along with other derivatives [30], have also been shown to inhibit IGF1R. The quinazoline ring in these molecules underscores its potential as a versatile scaffold for engaging the IGF1R active site, making it an attractive template for the design of next-generation inhibitors.

Compounds incorporating sulfonyl group (–SO_2–), including tosyl (4-methylphenylsulfonyl) moieties, are primarily known for their auxiliary functions in organic synthesis or for modulating physicochemical properties such as solubility and stability—including biochemical stability—while often preserving good bioavailability. Less frequently, they serve as essential pharmacophores in biologically active molecules, and reports on their use as selective kinase inhibitors, including IGF1R inhibitors, remain limited. Notably, GSK1904529A [31] (Fig. 1), a potent and selective IGF1R inhibitor, features a sulfonyl group in its side chain that is critical for interactions with the kinase active site. Moreover, sulfonyl-indole-based compounds have demonstrated significant IGF1R inhibitory activity [32]. This underscores the value of sulfonyl moieties as key interaction motifs in

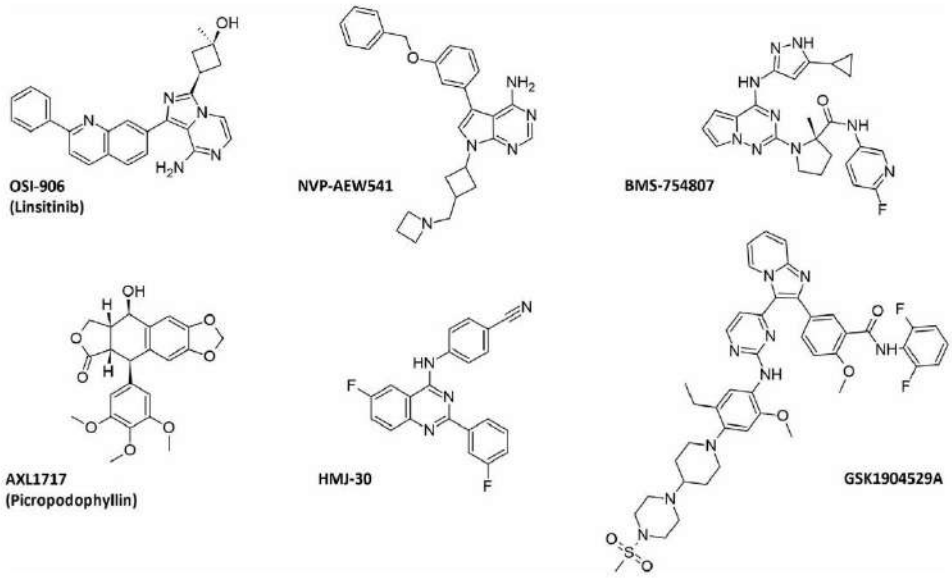

Fig. 1. The chemical structures of insulin-like growth factor 1 receptor (IGF1R) inhibitors.

the design of IGF1R-targeted inhibitors. In our group, we have been actively developing compounds containing a styrylquinazoline motif, focusing on their antiproliferative and tyrosine kinase inhibitory properties. We initially characterized a series of p53 reactivator analogues, such as CP-31398 [33]. Subsequently, we elucidated the mechanism of action of one derivative, IS20 (6b), demonstrating its capacity to induce oxidative stress by modulating *Ndrg1* gene expression and disrupting EGFR signaling [34]. Subsequent efforts explored thio-analogs of styrylquinazoline, which increase bioavailability and improve binding to different conformations in the DFG pocket of ABL kinase [35], as well as sulfamoyl derivatives as dual IDH1/ABL inhibitors [36]. Moreover, several benzenesulfonates revealed pronounced anti-GBM activity, driven by robust G2/M cell cycle arrest and enhanced tubulin polymerization [37,38].

Given the limited efficacy of current kinase inhibitors in aggressive and resistant tumors, there is a clear need to develop novel compounds with enhanced properties. Leveraging our expertise, we have designed and synthesized a novel series of derivatives featuring a unique 7-chloroquinazolinone core, a styryl moiety, and a tosyl group, a structural combination not previously reported. Among these, one compound has emerged as a promising IGF1R inhibitor, whose mechanism of action we have characterized in GBM cells, including under conditions of elevated glucose metabolism. Moreover, we have explored strategies for the effective combination of this approach with the EGFR inhibitor dacomitinib, emphasizing its potential for multi-targeted therapeutic approaches. As monotherapies, EGFR inhibitors such as dacomitinib or osimertinib are effective in the NSCLC [39], but display limited activity in GBM [40]. Likewise, quinazoline-based agents, such as lapatinib, have shown no efficacy in recurrent GBM [41]. In turn, afatinib demonstrated only modest activity in patients with recurrent GBM, and a similar outcome was observed for dacomitinib [40,42].

2. Material and methods

2.1. Chemistry

All of the reagents were purchased from Sigma Aldrich. Microwave syntheses were performed in a CEM Discover 2.0 microwave reactor. Thin-layer chromatography (TLC) experiments were performed on alumina-backed silica gel 460 F_{254} plates (Merck, Darmstadt, Germany). The plates were illuminated under UV (254 nm and 360 nm). The melting points

were determined on an Optimelt MPA-100 (SRS, USA). All ^{1}H and ^{13}C NMR spectra were recorded on a Bruker Avance III 500 MHz FT-NMR spectrometer (500 MHz for ^{1}H and 101/126 MHz for ^{13}C, Bruker Comp., Karlsruhe, Germany). Chemical shifts are reported in ppm (δ) using the signal of the solvent (DMSO-d_6) as the reference against the internal standard $Si(CH_3)_4$. Easily exchangeable signals were omitted when they were diffuse. Signals are designated as follows: s, singlet; d, doublet; dd, doublet of doublets; ddd, doublet of doublet of doublets; t, triplet; tt, triplet of triplets; td, triplet of doublets; m, multiplet. Mass spectra were measured using a maXis impact ESI/APCI-Q-TOF mass spectrometer (Bruker Daltonics, USA) with direct injection into an APCI source in the positive mode.

2.1.1. General procedure for the preparation of tosyl aldehyde derivatives (A-C)

A solution of hydroxybenzaldehyde (1.0 eq, 5 mmol), p-toluenesulfonyl chloride (1.1 eq, 5.5 mmol), and triethylamine (2.5 eq, 12.5 mmol) in dichloromethane (CH_2Cl_2, 40 mL) was placed in a 100 mL round bottom flask. The mixture was stirred at room temperature for 3 h. The reaction mixture was washed with water (3 × 20 mL), and the water layer was extracted with EtOAc (3 × 20 mL). The organic layer was dried by $MgSO_4$. After filtration and removal of the solvent under reduced pressure, the crude product was dried under air.

2.1.2. General procedure for the preparation of 2-methylquinazolin-4(3H)-one derivatives (W1-2)

The 2-aminobenzoic acid derivatives (23.4 mmol) were dissolved in acetic anhydride (110 mL), and the reaction mixture was stirred at 80 °C for 2 h. The solvent was then evaporated, and the crude product was washed with isopropanol and filtered out. To a dry solid (benzoxazin-4-one intermediates) was added 90 mL of ammonium hydroxide (32% NH_3), and they were stirred at room temperature for 6 days. The product precipitated from the solution was filtered out and washed with water. The solid compound was dried under vacuum overnight.

2.1.3. General procedure for the preparation of styrylquinazolinone derivatives (W1A-C, W2B)

A mixture of the appropriate 2-methylquinazolin-4(3*H*)-one derivative (W1-2) (1 mmol) and the appropriate tosyl aldehyde (A-C) (1 mmol) was heated in 3 mL of 80% concentrated acetic acid. The reaction was carried out in a microwave reactor at 130 °C for 1.5 h. The reaction mixture was then cooled in a refrigerator to precipitate the solid. The resulting solid was filtered under reduced pressure and recrystallized from acetic acid to afford the corresponding styrylquinazolinone derivative as a white solid.

The physicochemical data with spectroscopic analyses for all compounds are given in the Supplementary Information.

2.2. Molecular docking

The ligand molecule was drawn manually using Avogadro 1.1.1 software [43] and optimized within the UFF force field [44] (15 000 steps, steepest descent algorithm). The flexible, optimized ligand molecule was docked into the binding pocket of the five protein structures found in the PDB database: 1K3A (IGF1R), 1 M17 (EGFR), 2ZM3 (IGF1R), 3EKN (InsR) and 4HJO (EGFR). Vina software [45] was used for docking simulations, with all default procedures and algorithms implemented in AutoDock Vina during docking procedures. The docking procedure was carried out within the rectangular region of dimensions 22 × 22 × 16 $Å^3$, which covers the originally co-crystallized ligands present in the PDB structures as well as the closest amino acid residues that exhibit contact with those ligands. In addition to the flexibility of the ligand molecules, the rotation of selected sidechains (in particular: two Leu, one Lys, one Arg, one Val, two Met and two Asp) in the proximity of the co-crystalized ligands was allowed. Visual inspection of the location and orientation of the docked ligands was accompanied by RMSD-based clustering in order to control the uniformity of the binding pattern. Before docking the compound, the adopted methodology was validated by performing docking for each of the ligands present in the crystal structure of the given protein. All procedures were the same as described above.

2.3. Measurements of tyrosine kinase activity

RTK inhibition was measured using Kinase Selectivity Profiling Systems (TK-1 and TK-2) and ADP-Glo Kinase Assay (Promega). W1B was dissolved in 100 μM DMSO and a 1 μM solution was prepared in 1× Kinase Reaction Buffer (40 mM Tris—pH 7.5; 20 mM $MgCl_2$; 0.1 mg·mL^{-1} BSA; 50 μM DTT) with a final DMSO concentration of 5%. Then, each kinase (EGFR, HER2, HER4, IGF1R, InsR, KDR, PDGFRa, PDGFRb) or (ABL1, BRK, BTK, CSK,

Fyn A, Lck, Lyn B, Src) from an 8-well strip was dissolved in 95 µL of 2.5× Kinase Reaction Buffer, and the 8-well strips containing substrates in 15 µL of 100 µM ATP. The tyrosine kinase inhibition assay was performed on a white 384-well plate by transferring 1 µL of W1B solutions, then adding 2 µL of the previously prepared kinase and substrate solutions, then incubating for 1 h at room temperature. Kinase activity was detected by adding 5 µL of ADP-Glo™ Reagent to each well, shaking the plate for two minutes, and incubating for 40 min at room temperature. Then, 10 µL of Kinase Detection Reagent was added, remixed, and incubated for 30 min at room temperature. Luminescence was measured using a Varioskan LUX multidetector plate reader (Thermo Fisher Scientific, USA), with analysis and graphical representation employing GRAPHPAD PRISM 9 (GraphPad Software, USA).

2.4. Binding assays (microscale thermophoresis – MST)

W1B affinity to the IGF1R protein was measured by MST using the Monolith NT.115 Blue/Red device (NanoTemper Technologies, Germany). Experiments were performed in a buffer containing 50 mM HEPES (pH = 7.5), 300 mM NaCl, 10 mM $MgCl_2$ and 0.05% Tween 20. Recombinant human IGF-I R/IGF1R protein (His-tagged) (Bio-Techne) was labeled using the Monolith His-Tag RED-tris-NTA 2nd Generation labeling kit (NanoTemper Technologies). The final labeled protein concentration was 50 nM. Final serial dilutions of W1B were prepared starting at 10 µM, with 2-fold dilutions to 0.000305 µM in assay buffer. For Kd determination, labeled proteins were incubated with serial dilutions of W1B for 15 min at room temperature. Samples were then centrifuged (12 000 × *g* for 10 min), placed in standard capillaries (NanoTemper Technologies) and measured at 25 °C using 80% LED power and 40% MST power. Experiments were repeated at least three times. Data analysis was performed using MO.AFFINITY ANALYSIS 2.3 SOFTWARE (NanoTemper Technologies). All final graphs were prepared using GRAPHPAD PRISM 9.

2.5. Cell culture

The human GBM cell lines U87MG (RRID:CVCL_0022), T98G (RRID:CVCL_0556), LN18 (RRID:CVCL_0392) and LN229 (RRID:CVCL_0393) were purchased from ATCC. The human breast carcinoma cell line MCF-7 (RRID:CVCL_0031), and the lung adenocarcinoma PC-9 (RRID:CVCL_B260) were obtained from Merck. Normal human dermal fibroblasts (NHDF) were purchased from PromoCell. The U-251 (RRID:CVCL_0021) GBM cell line was kindly provided by Prof. G. Kramer-Marek from the Institute of Cancer Research in London, United Kingdom. GBM cell lines and MCF-7 cells were cultured in Dulbecco's modified Eagle's medium F-12 (DMEM), whereas PC-9 cells were cultured in RPMI 1640 medium. Both media were supplemented with 10% heat-inactivated fetal bovine serum—FBS (all reagents from Merck). For some experiments, LN229 cells (later named LN229 HG) were also cultured in DMEM containing high glucose (DMEM HG; Merck) and supplemented with 10% heat-inactivated FBS. The NHDF cell line was cultured in fibroblast growth medium with a low-serum content (PromoCell). Each complete medium contained penicillin and streptomycin (1% v/v; Gibco). Cell lines were cultured at 37 °C with a 5% CO_2 humidified atmosphere. Cell lines were routinely tested for *mycoplasma* contamination using the PCR technique. All cell lines used in this study were purchased specifically for the purposes of this research and have been authenticated within the past three years.

2.6. Cytotoxicity

Cells were seeded in 96-well plates (Nunc) at a density of 5000 cells per well (U-251, U87MG, T98G, LN18, LN229, LN229 HG, MCF-7, PC-9) or 4000 cells per well (NHDF) and incubated under standard conditions at 37 °C for 24 h. The assay was conducted after a 72 h incubation period with the various concentrations of the tested compounds. Then, DMEM without phenol red with CellTiter 96®AQueous One Solution-MTS (Promega) solution was added to each well and incubated for 1 h at 37 °C. The optical densities of the samples were measured at 490 nm using a multi-plate reader (Varioskan LUX). The obtained results were compared to the control and were calculated as inhibitory concentration (IC_{50}) values with GRAPHPAD PRISM 9. All experiments were performed independently four times, with each compound tested in triplicate.

2.7. Immunoblotting

The LN229 and LN229 HG cells were seeded in a 3 cm Petri dishes (Nunc) at a density of 500 000 and incubated for 24 h at 37 °C. After 24 h, DMEM or DMEM HG medium was removed and various concentrations of W1B compound were added. For the combination therapy experiments, LN229 HG cells were treated with W1B, dacomitinib, or their

combination at the IC_{50} dose. The cells were then incubated for an additional 24 h and collected, centrifuged, and lysed on ice in complete RIPA buffer containing Halt Protease Inhibitor Cocktail, Halt Phosphatase Inhibitor Cocktail, and 0.5 M EDTA (all Thermo Scientific). The protein amount was determined using a BCA Protein Assay Kit (Thermo Scientific) according to the manufacturer's protocol. Equal amounts of the proteins were electrophoresed on SDS/PAGE gels and transferred onto nitrocellulose membranes. After blocking with 5% non-fat milk with TTBS, the membranes were cut and incubated overnight at 4°C with one of the chosen primary antibodies (from CellSignaling or Abcam): EGFR (D38B1) (#4267), IGF-I Receptor β (D23H3) (#9750), Akt (#9272), phospho-Akt (Ser473) (D9E) (#4060), p70 S6 Kinase (49D7) (#2708), phospho-S6 Ribosomal Protein (Ser240/244) (D68F8) (#5364), RAS (EP1125Y) (#ab52939), vinculin (E1E9V) (#13901), GAPDH (14C10) (#2118), cyclophilin β (D1V5J) (#43603), and cofillin (D3F9) (#5175). The antibodies were diluted in 5% non-fat milk with TTBS. The membranes were then washed and incubated with horseradish peroxidase-conjugated secondary antibodies for 1 h at room temperature. The chemiluminescence signals were recorded after staining with a SuperSignal™ West Atto Chemiluminescent Substrate (Thermo Scientific) using a ChemiDoc™ XRS+ System (BioRad). The experiments were performed six times. The densitometric analysis was performed using ImageJ 1.41. Statistical analysis (one-way ANOVA with Dunnett's post hoc test) and graph preparation used GRAPHPAD PRISM 9.

2.8. Combination therapy with EGFR inhibitor

The LN229 or LN229 HG cells were seeded in 96-well plates (Nunc) at a density of 5000 cells per well and incubated at 37 °C for 24 h. After 24 h, solutions of W1B, dacomitinib, or their combination at IC_{50} were added and incubated for 72 h. Then, DMEM without phenol red with CellTiter 96®AQueous One Solution-MTS (Promega) solution was added to each well and incubated for 1 h at 37 °C. The optical densities of the samples were measured at 490 nm using a multi-plate reader (Varioskan LUX). Each variation was tested in triplicate in a single experiment with each experiment being performed at least three or four times. Drug combination effects were calculated using CompuSyn software [46]. The CI values are presented in Table S3. Statistical analysis (two-way ANOVA with Tukey's post hoc test) and graph preparation were performed using GRAPHPAD PRISM 9.

2.9. Computational and biomimetic studies

The ACD/Percepta software (version 2012, Advanced Chemistry Development, Inc., Toronto, ON, Canada) was used in the *in silico* studies. Statistical analysis of the results obtained was made using the Minitab 18 Statistical Software (Minitab Inc., State College, USA).

The Shimadzu Vp liquid chromatographic system (Shimadzu, Kyoto, Japan) equipped with LC 10AT pump, SPD 10A UV–Vis detector, SCL 10A system controller, CTO-10 AS chromatographic oven and Rheodyne injector valve with a 20 µL loop was applied in the HPLC-IAM measurements. The solution of W1B was prepared in methanol (Merck, Darmstadt, Germany) at a concentration of 1 $mg{\cdot}mL^{-1}$. The optimization process of the chromatographic separation was made before the experiment. The flow rate of the mobile phases was established to 1 $mL{\cdot}min^{-1}$ and the temperature was set at 20 °C. The tested compound was detected with the UV light at 340 nm. The IAM.PC.DD2 stationary phase (100 × 4.6 mm i.d., 10 µm; Regis Chemicals Company, Morton Grove, USA) was used as the stationary phase while the buffered solutions of acetonitrile were used as mobile phases. The mobile phases composition was in each measurement: 0.4; 0.5; 0.6; 0.7% v/v acetonitrile-buffer (pH = 7.4). The buffer was prepared from the solutions of both Na_2HPO_4 (0.02 $mol{\cdot}dm^{-3}$) and citric acid (0.01 $mol{\cdot}dm^{-3}$). The dead time values were measured from the citric acid peaks. All the reported logarithms of the retention factor were measured three times. The values of peak asymmetry factor were in the acceptable range.

2.10. *In vivo* studies

All experiments using the *Danio rerio* model were performed in accordance with European regulations, in particular the Directive 2010/63/EU, and the corresponding Polish legislation implementing this directive (Act of 15 January 2015 on the protection of animals used for scientific or educational purposes). According to these regulations, Danio rerio larvae up to 120 h post-fertilization (hpf) are not considered protected animals. Therefore, no animal experimentation license or ethical approval number was required for the procedures described in this study. All experiments using the *in vivo* model were carried out respecting the 3Rs principle and other guidelines (e.g., ARRIVE) for working with animals.

Strain: Wild-type AB strain. Developmental stage: Embryos (Toxicity assays were performed from 0 to

96 hpf. Microinjection experiments were conducted between 48 and 120 hpf). Sex: Sex cannot be determined at the embryonic and larval stages used in this study. In zebrafish, phenotypic sex differentiation occurs later during juvenile development (typically several weeks post-fertilization). Embryos and larvae were maintained under standard conditions at 26 °C in aerated water with oxygen saturation maintained at ≥ 80%. Embryos were kept in E3 embryo medium containing 5 mM NaCl, 0.17 mM KCl, 0.33 mM $CaCl_2$, and 0.33 mM $MgSO_4$.

2.10.1. Zebrafish toxicity studies

Toxicity testing was carried out following a modified OECD Guideline 236 protocol. In brief, freshly collected zebrafish (Danio rerio) embryos were placed into 24-well plates, five embryos per well, with two wells assigned to each treatment group. Embryos were maintained in E3 medium and exposed to W1B, lapatinib, dacomitinib, or osimertinib at concentrations ranging from 0 to 50 µM, each compound tested on a separate plate. Incubation was performed under controlled conditions at 28 ± 0.5 °C with a light–dark cycle of 14/10 h. After 96 h of continuous exposure, the following developmental endpoints were evaluated: (1) embryo coagulation, (2) lack of somite formation, (3) failure of tail detachment, and (4) absence of heartbeat. The half-maximal inhibitory concentration (IC_{50}) values were determined from dose–response curves generated for each compound, providing a quantitative measure of toxicity.

2.10.2. Zebrafish xenograft experiments

The LN229 cells were cultured until reaching approximately 70% confluence, washed with phosphate-buffered saline (PBS), and detached for labeling. Cells were stained with Vybrant CM-DiI (Thermo Fisher; 4 µL·mL^{-1} in 1× PBS) for 10 min at 37 °C in the dark. After staining, the cell suspension was adjusted in PBS to a final concentration of 2.5×10^8 cells·mL^{-1}. Approximately 500–1000 fluorescently labeled cells were microinjected into the yolk sac of 2 days post-fertilization (dpf) zebrafish embryos. Successful engraftment was verified by fluorescence imaging (Zeiss Discovery V8), after which embryos were randomly assigned to treatment groups: vehicle control (E3 medium), W1B, lapatinib, osimertinib, dacomitinib, each tested at concentrations of 5, 7.5, and 10 µM. In addition, the combination of W1B and dacomitinib at a dose of 7.5 µM was tested. Following treatment, embryos were incubated at 31 °C for 72 h, after which tumor size was evaluated. Fluorescence images were acquired using a Zeiss Discovery V8 microscope, and quantitative analysis was performed with FIJI/ImageJ software. Tumor-derived fluorescence was measured at baseline (immediately post-injection) and at 72 h and changes in tumor size were expressed as a percentage relative to the untreated E3 control group, which was set at 100%.

3. Results

3.1. Synthesis of novel compounds

The synthesis of styrylquinazolinones was performed in a multistep process as shown in Fig. 2. The first step involved the preparation of the starting quinazolinone cores, with 2-methyl-4(3*H*)quinazolinones (W1-2) synthesized via the cyclocondensation of anthranilic acid with acetic anhydride, followed by treatment with concentrated aqueous ammonia [47,48]. This method enabled efficient formation of the quinazolinone core substituted with a methyl group at the C-2 position. In parallel, tosylbenzaldehyde derivatives (A-C) were obtained through a nucleophilic substitution reaction between *p*-toluenesulfonyl chloride and various hydroxybenzaldehydes. The reaction was carried out in dichloromethane using triethylamine as a base [49,50]. The key step in the synthetic pathway involved the condensation of the obtained 2-methyl-4(3*H*)quinazolinone derivatives (W1-2) with the corresponding tosylbenzaldehyde derivatives (A-C). This reaction was performed under microwave irradiation at 130 °C for 90 min in glacial acetic acid [37]. The application of microwave-assisted heating enabled a substantial reduction in reaction time compared to conventional thermal methods [33]. All synthesized styrylquinazolinones (W1A-C and W2B) were purified by recrystallization in concentrated acetic acid. Their structures were confirmed by spectroscopic analyses, including ^{1}H and ^{13}C nuclear magnetic resonance (NMR) spectroscopy, as well as high-resolution mass spectrometry (HRMS). These data are provided in the Supplementary Information (Fig. S1-S8).

3.2. Antiproliferative activity of styrylquinazolinones toward glioblastoma

The synthesized compounds were assessed for antiproliferative activity against GBM cells. For this purpose, five human GBM cell lines with different genetic and proteomic profiles were selected. As summarized in Table 1, only one of the tested derivatives (W1B) containing a 7-chloroquinazoline ring with a tosyl group

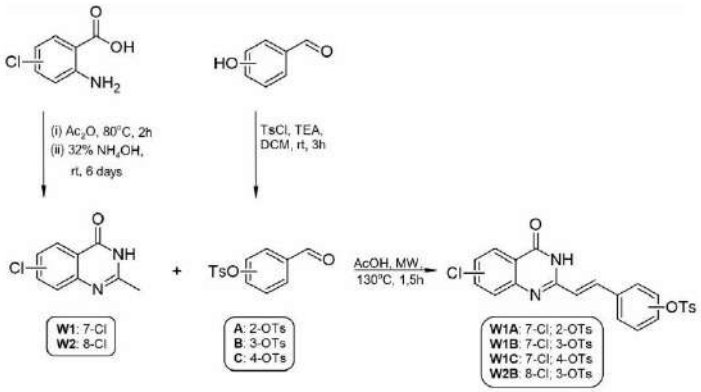

Fig. 2. Synthesis of the studied compounds.

Table 1. Antiproliferative activity of the tested compounds against a panel of glioblastoma human cell lines and normal human dermal fibroblasts (NHDF), expressed as IC_{50} values (concentration required to inhibit 50% of cell proliferation) ± SD.

	Antiproliferative activity–IC_{50} [μM]					
Compounds	U-251	U87MG	T98G	LN18	LN229	NHDF
W1A	> 25	> 25	> 25	> 25	> 25	-
W1B	5.43 ± 0.97	5.88 ± 1.20	21.01 ± 2.87	11.06 ± 1.50	3.57 ± 1.03	9.88 ± 1.18
W1C	> 25	> 25	> 25	> 25	> 25	-
W2B	> 20	> 15	> 25	> 20	> 20	-
Osimertinib	20.13 ± 0.34	11.24 ± 0.46	7.31 ± 2.19	7.35 ± 0.27	8.99 ± 0.37	6.27 ± 0.38
Lapatinib	11.37 ± 0.46	21.22 ± 1.37	17.87 ± 0.42	12.74 ± 1.29	12.60 ± 0.32	-
Dacomitinib	3.80 ± 0.61	3.66 ± 0.39	11.98 ± 0.41	5.56 ± 0.27	5.84 ± 0.17	-

substituted at position 3 in the styryl moiety showed very good biological activity. In contrast, two other 7-chloroquinazoline analogues were inactive, with the concentration required to inhibit 50% of cell proliferation (IC_{50}) exceeding 25 μM. The W2B derivative, containing an 8-chloroquinazoline scaffold, displayed poor solubility. Among the tested models, the LN229 cell line was the most susceptible, with W1B achieving an IC_{50} value of 3.57 μM. Notably, this derivative also exhibited strong activity against U-251 and U87MG cells, with IC_{50} values of 5.43 and 5.88 μM, respectively. In contrast, LN18 cells were more resistant to W1B (11.06 μM), whereas T98G cells exhibited markedly reduced susceptibility, with an IC_{50} of 21.01 μM. Evaluation of two additional epithelial cell lines (Table S1) revealed that compound W1B exhibited moderate antiproliferative activity against MCF-7 cells. In contrast, its activity against PC-9 cells ($IC_{50} = 6.54$ μM) was comparable to that observed in U-251 and U87MG cells.

In our assays, we also tested two FDA-approved reference drugs, including osimertinib, a third-generation EGFR inhibitor that crosses the BBB, and two quinazoline-based HER2/EGFR inhibitors, such as lapatinib and dacomitinib. In general, osimertinib exhibited a weaker activity profile than W1B, with two exceptions. In LN18 cells, its activity was comparable, whereas the EGFR inhibitor showed higher potency in T98G cells. In contrast, lapatinib consistently displayed lower activity across all tested cell lines. The third reference compound was dacomitinib, which exhibited a similar activity profile to W1B.

We further evaluated the selectivity of W1B against normal fibroblasts and compared it with osimertinib. The therapeutic index (TI) was calculated as the ratio of IC_{50} for normal cells to IC_{50} for cancer cells, with

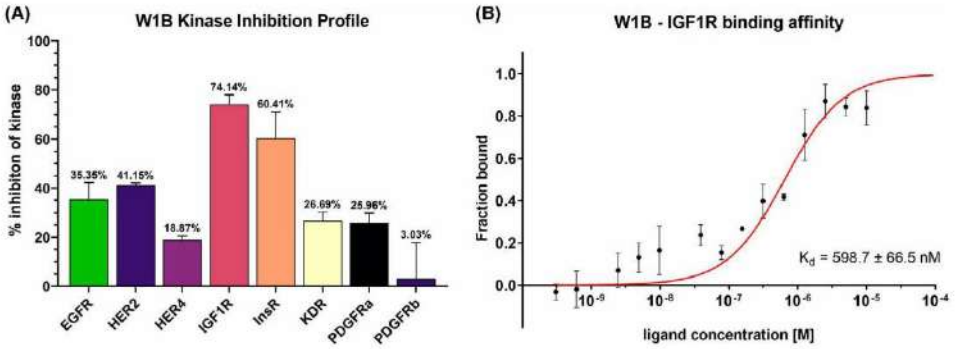

Fig. 3. Inhibition levels on the receptor tyrosine kinases by the W1B compound. A graphical representation of W1B inhibition is shown as mean [%] and standard deviation (SD) ($n = 4$) (A). The binding affinity of W1B to IGF1R was measured using the microscale thermophoresis (MST) method to determine the dissociation constant (K_d). A fraction bound line chart was plotted from the showcased mean points and their SD ($n = 3$) (B).

higher values indicating greater safety for normal tissues. W1B exhibited TI values of 2.8, 1.8, and 1.7 against LN229, U-251, and U87MG cells, respectively. In contrast, osimertinib showed limited selectivity (TIs below 0.8), consistent with the profile of many clinically approved anticancer agents.

3.3. Inhibitory profile of W1B on receptor tyrosine kinases

We screened our lead compound—W1B at a concentration of 1 μM, for inhibition of a panel of RTKs using Kinase Profiling System TK-1. This ATP-competitive profiling assay included eight representative RTKs: EGFR, HER2, HER4 (from ERBB family), as well as IGF1R, InsR, KDR, and two PDGFR isoforms. As depicted in Fig. 3A, W1B exhibited pronounced inhibitory activity against two insulin-related RTKs. The highest effect was observed for IGF1R, where kinase activity was diminished by more than 74%. In the case of InsR, a more than 60% reduction of kinase activity was observed. W1B also exhibited moderate inhibitory effects on two members of the ERBB family, reducing EGFR and HER2 kinase activities by 35% and 41%, respectively. Moreover, the tested compound showed rather weak inhibitory potential against HER4, KDR, and PDGFRs. We also assessed W1B with regard to inhibition of non-receptor tyrosine kinases, such as ABL, BRK, BTK, CSK, Fyn, Lck, Lyn, and Src. The results are presented in Table S2. Notably, our lead compound showed selective activity against RTKs. Indeed, W1B did not reduce the activity of any non-receptor kinase by more than 20%.

In further experiments, we focused on determining the binding affinity of W1B with IGF1R. For this purpose, a microscale thermophoresis (MST) technique was used, and the IGF1R His-Tag protein was labeled with a fluorescent tag. The binding curve showing the bound and unbound states of the ligand with the protein is presented in Fig. 3B. From these traces, the dissociation constant (K_d) for W1B was determined to be 598 nM.

3.4. Binding interactions of W1B with IGF1R and EGFR kinases

The next step involved molecular docking studies to further characterize W1B interactions with target kinases. Five protein structures were selected from the Protein Data Bank (PDB): 1K3A (IGF1R), 1M17 (EGFR), 2ZM3 (IGF1R), 3EKN (InsR), and 4HJO (EGFR), into whose binding pockets the ligand was docked. First, the docking protocol was verified by comparing the experimentally determined ligand pose (based on XRD data) with the most energetically favorable pose obtained by docking, as shown in Fig. S9. In all cases, it was possible to reconstruct the ligand position in the binding pocket with high accuracy, as well as its conformation (which is significant given the presence of many rotatable bonds in the W1B). The largest, yet still acceptable, deviations were observed for flexible side chains of erlotinib in PDB structures 1M17 and 4HJO.

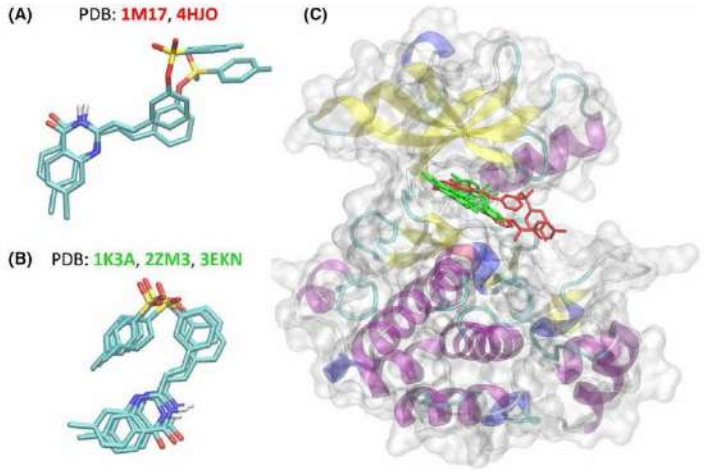

Fig. 4. Superposition of energetically favorable W1B arrangements docked to EGFR (PDB structures: 1M17 and 4HJO) (A) and to IGF1R/InsR (PDB: 1K3A, 2ZM3, and 3EKN) (B). Panel (C) provides a schematic representation of the possible ligand orientations shown in (A) and (B) relative to the protein structure of PDB: 1M17. Ligand colors correspond to the color coding of the respective PDB structures in panels (A) and (B).

The binding energies corresponding to the most energetically favorable W1B–protein arrangements were then determined for: 1K3A ($-8.1\,kcal{\cdot}mol^{-1}$), 1M17 ($-9.4\,kcal{\cdot}mol^{-1}$), 2ZM3 ($-8.6\,kcal{\cdot}mol^{-1}$), 3EKN ($-9.2\,kcal{\cdot}mol^{-1}$), and 4HJO ($-9.9\,kcal{\cdot}mol^{-1}$). It is worth noting some differences in the binding energies involving the two alternative structures of the same proteins, namely IGF1R and EGFR, which amounted to $0.6\,kcal{\cdot}mol^{-1}$ and $0.5\,kcal{\cdot}mol^{-1}$, respectively.

The next stage involved structural analysis of the W1B-protein complexes corresponding to the most favorable binding energies. Notably, all proteins are structurally similar, with an average RMSD per residue after superposition ranging from approximately 0.9 to 1.5 nm, depending on the pair compared. Therefore, a relatively similar ligand–protein interaction mechanism can be expected. As shown in Fig. 4A,B, W1B can adopt two distinct poses within the binding pocket, depending on the target protein, which are accompanied by different ligand conformations. In complexes with EGFR (PDB: 1M17 and 4HJO), W1B occupies the binding pocket in a more extended pose, associated with an elongated conformation of the molecule. In contrast, when bound to IGF1R and InsR (PDB: 1K3A, 2ZM3, and 3EKN), W1B adopts an alternative pose, characterized by a partially folded conformation driven in part by the rotation of an S–O bond. Regardless of these differences, the ligand occupies a similar binding pocket region (Fig. 4C), with slightly larger contact areas for the extended conformation, correlating with higher binding energies. Furthermore, significant conformational variability and different orientations of ligands with similar structural characteristics are typical for ligands present in the crystallized structures of the studied proteins.

Differences in ligand–protein interactions characteristic of the identified ligand orientations are illustrated in Fig. 5A,B, using PDB structures 1M17 (EGFR) and 2ZM3 as representative examples. First, we focused on the causes of different ligand orientations in proteins with similar structures. In addition to differences in the backbone conformation, which are conformationally-locked during docking, a potential cause could be differences in the primary sequence. The binding pocket fragment near the bound ligand differs in the type of amino acid residues present. For instance, Met1079 and Met1142 (present in IGF1R/InsR: 1K3A, 2ZM3, and 3EKN) are replaced by Leu and Thr in EGFR (1M17 and 4HJO). Additional substitutions include Gly1152 → Thr, Asp1086 → Cys, Glu1080 → Gln, Val1063 → Cys, Thr1083 → Pro, Met1165 → Leu, and Gln1007 → Ser. These changes, which affect the interaction characteristics between individual amino acid

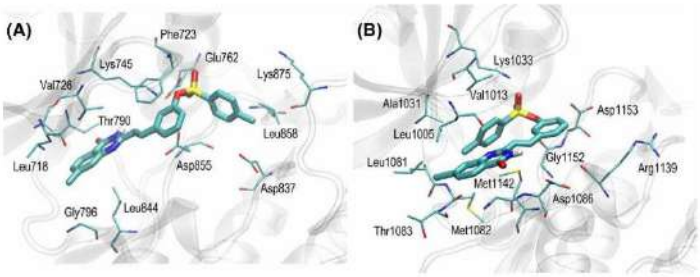

Fig. 5. The energetically favorable location of the ligand molecule bound to the EGFR (PDB: 1M17) (A) and to the IGF1R (PDB: 2ZM3) (B). The ligand molecule is shown as thick sticks whereas all the closest amino acid residues (< 0.4 nm) are represented by thin sticks.

residues and the W1B, qualitatively explain the structural differences in the ligand–protein complex. In particular, the presence of Leu858 in EGFR (1M17 and 4HJO) enables CH–π interactions with the aromatic–aliphatic portion of W1B, thereby stabilizing its extended conformation. In contrast, the absence of this interaction in the other structures favors a folded conformation of the ligand. Additionally, in the context of changes in the backbone conformation, the most significant structural difference in the proteins appears to be the deviation of the loop connecting the β-strands around Phe1010 (the equivalent in PDB: 1M17 is Phe723). This last change allows energetically favorable π-π interactions with the phenyl rings of W1B in the case of EGFR (PDB: 1M17 and 4HJO). In the other structures, the analogous residues are shifted away from the binding pocket and do not contact the ligand, while the space left unoccupied by Phe is instead filled by a fragment of W1B in its folded conformation.

When considering the residues involved in the driving force for binding, it is particularly worth mentioning the nonpolar residues (Leu, Val, Ala) and weakly polar residues (Met), whose cluster forms the main center of favorable interactions, primarily CH-π interactions, with the quinazoline ring of W1B. These favorable interactions in this region are further enhanced by contacts with the sidechains of Thr, which can be either polar or nonpolar, depending on the fragments of the sidechain and the ligand. In the case of the folded conformation of W1B in the IGF1R/InsR (PDB: 1K3A, 2ZM3, and 3EKN), interactions with the aforementioned nonpolar and weakly polar residues also involve the outer phenyl ring and its substituent. Here, the primary type of responsible interaction is also CH-π. Conversely, in the extended conformation of W1B in EGFR (PDB: 1M17, 4HJO), there is an additional π–π contact with the sidechain of Phe. These interactions are complemented by a series of polar interactions, mainly involving Asp residues and the flexible side chain of Lys, which acts as a donor for hydrogen bonds with the sulfonyl group.

3.5. W1B-mediated inhibition of IGF1R and EGFR signaling pathways

To further validate our previous findings, we assessed the cellular effects of W1B on IGF1R- and EGFR-mediated signaling pathways. In particular, we evaluated the protein levels of downstream signaling elements of these pathways, including Akt, p-Akt, Ras, as well as two mTOR-regulated proteins: p70 S6 kinase and p-S6 ribosomal protein. Representative western blot results are shown in Fig. 6A, with the corresponding densitometric analyses provided in Fig. S11. Uncropped blot images are provided in Fig. S12. The analysis revealed that W1B significantly reduced EGFR and IGF1R levels in LN229 cells. The most significant downregulation was observed at a concentration of 3.5 μM and 2.3 μM, at which the levels of both proteins decreased by more than 2-fold. As expected, this resulted in the inhibition of one of the key effectors of the signaling pathway cascade, namely Akt activation. We observed that both W1B concentrations reduced the level of Akt phosphorylation at Ser473. To further confirm inhibition of Akt signaling, the ratio of phosphorylated Akt to total Akt was analyzed and showed a comparable level of suppression (see Fig. S11).

Next, we examined two downstream effectors of mTOR signaling, which displayed an interesting expression pattern in response to treatment. At 2.3 μM, W1B reduced p70 S6K levels but enhanced p-S6 ribosomal protein expression. Conversely, treatment at 3.5 μM led to an almost 1.9-fold increase in p70 S6K

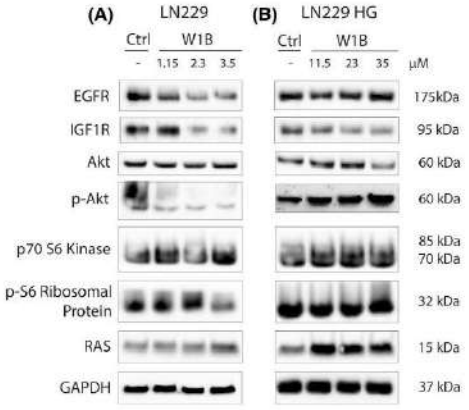

Fig. 6. Protein expression profiles in LN229 (A) and LN229 HG (B) cells following incubation with W1B at various concentrations. The immunoblots shown are representative of six independent experiments. Proteins were cropped, and full-length blots are provided in Fig. S12.

and a 1.6-fold reduction in p-S6 levels compared to untreated cells. Treatment with W1B had minimal effect on RAS levels.

Furthermore, we investigated the effect of the small-molecule inhibitor W1B on LN229 cells under conditions of elevated glucose availability. For this purpose, LN229 cells were cultured in high-glucose Dulbecco's modified Eagle's medium (DMEM) (hereafter referred to as LN229 HG). Under these conditions, the newly determined IC_{50} value was $34.4 \pm 3.5\,\mu M$, indicating that enhanced metabolic activity diminishes the potency of W1B to some extent. Consequently, we assessed the impact of W1B on the EGFR/IGF1R signaling axis in LN229 HG cells. As depicted in Fig. 6B, EGFR expression remained at high levels after treatment with W1B. In contrast, IGF1R levels were significantly reduced (almost 1.5-fold) after treatment with 23 μM and 35 μM of W1B. Despite the inhibition of IGF1R, the Akt/mTOR signaling pathway was upregulated in LN229 HG cells, as evidenced by increased levels of p-Akt and p70 S6K. Additionally, RAS abundance was also elevated under these high-glucose conditions.

3.6. Combination strategy of W1B with EGFR inhibitor

We evaluated the effects of a combination therapy regimen comprising W1B and dacomitinib on the IGF1R and EGFR kinases under conditions of elevated glucose concentration. As presented in Fig. 7, simultaneous administration of the compounds resulted in a comparable degree of IGF1R inhibition to that observed with W1B. However, a marked decrease in EGFR activity was observed when both inhibitors were administered simultaneously, compared to monotherapy. Uncropped blot images are provided in Fig. S13.

As the results were so interesting, we decided to verify the synergistic action more quantitatively. The efficacy of the therapy was assessed at its final stage (after 72 h) using a cytotoxicity assessment method. The results presented in Fig. 8 show a significant reduction in cell survival after combination therapy under standard conditions and conditions of increased glucose concentration. Supporting these observations, the combination yielded CI values of 0.94 in the LN229 cells and an even stronger synergistic score of 0.87 in the LN229 HG variant (Table S3 and Fig. S10).

3.7. *In silico* determination of BBB permeation

To pre-evaluate the ability of the novel quinazolinone derivative to cross the BBB, the *in silico* pharmacokinetic analysis was performed using ACD/Percepta software. The calculated parameters included BBB penetration (logBB), passive diffusion (logPS), brain-plasma equilibrium ($logPS^*_{fu,brain}$), and the unbound fractions in plasma (Fu) and brain tissue (Fb). These descriptors provide an initial indication of CNS pharmacokinetics and are summarized in Table 2.

In our study, W1B had very low unbound fractions in both brain ($Fb = 0.0016$) and plasma ($Fu = 0.11$), while the equilibrium rate between brain and plasma (logPS-fu, brain $= -3.1$) was relatively high.

To further refine BBB permeability predictions, additional physicochemical properties were assessed using the Hansch method (see Table 3). Steric, electronic, and hydrophobic descriptors were calculated, since molecular size, shape, and lipophilicity are critical for both target binding and membrane permeation. Lipophilicity was quantified by partition coefficients between n-octanol and water (logPow) and between cyclohexane and water (logPcw), which provide complementary insights into solvation and membrane affinity.

W1B, with a molecular weight of $452.9\,g \cdot mol^{-1}$, exhibits pronounced polarizability, as well as has a topological polar surface area (TPSA) of $93.2\,Å^2$ and an n-octanol/water partition coefficient (logPow) calculated as 4.206.

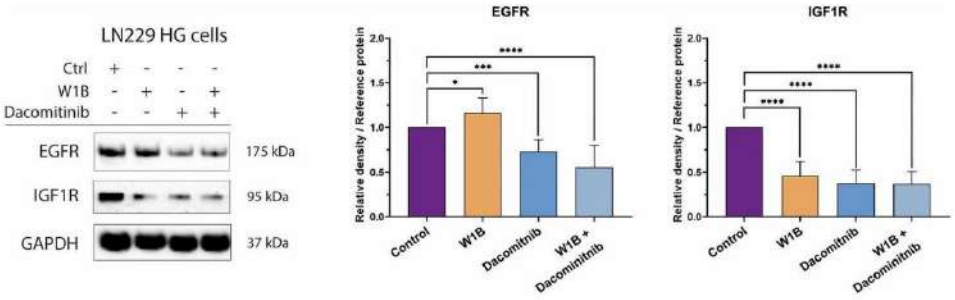

Fig. 7. Protein expression in LN229 HG cells after 24 h treatment with W1B (35 μM), dacomitinib (5.4 μM), or their combination. Relative protein levels were normalized to the reference protein and compared to control (untreated) cells. The immunoblots shown are representative of six independent experiments. Proteins were cropped, and full-length blots are provided in Fig. S13. Data are presented as mean ± SD ($n = 6$) and were analyzed using one-way ANOVA with Dunnett's post hoc test (*$P < 0.05$, ***$P < 0.001$, ****$P < 0.0001$).

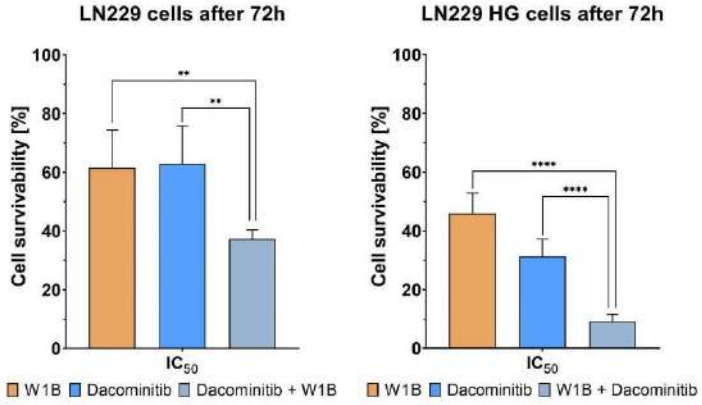

Fig. 8. Survivability of LN229 and LN229 high-glucose (HG) cells following treatment with W1B, dacomitinib, or their combination. Data are presented as mean ± SD ($n = 6$) and were analyzed using two-way ANOVA with Tukey's post hoc test (**$P < 0.01$, ****$P < 0.0001$).

Table 2. The BBB Pharmacokinetic Descriptors of W1B Calculated *in silico* (ACD/Percepta software).

Log BB	Log PS	$LogPS^{*}_{fu,brain}$	Fu	Fb
−0.87	−1.1	−3.1	0.0016	0.01

Table 3. Physicochemical parameters calculated *in silico*.

LogPow	LogPcw	MW [g·mol $^{-1}$]	TPSA [Å^2]
4.206	1.717	452.91	93.21

3.8. Biomimetic studies on the lipophilicity

Lipophilicity is a key determinant of CNS accessibility, given its decisive role in barrier penetration and systemic distribution. To experimentally assess this property for W1B, we employed non-cell-based biomimetic *in vitro* studies as a model of passive transport and absorptive behavior across biological membranes. Specifically, high-performance liquid chromatography (HPLC) with an immobilized artificial membrane (IAM) system was used.

Chromatographic experiments were performed using an IAM.PC.DD2 column as the stationary phase, while buffered acetonitrile solutions served as mobile

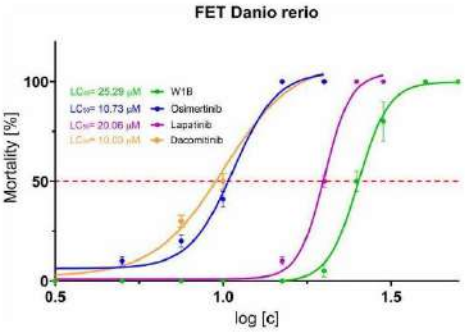

Fig. 9. Toxicity of W1B, osimertinib, lapatinib, and dacomitinib showed as mortality rate [%] ± SD of zebrafish embryos (Danio rerio) exposed to a range of concentrations: 0–50 µM. Calculated values of LD_{50} for W1B, osimertinib, lapatinib, and dacomitinib: 25.29, 10.73, 20.06, and 10.03 µM respectively.

phases (0.4, 0.5, 0.6, 0.7% v/v acetonitrile/buffer; pH = 7.4). The logarithm of retention factors extrapolated to a purely aqueous mobile phase (log kw) was calculated according to the Soczewinski–Wachtmeister Eq. [1]:

$$\log k = \log kw - s\phi \quad (1)$$

where log k is the logarithm of the retention factor measured in the mixed aqueous–organic effluent system, φ is the volume fraction of the organic modifier, and s is the solute-specific slope characteristic for the chromatographic system.

Application of this model yielded an extrapolated log kw value of 2.533 for W1B, with a solute-specific slope $s = 4.787$ and an excellent correlation coefficient ($R^2 = 0.98$), confirming the robustness of the linear fit.

3.9. *In vivo* studies

W1B displayed a safety profile comparable to lapatinib and clearly superior to osimertinib and dacomitinib (Fig. 9). The LC_{50} values obtained from the zebrafish embryo acute toxicity assay were 25.29 µM for W1B, 20.06 µM for lapatinib, 10.73 µM for osimertinib, and 10.03 µM for dacominitib.

In terms of therapeutic efficacy, W1B demonstrated strong antitumor activity in xenografted zebrafish embryos, with outcomes consistent with prior *in vitro* data (Fig. 10A–D). Tumor growth was significantly reduced at all tested concentrations, with the most pronounced effect observed at the highest dose. At this concentration, tumor size was decreased to 76.09% in the W1B-treated group and to 76.97% in the osimertinib group and 87.42% in case of dacomitinib treatment, whereas lapatinib-treated embryos showed only a modest reduction to 91.44% (Fig. 10E). These results are in agreement with the antiproliferative activity observed *in vitro*, where W1B exhibited a potent effect ($IC_{50} = 3.57 \pm 1.03$ µM), superior to all of them: osimertinib ($IC_{50} = 8.99 \pm 0.37$ µM), dacomitinib ($IC_{50} = 5.84 \pm 0.17$ µM) and lapatinib ($IC_{50} = 12.60 \pm 0.32$ µM). Notably, at 7.5 µM, the combination of W1B and dacomitinib achieved an antitumor effect superior to that observed for either compound alone. The selection of the 7.5 µM dose for both compounds was dictated by the toxicity profile of dacomitinib ($LC_{50} = 10.03$ µM). Consequently, this combination demonstrates efficacy at sub-10 µM concentrations while maintaining a favorable toxicity profile (Fig. 10F).

4. Discussion

The therapeutic management of glioblastoma is severely compromised by the tumor's intrinsic molecular complexity and the restrictive properties of the BBB. Consequently, developing novel small molecules with favorable physicochemical profiles for CNS penetration that selectively target tumor proliferation is of paramount importance. In evaluating the antiproliferative spectrum of our synthesized compounds, the robust activity of the W1B derivative against both GBM and specific epithelial models is of particular interest. Our findings highlight a stringent structure–activity relationship within this novel class of styrylquinazolinones. The striking potency discrepancy between W1B and its inactive analogues underscores that the specific combination of a 7-chloroquinazoline scaffold with a tosyl group substituted at position 3 of the styryl moiety is critical for conferring significant biological activity. Beyond brain tumors, we expanded our evaluation to include the PC-9 cell line, an EGFR-mutant non-small cell lung cancer (NSCLC) model. Notably, NSCLC has a well-documented clinical propensity for brain metastasis, making PC-9 a highly relevant complementary model in the context of our brain-targeted, glioblastoma-oriented research. The fact that W1B's activity against PC-9 cells was comparable to that observed in standard GBM models (U-251 and U87MG) underscores its potential against malignancies capable of penetrating the CNS. Furthermore, the comparison of W1B with clinically utilized EGFR/HER2 inhibitors highlights its favorable safety profile. While osimertinib showed limited selectivity (TIs below 0.8), a characteristic consistent with the profile of many clinically approved anticancer agents.

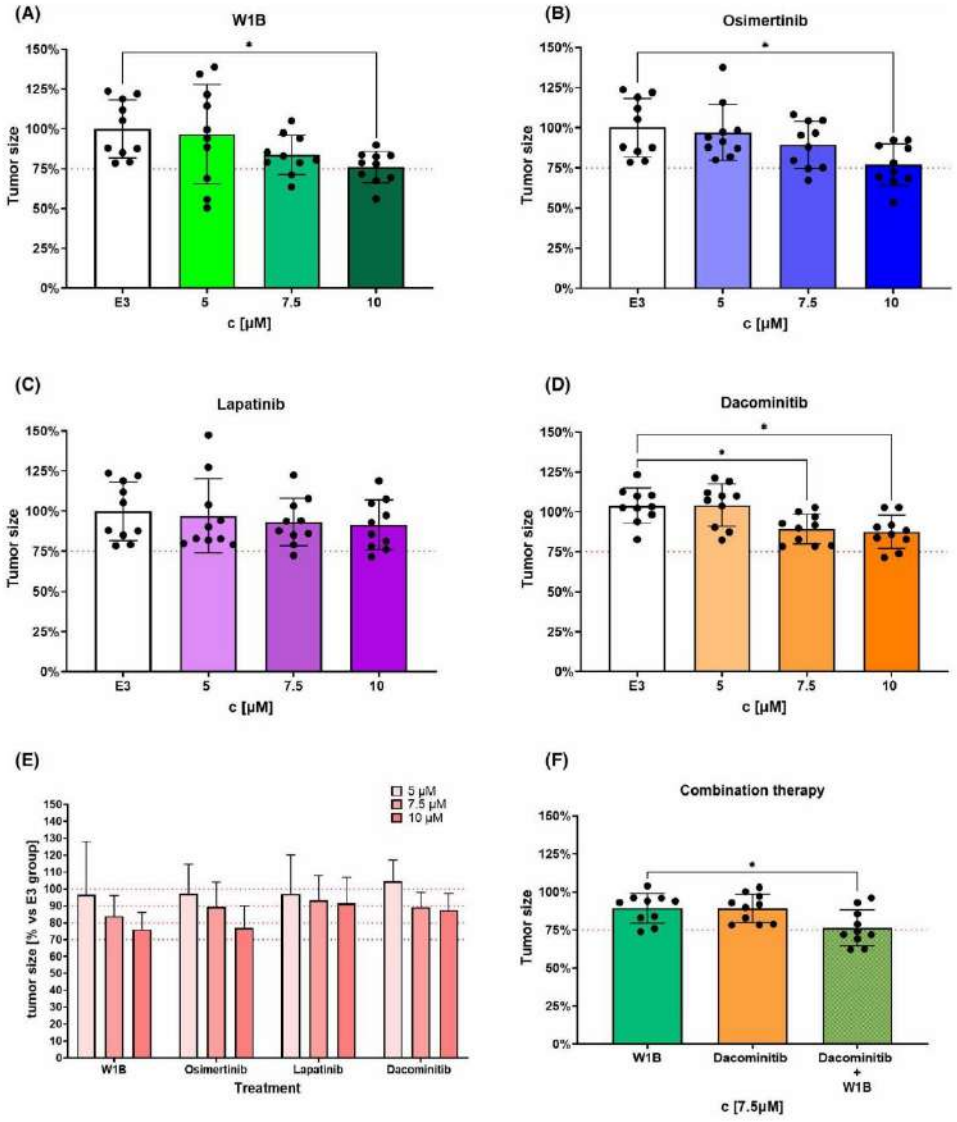

Fig. 10. Antitumor effectiveness of W1B, osimertinib and lapatinib in Danio rerio xenograft model evaluated as a percentage of tumor area measurements for the LN229 xenograft after 72 h of incubation with tested compounds: (A) W1B, (B) osimertinib, (C) lapatinib, (D) dacominitib. (E) Comparison of treatment efficacy at three different concentrations: 5, 7.5, and 10 μM of applied antitumor substances, presented as percentage of tumor size versus the untreated control group (E3) (F) co-treatment of W1B and dacominitib at the dose of 7.5 μM. Data are presented as mean ± SD ($n = 4$) and were analyzed using one-way ANOVA; *$P < 0.05$.

In contrast, W1B demonstrated a superior safety margin for normal tissues. Thus, the promising antiproliferative activity and favorable selectivity of W1B prompted us to explore further its inhibitory effects on several RTKs relevant to GBM.

RTK signaling pathways represent the most commonly dysregulated signaling networks in GBM, with alterations occurring in nearly 90% of tumors [51]. These aberrations, arising from both mutations and gene amplification, lead to receptor overexpression and constitutive activity, thereby highlighting them as key therapeutic targets. Among these, the most prominent are EGFR, IGF1R, PDGFR, and VEGFR. The enzymatic profiling of W1B revealed a distinct selectivity profile, demonstrating preferential activity against specific RTKs. Most notably, W1B exhibited potent inhibitory activity against IGF1R, decreasing its activity by more than 74%. This marked reduction in enzymatic activity in the presence of W1B is indicative of its mechanism as a competitive inhibitor, efficiently engaging the ATP-binding site and thereby impeding the phosphorylation process required for receptor activation. This robust target engagement was further corroborated by MST analysis, which yielded a submicromolar dissociation constant ($K_d = 598$ nM). Such a value highlights a strong and specific interaction between W1B and IGF1R, further supporting its potential as a promising inhibitor. However, it should be emphasized that the full utility of the compound will be established through cellular studies, specifically by evaluating its ability to inhibit receptor-mediated signaling pathways.

Our *in silico* studies provided deep structural insights into the interaction profile of W1B. All calculated binding energies were substantial, indicating strong ligand–protein affinity and effective occupancy of the binding pocket. The slight variability in binding energies between alternative structures of the same proteins (such as IGF1R and EGFR) indicates non-negligible differences in the conformation of the protein's backbone. These results are partially consistent with experimental data; however, they may not fully capture the influence of the complete protein environment or the differences in the inhibitory potency and behavior of W1B toward EGFR and IGF1R.

A critical observation from the structural analysis is the ligand's ability to adopt two distinct poses depending on the target protein. This divergent structural pattern can be rationalized by specific sequence variations within the binding pockets. The structural differences in the ligand–protein complex are qualitatively explained by changes in the interaction characteristics between individual amino acid residues and the W1B. In particular, the presence of Leu858 in EGFR enables CH–π interactions with the aromatic–aliphatic portion of W1B, thereby stabilizing its extended conformation. In contrast, the absence of this interaction in the other structures favors a folded conformation of the ligand. Additionally, regarding changes in the backbone conformation, the most significant structural difference in the proteins appears to be the deviation of the loop connecting the β-strands around Phe1010 (the equivalent in PDB: 1M17 is Phe723). This change allows energetically favorable π-π interactions with the phenyl rings of W1B in the case of EGFR. In the other structures, the analogous residues are shifted away from the binding pocket and do not contact the ligand, while the space left unoccupied by Phe is instead filled by a fragment of W1B in its folded conformation. In addition, the main driving force for binding is the CH–π interactions involving a cluster of nonpolar residues (Val, Leu, and Ala), present in the binding pocket of every considered protein, with the quinazoline scaffold of the W1B. However, the final arrangement of the other fragments of the ligand in the pocket and its conformation strongly depend on the primary structure of the protein.

At the cellular level, activation of IGF1R and EGFR initiates signaling cascades through Akt and RAS proteins, ultimately modulating mTOR expression and regulating key cellular processes such as metabolism, proliferation, growth, survival, and motility. To investigate the mechanism underlying the action of W1B, the protein levels of IGF1R and EGFR, and their downstream signaling elements, including Akt, p-Akt, RAS, as well as two mTOR-regulated proteins: p70 S6 kinase and p-S6 Ribosomal protein were evaluated. Our analysis demonstrated that W1B effectively downregulates both receptors in LN229 cells, leading to a potent inhibition of Akt activation. Interestingly, two downstream effectors of mTOR signaling displayed an interesting expression pattern in response to treatment. First was p70 S6K, a direct substrate of mTORC1, which cooperates with it to augment protein synthesis, ribosomal biogenesis, and stimulate overall anabolic processes [52]. It is also worth mentioning that full activation of mTORC1 requires the presence of amino acids and insulin stimulation [53]. Our analysis demonstrated a significant reduction in the p70 S6K abundance when GBM cells were treated with W1B at 2.3 μM. In contrast, treatment with the higher concentration (3.5 μM) led to an almost 1.9-fold increase compared to untreated cells. A possible explanation for this nonlinear protein response is the differential phosphorylation kinetics at multiple activation sites. This behavior may reflect the

fact that S6K activity and subcellular localization are modulated in response to diverse stimuli [54]. In addition, the p70 S6K may contribute to PI3K/Akt/mTOR feedback loop regulation by suppressing mTORC2 complex and PDK1 activity, thereby leading to Akt inhibition [54–56]. Conversely, the opposite situation was registered for the second analyzed protein – phosphorylated S6 Ribosomal protein, which is also involved in the regulation of protein synthesis, ribosome biogenesis, and cell growth downstream of the mTORC1 signaling pathway. Indeed, W1B significantly reduced the protein level at 3.5 μM concentration (almost 1.6-fold), whereas the lower concentration enhanced protein expression. The last protein analyzed was RAS, an alternative signaling mediator downstream of EGFR and IGF1R activation. Within the RAS pathway, ERK and MEK phosphorylate numerous substrates to regulate cellular responses, including promoting proliferation and differentiation while inhibiting apoptosis. RAS can also bind to the p110 subunit of PI3K, thereby facilitating the activation of Akt [57]. Notably, W1B treatment had minimal effect on RAS levels, suggesting that this pathway is not involved in the cellular response. Collectively, these findings indicate that the novel derivative exerts a strong inhibitory effect on kinase signaling at the cellular level.

Importantly, GBM cells are characterized by reprogrammed metabolism that supports their rapid proliferation, division, and resistance to therapy. A hallmark of this metabolic shift is the increased uptake of glucose and elevated lactate production, even under normoxic conditions. This phenomenon is known as aerobic glycolysis, or the Warburg effect, which provides both energy and biosynthetic precursors to sustain tumor growth. In addition, glucose and acetate have been shown to promote EGFRvIII signaling through mTORC2 in GBM [58]. Elevated levels of pyruvate kinase M2, the enzyme catalyzing the final step of glycolysis, have also been reported in GBM and correlate with enhanced EGFR activity and increased glioma malignancy [59]. Bao *et al.* also showed that high glucose levels increase the activity of GPCR and EGFR receptors, promoting the migration and growth of GBM cells [60]. Another report revealed that EGFR participates in and facilitates glucose transport into cells by binding to and stabilizing sodium/glucose cotransporter 1 (SGLT1) [61,62]. Our experiments showed that culturing LN229 cells in a high-glucose environment (LN229 HG) diminished the potency of W1B, increasing the IC_{50} value to 34.4 μM. In addition, the EGFR expression remained high in glucose-driven GBM cells after exposure to W1B. This lack of EGFR susceptibility is consistent with the findings of Ren *et al.*, who postulated that modulation of EGFR activity does not disrupt its interaction with SGLT1 in prostate cancer [63]. Notably, 23 μM and 35 μM of W1B caused a significant, almost 1.5-fold reduction in IGF1R levels in LN229 HG. These findings indicate that W1B effectively binds to and inhibits IGF1R activity. However, further western blot analysis confirmed the upregulation of the Akt/mTOR signaling pathway, as evidenced by increased levels of p-Akt and p70 S6K. This effect was likely driven by crosstalk between insulin-like receptors and EGFR, reflecting an intracellular compensatory mechanism that is crucial for the efficacy of treatment. Thus, inhibition of IGF1R by W1B and its effect on downstream targets may be counteracted by a robust EGFR-driven activation signal. In addition, Akt activation may govern glucose uptake by directing GLUT expression and trafficking to the cell surface [64], which may also maintain EGFR expression. Moreover, RAS abundance was elevated in LN229 HG cells after treatment with W1B. Such an increase likely reflects a known compensatory feedback mechanism [65], whereby partial inhibition of tyrosine receptors leads to transcriptional upregulation of RAS, enabling downstream signaling to persist despite blockade.

Comparing standard and elevated glucose conditions revealed distinct differences in W1B's efficacy against two key RTKs. While enhanced, glucose-driven cellular metabolism significantly attenuated the compound's inhibition of EGFR, its ability to block IGF1R remained entirely unaffected. This finding corroborates our earlier data from isolated kinase assays, where W1B also exhibited its most potent inhibitory activity against IGF1R. Our strategy for investigating the reduced potential of W1B to inhibit EGFR under conditions of elevated metabolism was to utilize dacomitinib—a quinazoline-based irreversible inhibitor of the ERBB family of kinases, including EGFR, ERBB2 (HER2), and ERBB4 (HER4). Our combination therapy data revealed that the simultaneous administration of W1B and dacomitinib not only preserves the strong suppression of IGF1R but also successfully restores and markedly enhances the inhibition of EGFR activity in the high-glucose model. The quantitative assessment of cytotoxicity further confirmed this interaction, revealing clear synergy (CI = 0.87), particularly in the metabolically active LN229 HG cells.

Collectively, these data demonstrate the high potential of W1B, not only as an IGF1R inhibitor in monotherapy, but also as an EGFR inhibitor in combination therapy, even under conditions of increased cellular metabolism. These findings are

promising and warrant further research, especially in the context of overcoming metabolic-driven drug resistance and developing robust, multi-targeted therapy against GBM.

Our further analyses focused on predicting the ability of W1B to cross the BBB. Among the *in silico* parameters used to determine of BBB permeation, logBB is the most widely applied predictor, reflecting the steady-state distribution ratio between brain and blood. Compounds with logBB ≥ 0.3 are considered readily permeable, $-1 <$ logBB < 0.3 moderately permeable, and logBB < -1 poorly permeable [66,67]. Based on these thresholds, the logBB value of -0.87 determined *in silico* indicates that W1B is only able to cross an intact BBB to a limited extent. However, given that glioblastoma is often associated with focal BBB disruption, this limited penetration could still allow meaningful drug exposure within tumor regions. Although these computational predictions are encouraging, experimental validation in relevant *in vitro* or *in vivo* models is necessary. In addition to the overall penetration of the BBB, the rate at which a substance equilibrates between plasma and brain tissue is influenced by its permeability surface area product (PS) and the unbound fraction in the brain (Fb). When PS or Fb values are low, distribution equilibrium in the CNS is delayed [68]. For a drug to exert its pharmacological effect, only the unbound fraction in the bloodstream is pharmacologically active, although drugs can also associate with plasma proteins and erythrocytes. These principles are fundamental to the free drug hypothesis, which states that distribution in tissue is primarily determined by the concentration of the unbound drug [69,70]. The combination of the relatively high equilibrium rate and very low unbound fractions suggests that W1B is able to efficiently penetrate brain tissue despite the low unbound fraction, probably due to favorable permeability (PS) and limited binding in the brain. Together with the logBB value, these data indicate that W1B has at least partial CNS accessibility, supporting its potential as a candidate for glioblastoma therapy.

Based on physicochemical profiling, W1B can be classified as a highly lipophilic molecule with the capacity to cross biological barriers, including the BBB. According to the Hansch framework, membrane permeability is determined not only by lipophilicity but also by steric and electronic factors. A key predictor of CNS penetration is the topological polar surface area (TPSA), which reflects the number of polar atoms that can form hydrogen bonds. Compounds with TPSA $< 90\,\text{Å}^2$ are generally favored for passive BBB diffusion. W1B has a TPSA of $93.2\,\text{Å}^2$, slightly above this threshold; however, its pronounced lipophilicity may compensate for this limitation. Moreover, the localized BBB disruption commonly observed in glioblastoma could further facilitate drug entry into tumor tissue.

It is important to emphasize that the ability of a drug to cross the BBB is largely determined by its physicochemical properties, with lipophilicity playing a central role alongside potential contributions from active transport mechanisms [71]. The lipophilic properties influence not only the distribution in the membrane, but also the interactions with competing binding sites and metabolizing enzymes. As hydrophobic interactions are crucial for molecular recognition and transport, lipophilicity is usually quantified by partition coefficients measured in different experimental systems [72]. Given its decisive role in barrier penetration and systemic distribution, lipophilicity is a key determinant of CNS accessibility. To complement *in silico* predictions, we utilized HPLC with IAM system, which is consists of a monolayer of phosphatidylcholine covalently bound to a propylamino-silicate carrier and is widely recognized as a robust, non-cell-based *in vitro* approach. The permeability of a substance through biological barriers is largely determined by its membrane partition coefficient, which is difficult to determine directly *in vivo* [73]. The IAM stationary phases are designed to mimic the amphiphilic character of biological membranes, providing a suitable model for assessing passive membrane partitioning and the interactions of compounds with phospholipid-like environments. This approach yields an experimentally robust estimate of a molecule's ability to traverse lipid bilayers, thereby complementing *in silico* predictions and highlighting the central role of lipophilicity in CNS penetration. Although the extrapolated log kw (2.533) is slightly lower than the calculated logPow (4.206), reflecting the distinct experimental setup, both measures consistently support the high lipophilicity of W1B, reinforcing its potential to efficiently cross biological membranes. Although these predictive and biomimetic findings are very promising, they ultimately require experimental validation in complex biological models. A major limitation of *in silico* modeling and non-cell-based IAM systems is their inability to account for active efflux transporters, such as P-gp or BCRP, which heavily restrict CNS entry for many lipophilic drugs. Therefore, the actual brain penetrance of W1B warrants assessment using cell-based *in vitro* BBB models (e.g., Transwell assays) or pharmacokinetic profiling in mouse models. Should passive diffusion prove insufficient under physiological conditions, the delivery of W1B could be supported by advanced

formulation strategies, such as encapsulation in nanocarriers or liposomes, to ensure effective therapeutic concentrations within the brain.

The translation of *in vitro* efficacy to *in vivo* models is a critical step in preclinical drug development. Our zebrafish embryo assays confirmed that W1B possesses a highly favorable safety profile, allowing for administration at higher concentrations without inducing significant toxicity. This indicates a broader therapeutic window for W1B compared to osimertinib and dacomitinib, a finding of particular clinical importance, as systemic toxicity frequently represents a limiting factor in the application of small-molecule kinase inhibitors. In terms of therapeutic efficacy, the robust antitumor activity of W1B in the xenograft model strongly corroborates our earlier *in vitro* findings. The potent *in vivo* tumor reduction (to 76.09%) mirrors the superior *in vitro* antiproliferative effect of W1B ($IC_{50} = 3.57\,\mu M$) when compared to osimertinib ($IC_{50} = 8.99\,\mu M$), dacomitinib ($IC_{50} = 5.84\,\mu M$), and lapatinib ($IC_{50} = 12.60\,\mu M$). While lapatinib demonstrated a toxicity profile similar to W1B, it was markedly less effective in both experimental settings. Conversely, osimertinib and dacomitinib, despite showing comparable or slightly lower efficacy, are associated with significantly greater toxicity. Importantly, the combination of W1B and dacomitinib at $7.5\,\mu M$ concentrations demonstrated an enhanced, synergistic antitumor effect without an accompanying increase in toxicity. This suggests a modest synergistic therapeutic effect and non-overlapping toxicity profiles between the two agents, reinforcing the rationale for our dual-targeted strategy.

Taken together, the concordance between *in vitro* and *in vivo* findings supports the robustness of W1B's anticancer activity. By offering an advantageous balance between safety and efficacy, W1B emerges as a highly promising therapeutic candidate, and its consistent performance across different experimental models provides a strong rationale for advancing it into further preclinical investigations.

5. Conclusion

The study identified W1B, a novel styrylquinazolinone-based small-molecule with potent antiproliferative activity against GBM cells. W1B displayed strong inhibition of IGF1R kinase activity, with additional effects on EGFR and HER2, to a lesser extent. Microscale thermophoresis confirmed high binding affinity toward IGF1R, while molecular docking predicted favorable binding energies and different binding poses within IGF1R and EGFR. Importantly, W1B exerted robust dual receptor inhibition in cellular GBM models and attenuated signaling along the Akt/mTOR axis. Under high-glucose conditions, which more closely reflect the reprogrammed metabolism of GBM, the compound retained selective IGF1R inhibition, although a compensatory mechanism was observed that enhanced activation of the Akt pathway. Combination studies under high-glucose conditions revealed a pronounced synergistic effect with the EGFR inhibitor dacomitinib, underscoring the therapeutic relevance of simultaneously targeting IGF1R and EGFR. Notably, co-administration of both inhibitors led to a marked reduction in receptors' activity in glucose-driven GBM cells. The presented measurements of biomimetic lipophilicity showed that W1B has the potential to penetrate biological membranes, confirming its ability to affect the CNS. Finally, *in vivo* studies on the zebrafish xenograft model confirmed the high anticancer potential of W1B and its favorable safety profile. Given its structural novelty and promising activity profile, W1B represents a valuable lead for the development of multifunctional IGF1R-targeted therapies in GBM. Moreover, W1B demonstrates strong potential for combination therapy, enhancing therapeutic efficacy without compromising the safety profile.

Acknowledgements

This study was financed by National Science Centre grant 2019/35/B/NZ5/04208 and 2024/53/B/NZ5/04013 (KM).

Conflict of interest

The authors declare no conflict of interest.

Author contributions

PR performed microscale thermophoresis, combination therapy, immunoblotting studies, and wrote the text; WC designed and synthesized compounds and wrote the chemistry part; WP performed and analyzed the molecular docking; KS performed and analyzed biomimetic experiments; ABC and EK performed and analyzed *in vivo* studies; RM supervised MJ; MJ synthesized compounds; AMW discussed the results and wrote the manuscript; KM created the research hypothesis, designed the biological experiments, performed the cytotoxicity and kinase inhibition studies, discussed the results, and wrote the manuscript. All the authors read and approved the final version of the manuscript.

Peer review

The peer review history for this article is available at https://www.webofscience.com/api/gateway/wos/peer-review/10.1002/1878-0261.70274.

Data accessibility

Data supporting the findings of this study are available within the article. Source data are available from the corresponding author on request (katarzyna.malarz@us.edu.pl).

References

1 LeRoith D, Roberts CT Jr. The insulin-like growth factor system and cancer. *Cancer Lett*. 2003;**195**(2):127–37.

2 Pollak M. Insulin and insulin-like growth factor signalling in neoplasia. *Nat Rev Cancer*. 2008;**8**(12):915–28.

3 Hemmings BA, Restuccia DF. PI3K-PKB/Akt pathway. *Cold Spring Harb Perspect Biol*. 2012;**4**(9):a011189.

4 Hua H, Kong Q, Yin J, Zhang J, Jiang Y. Insulin-like growth factor receptor signaling in tumorigenesis and drug resistance: a challenge for cancer therapy. *J Hematol Oncol*. 2020;**13**(1):64.

5 Baserga R. The insulin-like growth factor I receptor: a key to tumor growth? *Cancer Res*. 1995;**55**(2):249–52.

6 Pellegrino M, Secli V, D'Amico S, Petrilli LL, Caforio M, Folgiero V, et al. Manipulating the tumor immune microenvironment to improve cancer immunotherapy: IGF1R, a promising target. *Front Immunol*. 2024;**15**:1356321.

7 Carnevalli LS, Sinclair C, Taylor MA, Gutierrez PM, Langdon S, AML C-S, et al. PI3Kalpha/delta inhibition promotes anti-tumor immunity through direct enhancement of effector CD8(+) T-cell activity. *J Immunother Cancer*. 2018;**6**(1):158.

8 Maris C, D'Haene N, Trépant AL, le Mercier M, Sauvage S, Allard J, et al. IGF-IR: a new prognostic biomarker for human glioblastoma. *Br J Cancer*. 2015;**113**(5):729–37.

9 Yin S, Girnita A, Stromberg T, Khan Z, Andersson S, Zheng H, et al. Targeting the insulin-like growth factor-1 receptor by picropodophyllin as a treatment option for glioblastoma. *Neuro Oncol*. 2010;**12**(1):19–27.

10 Niedbala M, Malarz K, Sharma G, Kramer-Marek G, Kaspera W. Glioblastoma: pitfalls and opportunities of immunotherapeutic combinations. *Onco Targets Ther*. 2022;**15**:437–68.

11 Colclough N, Chen K, Johnström P, Strittmatter N, Yan Y, Wrigley GL, et al. Preclinical comparison of the blood-brain barrier permeability of Osimertinib with other EGFR TKIs. *Clin Cancer Res*. 2021;**27**(1):189–201.

12 Padfield E, Ellis HP, Kurian KM. Current therapeutic advances targeting EGFR and EGFRvIII in glioblastoma. *Front Oncol*. 2015;**5**:5.

13 Jentzsch V, Osipenko L, Scannell JW, Hickman JA. Costs and causes of oncology drug attrition with the example of insulin-like growth Factor-1 receptor inhibitors. *JAMA Netw Open*. 2023;**6**(7):e2324977.

14 Tomoszková S, Škarda J, Lipina R. Potential diagnostic and clinical significance of selected genetic alterations in glioblastoma. *Int J Mol Sci*. 2024;**25**(8):4438.

15 Saleem H, Kulsoom Abdul U, Küçükosmanoglu A, Houweling M, Cornelissen FMG, Heiland DH, et al. The TICking clock of EGFR therapy resistance in glioblastoma: target Independence or target compensation. *Drug Resist Updat*. 2019;**43**:29–37.

16 Lemmon MA, Schlessinger J. Cell signaling by receptor tyrosine kinases. *Cell*. 2010;**141**(7):1117–34.

17 Riedemann J, Takiguchi M, Sohail M, Macaulay VM. The EGF receptor interacts with the type 1 IGF receptor and regulates its stability. *Biochem Biophys Res Commun*. 2007;**355**(3):707–14.

18 Kiely PA, O'Gorman D, Luong K, Ron D, O'Connor R. Insulin-like growth factor I controls a mutually exclusive association of RACK1 with protein phosphatase 2A and beta1 integrin to promote cell migration. *Mol Cell Biol*. 2006;**26**(11):4041–51.

19 Buck E, Gokhale PC, Koujak S, Brown E, Eyzaguirre A, Tao N, et al. Compensatory insulin receptor (IR) activation on inhibition of insulin-like growth factor-1 receptor (IGF-1R): rationale for cotargeting IGF-1R and IR in cancer. *Mol Cancer Ther*. 2010;**9**(10):2652–64.

20 Ma Y, Tang N, Thompson RC, Mobley BC, Clark SW, Sarkaria JN, et al. InsR/IGF1R pathway mediates resistance to EGFR inhibitors in glioblastoma. *Clin Cancer Res*. 2016;**22**(7):1767–76.

21 Aiken R, Axelson M, Harmenberg J, Klockare M, Larsson O, Wassberg C. Phase I clinical trial of AXL1717 for treatment of relapsed malignant astrocytomas: analysis of dose and response. *Oncotarget*. 2017;**8**(46):81501–10.

22 Singh R, Tavares D, Dagdigian N. Anti-IGF-I receptor antibody. 2002 US.

23 Hariharan K. Anti-IGF-1R antibodies and uses thereof. 2006 US.

24 Dimitrov DS, Zhu Z, Zhao Q. Human monoclonal antibodies that bind insulin-like growth factor (IGF) I and II. 2014 US.

25 Goetsch L, Broussas M, Charlotte BL, Champion T, Robert A. Igf-1r antibody and its use as addressing vehicle for the treatment of cancer. US.

26 Garcia-Echeverria C, Pearson MA, Marti A, Meyer T, Mestan J, Zimmermann J, et al. *In vivo* antitumor activity of NVP-AEW541-a novel, potent, and selective inhibitor of the IGF-IR kinase. *Cancer Cell*. 2004;**5**(3):231–9.
27 Wittman MD. Pyrrolotriazine kinase inhibitors. US.
28 Carboni JM, Wittman M, Yang Z, Lee F, Greer A, Hurlburt W, et al. BMS-754807, a small molecule inhibitor of insulin-like growth factor-1R/IR. *Mol Cancer Ther*. 2009;**8**(12):3341–9.
29 Chiu YJ, Hour MJ, Jin YA, Lu CC, Tsai FJ, Chen TL, et al. Disruption of IGF-1R signaling by a novel quinazoline derivative, HMJ-30, inhibits invasiveness and reverses epithelial-mesenchymal transition in osteosarcoma U-2 OS cells. *Int J Oncol*. 2018;**52**(5):1465–78.
30 Treu M. 5,8-dihydro-6H-pyrazolo[3,4-h]quinazolines as IGF-1R/IR inhibitors. US.
31 Sabbatini P, Rowand JL, Groy A, Korenchuk S, Liu Q, Atkins C, et al. Antitumor activity of GSK1904529A, a small-molecule inhibitor of the insulin-like growth factor-1 receptor tyrosine kinase. *Clin Cancer Res*. 2009;**15**(9):3058–67.
32 Roychowdhury A, Dinsmore CJ, Roychowdhury A, Sharma R, Vishwakarma RA. Insulin-like growth Factor-1 receptor inhibitors. US.
33 Mularski J, Malarz K, Pacholczyk M, Musiol R. The p53 stabilizing agent CP-31398 and multi-kinase inhibitors. Designing, synthesizing and screening of styrylquinazoline series. *Eur J Med Chem*. 2019;**163**:610–25.
34 Malarz K, Kuczak M, Rurka P, Rawicka P, Boguszewska-Czubara A, Jampilek J, et al. Unveiling the role of Ndrg1 gene on the oxidative stress induction behind the anticancer potential of styrylquinazoline derivatives. *Sci Rep*. 2025;**15**(1):16081.
35 Malarz K, Mularski J, Pacholczyk M, Musiol R. Styrylquinazoline derivatives as ABL inhibitors selective for different DFG orientations. *J Enzyme Inhib Med Chem*. 2023;**38**(1):2201410.
36 Malarz K, Mularski J, Pacholczyk M, Musiol R. The landscape of the anti-kinase activity of the IDH1 inhibitors. *Cancers (Basel)*. 2020;**12**(3):536.
37 Malarz K, Mularski J, Kuczak M, Mrozek-Wilczkiewicz A, Musiol R. Novel benzenesulfonate scaffolds with a high anticancer activity and G2/M cell cycle arrest. *Cancers (Basel)*. 2021;**13**(8):1790.
38 Rurka P, Mularski J, Ziola P, Boguszewska-Czubara A, Jampilek J, Mrozek-Wilczkiewicz A, et al. An insight into the anticancer potential of sulfonated styrylquinazolines as multifunctional agents targeting microtubules. *Bioorg Chem*. 2026;**170**:109517.
39 Shin JE, Jung HA, Park S, Sun JM, Lee SH, Ahn JS, et al. Real-world data of dacomitinib as first-line treatment for patients with EGFR-mutant non-small-cell lung cancer. *Sci Rep*. 2025;**15**(1):4593.
40 Sepulveda-Sanchez JM, Vaz MÁ, Balañá C, Gil-Gil M, Reynés G, Gallego Ó, et al. Phase II trial of dacomitinib, a pan-human EGFR tyrosine kinase inhibitor, in recurrent glioblastoma patients with EGFR amplification. *Neuro Oncol*. 2017;**19**(11):1522–31.
41 Thiessen B, Stewart C, Tsao M, Kamel-Reid S, Schaiquevich P, Mason W, et al. A phase I/II trial of GW572016 (lapatinib) in recurrent glioblastoma multiforme: clinical outcomes, pharmacokinetics and molecular correlation. *Cancer Chemother Pharmacol*. 2010;**65**(2):353–61.
42 Reardon DA, Nabors LB, Mason WP, Perry JR, Shapiro W, Kavan P, et al. Phase I/randomized phase II study of afatinib, an irreversible ErbB family blocker, with or without protracted temozolomide in adults with recurrent glioblastoma. *Neuro Oncol*. 2015;**17**(3):430–9.
43 Hanwell MD, Curtis DE, Lonie DC, Vandermeersch T, Zurek E, Hutchison GR. Avogadro: an advanced semantic chemical editor, visualization, and analysis platform. *J Chem*. 2012;**4**(1):17.
44 Rappe AK, Casewit CJ, Colwell KS, Goddard WA III, Skiff WM. UFF, a full periodic table force field for molecular mechanics and molecular dynamics simulations. *J Am Chem Soc*. 2002;**114**(25):10024–35.
45 Trott O, Olson AJ. AutoDock Vina: improving the speed and accuracy of docking with a new scoring function, efficient optimization, and multithreading. *J Comput Chem*. 2010;**31**(2):455–61.
46 Chou TC, Martin N. CompuSyn for drug combinations: PC software and user's guide: a computer program for quantitation of synergism and antagonism in drug combinations, and the determination of IC50 and ED50 and LD50 values. 2005 ComboSyn, Inc.
47 Baska F, Sipos A, Őrfi Z, Nemes Z, Dobos J, Szántai-Kis C, et al. Discovery and development of extreme selective inhibitors of the ITD and D835Y mutant FLT3 kinases. *Eur J Med Chem*. 2019;**184**:111710.
48 Kulkarni SS, Singh S, Shah JR, Low WK, Talele TT. Synthesis and SAR optimization of quinazolin-4(3H)-ones as poly(ADP-ribose)polymerase-1 inhibitors. *Eur J Med Chem*. 2012;**50**:264–73.
49 Chen EM, Lu PJ, Shaw AY. Synthesis and Antiproliferative evaluation of 2′-Arenesulfonyloxy-5-benzylidene-thiazolidine-2,4-diones. *J Heterocyclic Chem*. 2012;**49**(4):792–8.
50 Rerkrachaneekorn T, Tankam T, Sukwattanasinitt M, Wacharasindhu S. NaI-mediated oxidative amidation of benzyl alcohols/aromatic aldehydes to benzamides via electrochemical reaction. *Tetrahedron Lett*. 2021;**70**:153017.
51 Cancer Genome Atlas Research, N. Comprehensive genomic characterization defines human glioblastoma genes and core pathways. *Nature*. 2008;**455**(7216):1061–8.

52 Artemenko M, Zhong SSW, To SKY, Wong AST. p70 S6 kinase as a therapeutic target in cancers: more than just an mTOR effector. *Cancer Lett.* 2022;**535**:215593.
53 Valvezan AJ, Manning BD. Molecular logic of mTORC1 signalling as a metabolic rheostat. *Nat Metab.* 2019;**1**(3):321–33.
54 Wu X, Xie W, Xie W, Wei W, Guo J. Beyond controlling cell size: functional analyses of S6K in tumorigenesis. *Cell Death Dis.* 2022;**13**(7):646.
55 Jiang Q, Zhang X, Dai X, Han S, Wu X, Wang L, et al. S6K1-mediated phosphorylation of PDK1 impairs AKT kinase activity and oncogenic functions. *Nat Commun.* 2022;**13**(1):1548.
56 Liu P, Gan W, Inuzuka H, Lazorchak AS, Gao D, Arojo O, et al. Sin1 phosphorylation impairs mTORC2 complex integrity and inhibits downstream Akt signalling to suppress tumorigenesis. *Nat Cell Biol.* 2013;**15**(11):1340–50.
57 Krygowska AA, Castellano E. PI3K: a crucial piece in the RAS signaling puzzle. *Cold Spring Harb Perspect Med.* 2018;**8**(6):a031450.
58 Masui K, Tanaka K, Ikegami S, Villa GR, Yang H, Yong WH, et al. Glucose-dependent acetylation of Rictor promotes targeted cancer therapy resistance. *Proc Natl Acad Sci U S A.* 2015;**112**(30):9406–11.
59 Yang W, Xia Y, Cao Y, Zheng Y, Bu W, Zhang L, et al. EGFR-induced and PKCepsilon monoubiquitylation-dependent NF-kappaB activation upregulates PKM2 expression and promotes tumorigenesis. *Mol Cell.* 2012;**48**(5):771–84.
60 Bao Z, Chen K, Krepel S, Tang P, Gong W, Zhang M, et al. High glucose promotes human glioblastoma cell growth by increasing the expression and function of chemoattractant and growth factor receptors. *Transl Oncol.* 2019;**12**(9):1155–63.
61 Engelman JA, Cantley LC. A sweet new role for EGFR in cancer. *Cancer Cell.* 2008;**13**(5):375–6.
62 Weihua Z, Tsan R, Huang WC, Wu Q, Chiu CH, Fidler IJ, et al. Survival of cancer cells is maintained by EGFR independent of its kinase activity. *Cancer Cell.* 2008;**13**(5):385–93.
63 Ren J, Bollu LR, Su F, Gao G, Xu L, Huang WC, et al. EGFR-SGLT1 interaction does not respond to EGFR modulators, but inhibition of SGLT1 sensitizes prostate cancer cells to EGFR tyrosine kinase inhibitors. *Prostate.* 2013;**73**(13):1453–61.
64 Li X, Hu S, Cai Y, Liu X, Luo J, Wu T. Revving the engine: PKB/AKT as a key regulator of cellular glucose metabolism. *Front Physiol.* 2023;**14**:1320964.
65 Feng J, Hu Z, Xia X, Liu X, Lian Z, Wang H, et al. Feedback activation of EGFR/wild-type RAS signaling axis limits KRAS(G12D) inhibitor efficacy in KRAS (G12D)-mutated colorectal cancer. *Oncogene.* 2023;**42** (20):1620–33.
66 Fan Y, Unwalla R, Denny RA, di L, Kerns EH, Diller DJ, et al. Insights for predicting blood-brain barrier penetration of CNS targeted molecules using QSPR approaches. *J Chem Inf Model.* 2010;**50** (6):1123–33.
67 Vilar S, Chakrabarti M, Costanzi S. Prediction of passive blood-brain partitioning: straightforward and effective classification models based on in silico derived physicochemical descriptors. *J Mol Graph Model.* 2010;**28**(8):899–903.
68 Liu X, Smith BJ, Chen C, Callegari E, Becker SL, Chen X, et al. Use of a physiologically based pharmacokinetic model to study the time to reach brain equilibrium: an experimental analysis of the role of blood-brain barrier permeability, plasma protein binding, and brain tissue binding. *J Pharmacol Exp Ther.* 2005;**313**(3):1254–62.
69 Celestin MN, Musteata FM. Impact of changes in free concentrations and drug-protein binding on drug dosing regimens in special populations and disease states. *J Pharm Sci.* 2021;**110**(10):3331–44.
70 Liu H, Dong K, Zhang W, Summerfield SG, Terstappen GC. Prediction of brain:blood unbound concentration ratios in CNS drug discovery employing in silico and in vitro model systems. *Drug Discov Today.* 2018;**23**(7):1357–72.
71 Waterhouse RN. Determination of lipophilicity and its use as a predictor of blood-brain barrier penetration of molecular imaging agents. *Mol Imaging Biol.* 2003;**5** (6):376–89.
72 Kempińska D, Chmiel T, Kot-Wasik A, Mróz A, Mazerska Z, Namieśnik J. State of the art and prospects of methods for determination of lipophilicity of chemical compounds. *TrAC Trends Anal Chem.* 2019;**113**:54–73.
73 Ong S, Liu H, Qiu X, Bhat G, Pidgeon C. Membrane partition coefficients chromatographically measured using immobilized artificial membrane surfaces. *Anal Chem.* 1995;**67**(4):755–62.

Supporting information

Additional supporting information may be found online in the Supporting Information section at the end of the article.

Fig. S1. ^{1}H NMR and ^{13}C NMR data for compound W1A.
Fig. S2. ^{1}H NMR and ^{13}C NMR data for compound W1B.
Fig. S3. ^{1}H NMR and ^{13}C NMR data for compound W1C.
Fig. S4. ^{1}H NMR and ^{13}C NMR data for compound W2B.
Fig. S5. HRMS data for compound W1A.

Fig. S6. HRMS data for compound W1B.
Fig. S7. HRMS data for compound W1C.
Fig. S8. HRMS data for compound W2B.
Fig. S9. Validation of the adopted docking protocol: comparison of crystallographic poses (colors correspond to atom types) and poses obtained by docking (pink colors). Protein structures from PDB: 1K3A (IGF1R), 1 M17 (EGFR), 2ZM3 (IGF1R), 3EKN (InsR), and 4HJO (EGFR).
Fig. S10. Synergistic effect of W1B and dacomitinib combination therapy in LN229 and LN229 HG cells. Dose–response curves illustrating the effect of W1B, dacomitinib, and their combination and polygonogram graphically representing the drug interactions.
Fig. S11. Densitometric analyses of protein expression. Relative band intensities were normalized to the reference protein (GAPDH, vinculin, cyclophilin β, or cofilin) and expressed as fold-change relative to untreated control cells. Data are presented as mean ± SD ($n = 6$) and were analyzed using one-way ANOVA with Dunnett's post hoc test ($^{*}P < 0.1$, $^{**}P < 0.01$, $^{***}P < 0.001$, $^{****}P < 0.0001$).
Fig. S12. The uncropped western blots treated LN229 and LN229 HG cell lines with W1B compound in 3 different concentrations.
Fig. S13. The uncropped western blots of LN229 HG cells treated with W1B compound, dacomitinib, and their combination.
Table S1. Antiproliferative activity of the tested compounds against MCF-7 and PC-9 cells.
Table S2. Inhibition profile of W1B against non-receptor tyrosine kinases.
Table S3. Combination Index (CI) values shown at fraction affected (Fa) for W1B and Dacomitinib combination in LN229 and LN229 HG cell lines.

12. Scientific achievements

Publications that are not included in the doctoral thesis:

1. P. Rawicka, M. Korzec, M. Dulski, J. Mularski, **P. Rurka**, M. Książek, A. Mrozek-Wilczkiewicz, K. Malarz, Novel pyrido[2,3-d]pyrimidines for bioimaging: Effect of water content on enhanced fluorescence and the mechanism of aggregation-induced blue-shifted emission, Spectrochimica Acta Part A: Molecular and Biomolecular Spectroscopy 344 (2026) 126729. https://doi.org/https://doi.org/10.1016/j.saa.2025.126729

   IF_{2026} = 4.3; MNiSW: 140

2. K. Malarz, J. Korzuch, A. Mrozek-Wilczkiewicz, M. Szubka, **P. Rurka**, K. Małota, A. Herraiz, D. Dreszer, K. Kocot, F. Herranz, M. Rost-Roszkowska, T. Sun, R. Musioł, M. Serda, Aminofullerenes as targeted inhibitors of EGFR: from pancreatic cancer inhibitors to Drosophila m. Toxicology, Nanomedicine 20(6) (2025) 585-601. https://doi.org/10.1080/17435889.2025.2461985.

   IF_{2025} = 4.4; MNiSW: 100

3. P. Zaręba, A.K. Drabczyk, A. Wnorowski, M. Maj, **P. Rurka**, K. Malarz, G. Latacz, K. Nędza, K. Ciura, K.E. Greber, A. Boguszewska-Czubara, P. Śliwa, J. Kuliś, Long-Chain Cyclic Arylguanidines as Multifunctional Serotonin Receptor Ligands with Antiproliferative Activity, ACS Omega 10(7) (2025) 6446-6469. https://doi.org/10.1021/acsomega.4c06456.

   IF_{2025} = 4.3; MNiSW: 70

4. K. Malarz, P. Ziola, D. Zych, **P. Rurka**, A. Mrozek-Wilczkiewicz, Imbalance of redox homeostasis and altered cellular signaling induced by the metal complexes of terpyridine, Scientific Reports 14(1) (2024) 26951. https://doi.org/10.1038/s41598-024-77575-4.

   IF_{2024} = 3.9; MNiSW: 140

5. P. Zaręba, A.K. Drabczyk, A. Wnorowski, M. Maj, K. Malarz, **P. Rurka**, G. Latacz, B. Duszyńska, K. Ciura, K.E. Greber, A. Boguszewska-Czubara, P. Śliwa, J. Kuliś, Low-Basicity 5-HT6 Receptor Ligands from the Group of Cyclic Arylguanidine Derivatives and Their Antiproliferative Activity Evaluation, International Journal of Molecular Sciences 25(19) (2024) 10287. https://doi.org/10.3390/ijms251910287

   IF_{2024} = 4.9; MNiSW: 140

6. M. Kuczak, M. Musiał, K. Malarz, **P. Rurka**, E. Zorębski, R. Musioł, M. Dzida, A. Mrozek-Wilczkiewicz, Anticancer potential and through study of the cytotoxicity mechanism of ionic liquids that are based on the trifluoromethanesulfonate and bis(trifluoromethylsulfonyl)imide anions, Journal of Hazardous Materials 427 (2022) 128160. https://doi.org/https://doi.org/10.1016/j.jhazmat.2021.128160.

   IF_{2022} = 13.6; MNiSW: 200

Patent applications:

1. K. Malarz, W. Cieślik, A. Mrozek-Wilczkiewicz, **P. Rurka**, M. Jasica, R. Musioł; „Pochodna styrylochinazolinonu oraz jej zastosowanie do wytwarzania leków o działaniu przeciwnowotworowym”, 2025, P.452377

Conference presentations:

1. **P. Rurka**, J. Mularski, P. Zioła, P. Rawicka, R. Musioł, K. Bialik-Wąs, A. Mrozek-Wilczkiewicz, K. Malarz; „Advancing Glioblastoma Therapy: Nanocarrier-Enhanced Transport of Quinazolinones”, Young Medicinal Chemists' Symposium, Rome, Italy, September 2024
2. **P. Rurka**, M. Kuczak, P. Rawicka, J. Mularski, A. Mrozek-Wilczkiewicz, K. Malarz; „Inhibiting Tyrosine Kinases with 2-Styrylquinazoline: A Novel Approach to Glioblastoma and Leukemia”, Berlin Brain Tumor Meetings 2024, Berlin, Germany, May 2024
3. **P. Rurka**, P.Rawicka, P. Zioła, A.Foryś, J.Mularski, A. Mrozek-Wilczkiewicz, K. Malarz; „Wykorzystanie nośników liposomowych w kierunku poprawy transportu styrylochinazolonów do komórek glejaka wielopostaciowego”, XI Silesian Scientific Meetings, Ustroń, Poland, May 2024
4. **P. Rurka**, P. Zioła, M. Kuczak, P. Rawicka, R. Musiol, A. Mrozek-Wilczkiewicz, K. Malarz; „MECHANISM OF MOLECULAR ACTION OF STYRYLQUINAZOLINE DERIVATIVE ON GLIOBLASTOMA AND LEUKEMIA CELLS WITH DIFFERENT P53 PROTEIN STATUS”, X Silesian Scientific Meetings, May 2023
5. **P. Rurka**, J. Mularski, P. Zioła, M. Kuczak, P. Rawicka, R. Musiol, A. Mrozek-Wilczkiewicz, K. Malarz; „A NOVEL AND HIGLY SELECTIVE QUINAZOLINONE-BASED DERIVATIVE WITH MULTIAFACED MECHANISM OF ACTION FOR GLIOBLASTOMA THERAPY”, Polish Society of Medicinal Chemistry eliminations, May 2023
6. **P. Rurka**, J. Mularski, P. Zioła, A. Mrozek-Wilczkiewicz, K. Malarz; „NOWE POCHODNE BENZENOSULFONIANOWE O WŁAŚCIWOŚCIACH ANTYMITOTYCZNYCH”, Gliwice Scientific Meetings, May 2022

Other presentations with my contribution = 8

Rewards:

HarSval (RiS ID:12399), WP 2 Grant for bioinformatics course – Oslo, October-November 2024

Polish Society of Medicinal Chemistry, Polish representative for YMCS-EFMC at Rome, September 2024

Travel Grant Nominee for Berlin Brain Tumor Meetings, May 2024

Travel Grant Nominee for XI Silesian Scientific Meetings, May 2024

1st place in X Silesian Scientific Meetings, May 2023 – Best oral presentation

2nd place in Polish Society of Medicinal Chemistry eliminations, May 2023